

UNIVERSITY OF PAVIA

DOCTORAL THESIS

---

**Advanced patient-specific  
modeling and analysis of complex  
aortic structures by means of  
Isogeometric Analysis**

---

*Author:*  
Margherita CODA

*Supervisors:*  
Prof. A. REALI  
Prof. F. AURICCHIO  
*Coadvisors:*  
Prof. R. L. TAYLOR  
Prof. S. TRIMARCHI

*A thesis submitted in fulfillment of the requirements  
for the degree of Doctor of Philosophy*

*in the*

Department of Civil Engineering and Architecture  
Computational Mechanics and Advanced Material Group

January 20, 2019

*“Alcune volte vinci, tutte le volte impari.”*

Proverbio Giapponese

UNIVERSITY OF PAVIA

*Abstract***Advanced patient-specific modeling and analysis of complex aortic structures by means of Isogeometric Analysis**

by Margherita CODA

Isogeometric Analysis (IgA) is an approach steadily consolidating in the field of computational mechanics and based on high-continuity functions, generally used in computer graphics for generating and representing curves and surfaces. The ultimate goal of this doctoral research, is the creation of a set of computational tools based on IgA to provide support to vascular surgeons during the pre-operative planning phase. In particular, one of the major innovations of our work is the use of IgA for structural isogeometric analysis performed on healthy and pathological thoracic aortas as well as the use of a particular type of knot vectors, essential ingredients of IgA, for the construction and analysis of the patient-specific models.

In Chapter 2, pathologies of the aorta will be described in deep in order to understand which are the current medical needs. Subsequently, a review of the computational tools mostly used in cardiovascular biomechanics will be provided.

Chapter 3 focuses on describing IgA basic ingredients. In particular, a detailed explanation of B-splines, NURBS and T-splines basis functions will be provided. Particular attention will be given to the so-called (and so far not extensively used in the IgA community) "unclamped" concept, for the construction of closed and periodic curves and surfaces. The unclamped concept is the key for the creation of a semi-automatic pipeline for the generation and analysis of reliable patient-specific isogeometric models of Thoracic Aortic Aneurysms, starting from DICOM images. The pipeline that will be presented in Chapter 4 is tested on a bigger cohort of patients, belonging to the "iCardioCloud project", a database of CFD studies on patients with thoracic aortic diseases. The ultimate goal of the pipeline is the identification of patients potentially at risk of aneurysm enlargement and rupture.

A more advanced pipeline based on the T-spline technology for the generation of complex bifurcated aortic geometries characterized by an arbitrary topology will be approached in Chapter 5. This framework was born as an attempt to overcome the limitation of the rigid tensor-product structure of B-splines and NURBS basis functions, applied to the creation of branched geometries.

Two real-life applications of NURBS-based IgA to 3D frictionless contact problems between stent devices (for Carotid Artery Stenting - CAS) and deformable surfaces undergoing large deformations will be described in Chapter 6. Performance comparison between IgA and linear (h-FEA) and higher-order FEA (p-FEA) with respect to solution accuracy and computational efficiency will

be shown.

Based on the presented analysis framework, real clinical problems, studied in collaborations with physicians from IRCCS Policlinico San Donato will be approached in Chapter 7. In particular, the application on a case study of thoracic aorta showing a retrograde type A dissection will be presented together with a new algorithm for the application of the real patient-specific pressure distribution derived from CFD analyses on the control points of the Isogeometric model representing the thoracic aorta, to check how the stress distribution at the vessel wall changes with respect to the application of a constant pressure value.

We conclude that we are able to provide physicians with computational tools based on IgA to be used in the pre-operative planning phase and in clinical practice, for reliably simulating big cohorts of patients in a relatively short time, and extracting both single-patient and population-based results.



# Acknowledgements

These last three years have been amazing for me: I had the opportunity to work with great people while traveling and working on things that I really love. For this, I would like to express my special appreciation to Prof. Alessandro Reali: he is the Professor everyone would want, always supportive, encouraging and on your side. He has been a mentor to me and I will always be grateful to him for offering me a PhD position in April 2015 and for having had the opportunity to work with him. He is a great person.

Another giant thanks goes to Prof. Ferdinando Auricchio: if I am passionate about biomechanics it is for you. I still remember when you entered the classroom on my first day of Biomechanics class when I was just a simple undergrad student. The pictures of the amazing things your group was able to do will always be a part of my university memories! Your advices through all these years have been priceless to me.

My highest gratitude goes to Prof. Robert L. Taylor: I will always remember Mary Lou and you as my US grandparents. Thanks for being a tremendous mentor to me, for encouraging me, for teaching me infinite things (both on human and research side) and for making my US days the most special ones. The two experiences I had with you in the US are two of the most valuable things I ever did in my life.

I would like to thank Prof. Michele Conti and Prof. Simone Morganti for being the right men at the right moment, in the right place. This is my final take-home message!

A special and affectionate thanks goes to Elena Faggiano: if I could finish this PhD it is for her. What she did for me between the first and second year of my PhD program, inciting me to reach my goals and pushing me to believe more in my capabilities, has been priceless.

I am really thankful to Prof. Santi Trimarchi and Massimiliano Marrocco Trischitta from Policlinico San Donato for their precious collaboration and for making possible this PhD.

To all my colleagues in the CompMech group: guys, thank you! A special thanks goes to my great office mate Massimo and his capability to always making me laugh (coffee breaks and happy hours won't be the same without you), to Giorgione, Vale and Isa. Thanks for all the times we had a mental break from our computer to build our friendship. You know that having the opportunity to share with you my emotions and feelings about everything has been fantastic and super helpful to me.

None of this would have been possible without the support and deep love of my family. Thanks mom and dad for making me the person I am now: thinking back to all the things we have done since my first day of elementary school make me cry for how much I am grateful to you. And thanks also to my brother Lorenzo and my other "me" Beatrice (chiqui), for all the things that enrich every day our special bond as brothers and sisters.

I left part of my heart in 2315 Camino Dolores, Castro Valley, California and this belongs to two amazing people: Susana and Joseph. It was a sign of the destiny when I choose your room on the AirBnB website as well as learning that you were born the same day of the same year of my mum. I know that I am the daughter that....(you know) and you will always be like a mum to me. Everything we did together, from the garage sales on Saturday mornings to preparing chimichurri at late night with me trying to learn some words in Spanish, are wonderful memories I will always keep in my heart. Muchisimas gracias para todo!

This last part is for you, Rodrigo, for whom I still barely realize how much life has been generous to me: without your love and constant support nothing would have been possible. You made me become aware of who I am, made me understand that sometimes pushing the limit is not too much. No sè lo que haria sin vos: sos el amor de mi vida (con bigote o sin bigote!) y tu hombro siempre serà mi lugar preferido donde relajarme.

# Contents

<b>Abstract</b>	<b>iii</b>
<b>Acknowledgements</b>	<b>v</b>
<b>1 Introduction</b>	<b>1</b>
1.1 Aim of this doctoral research . . . . .	1
1.2 Organization . . . . .	2
<b>2 Thoracic Aortic Disease</b>	<b>5</b>
2.1 Aneurysm: origin, complications and treatment . . . . .	5
2.1.1 The normal aorta . . . . .	5
2.1.2 Origin, prognosis and complications of TAA and TAD . . . . .	7
2.1.3 Current treatment options: open surgery and TEVAR . . . . .	10
2.2 Biomechanics of the TAA . . . . .	14
2.2.1 Main criteria to assess rupture potential . . . . .	16
2.2.2 Biomechanics by means of IgA . . . . .	17
<b>3 Isogeometric Analysis Fundamentals</b>	<b>19</b>
3.1 Introduction . . . . .	19
3.2 B-splines . . . . .	20
3.2.1 Knot vectors and B-spline basis . . . . .	20
3.2.2 B-splines curves . . . . .	22
3.2.3 Clamped and unclamped knot vectors . . . . .	23
3.2.4 Non-uniform rational B-splines (NURBS) . . . . .	32
3.2.5 NURBS surfaces and solids . . . . .	33
3.2.6 Limitations of NURBS-based IgA . . . . .	34
3.2.7 The unstructured T-mesh . . . . .	34
3.2.8 Conclusion . . . . .	38
<b>4 Patient-specific geometrical modeling of thoracic aortic aneurysms</b>	<b>41</b>
4.1 Introduction . . . . .	41
4.1.1 The patient-specific concept in biomechanics . . . . .	41
4.1.2 Aim of the chapter . . . . .	43
4.2 Triangulated Surface Mesh Post-Processing . . . . .	43
4.3 Conduction-based method to get cross-sections of points . . . . .	46
4.4 From cross-sections of points to an IgA-suitable unclamped surface model . . . . .	49
4.5 From an IgA unclamped surface model to an IgA solid model. . . . .	56
4.6 Thoracic Aortic Geometry . . . . .	60
4.7 Analysis Setup . . . . .	60

4.7.1	Material Properties . . . . .	60
4.7.2	Numerical simulations . . . . .	61
4.7.3	Surface extraction operator in FEAP . . . . .	63
4.8	Results . . . . .	64
4.9	Conclusions . . . . .	67
<b>5</b>	<b>Patient-specific modeling of bifurcated geometries</b>	<b>77</b>
5.1	Introduction . . . . .	77
5.2	Preliminary branched geometries . . . . .	77
5.3	Patient-specific complete model of TAA using T-spline . . . . .	83
5.3.1	Conclusion . . . . .	87
<b>6</b>	<b>Towards an accurate simulation of complex contact interactions in biomechanics problems using IgA</b>	<b>97</b>
6.1	Contact problems in vascular biomechanics . . . . .	98
6.1.1	Basic concepts in computational contact mechanics . . . . .	98
6.1.2	Stent crimping simulations . . . . .	101
6.1.3	Stent implant simulation . . . . .	107
6.2	Conclusion . . . . .	113
<b>7</b>	<b>Patient-specific application of the developed methodologies</b>	<b>115</b>
7.1	Collaboration with IRCCS Policlinico San Donato . . . . .	115
7.2	Patient-specific isogeometric structural analyses on TAAs . . . . .	116
7.3	Case study on Retrograde Type A dissection . . . . .	118
7.3.1	Results obtained on the pre- and post-TEVAR geometry . . . . .	121
7.4	Application of the patient-specific pressure distribution obtained from CFD analyses . . . . .	127
7.4.1	Algorithm details . . . . .	128
<b>8</b>	<b>Final remarks</b>	<b>137</b>
8.1	Future developments . . . . .	141
<b>A</b>	<b>FEAP NURBS patch input</b>	<b>143</b>
<b>B</b>	<b>Implementation of the Vorp constitutive model in FEAP</b>	<b>149</b>
<b>C</b>	<b>T-splines input files for FEAP</b>	<b>153</b>
	<b>Bibliography</b>	<b>157</b>

# List of Figures

2.1	Segments of the aorta. rPA = right pulmonary artery. Reproduced from (Erbel et al., 2015) . . . . .	5
2.2	Axial section of the aorta showing its layers: intima, media and adventitia. Reproduced from <i>www.deltagen.com</i> . . . . .	6
2.3	CT scans of thoracic aortas (depicted in red color). A: healthy aorta. B: TAA, note the enlargement in the descending portion with its surrounding thrombus (yellow highlighted area). . . .	8
2.4	Stanford classification of TAD. If the ascending aorta is involved, dissection is defined as Type A. Otherwise, is defined as Type B. . . . .	9
2.5	Axial CT slices of acute (A) and chronic (B) TAD in the descending aorta. . . . .	10
2.6	(a) Fenestrated and a branched devices for arch endovascular replacement. (b) The chimney procedure, all the supraortic vessels are rerouted from the proximal ascending aorta. Reproduced from (Kuratani, 2014) . . . . .	12
2.7	Deployment of a stent-graft for TEVAR. A catheter-guided wire reaches the aneurysmatic section and the the stent-graft is deployed. Reproduced from <a href="http://www.aorta.ca/treatment/tevar/">http://www.aorta.ca/treatment/tevar/</a> . .	13
2.8	Types of endoleak. Classification is based on the anatomical origin of the re-perfusion. Reproduced from (Erbel et al., 2015). .	15
2.9	Patient showing distal endograft migration. Left: CT after surgery. Right: 14 month follow up. . . . .	16
2.10	The Law of Laplace computes the stress acting on the wall (H) based on the blood pressure (P), radius of the chamber (r) and the vascular wall thickness (T). . . . .	17
3.1	(a) Clamped curve. (b) Result of unclamping the quadratic curve in (a). Note how the start and end points of the curve coincide with control points in the case of the clamped curve (a) and how they do not coincide with control points in the case of the unclamped curve (b). . . . .	24
3.2	Close B-spline ring using clamped and unclamped knot vector. The <i>red</i> control point of (a) is $C^0$ and the <i>red</i> overlap of (b) maintains the $C^2$ continuity of the cubic curve. . . . .	25
3.3	Close ring B-splines for clamped and unclamped knot vector respectively. . . . .	25
3.4	Examples of unclamping a degree (2,2) surface in different directions. . . . .	26

3.5	Clamped cubic circular ring defined on the uniform knot vector [3 3 3 3 4 5 6 7 8 8 8 8]. . . . .	27
3.6	Examples of unclamping the clamped closed ring of Figure 3.5 with different knot vectors. (a) unclamping with no wraparound; (c) unclamping with wraparound. . . . .	28
3.7	IgA refinement techniques: $h,p$ and $k$ refinement. . . . .	28
3.8	Unclamped closed ring before (3.8a) and after refinement (3.8b) and their correspondent B-spline basis functions. . . . .	30
3.9	(a) Control polygon of a not-refined cylindric surface. (b) Control polygon of the same cylindric surface, but $k$ -refined. In particular the order of the spline has been raised from $p = 1$ to $q = 2$ only along $v$ , whereas knot insertion has been performed along $u$ & $v$ . Moreover, note how the original (a) and the elevated (b) surfaces are parametrically and geometrically equal. . . . .	31
3.10	Example of FEA mesh obtained from its IgA counterpart. . .	32
3.11	Toroidal geometry: (a) surface, (b) and its control net. . . . .	35
4.1	Flowchart depicting the main steps in a typical patient-specific vascular modeling pipeline: 1) Image processing, 2) Analysis suitable model generation and 3) Analysis. . . . .	42
4.2	Flowchart depicting the main steps in our patient-specific (cardio)vascular modeling pipeline: 1) Image processing, 2) Analysis suitable model generation and 3) Analysis. . . . .	44
4.3	Example of segmentation of an abdominal aorta from CT images. (a) Interactive initialization of a branch through the specification of two seed points (depicted in red color), one within the suprarenal aorta and the other within the right renal artery; (b) result of segmentation after level set evolution. . . . .	45
4.4	Example of segmentation of a thoracic aorta from CT images. Interactive initialization of the main vascular tract through the specification of two seed points (depicted in red color). . . . .	45
4.5	Example of removing and capping the supra-aortic branches of a patient-specific TA. (a) Original TA. (b) Manual selection of the branch that has to be removed. (c) Removal of only one branch. (d) Complete removal and subsequent capping of the branches. . . . .	46
4.6	Example on a test case of the "conduction-based" method we use to get cross-sections of points. (a) Triangulated base mesh. (b) Perform harmonic mapping using the temperature as boundary conditions (i.e., diffuse the temperature). (c) Spline interpolation of the boundary at $t = 1$ with a number of points specified by the user (black points). Perform steepest gradient descent from boundary with temperature $t=1$ downward to temperature $t=0$ , along diffused temperature values. (d) Spline-interpolation of isolines for monotonically increasing temperature values. Starting points for each cross-section have to be aligned to avoid unpleasant effects in the final IgA model. . .	47

4.7	Example on a patient-specific case of the "conduction-based" method we use to get cross-sections of points. (a) Triangulated patient-specific base mesh. (b) Perform harmonic mapping using the temperature as boundary conditions (i.e., diffuse the temperature). (c) Spline interpolation of the boundary at $t = 1$ with a number of points specified by the user (black points). Perform steepest gradient descent from boundary with temperature $t=1$ downward to temperature $t=0$ , along diffused temperature values. (d) Spline-interpolation of iso-lines for monotonically increasing temperature values. Starting points for each cross-section have to be aligned to avoid unpleasant effects in the final patient-specific IgA model. . . .	48
4.8	Example of the application on a test case of the conduction based method including "local refinement" of the sections of points in the regions on the surface that show higher curvature. In particular, the harmonic mapping result obtained using the temperature as boundary condition is shown. . . . .	49
4.9	Parametric directions adopted in the construction of each patient-specific IgA geometry. . . . .	50
4.10	Mapping procedure example on a patient-specific case. In Figure 4.10b, 4.10c and 4.10d, models are shown with their associated control polygon. . . . .	52
4.11	Summary of the main steps we perform to get the patient-specific unclamped surface model of TAA starting from the triangulated mesh extracted from medical images. . . . .	53
4.12	Difference in results in the mapping operation if a clamped (top view) or an unclamped (bottom view) knot vector is used along the circumferential direction of each patient-specific model. The blue arrow helps to focus the attention of the unphysical $C^0$ line(s) that crosses the model vertically if a clamped knot vector is used along $u$ . . . . .	54
4.13	Example on a test case of what can happen after mapping operation if starting points of the sections are not aligned. . . . .	55
4.14	Original branched patient-specific surface used to test the "local refinement" capability addition to the "conduction-based" method, after clipping and capping operations performed using the VTK-based Python code described in Section 4.2. . . .	56

- 4.15 Example of application on the patient-specific case depicted in Figure 4.14 of the "conduction-based" method with the "local refinement" addition in the regions on the surface that show higher curvature. Distance [mm] with respect to the (clipped and capped) original surface extracted from medical images is shown in three cases: IgA model constructed using clamped knot vectors along all the parametric directions (left), IgA model constructed using unclamped knot vectors along the circumferential direction of the model (middle), IgA model obtained using unclamped knot vectors along the circumferential direction of the model and "local refinement" in the zones with higher curvature of the surface, while performing the conduction-based method to get the ordered section of points (right). . . . . 57
- 4.16 Some of the sections computed along the centerline of the capped and cropped version of the model shown in Figure 4.14 are intersecting because of how the algorithm we adopted to compute sections of points along the centerline (`vmtkcenterlinesections`) actually works. . . . . 58
- 4.17 Comparison between the original mapping operation (i.e., the one employing clamped knot vectors along  $u$  and  $v$  parametric directions) result using cross-sections of points obtained with the "conduction-based" method (left figure) and cross-sections of points computed along the centerline of the model (right figure). This picture wants to demonstrate how the unsuitability of the approach that computes cross-sections of points along the centerline was evident since the very beginning of the work, besides the use of clamped knot vector along  $u$  and  $v$  parametric directions. . . . . 59
- 4.18 (a) Cross-section of points of the 3D inner lumen surface plus source points for the steepest gradient descent operation (black points). (b) Normal extrude of a radius-dependent thickness the 3D inner lumen surface to get the 3D outer arterial wall surface. (c) Correspondent cross-sections of points between the inner and outer 3D surfaces (top view). (d) Solid model obtained imposing a linear clamped B-splines between the 3D IgA representations of the inner lumen and outer aortic wall. . . . . 68
- 4.19 Construction of the solid model (c) starting from the 3D inner lumen (a) and outer arterial wall (b) surfaces for a patient specific case. The 3D inner lumen surface is depicted as a quadrilateral mesh (a - Paraview version) just to highlight the difference with the outer arterial wall surface (b - Paraview version) and the solid final model (c - Paraview version). . . . . 69
- 4.20 Parametric directions adopted in the construction of each patient-specific IgA solid model.  $P=3$  is adopted along the circumferential parametric direction  $u$ .  $Q=2$  and  $R=2$  are adopted along the longitudinal parametric direction  $v$  and along the thickness, respectively. . . . . 69



4.21	Thoracoabdominal aneurysms considered in the study. . . . .	70
4.22	a) Key ingredients for IgA TAA Inflation simulations. b) Boundary conditions and model domain. . . . .	71
4.23	Zero-pressure geometries obtained using the method proposed in (Bols et al., 2013). Application on a test - images (a) and (b) - and on a patient-specific case images (c) and (d)). . . . .	72
4.24	Difference between a clamped (left) and an unclamped (right) patient-specific geometry in terms of von Mises stress distribution. Discontinuity in the stress field can be seen in the figure on the left and it is also highlighted by a black arrow. . . . .	73
4.25	Results in terms of von Mises stress ([MPa]) at the vessel wall obtained from IgA-FEAP inflation simulations. In all cases, blue represents the lowest stress magnitude, and red the highest stress magnitude. . . . .	76
4.26	From medical images to analysis: comparison between how much time is required to perform each operation of the pipeline presented in Sections 4.2, 4.3, 4.4 and 4.5 and introduced in Figure 7.3 in case of IgA (top) and FEA (bottom). The names "Definition of computational domain" and "Computational IgA/FEM geometry", are linked to the labels of the columns of Table 4.1. . . . .	76
5.1	Example of branch splitting on a patient-specific carotid artery geometry. Original carotid artery (left). Carotid artery splitted into its main constitutive branches (right). . . . .	78
5.2	Example of a skeleton of an artery turned into a graph. A's represents the connecting nodes and the polylines are the arteries' centerlines. . . . .	79
5.3	(a) Example on a carotid artery patient-specific case of the circumferential map that takes into account the position of each point on the surface mesh, parameterized with respect to the centerline. It spans the interval $(-\pi, +\pi)$ . (b) Sections of points for each branch obtained using the harmonic mapping methods we presented in Chapter 4. . . . .	80
5.4	Ordered (according to the "AngularMetric" array) sections of points for each branch. . . . .	80
5.5	(a) Example of NURBS "Y" basic template (1 "Y") and its control polygon. (b) Example of NURBS "Y" template with 3 "Y"s and its control polygon. . . . .	81
5.6	Sections of points for each branch has to be ordered accordingly to the orientation of the longitudinal direction of each patch. The position of the first section of points for each branch in (a) should coincide with $v = 0$ in the correspondent cylindrical patch in (b). . . . .	82
5.7	Examples of IgA mapping of two patient-specific carotid arteries. . . . .	89
5.9	Example of T-spline surface created from scratch inside the T-spline plug-in for Rhino. . . . .	91

5.10	Examples of transformation of a ".stl" file (a) into a quad-based ".obj" file (b) using the Autodesk ReCap Photo software. . . .	91
5.11	Examples of patient-specific T-meshes created by converting an ".stl" file into a ".obj" file and then the ".obj" file into a T-mesh. . . .	92
5.12	Example of extraordinary points on the T-mesh shown in Figure 5.11a (Rhino view). . . . .	93
5.13	Fine mesh location around extraordinary points in IgA-FEAP for the patient-specific model depicted in Figure 5.11a. . . . .	93
5.14	von Mises stress results on two examples of pathological carotid arteries (CA-1 & CA-2) T-spline meshes. . . . .	94
5.15	von Mises stress result on a patient-specific TA T-spline mesh (TA-1). . . . .	95
5.16	von Mises stress result on a complete patient-specific aorta T-spline mesh (A-1). . . . .	95
6.1	2D contact problem. (a) no contact; (b) contact state. . . . .	99
6.2	Node To Surface (NTS) contact. . . . .	99
6.3	Not uniqueness of the master projection. Left: two projection on the master side. Right: no projection on the master side. . .	100
6.4	Knot-to-segment contact: the Gauss points on the slave surface are highlighted as x. . . . .	100
6.5	Stent model in undeformed configuration with its cylindrical crimper. . . . .	103
6.6	Stent crimping test: radial displacement contour plot. . . . .	104
6.7	Stent Z coordinate. . . . .	105
6.8	Stent crimping test results. Radial reaction force ([N]) taken at different values of the stent Z coordinate for different discretization techniques and for different refinement of the crimper mesh. . . . .	105
6.9	Comparison of the performances on a per-degree-of-freedom basis, between IgA, p-FEA and h-FEA with respect to the resultant reaction force quantity ([N]) in reproducing the stent crimping non-linear effect, using a particular stent design. . .	106
6.10	Stent implant results from (Conti et al., 2011; Auricchio et al., 2011; Conti et al., 2009) . . . . .	108
6.11	Analysis setup specification for stent implant simulation. . . .	108
6.12	Patient-specific vessel modeling for the stent implant simulation. .	109
6.13	Stent deployment test: (a) vessel model; (b) stent model; (c) Deformed configuration after crimping; (d) Deformed configuration after deployment. . . . .	110
6.14	Von Mises stress distribution [MPa] in the post-stenting vessel. . .	111
6.15	Von Mises stress distribution [MPa] in the stent structure. . . .	111
6.16	(a) Artery deformation energy [Nmm] plot for each one of the considered five (5) meshes with respect to simulation time [s]. In each mesh, the number of degrees of freedom of the artery has been progressively increased. "IgA-overkill" is the mesh that shows the finest artery model. (b) Artery deformation energy [Nmm] with respect to the artery DOFs. . . . .	112

6.17	Numerical errors evaluated with respect to the deformation energy of the "IgA-overkill" mesh at the last time-step of the analysis are plot against DOFs (a) and CPU time (b). . . . .	112
6.18	Deformation energy [Nmm] versus simulation time [s] for IgA and the corresponding h-FEA meshes. The results demonstrate how h-FEA low order meshes are far from converging to the same artery deformation energy of the high-order corresponding ones. For this reason, to investigate the issue, we suggest increasing the number of DOFs of the artery as well as running the same contact analyses in another finite element solver like Abaqus. . . . .	113
7.1	Joint collaboration between doctors from IRCCS Policlinico San Donato (MI) and biomedical engineers from University of Pavia (CompMech Group - DICAR). . . . .	116
7.2	iCardioCloud philosophy. Interaction between doctors end engineers is based on a shared cloud technology for exchanging data. . . . .	116
7.3	From medical images to analysis: flowchart summarizing the steps required to obtain a complete patient-specific unclamped TAA solid model. . . . .	117
7.4	From medical images to analysis: example of application on a patient-specific case of the previously introduced flowchart. Colors around each box are related to their corresponding block in Figure 7.3. . . . .	117
7.5	(a) Displacement forces projected in the different proximal landing zones for TEVAR in a Type 2 aortic arch according to the new MALAN classification (Marrocco-Trischitta et al., 2017). Both magnitude and direction of the displacement forces change significantly between adjacent landing zones. (b) Displacement forces mapped in the proximal landing zones for TEVAR per Type of Arch. Displacement forces in zone 3 of Type I arches have smaller magnitude compared to those in zone 3 of Type II and III arches. Both pictures are taken from (Bakel et al., 2017) . . . . .	119
7.6	3D reconstruction of the vessel lumen (a) and the stent-graft wires for the patient under study. . . . .	120
7.7	(a) DF on the pre-TEVAR geometry computed by means of CFD analysis. (b) von Mises stress result computed on the pre-TEVAR geometry by means of the pipeline described in Chapter 4. . . . .	122
7.8	(a) DF on the post-TEVAR geometry computed by means of CFD analysis. (b) CT-scan showing the retrograde Type A dissection. . . . .	122
7.9	Zone subdivision performed on the patient-specific model shown in Figure 7.6. The zone depicted in grey represents the zone where the stent landed. The other two zones represent the native aorta. . . . .	123

7.10	(a) Example of application of the "aba2feap" command. The Medtronic Valiant stent (46-46-150 mm) was first created in Abaqus and then imported in FEAP for testing the conversion code. (b) Quarter of cell of the same stent-graft mesh used for obtaining the properties of the RVE to employ in the simulations.	125
7.11	(a) von Mises stress distribution pre-TEVAR and (b) von Mises stress distribution post-TEVAR using homogenized properties for the surface representing the stent. . . . .	126
7.12	Comparison, on a von Mises stress base, between a test case geometry (a) and the patient-specific case under study, in order to understand if the results we showed in Figure 7.11 were correct. Results between the test and the patient-specific case agree. Results agree also between Figure 7.11b and (b) because they present the same von Mises stress pattern at the vessel wall. Von Mises stress values are different because the ones in Figure 7.11b have been rescaled to the von Mises stress values obtained in the pre-TEVAR case. . . . .	126
7.13	Patient-specific pressure distribution taken at systole and computed by means of CFD analyses on the patient shown in Figure 7.6). . . . .	128
7.14	Longitudinal and circumferential view of the results obtained using a variable pressure applied to the control points of the IgA mesh (Left) and a constant one (Right). . . . .	134
A.1	Examples of unclamping of a $n$ -piece circle with $(2n+1)$ CPs using the strategy described in Chapter 2. The resulting control polygons do not wrap around (see Figures TOP and BOTTOM, RIGHT) because the circles are only $C^0$ continuous in the homogeneous space. The result of the unclamping is that the number of $C^0$ lines is just decreased by one (1) in the final unclamped circle. . . . .	147
A.2	Example of unclamping two $n$ -piece circles by eliminating all junction points (RIGHT, BOTTOM). The difference between the original (RIGHT,TOP) and final (RIGHT,BOTTOM) B-splines basis functions is also showed. . . . .	148
C.1	Example of bicubic T-mesh created in Rhino and imported in FEAP. . . . .	154
C.2	von Mises stress result on the patient-specific TA T-spline mesh shown in Figure C.1. . . . .	156

# List of Tables

4.1	Summary of the time required to perform the operations previously described in Section 4.3, 4.4 and 4.5, to derive the 3D IgA solid geometry for each one of the 10 patient-specific cases under study. In particular, in the column “Definition of computational domain”, the time required to perform steps described in Section 4.3 is indicated, without taking into account the time for the segmentation process and triangulated surface mesh post-processing (see Section 4.2), which usually takes 20 minutes if performed by an expert user. The column “Computational geometry” shows the time required to fulfill steps described in Sections 4.4 and 4.5. Once obtained the stress-free configuration, each derived model is inflated with pressure. The time required to run such structural simulations in IgA-FEAP is listed in column “FEAP CPU time”. . . . .	65
5.1	CPU time for the inflation simulations whose results are shown in Figures 5.14, 5.15, 5.16. . . . .	87
6.1	Parameters values used for the stent in the contact simulations.	103
6.2	Table summarizing for each mesh for each discretization method the value of the radial resultant reaction force obtained in the non linear stent crimping simulations, as well as the number of DOFs of the crimper. . . . .	107
6.3	Analysis of stent deployment: relative errors are evaluated with respect to the finest IgA simulation, i.e. “IgA-overkill” mesh. . . . .	113



# List of Abbreviations

<b>AAA</b>	<b>Abdominal Aortic Aneurysm</b>
<b>ASG</b>	<b>Analysis Suitable Geometry</b>
<b>CAD</b>	<b>Computer Aided Design</b>
<b>CAS</b>	<b>Carotid Artery Stenting</b>
<b>CFD</b>	<b>Computational Fluid Dynamics</b>
<b>CT</b>	<b>Computer Tomography</b>
<b>DICOM</b>	<b>Digital Imaging and COmmunications in Medicine</b>
<b>DOF</b>	<b>Degrees Of Freedom</b>
<b>EVAR</b>	<b>Endovascular Aortic Repair</b>
<b>FEA</b>	<b>Finite Element Analysis</b>
<b>FEAP</b>	<b>Finite Element Analysis Program</b>
<b>FEM</b>	<b>Finite Element Method</b>
<b>FL</b>	<b>False Lumen</b>
<b>KTS</b>	<b>Knot-To-Segment</b>
<b>LZ</b>	<b>Landing Zone</b>
<b>MAP</b>	<b>Mean Arterial Pressure</b>
<b>NTS</b>	<b>Node-To-Segment</b>
<b>NURBS</b>	<b>Non Uniform Rational B Splines</b>
<b>IgA</b>	<b>Isogeometric Analysis</b>
<b>P.S.</b>	<b>Patient Specific</b>
<b>PSCVM</b>	<b>Patient Specific Cardio-Vascular Modeling</b>
<b>PWS</b>	<b>Peak Wall Stress</b>
<b>STL</b>	<b>stereolithography file</b>
<b>TAA</b>	<b>Thoracic Aortic Aneurysm</b>
<b>TAD</b>	<b>Thoracic Aortic Dissection</b>
<b>TEVAR</b>	<b>Thoracic Endovascular Aortic Repair</b>
<b>TL</b>	<b>True Lumen</b>





*Alla mia nonna Giovanna*



# Chapter 1

## Introduction

### 1.1 Aim of this doctoral research

Modern clinical practice for the treatment of cardiovascular diseases is mainly based on the implant of minimally invasive endoprosthesis. To be more effective this requires continuous technological improvements with respects to surgical procedures, planning techniques and device design. In order to achieve a particular patient morphology, it is becoming more and more important in the clinical world to provide physicians an opportunity to simulate the best combination of procedure strategies and medical devices prior to surgical intervention. The ultimate goal of the present research is the creation of a set of computational tools to provide support and “predictive medicine” to vascular surgeons during the pre-operative planning phase. The main area of this work is the establishment of healthy and pathologic thoracic aorta. A focus on stent devices both for TEVAR (Thoracic Endovascular Aortic Repair) and for CAS (Carotid Artery Stenting) is also considered. The work has been developed in collaboration with physicians from IRCCS Policlinico San Donato, San Donato M.se, Milano, Italy.

The development of predictive tools requires a good knowledge of the physiology and pathophysiology of the affected portion of the aorta, as well as a mix of expertise in computational mechanics and constitutive modeling. In particular, a viable constitutive model for the aortic wall is extremely important to predict the non-linear behavior of the thoracic aorta. The same applies to behavior of stent devices, for which computational tools can contribute to designing the “ideal” combination of clinical requirements, as well as to model related procedures like stent crimping and deployment.

To achieve the above goal, a set of proper computational techniques is mandatory to provide an accurate geometric description of the domain, high-continuity of the stress field, reduced computational costs and information to be included in the decision time-line of the clinical routine. These requirements match the key features of Isogeometric Analysis (IgA), a computational approach based on high-continuity functions and steadily consolidating in the field of computational mechanics. An initial motivation behind IgA was a desire to fill the gap between the finite element analysis (FEA) community and the computer aided design (CAD) community. The basic idea is to develop

a computational framework in which the traditional FEA basis functions are replaced by those employed in CAD systems. This implies the ability to describe exactly the computational domain geometry throughout the analysis process, including at the same time, the chance to tune basis functions continuity. All the frameworks that will be proposed here aim at providing a basis for developing accurate and efficient predictive tools that can help clinical researchers.

## 1.2 Organization

The thesis is organized as follow:

- Chapter 2: **Thoracic Aortic Diseases.**

This Chapter builds the bases for describing the aorta, its most common diseases and complications related to aging: Thoracic Aortic Aneurysms (TAA) and Thoracic Aortic Dissections (TAD). Current surgical options are analyzed in depth. Then, an overview of the main criteria to assess aneurysm rupture potential will be given along with a review of the computational tools used in biomechanics to investigate TAA trends of enlargement and rupture using computer models.

- Chapter 3: **Isogeometric Analysis basic concepts.**

This Chapter covers the basics of B-splines, NURBS and T-splines for use in computational analysis. Special attention is focused on the concept of unclamped knot vectors as well as on construction of analysis-suitable geometries.

- Chapter 4: **Patient-specific geometrical modeling of thoracic aortic aneurysms.**

This Chapter illustrates in detail all the steps required for the creation of patient-specific Isogeometric unclamped geometries of TAA's starting from medical (DICOM) images. All the additions used in this doctoral research for the simulations are presented together with results of structural inflation simulations performed on analysis suitable geometries. The final goal of the chapter is demonstrating that we are able to provide physicians with a consistent and objective decision making tool to improve the surgery planning operation-phase. The work performed takes into account that computational simulations should be accurate but also characterized by reduced computational costs to keep pace with the clinical time-line. The identification of patients potentially at risk of aneurysm enlargement and rupture is a rationale behind this chapter. A special focus on the patient-specific concept is given. The results of the above development are implemented in an extended version of the finite element program FEAP (Taylor, 2017) which is denoted as IgA-FEAP.

- Chapter 5: **Patient-specific modeling of bifurcated geometries.**

This Chapter provides specifics for a second option of advanced mesh generation. The developments are directed at creating patient-specific bifurcated aortic geometries characterized by complex and arbitrary topology. To achieve this goal we use a T-spline technology. In particular, the steps to obtain patient-specific analysis-suitable T-meshes starting from medical DICOM images are developed. Some results of preliminary structural inflation simulations are run in IgA-FEAP on these geometries. The focus is application-oriented, always taking into account the needs of the clinical routine time-line.

- Chapter **6: Towards an accurate simulation of complex contact interactions in biomechanics problems using IgA.**

The basic idea behind IgA is to provide a smooth basis able to describe exactly the computational domain geometry throughout the analysis process, including, at the same time, the ability to control the basis function continuity. These peculiar features have been applied with benefits on many critical aspects of FEA, including also contact mechanics. This Chapter focuses on real-life applications of NURBS-based IgA to 3D frictionless contact problems between stent devices and deformable surfaces, undergoing large deformations.

- Chapter **7: Collaborations with IRCCS Policlinico San Donato.**

This Chapter presents some examples of collaboration with physicians from IRCCS Policlinico San Donato. In particular, three studies are presented: the rationale behind each study is given together with all the additions we made in IgA-FEAP and in the previously mentioned pipelines in order to be able to answer physicians requests.

- Chapter **8: Conclusions and future developments.**

This Chapter presents final conclusions of the doctoral research. Moreover, further research developments also are outlined.



## Chapter 2

# Thoracic Aortic Disease

## 2.1 Aneurysm: origin, complications and treatment

### 2.1.1 The normal aorta

The aorta is the ultimate conduit, carrying, in an average lifetime, almost 200 million liters of blood to the body (Erbel et al., 2015). As depicted in Figure 2.1, it is divided by the diaphragm into the thoracic (ascending, arch and descending) and abdominal aorta.

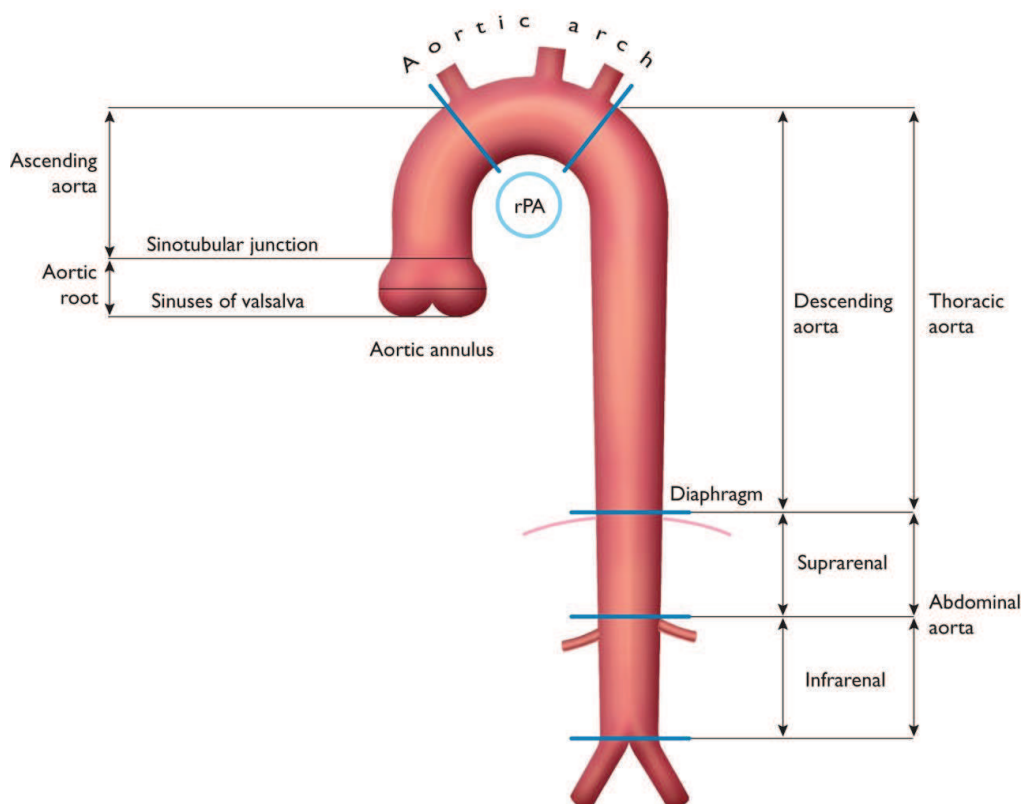


**Figure 2.1** Segments of the aorta. rPA = right pulmonary artery. Reproduced from (Erbel et al., 2015)

The aortic wall is composed histologically of three layers (Erbel et al., 2015): a thin inner tunica intima lined by the endothelium; a thick tunica media characterized by concentric sheets of elastic and collagen fibers with the border zone of the lamina elastica interna and externa, as well as smooth muscle cells; and the outer tunica adventitia containing mainly collagen, vasa vasorum and lymphatic vessels. These layers are shown in a transversal cut in Figure 2.2. In addition to the conduit function, the aorta plays an important role in the control of systemic vascular resistance and heart rate, via pressure-responsive receptors located in the ascending aorta and aortic arch. An increase in aortic pressure results in a decrease in heart rate and systemic vascular resistance, whereas a decrease in aortic pressure results in an increase in heart rate and systemic vascular resistance. Through its elasticity, the aorta has the role of a 'second pump' (Windkessel function) during diastole, which is of utmost importance-not only for coronary perfusion.

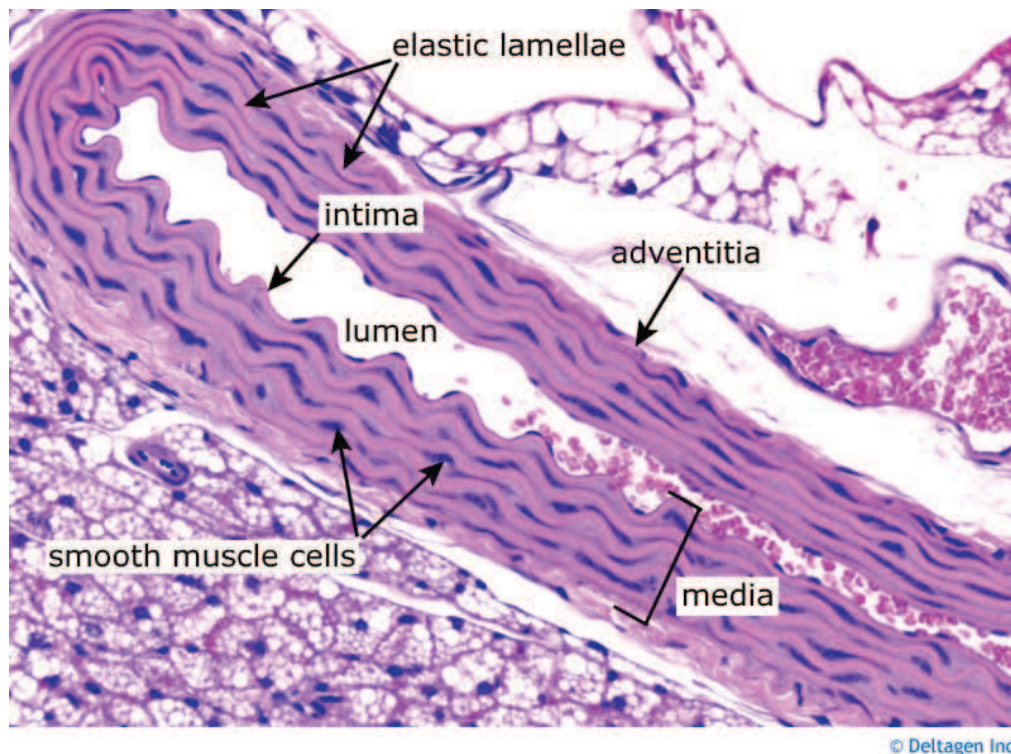


**Figure 2.2** Axial section of the aorta showing its layers: intima, media and adventitia. Reproduced from *www.deltagen.com*.

In healthy adults, aortic diameters do not usually exceed 40 mm and taper gradually downstream. They are variably influenced by several factors including age, gender, body size and blood pressure (Lam et al., 2010). In this regard, the rate of radial expansion is about 0.9 mm in men and 0.7 mm in women for each decade of life (Vriz et al., 2013). This slow but progressive aortic dilation over mid-to-late adulthood is thought to be a consequence of



ageing, related to a higher collagen-to-elastin ratio, along with increased stiffness and pulse pressure (Braverman, Thompson, and Sanchez, 2012; Kälisch et al., 2013).

### 2.1.2 Origin, prognosis and complications of TAA and TAD

Also with ageing, the aortic wall might become pathologically remodeled, and two of the most common aortic syndromes are: Thoracic Aortic Aneurysms (TAA) and Thoracic Aortic Dissection (TAD). In this work we focus extensively on Thoracic Aortic Aneurysms but a brief introduction on Thoracic Aortic Dissection will be also given.

#### Thoracic Aortic Aneurysm

By definition, an aneurysm is an enlargement of more than 50% of the normal diameter of the aortic lumen (Johnston et al., 1991). It constitutes the second most frequent disease of the aorta after atherosclerosis and, depending on its location, is divided into TAA (in the thoracic aorta) or "AAA", acronym for Abdominal Aortic Aneurysm (in the abdominal aorta). Causes and origin of TAA are not completely clear besides congenital pathologies such as Marfan syndrome and bicuspid aortic valve (BAV). The aneurysmal thoracic aorta grows in an indolent manner, increasing by about 1 mm each year (Chau and Elefteriades, 2013). When a certain size is reached, the risk of rupture, dissection, and death increases dramatically. Since it is a commonly "silent" pathology (Kuzmik, Sang, and Elefteriades, 2012), many TAAs are not diagnosed until such complications occur (Elefteriades, 2002; Kuzmik, Sang, and Elefteriades, 2012; Goldfinger et al., 2014). Usually, the diagnosis is made following imaging, performed either for other investigative reasons or for screening purposes. TAA is less frequently revealed by clinical signs of compression, chest pain, aortic valve murmur, or during a complication. In general, patients undergo contrast enhanced CT scans which can visualize thorax vasculature. If an enlargement is seen, the whole aorta tends to be reconstructed and measured in order to isolate the extent of the disease. Figure 2.3 shows a CT slice of a normal aorta and of an aneurysmatic case, together with their 3D reconstruction.

Initial diameter and female sex constitute the primary independent risk factors associated with TAA catastrophic rupture (Brown and Powell, 1999). However, decision to treat TAA is based on many variables such as familial history, rate of growth, location within the arch and, naturally, the general condition of the patient. The principal risk derived from an aneurysm is its rupture with a consequent internal bleeding. Depending on the location of the TAA (ascending aorta, arch or descending aorta), prognosis is known to be different since they are associated with diverse growth rates (Erbel et al., 2015). In a first stage, medical therapy constitutes an appropriate step to reduce shear stress on the diseased segment of the aorta by reducing blood pressure and cardiac contractility. As a reminder, the shear induced by blood in the wall of the vessel is known to be responsible for the initiation

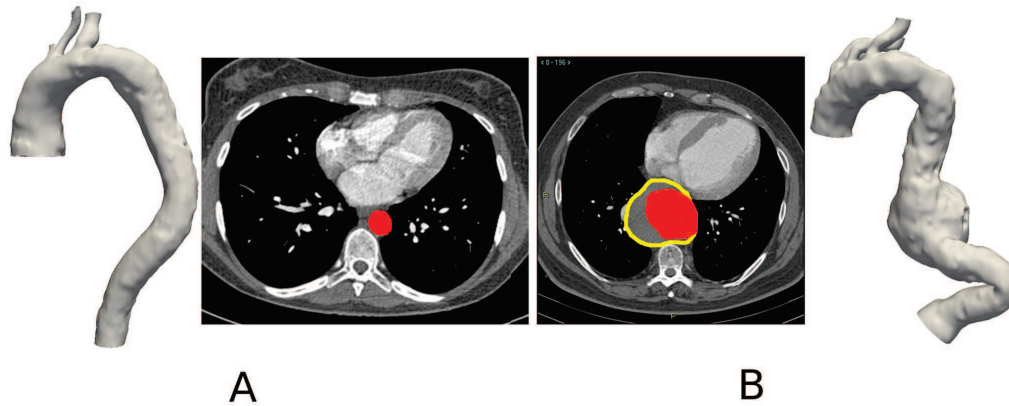


**Figure 2.3** CT scans of thoracic aortas (depicted in red color).  
A: healthy aorta. B: TAA, note the enlargement in the descending portion with its surrounding thrombus (yellow highlighted area).

of the atherosclerosis (Ku et al., 1985). Both its magnitude and its oscillatory nature account for endothelial damage. For more information regarding shear stress and its role in atherosclerosis, the interested reader is referred to (Malek, Alper, and Izumo, 1999). A large number of patients with aortic diseases have co-morbidities such as coronary artery disease, chronic kidney disease, diabetes mellitus, dyslipidaemia, hypertension, etc. Therefore treatment and prevention strategies must be similar to those indicated for these diseases. In chronic conditions, blood pressure should be controlled below 140/90 mmHg, with lifestyle changes and use of antihypertensive drugs, if necessary. An ideal treatment would be the one that reverses the formation of an aneurysm, even though this is still an open issue.

### Thoracic Aortic Dissection

Thoracic Aortic Dissection (TAD) is a member of the so-called acute aortic syndromes. It is defined as the disruption of the medial layer provoked by intramural bleeding, resulting in separation of the aortic wall layers and subsequent formation of a True Lumen (TL) and a False Lumen (FL) with or without communication. In most cases, an intimal tear is the initiating condition, resulting in tracking of the blood in a dissection plane within the media. This process is followed either by an aortic rupture in the case of adventitial disruption or by a reentering into the aortic lumen through a second intimal tear. The dissection can be either antegrade or retrograde (Criado, 2011).

The Stanford classification, as shown in Figure 2.4, takes into account the extent of dissection, rather than the location of the entry tear. The propagation can also affect side branches. Complications include tamponade, aortic valve

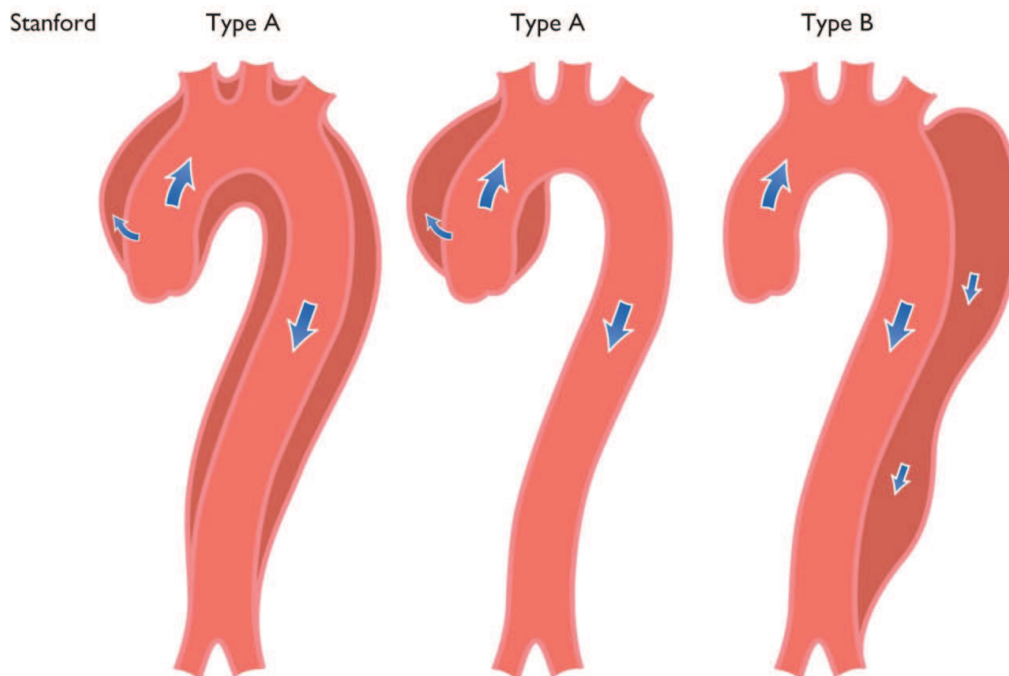


**Figure 2.4** Stanford classification of TAD. If the ascending aorta is involved, dissection is defined as Type A. Otherwise, is defined as Type B.

regurgitation, and proximal or distal malperfusion syndromes. The inflammatory response to thrombus in the media is likely to initiate further necrosis and apoptosis of smooth muscle cells and degeneration of elastic tissue, which potentiates the risk of medial rupture. Opposedly to TAA, abrupt onset of severe chest and/or back pain is the most typical feature of TAD. The pain may be sharp, ripping, tearing, knife-like, and typically different from other causes of chest pain; the abruptness of its onset is the most specific characteristic. Anterior chest pain is more commonly associated with Type A TAD, whereas patients with Type B dissection present more frequently with pain in the back or abdomen. The pain may migrate from its point of origin to other sites, following the dissection path as it extends through the aorta. Following CT scan to confirm diagnosis, the main determinant whether to conduct surgery is the extent of the disease and organ ischaemia. Type A dissection usually involves disruption of the wall in the aortic branches of the arch which feed the brain. In this case, surgery is conducted immediately. Patients with acute Type A dissection suffer double the mortality of individuals presenting with Type B dissection: 25% and 12%, respectively (Moro, Hayashi, and Sogawa, 1999). In the case of type B dissection, the contrast enhanced scan shows whether the arteries supplying blood to the kidneys, liver and intestine initiate at the TL or the FL. In the first case, the patient is recommended medical therapy as described earlier for TAA. In the later, surgery is planned in order to reestablish blood flow to peripheral organs. Besides end-organ ischaemia, complications associated with TAD are aortic valve regurgitation with the subsequent development of congestive

heart failure, myocardial ischaemia or infarction and the development of a post-dissecting aneurysm. When a patient presents no further risk, medical therapy is conducted and follow-up scans are scheduled yearly. It may also be the case in which TAD has no symptoms for years and it is first diagnosed in its chronic phase. Chronicity of aortic dissection is suggested by CT imaging characteristics: thickened, immobile intimal flap, presence of thrombus in the FL, or aneurysms of the thoracic aorta, mostly developed in the distal aortic arch. In symptomatic patients, signs of (contained) rupture such as mediastinal haematoma or pleural effusion may be present. Figure 2.5 shows a typical diagnosis CT for TAD. Notably, in the acute case both the TL and FL are permeable to the contrast medium whereas the chronic case has a fully clotted FL.

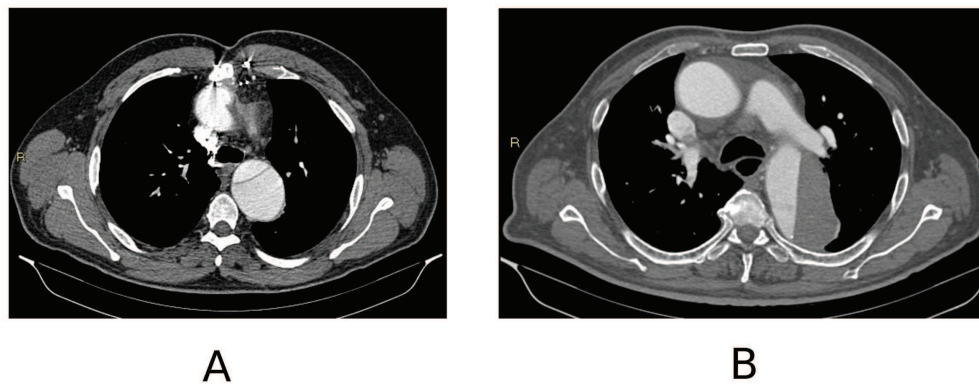


**Figure 2.5** Axial CT slices of acute (A) and chronic (B) TAD in the descending aorta.

### 2.1.3 Current treatment options: open surgery and TEVAR

Currently, there are different treatment options based on the location of the disease.

#### Open aortic repair

If the aneurysm is located in the ascending aorta, the main principle of surgery is that of preventing the risk of dissection or rupture by restoring the normal dimension of the portion. A tubular graft is placed under a short period of aortic clamping, with the distal anastomosis just below the aortic arch. Surgical mortality for isolated elective replacement of the ascending aorta (including the aortic root) ranges from 1.6 – 4.8% and is dependent largely on age and other well-known cardiovascular risk factors at the time of operation (Kallenbach et al., 2013). Mortality rates for elective ascending/arch repair remain low (Perreas et al., 2012; Achneck et al., 2007). In the case of the arch reconstruction, risk of surgery has been also significantly reduced. Innovative arch prostheses, including branching for supra-aortic vessel reconnection, have made the timing of arch reconstruction more predictable. This

is the case for the majority of reconstructions, including acute and chronic dissection, requiring total arch replacement and arrest times from 40 to 60 minutes. Various extents and variants of aortic rerouting (left subclavian, left common carotid and finally brachiocephalic trunk, autologous vs. alloplastic) might also be used. Nowadays, many arch replacements are re-operations for dilated aneurysms after Type A dissection following limited ascending aorta replacement or proximal arch repair performed in emergency (Erbel et al., 2015). The surgical approach to the descending aorta is a left thoracotomy between the fourth and seventh intercostal spaces, depending on the extension of the aortic pathology. Usually the section to be operated is by-passed and a centrifugal pump is used. Since there are no important vessels emerging from this portion, the procedure is much safer. Again, the diseased part is replaced with an arterial graft.

## TEVAR

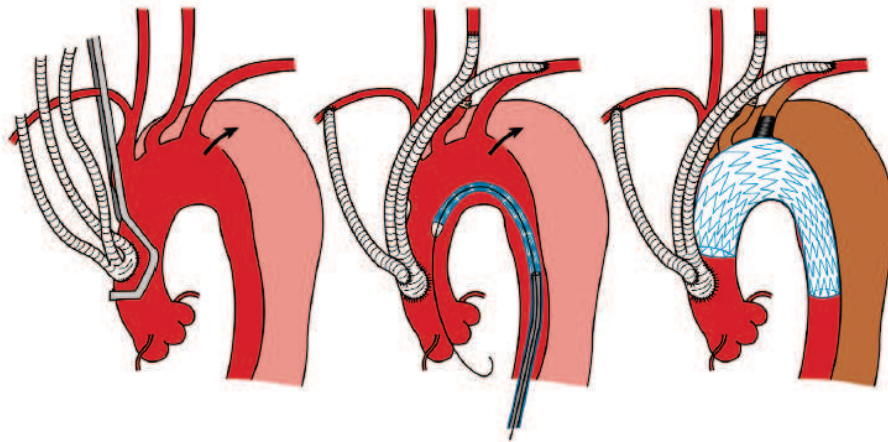
Thoracic Endovascular Aortic Repair aims at excluding an aortic lesion (i.e. aneurysm or FL after dissection) from the circulation by the implantation of a membrane-covered stent-graft across the lesion, in order to prevent further enlargement and ultimate aortic rupture. It is usually associated with relatively low perioperative morbidity and mortality rates (Goodney et al., 2011; Gopaldas et al., 2010; Sachs et al., 2010). Careful planning is of utmost importance for a successful TEVAR procedure. Contrast-enhanced CT represents the imaging modality of choice for planning TEVAR, taking slices from the proximal supra-aortic branches down to the femoral arteries. The diameter and length of the healthy proximal and distal landing zone (LZ) are evaluated to assess the feasibility of TEVAR, along with assessment of the length of the lesion and its relationship to side branches and the iliofemoral access route. Device producers' criteria vary for the LZ characteristics but in average the healthy neck should be of at least 2 cm. In TAA, the stent-graft diameter should exceed the reference aortic diameter at the landing zones by at least 10 to 15% (Kicska and Litt, 2009). This concept is named oversizing and aims at increasing device mechanical stability. In patients with Type B dissection, the stent-graft is implanted across the proximal entry tear to obstruct blood flow into the FL, depressurize the FL, and induce a process of aortic remodeling with shrinkage of the FL and enlargement of the TL. In contrast to TAA, almost no oversizing of the stent-graft is applied. In situations involving important aortic side branches (mostly when the lesion is in the arch), TEVAR is often preceded by limited surgical revascularization of these branches. Another option is a surgical de-branching or the use of fenestrated and branched endografts or the 'chimney technique'. An alternative may be a single, branched stent-graft. Figure 2.6 shows a fenestrated and a branched stent-graft together with a scheme of the chimney technique.

TEVAR is performed by retrograde transarterial advancement of a delivery device carrying the collapsed self-expandable stent-graft as shown in Figure 2.7. Arterial access is obtained either surgically or by the percutaneous approach, using suture-mediated access site closure. From the contralateral





(a)



(b)

**Figure 2.6** (a) Fenestrated and a branched devices for arch endovascular replacement. (b) The chimney procedure, all the supraortic vessels are rerouted from the proximal ascending aorta. Reproduced from (Kuratani, 2014)

femoral side or from a brachial or radial access, a pigtail catheter is advanced for angiography. The stent-graft is delivered over a stiff guide wire. In dissections, it may be challenging to navigate the guide wire into a narrow

TL, which is essential for stent-graft placement. When the target position is reached, the blood pressure is reduced either pharmacologically or using rapid right ventricular pacing to avoid downstream displacement, and the stent-graft is then deployed. Completion angiography is performed to detect any proximal Type I endoleak (an insufficient proximal seal), which usually mandates immediate treatment.

As already introduced, current guidelines for TEVAR use length, size and angulation of the proximal and distal landing zones to determine suitability for endograft deployment (Erbel et al., 2015). However, these criteria do not take into account the local hemodynamic environment in the aorta. The key aspect for endograft stability is secure sealing in the landing zones. Secure sealing depends on frictional stability between the endograft and the aortic wall in the proximal and distal sealing zones to counteract the hemodynamic Displacement Forces (DFs) that act on the surface of the endograft with every heartbeat. Factors that influence this frictional stability are landing zone length and angulation, and the contact condition of the endograft and the aortic wall (Altnji, Bou-Said, and Walter-Le Berre, 2015). Therefore, correct endograft sizing and local landing zone anatomy are crucial factors to secure frictional stability in the landing zones. Factors that influence the hemodynamic DFs are less evident, making them hard to predict in individual cases. Thanks to the advances in computer science, Computational Fluid Dynamics (CFD) can be used to calculate hemodynamics DFs in patient-specific models of the aorta. For a more detailed review on the current available literature on DFs acting on endografts after deployment on the thoracic and abdominal aorta, please see (Bakel et al., 2017).

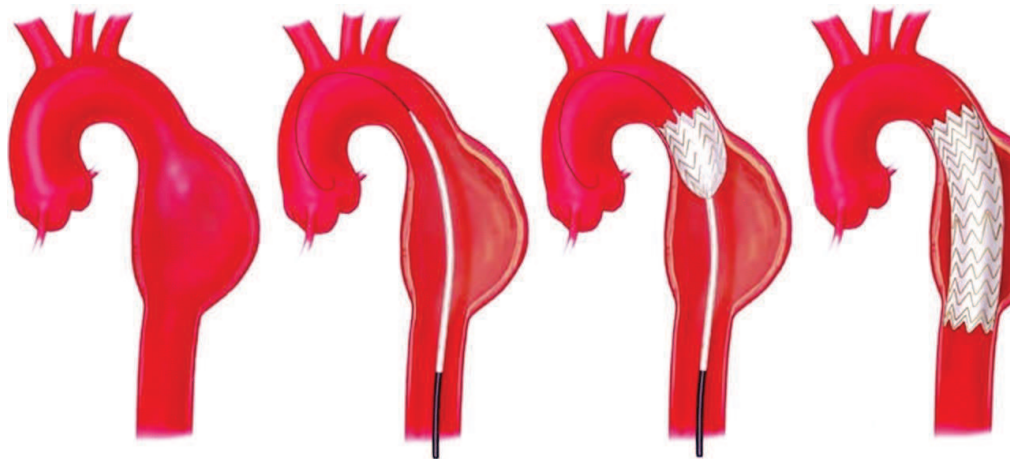


**Figure 2.7** Deployment of a stent-graft for TEVAR. A catheter-guided wire reaches the aneurysmatic section and the stent-graft is deployed. Reproduced from <http://www.aorta.ca/treatment/tevar/>.

### TEVAR complications

### Surgical complications

In TEVAR, vascular complications at the puncture site, as well as aortic and neurological complications, and/or endoleaks have been reported. Ideally, access site complications may be avoided by careful pre-procedural planning. Paraparesis/paraplegia and stroke rates range between 0.8–1.9% and 2.1–3.5%, respectively, and appear lower than those for open surgery (Ben-Shlomo et al., 2014). Mostly along the descending aorta, small vessels named vertebral arteries supplying blood to the spinal cord might be covered with the endoprosthesis fabric, causing stroke. Retrograde dissection of the ascending aorta after TEVAR is reported in 1.3% of patients (Eggebrecht et al., 2008).

### Long term complications

Endoleak describes perfusion of the excluded aortic pathology and occurs both in thoracic and abdominal (T)EVAR. Different types of endoleaks are illustrated in Figure 2.8.

Type I and Type III are regarded as treatment failures and warrant further treatment to prevent the continuing risk of rupture, while Type II endoleaks are normally managed conservatively by a ‘wait-and-watch’ strategy to detect aneurysmal expansion, except for supra-aortic arteries. Endoleaks Types IV and V are indirect and have a benign course. In particular, in Type IV endoleaks, blood can escape into the aneurysm sac through stent material. This type of endoleak is now rare as a result of improved stent prostheses. In endoleaks of Type V, checkups reveal an increase in aneurysm diameter, but no contrast substance can be detected outside the stent prosthesis. This is thought to be caused by a remaining increase in pressure following endovascular aneurysm repair. Treatment is required in case of aneurysm expansion. It is important to note that plain chest radiography can be useful as an adjunct to detect material fatigue of the stent-graft and to follow ‘stent-graft’ and ‘no stent-graft’-induced changes in width, length and angulation of the thoracic aorta. Stent-graft migration is another complication related to the wrong apposition of the device to the arterial wall, which can happen during surgery and in a long-term basis. Usually, prostheses migrate proximally to the heart opposedly to the direction of blood flow. Device migration can cause type I endoleak, damage the arterial wall or obstruct peripheral vessels. Figure 2.9 shows a post-TEVAR patient with a successful surgery that presented proximal migration after 14 months of surgery.

Complete details on TEVAR planning, complications and clinical outcomes can be found in (Grabenwöger et al., 2012) and (Fillinger et al., 2010).

## 2.2 Biomechanics of the TAA

As we have already stated in subsection 2.1.2, since TAA is a commonly “silent” pathology (Kuzmik, Sang, and Elefteriades, 2012), many TAAs are not diagnosed until complications like rupture, dissection and death occur (Elefteriades, 2002; Kuzmik, Sang, and Elefteriades, 2012; Goldfinger et al., 2014). Therefore, there is an increasing need for parameters and markers to



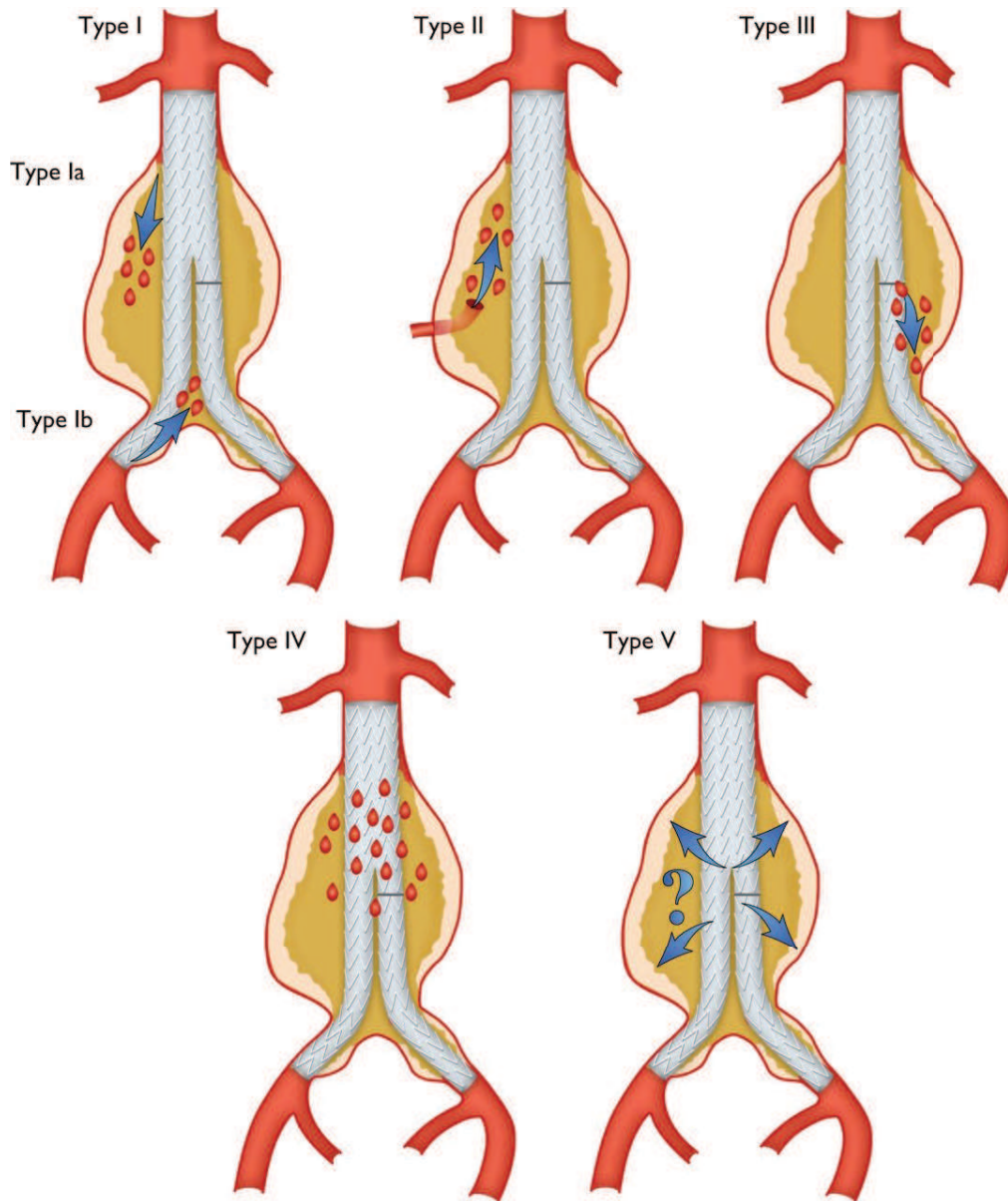


**Figure 2.8** Types of endoleak. Classification is based on the anatomical origin of the re-perfusion. Reproduced from (Erbel et al., 2015).

be used in diagnosing and monitoring TAA so as to prevent natural complications of this disease. Therefore, especially in recent years, many biomedical engineers are trying to understand and explain TAA behaviours and trends of enlargement and rupture using computer models (Shang et al., 2013b; Pasta et al., 2013; Akai et al., 2015). Modern computational techniques can be conveniently applied to TAA modeling, a very interesting but challenging research activity that may lead to the development of some diagnostic and objective decision-making tools for preoperative-planning.

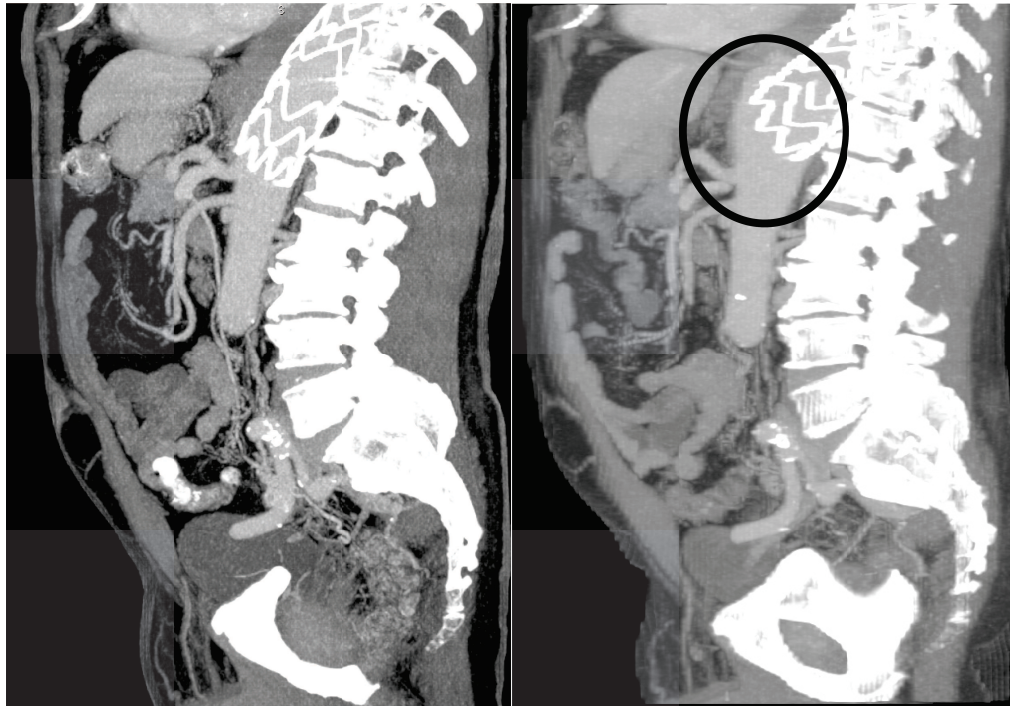


**Figure 2.9** Patient showing distal endograft migration. Left: CT after surgery. Right: 14 month follow up.

### 2.2.1 Main criteria to assess rupture potential

As reported in the literature, current widespread clinical thinking is that TAA rupture is best predicted by monitoring its maximum diameter (Davies et al., 2002). Specifically, in case of asymptomatic aneurysms (symptomatic ones should be resected regardless the size), the risk of rupture is higher when the aneurysm diameter reaches 5.5 cm for the ascending aorta and 6.5 cm for the descending aorta (Elefteriades, 2002; Fillinger et al., 2003). The previous assessment is still under discussion (Fillinger, 2007), since smaller aneurysms also rupture not infrequently (Elefteriades and Farkas, 2010), which undoubtedly questions the “maximum diameter criterion” to evaluate TAA severity. Many (Coady et al., 1997; Azadani et al., 2013) point to the Law of Laplace (Choke et al., 2005) as the theoretical basis for using the “maximum diameter criterion” for TAA rupture potential prediction. This “law” asserts that the stress in the TAA wall is proportional to its diameter (see Figure 2.10).

However, its use to predict TAA rupture potential is inaccurate (Vorp, Raghavan, and Webster, 1998a; Polzer and Gasser, 2015) for two reasons. On one hand, the TAA wall geometry is not a simple cylinder or sphere with a single radius of curvature, for which the Law of Laplace is valid; the TAA wall has a complex shape with both major and minor wall curvatures. The use of only the maximum diameter to predict wall stress in TAA does not take into account the fundamental contributions of local complex wall surface shapes (Vorp, 2007), e.g. profile, tortuosity and asymmetry. On the other hand,

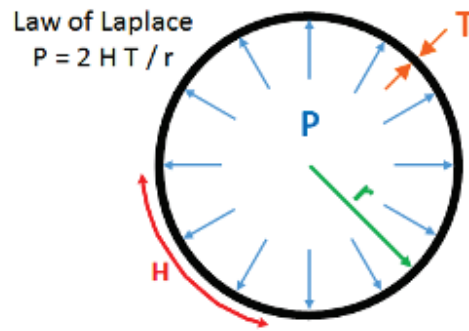


**Figure 2.10** The Law of Laplace computes the stress acting on the wall ( $H$ ) based on the blood pressure ( $P$ ), radius of the chamber ( $r$ ) and the vascular wall thickness ( $T$ ).

wall stress alone is not sufficient to predict TAA rupture. Material failure, including that accompanying TAA rupture, occurs when the mechanical stress acting on the material exceeds its wall strength. So, the greater is the ratio between stress and strength for a particular aneurysm, the greater is the likelihood of rupture. Several studies (Fillinger et al., 2002; Fillinger et al., 2003; Venkatasubramaniam et al., 2004; Heng et al., 2008; Li et al., 2010), mainly conducted on AAAs, by means of Finite Element Analysis (FEA) techniques have demonstrated the superiority of computational wall stress evaluation over the “maximum diameter criterion”. In fact, the maximum stress found anywhere on a particular aortic wall, i.e., the Peak Wall Stress - PWS (Shang et al., 2013b) has been found to estimate the risk of rupture more reliably than the maximum diameter itself (Fillinger et al., 2002; Venkatasubramaniam et al., 2004; Heng et al., 2008). Peak wall stress has been shown in AAAs to be associated with rupture (Fillinger et al., 2003) and aneurysm growth (Li et al., 2010).

As stated by (Martufi et al., 2016), there are sparse applications of numeric simulation techniques to the study of TAAs (Wisneski et al., 2014; Krishnan et al., 2015; Martin, Sun, and Elefteriades, 2015). However, in the work of (Shang et al., 2013b), PWS in TAAs has been found to correlate closely with observed aneurysmal growth rates.

### 2.2.2 Biomechanics by means of IgA

In order for the numerical simulations in aortic aneurysms to be accurate and effective, they usually require a precise reconstruction of the aneurysm geometry, realistic material properties for the arterial wall, inclusion of other aneurysm components (e.g., intraluminal thrombus and wall calcifications), highly accurate and continuous description of the stress field, and reduced computational costs to keep the pace with the clinical routine timeline. All these requirements match the key features of Isogeometric Analysis (Hughes, Cottrell, and Bazilevs, 2005), a computational approach steadily consolidating in the field of computational mechanics and based on high-continuity functions (e.g., Non Uniform Rational B-Splines - NURBS) generally used

in computer graphics for generating and representing curves and surfaces. Therefore, in the present doctoral dissertation we propose new IgA-based modeling and analysis frameworks for the simulation and investigation of wall stress distribution on patient-specific aortic models directly derived from medical images. IgA has already been used in the field of cardiovascular biomechanics as an accurate and cost-effective alternative to classical isoparametric Finite Element Analysis, mainly applied to the study of endovascular stenting (Auricchio et al., 2015), aortic valve closure (Morganti et al., 2015), and structural dynamics simulations of a bioprosthetic heart valve (Kiendl et al., 2015). Moreover, it has been employed for constructing patient-specific models for hemodynamics (Zhang et al., 2007) and for FSI simulations, in particular on bioprosthetic and patient-specific aortic valves (Hsu et al., 2015; Xu et al., 2018). One of the major innovation of our work is the use of IgA for structural isogeometric analysis of thoracoabdominal aneurysms as well as the use of a particular type of knot vectors, essential ingredients of IgA, along the circumferential direction of the isogeometric patient-specific aortic model with the aim to further (and significantly) improve the description of the stress field. Specifically, these particular type of knot vectors are called “unclamped” or “closed”, to be distinguished from the commonly adopted “clamped” or “open” ones. Unclamped knot vectors allow for the creation of periodic surfaces and solids and, in the context of structural IgA of tube-like domains, may guarantee a fully continuous stress field.

## Chapter 3

# Isogeometric Analysis Fundamentals

### 3.1 Introduction

IgA is an emergent and cutting-edge technology that tightly connects computer aided design (CAD) and FEA, hence opening the door for integrated design-through-analysis frameworks (Cottrell, Hughes, and Bazilevs, 2009; Hughes, Cottrell, and Bazilevs, 2005). The central idea of IgA is to leverage, as a basis for analysis, the smooth basis functions used to define the CAD geometry. Therefore, for properly constituted CAD models, isogeometric methods may bypass the mesh generation and refinement steps of classic FEA, which rendered an approximation of the original CAD geometry and may represent up to 80% of the required time to perform the analysis of complex engineering designs or scientific models. CAD descriptions which are suitable for analysis are called analysis-suitable geometries (ASG). The higher-order smooth ASG bases that are used in IgA have been shown to produce superior results when compared to standard  $C^0$  discretizations. The advantages of IgA have been demonstrated in a wide variety of fields of science and engineering, including structural analysis (Casquero et al., 2017; Cottrell et al., 2006; De Lorenzis et al., 2011; Kiendl et al., 2009), fluids (Bazilevs and Akkerman, 2010; Bazilevs et al., 2007; Bazilevs et al., 2010a), fluid-structure interaction (Bazilevs et al., 2008; Bueno et al., 2015; Casquero, Bona-Casas, and Gomez, 2015; Casquero et al., 2016), fracture and damage (Borden et al., 2012; Verhoosel et al., 2011b; Verhoosel et al., 2011a), phase-field analysis (Borden et al., 2012; Gómez et al., 2008; Gomez et al., 2010), shape optimization (Wall, Frenzel, and Cyron, 2008), electromagnetics (Buffa, Sangalli, and Vázquez, 2010), and biomedicine (Bazilevs et al., 2006; Bazilevs et al., 2009; Hsu et al., 2015; Vilanova, Colominas, and Gomez, 2013; Vilanova, Colominas, and Gomez, 2014; Xu, Vilanova, and Gomez, 2016). Additionally, several research groups have been actively developing powerful software packages for IgA, such as GeoPDEs (Falco, Reali, and Vázquez, 2011), igatools (Pauletti et al., 2015), PetIGA (Dalcin et al., 2016).

B-splines and NURBS (Farin and Farin, 2002; Piegl and Tiller, 1997; Rogers, 2000) were the first functional spaces employed to perform IgA and they



are still extensively used nowadays. They are ubiquitous in CAD and can be easily handled to perform analysis. In particular, isogeometric methods based on these functional spaces are geometrically exact, provide enhanced accuracy per degree of freedom, and enable higher global continuity ( $C^{p-1}$  for spline spaces with polynomial degree  $p$ ) (Akkerman et al., 2008; Cottrell, Hughes, and Bazilevs, 2009). Methodologies such as Bèzier extraction (Borden et al., 2011; Scott et al., 2011) simplify the implementation of isogeometric basis function technology into existing finite element frameworks.

Standard Galerkin discretizations and Gaussian quadrature are commonly used in IgA (Cottrell, Hughes, and Bazilevs, 2009). Recent developments have provided promising quadrature strategies to improve the efficiency of isogeometric methods (Auricchio et al., 2012; Calabro, Sangalli, and Tani, 2017; Hughes, Reali, and Sangalli, 2010). However, there are alternative numerical methods that are compatible with IgA, such as collocation, least-square FEA, and meshless methods (Cottrell, Hughes, and Bazilevs, 2009). Another important property of IgA that has been recently proven is that Galerkin solutions can be obtained with only one evaluation per degree of freedom using the concept of variational collocation (Gomez and De Lorenzis, 2016).

Other ASG descriptions have been proposed, such as hierarchical B-splines (D’Angella et al., 2018) and locally refined splines (LR splines) to accommodate local adaptivity in IgA (extremely useful to address those problems whose solution presents highly localized features that call for a finer mesh, while coarser elements can be used elsewhere), and T-splines, a generalization of NURBS that are locally refinable and capable of modeling complicated designs as a single, watertight geometry. Analysis-suitable T-splines are a subset of T-splines with the same mathematical properties as NURBS.

In the following sections, the fundamentals of B-splines, NURBS and T-splines will be illustrated.

## 3.2 B-splines

### 3.2.1 Knot vectors and B-spline basis

The B-spline parametric space is local to *patches* rather than elements. Patches play the role of *subdomains* within which element types and material models are assumed to be uniform. A knot vector in one dimension is a sequence in ascending order of parameter values, written as  $\Xi = \{\xi_1, \xi_2, \dots, \xi_{n+p+1}\}$ , where  $\xi_A$  is the  $A^{th}$  knot,  $A$  is the knot index,  $A = 1, 2, \dots, n + p + 1$ ,  $p$  is the order of the B-spline basis, and  $n$  is the number of basis functions which comprise the B-spline. Given a knot vector  $\Xi$ , the B-spline basis functions are defined recursively by the Cox-de Boor recursion formula, starting with the zeroth order basis function ( $p = 0$ ) given by:

$$N_A^0(\xi) = \begin{cases} 1 & \text{if } \xi_A \leq \xi < \xi_{A+1}, \\ 0 & \text{otherwise} \end{cases} \quad (3.1)$$

For  $p = 1, 2, 3, \dots$  the basis functions are defined by using the Cox-de Boor recursion formula:

$$N_A^p(\xi) = \frac{\xi - \xi_A}{\xi_{A+p} - \xi_A} N_A^{p-1}(\xi) + \frac{\xi_{A+p+1} - \xi}{\xi_{A+p+1} - \xi_{A+1}} N_{A+1}^{p-1}(\xi) \quad (3.2)$$

B-splines are characterized by the following properties:

- *Partition of unity*

$$\sum_{A=1}^n N_{A,p}(\xi) = 1 \text{ with } \xi \in [\xi_1, \xi_{n+p+1}] \quad (3.3)$$

- *Pointwise non-negativity*

$$N_{A,p}(\xi) \geq 0 \text{ with } A = 1, 2, \dots, n \quad (3.4)$$

- *Linear independence*

$$\sum_{A=1}^n c_A N_{A,p} = 0 \Leftrightarrow c_A = 0, A = 1, 2, n \quad (3.5)$$

- *Compact support*

$$\{\xi | N_{A,p}(\xi) > 0\} \subset [\xi_A, \xi_{A+p+1}] \quad (3.6)$$

- *Control of continuity.* If  $\xi_A$  has multiplicity  $k$  (i.e.,  $\xi_A = \xi_{A+1} = \dots = \xi_{A+k+1}$ ), then the basis functions are  $C^{p-k}$ -continuous at  $\xi_A$ . When  $k = p$ , the basis is  $C^0$  and interpolatory at the location.

All these features are useful in a finite element context. The first four properties we mentioned above ensure a well conditioned and sparse stiffness matrix. The last property allows continuity to be reduced to better resolve steep gradients, while the higher continuity leads to superior accuracy per DOF compared with  $C^0$ -continuous bases. Additionally, B-splines can be used to build a basis that spans the same space as classical  $p$ -version finite elements (i.e., a basis of order  $p$  that is  $C^0$  across element boundaries). This is the Bernstein basis (Lorentz, 2012). The mathematical properties we introduced (partition of unity, non-negativity, convex hull property, linear independence), contributes to the definition of the "analysis-suitable" concept.

In particular, by "analysis-suitable" we mean the exact representation of the geometry due to the smooth geometric basis functions with efficient mathematical properties. "Smooth" refers to the  $C^l$  inter-element continuity, with  $0 \leq l < p$ , and  $p$  is the polynomial order.

### 3.2.2 B-splines curves

B-spline curves in  $\mathbb{R}^{d_s}$  are constructed by taking a linear combination of B-splines basis functions, where  $d_s$  is the spatial dimension. The coefficients of the basis functions are referred to as *control points*, which are the analogous to the nodal coordinates in the finite element analysis. Piecewise linear interpolation of the control points gives the so called *control polygon*. Generally, control points are not interpolated by B-spline curves. Given  $n$  basis functions,  $\mathbf{N} = \{N_{A,p}\}_{A=1}^n$  and the corresponding control points  $\mathbf{P} = \{\mathbf{P}_A\}_{A=1}^n$ , a piecewise-polynomial *B-spline curve* is given by:

$$\mathbf{C}(\xi) = \sum_{A=1}^n N_{A,p}(\xi) \mathbf{P}_A \quad (3.7)$$

Important properties of the B-splines can be summarized as follow:

- They have continuous derivatives of order  $p - 1$  in the absence of repeated knots or control points.
- The number of continuous derivatives by  $k$  is decreased by repeating a knot or control point  $k$  times.
- An affine transformation of a B-spline curve is obtained by applying the transformation to the control points. This property is referred to as *affine covariance*.

A multivariate B-spline basis is defined from a tensor product of univariate B-spline bases (Farin and Farin, 2002; Piegls and Tiller, 1997; Rogers, 2000). The properties of multivariate B-spline basis functions follow from the corresponding properties of their univariate counterparts. B-spline surfaces and solids can be built using a bivariate or trivariate spline basis in Eq. 3.2.2, respectively. In particular, given three knot vectors  $\Xi^1 = \{\xi_1, \xi_2, \dots, \xi_{n+p+1}\}$ ,  $\Xi^2 = \{\eta_1, \eta_2, \dots, \eta_{m+q+1}\}$ ,  $\Xi^3 = \{\zeta_1, \zeta_2, \dots, \zeta_{l+r+1}\}$ , (one for each direction), and their associate univariate B-spline basis functions  $N_{i,p}(\xi)$ ,  $M_{j,q}(\eta)$ , and  $L_{k,r}(\zeta)$ , B-spline basis functions for surfaces and volumes are defined by the tensor product of the univariate B-spline basis functions. In two dimensions, the surface B-spline basis functions are defined as:

$$R_A^{p,q}(\xi, \eta) = \sum_{i=1}^n \sum_{j=1}^m N_{i,p}(\xi) M_{j,q}(\eta) P_{i,j} \quad (3.8)$$

In three dimensions, the volume B-spline basis functions are defined as:

$$R_A^{p,q,r}(\xi, \eta, \zeta) = \sum_{i=1}^n \sum_{j=1}^m \sum_{k=1}^l N_{i,p}(\xi) M_{j,q}(\eta) L_{k,r}(\zeta) P_{i,j,k} \quad (3.9)$$



For a detailed review on splines, the interested reader is referred to (Farin and Farin, 2002; Piegl and Tiller, 1997; Rogers, 2000).

### 3.2.3 Clamped and unclamped knot vectors

A knot vector  $\Xi$  can be “clamped” (or “open”) or “unclamped” (or “closed”); the term refers to whether or not the first and last knot values are repeated with multiplicity equal to  $p + 1$ , i.e., polynomial degree of the spline plus one. A knot vector can be uniform or non uniform with reference to the knot spacing. To be uniform and unclamped, only the “internal” knot spans must be of equal length. Some examples of knot vectors are:

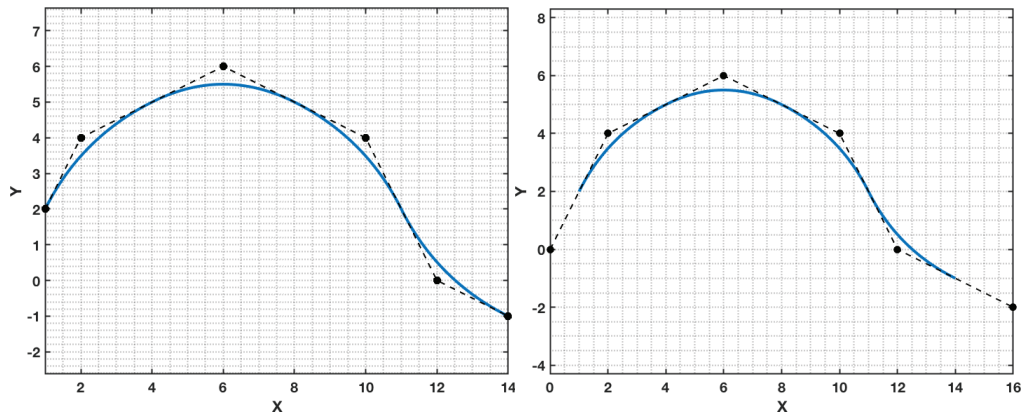
- clamped, uniform:  
 $\{0\ 0\ 0\ 0\ 1\ 2\ 3\ 4\ 4\ 4\ 4\}$   
 $\{-0.5\ -0.5\ -0.5\ 1\ 2.5\ 4\ 4\ 4\}$
- clamped, nonuniform:  
 $\{0\ 0\ 0\ 2\ 3\ 6\ 7\ 7\ 7\}$   
 $\{0\ 0\ 0\ 0\ 1\ 2\ 2\ 3\ 4\ 5\ 5\ 5\ 5\}$
- unclamped, uniform:  
 $\{-3\ -2\ -1\ 0\ 1\ 2\ 3\ 4\ 5\}$   
 $\{0\ 1\ 2\ 3\ 4\ 5\ 6\ 7\ 8\ 9\ 10\ 11\}$
- unclamped, nonuniform:  
 $\{0\ 0\ 1\ 2\ 3\ 4\}$   
 $\{-2\ -1\ 0\ 4\ 5\ 6\ 7\}$

Clamped knot vectors generate B-splines basis functions enjoying the Kronecker delta property at the extremes of a patch. This means that the values of the B-splines basis functions at the extreme of the patch is equal to 1. This is different in the case of unclamped knot vectors. As a matter of fact, unclamped, uniform B-splines basis functions are all translates of one another, without enjoying at the extremes of a patch the Kronecker delta property, even if still maintaining the partition of unity one. Unclamped is mathematically equivalent to periodic, uniform, and these knot vectors can be used to construct closed curves and surfaces or to maintain greater than  $C^0$  continuity between patches. This is obtained by setting the coordinates of the start and end  $p$  control points to the same values. For this case, the beginning and ending overlapped knot spacings must be equal. On the other hand, clamped is synonymous with non-periodic. Hence, these knot vectors can be used to define open curves and surfaces, both uniform and non-uniform.

To give some simple examples of the unclamped concept, we first consider a *quadratic* clamped and unclamped B-spline curve (see Figure 3.1) and a

clamped and an unclamped B-spline circular *cubic* ring (see Figure 3.2). Figure 3.1 would like to show how, if a clamped knot vector is used, the start and end points of the curve coincide with control points (Figure 3.1a), whereas this does not happen in the case of unclamped knot vectors. Figure 3.2 (left) shows the control polygon and ring (which is not a perfect circle since all the control weights are unity) of the curve constructed using a clamped knot vector (i.e., [0 0 0 0 1 2 3 4 5 6 7 8 8 8 8]). The red marked control point is a location that can only be  $C^0$ . The right figure shows the *same* ring built using an *unclamped knot vector* (i.e., [0 1 2 3 4 5 6 7 8 9 10 11 12 13 14]). The red marked portion denotes control-points that are overlapped to preserve continuity. Figure 3.3 shows the spline functions for each of clamped and unclamped knots. There are eleven (11) functions for each form; however, *due to the overlap of the control points*, three (3) of the functions are in fact continuations of one another as the number indicate.

Both curves in the parametric space are geometrically continuous; the one in Figure 3.2a shows the presence of a  $C^0$  line, whereas the one in Figure 3.2b is closed with  $C^{p-1}$  continuity and no  $C^0$  lines are present. This is strictly connected with the fact that the first and last points of the curve coincide with **control points** in the case of the clamped B-spline curve (Figure 3.2a) whereas this does not happen in the unclamped B-spline curve case (Figure 3.2b).  $P$  control points are wrapped around at the end. In this example,  $p = \text{three (3)}$ ; hence, three (3) control points,  $P_9 = P_1$ ,  $P_{10} = P_2$ ,  $P_{11} = P_3$  are wrapped around at the end (see Figure 3.2b). In Appendix A the reader may find the data necessary to build in the Finite Element Analysis Program (FEAP) (Taylor, 2017), used in this work for the simulations, the clamped and unclamped ring shown in Figure 3.2.



(a) Clamped quadratic curve defined on the knot vector [-1 -1 -1 0 1 2 3 3 3]. (b) Unclamped quadratic curve defined on the knot vector [-3 -2 -1 0 1 2 3 4 5].

**Figure 3.1** (a) Clamped curve. (b) Result of unclamping the quadratic curve in (a). Note how the start and end points of the curve coincide with control points in the case of the clamped curve (a) and how they do not coincide with control points in the case of the unclamped curve (b).

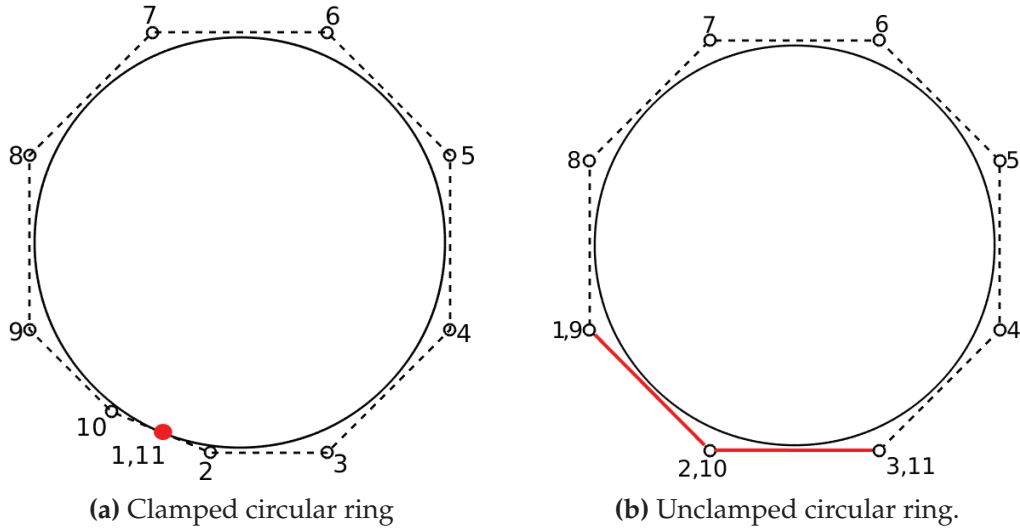


**Figure 3.2** Close B-spline ring using clamped and unclamped knot vector. The *red* control point of (a) is  $C^0$  and the *red* overlap of (b) maintains the  $C^2$  continuity of the cubic curve.

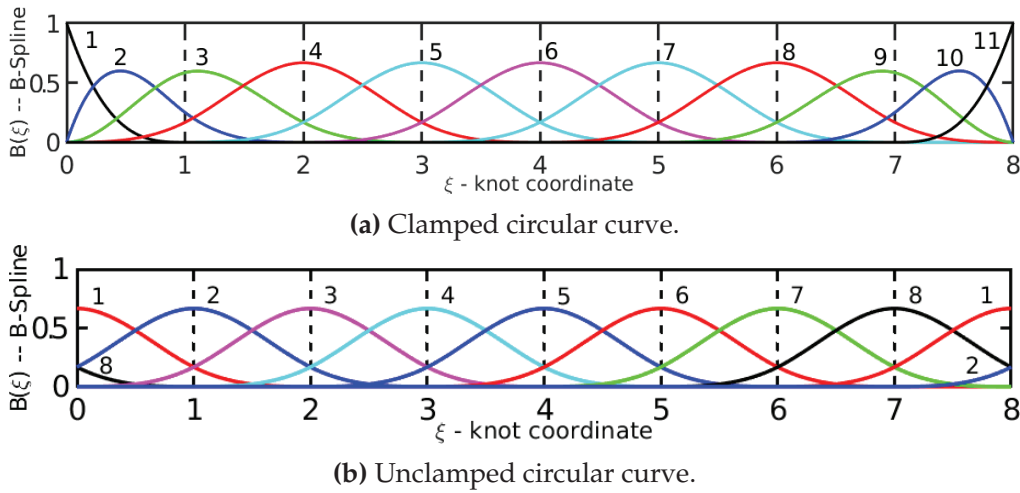


**Figure 3.3** Close ring B-splines for clamped and unclamped knot vector respectively.

One clarification has to be done: the fact that, in the case of an unclamped curve, the first and last  $p$  control points have to be coincident is an analysis-suitable requirement we adopted in FEAP. This requirement, in other words, means that the control polygon as well as the final curve have to be closed and the first and last  $p$  control points must have the same unknowns (as in Figure 3.2b). As can be read in (Piegl and Tiller, 1997), unclamping with no wraparound of the control points is also possible. This is because, if we start from a clamped knot vector, unclamping is essentially a knot-removal operation. One is free to choose the new  $2p$  new end knots rather arbitrarily and the position of the control points depends on the knots. We adopted the algorithm presented in (Piegl and Tiller, 1997) which produces wraparound of

$p$  control points in case the clamped curve is closed with  $C^{p-1}$  continuity. For an example of unclamping of the closed clamped cubic ring shown in Figure 3.5 starting from different knot vectors, see Figure 3.6. The extension to surfaces of all these concepts is straightforward. For an example of unclamping a degree (2,2) surface (i.e., bi-quadratic), please see Figure 3.4.

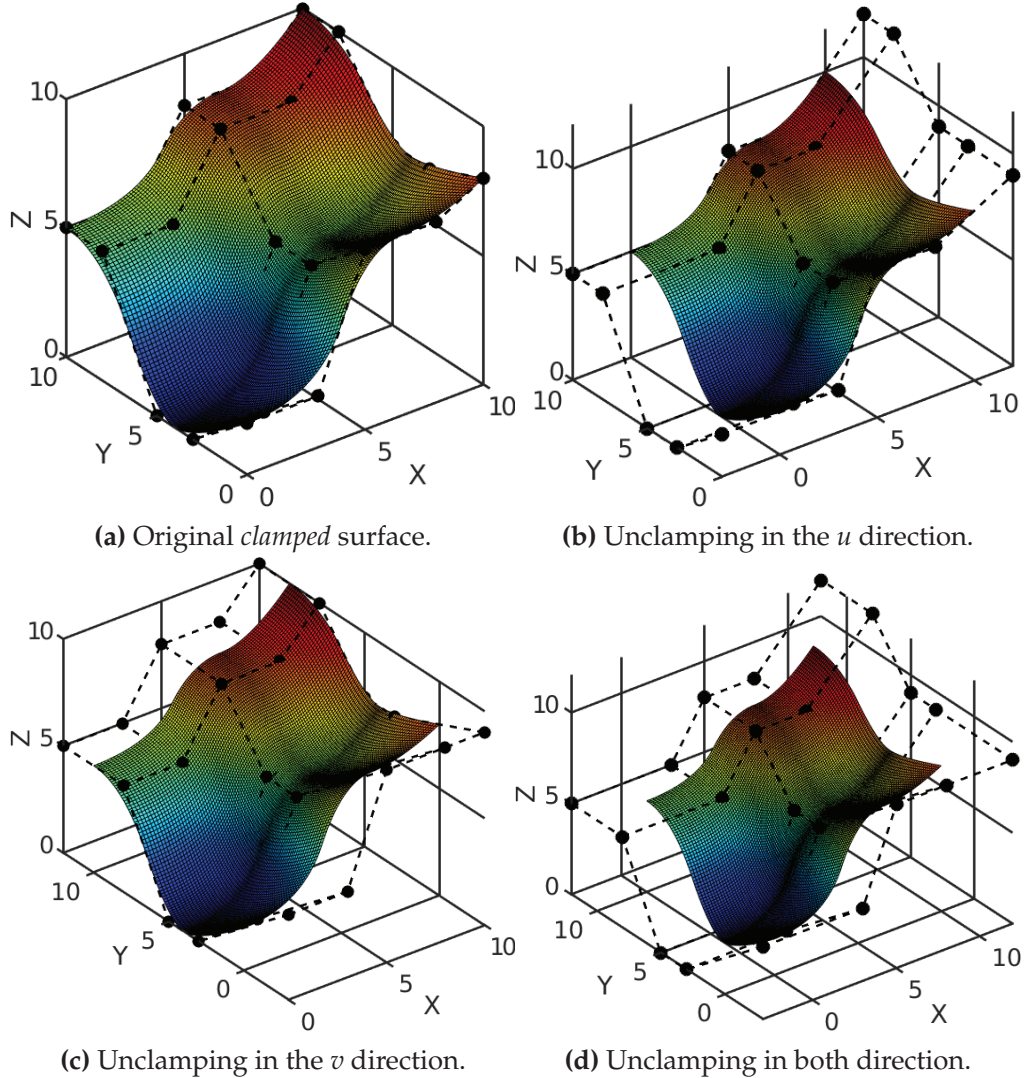


**Figure 3.4** Examples of unclamping a degree (2,2) surface in different directions.

The introduction of unclamped knot vectors in FEAP required a small modification in the routine responsible of the Bèzier extraction operation (Borden et al., 2011), used in this software for the calculation of Isogeometric objects. In particular, the construction of B-spline basis functions using the Cox-de Boor formula described above may become time-consuming for high-degree functions. Therefore, the alternative is to use Bèzier extraction to relate the B-spline functions in each non-zero interval to Bernstein polynomials. For each knot interval a  $(p+1) \times (p+1)$  matrix  $C^e$  may be described so that:

$$B_{i,p}(\xi) = C_{ij}^e b_{j,p}(\xi) \quad (3.10)$$

where  $b_{j,p}$  are Bernstein polynomials. Use of Bèzier extraction greatly simplifies the construction of shape functions once the *extraction matrices*  $\mathbf{C}^e$  are known.

Together with unclamped knot vectors, we introduced in FEAP two other types of knot vectors: LCLamped knot vectors, which are clamped at the start values and unclamped at the end values and RCLamped which are unclamped at the start value and clamped at the end value. For an example of FEAP input file regarding the use of different types of knot vectors and some additional details regarding unclamping, please see [Appendix A](#).

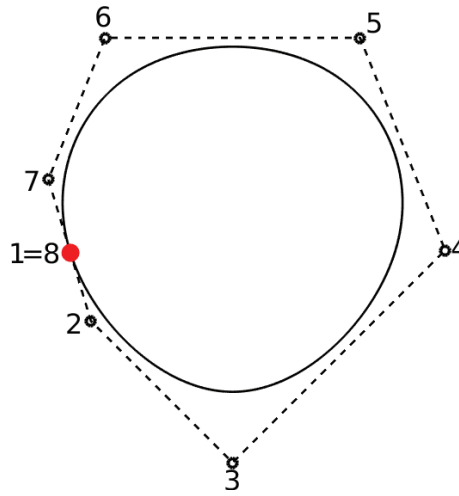


**Figure 3.5** Clamped cubic circular ring defined on the uniform knot vector  $[3\ 3\ 3\ 3\ 4\ 5\ 6\ 7\ 8\ 8\ 8\ 8]$ .

With B-splines, both clamped and unclamped, it is possible to perform refinement operation. In general, IgA refinement techniques slightly differ from their FEA counterparts. First, B-splines basis can be enriched while leaving the underlying geometry and its parameterization intact. Moreover, besides control over the element size and the order of the basis, IgA allows to control the continuity of the basis as well. The three IgA refinement techniques, i.e.,  $h$ ,  $p$  and  $k$  refinement are briefly presented and compared, when available, with their FEA counterpart.

- $h$ -refinement, i.e., the **knot insertion**: this technique is the most intuitive one to enrich the B-spline basis. In knot insertion, the knot spans are divided into smaller ones by inserting new knots, without changing the B-spline curve geometrically or parametrically. For each knot inserted, an additional control point is inserted too. Also knot values already present in the knot vector may be repeated, increasing their multiplicity and reducing the continuity at that knot location. The knot multiplicity cannot be increased beyond the order of the spline and outside the interval of definition of the knot vector. Insertion of new knot

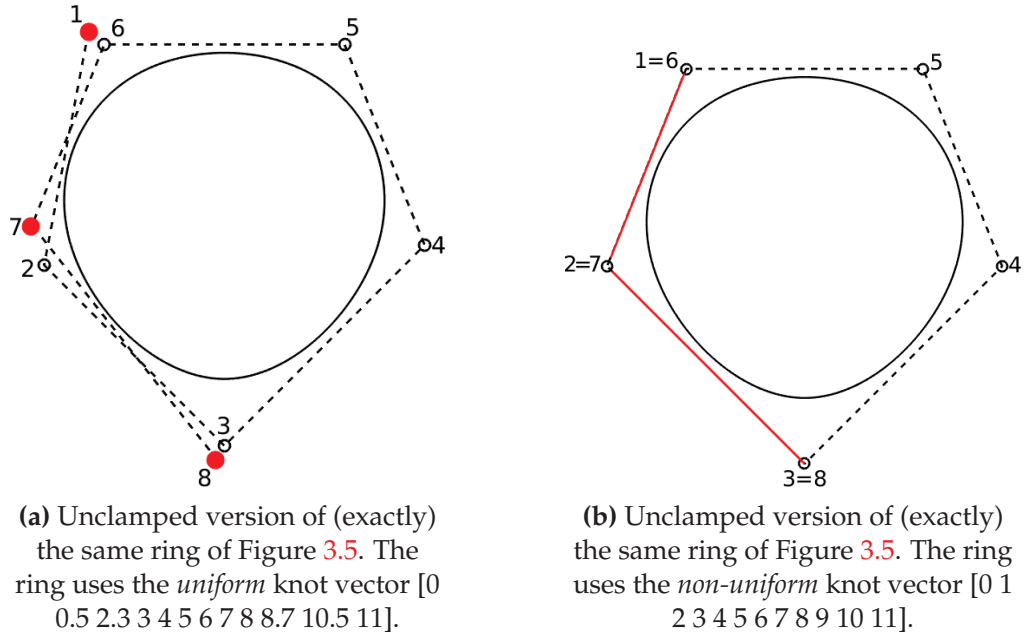


**Figure 3.6** Examples of unclamping the clamped closed ring of Figure 3.5 with different knot vectors. (a) unclamping with no wraparound; (c) unclamping with wraparound.

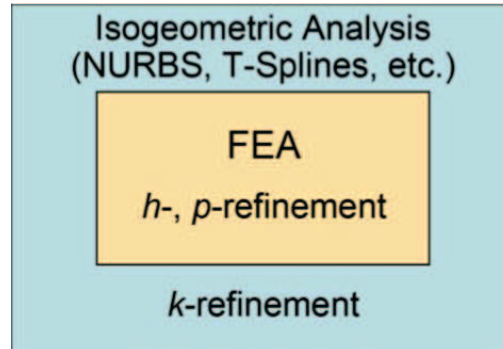


**Figure 3.7** IgA refinement techniques:  $h$ ,  $p$  and  $k$  refinement.

values clearly has similarities with the classical  $h$ -refinement strategy in FEA. It differs, however, in the lower number of new functions that are created, as well as in the continuity of the basis across the newly created element boundaries.

- $p$ -refinement, i.e., the **order elevation**: this refinement type involves rising the polynomial order of the basis functions used to represent the geometry. When order  $p$  is increased, knot multiplicity  $k$  must be increased too, in order to preserve the original  $C^{p-k}$  continuity at knot locations. After performing order elevation, the location of the control points change, but the elevated curve is geometrically and parametrically identical to the original curve. Order elevation has many similarities with the classical  $p$ -refinement strategy in FEA. The major



difference is that  $p$ -refinement always begins with a basis that is  $C^0$  everywhere, whereas order elevation is compatible with any combination of continuities that exist in the original B-spline curve.

- **$k$ -refinement:** while knot insertion and degree elevation find similarities with traditional FEA refinement techniques, IgA offers additional possibilities. In particular,  $k$ -refinement, i.e., a sort of high continuity  $h$  refinement, is available. Starting from the fact that  $h$  and  $p$ -refinement techniques *do not* commute, two possible situations can happen: if a unique knot  $\xi_i$  is inserted between two distinct knot values in a B-spline curve of order  $p$ , the basis will be  $C^{p-1}$  at that knot location. If the order is then elevated to  $q$ , the multiplicity of every distinct knot value (including the knot just inserted) is increased so that discontinuities of the basis are preserved. In such a process, the basis is still  $C^{p-1}$  at  $\xi_i$ , even if the polynomial order is now  $q$ . This process is defined as  $hp$ -refinement. On the other hand, if the B-spline basis is first elevated from order  $p$  to order  $q$  and then the knot  $\xi_i$  is inserted, the resulting basis will be  $C^{q-1}$  at this knot location. This process is defined as  $k$ -refinement and there is no analogous technique in standard FEA.

For an example of knot insertion performed on the unclamped curve shown in Figure 3.2, please see Figure 3.8. In particular, starting from the curve defined on the unclamped knot vector  $[0 \ 1 \ 2 \ 3 \ 4 \ 5 \ 6 \ 7 \ 8 \ 9 \ 10 \ 11 \ 12 \ 13 \ 14]$  (3.8a), by inserting the knot at location 3.5 we obtain the new knot vector  $[0 \ 1 \ 2 \ 3 \ 3.25 \ 4 \ 5 \ 6 \ 7 \ 8 \ 9 \ 10 \ 11 \ 11.25 \ 12 \ 13]$  on which we define the new refined curve (3.8b). Please note how the curves are geometrically and parametrically equal and how the addition of the new knot value produces a change at the end of the knot vector: this change is fundamental to ensure wraparound of  $p$  control points and it is a consequence of the algorithm presented in (Piegl and Tiller, 1997) we decided to adopt in this work.

The refinement techniques just described are valid not only for clamped and unclamped B-splines, but also for NURBS and they are implemented in an in-house Matlab code based on the NURBS toolbox (Falco, Reali, and Vázquez, 2011; Spink, 2014) and a set of routines implementing the algorithms included in (Piegl and Tiller, 1997), as well as in FEAP. For our purposes, they have been modified in order to be able to work with unclamped knot vectors. They have been extensively used in this thesis work.

For an example of the previously described  $k$ -refinement operation performed on an unclamped along  $u$  cylindric surface, please see Figure 3.9.

In order to get a set of reliable finite element meshes (starting from an idea by Dr. Mauro Ferraro, explained in his thesis work), we performed a set of fictitious knot insertions in order to subdivide each knot span into  $n$  distinct subdivisions, so that the continuity at that knot location becomes  $C^0$ . Each fictitious knot location in the parametric space, defined as *evaluation point*, has a mapped counterpart in the physical space. This information can be used to build an equivalent finite element mesh with the *mapped* evaluation points as nodal coordinates and element connections derived from the

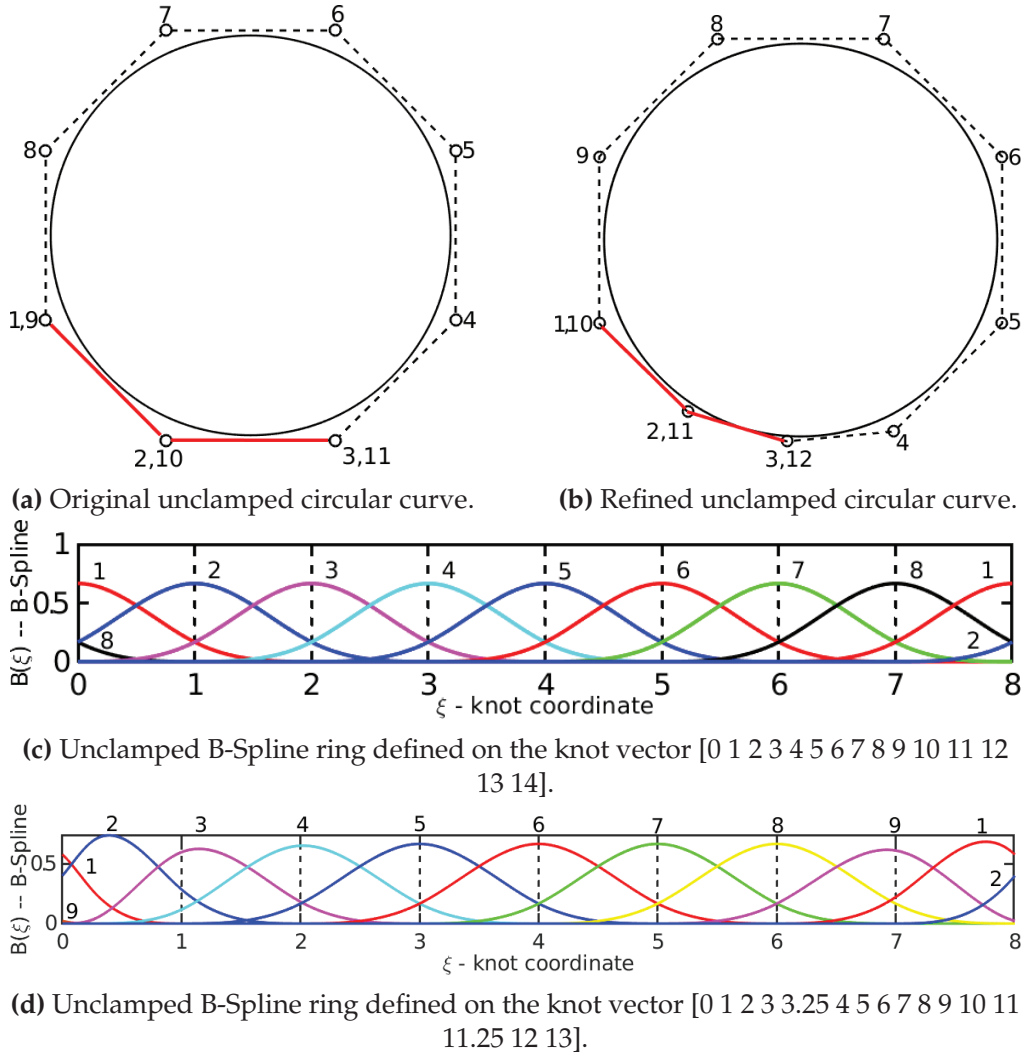


**Figure 3.8** Unclamped closed ring before (3.8a) and after refinement (3.8b) and their correspondent B-spline basis functions.



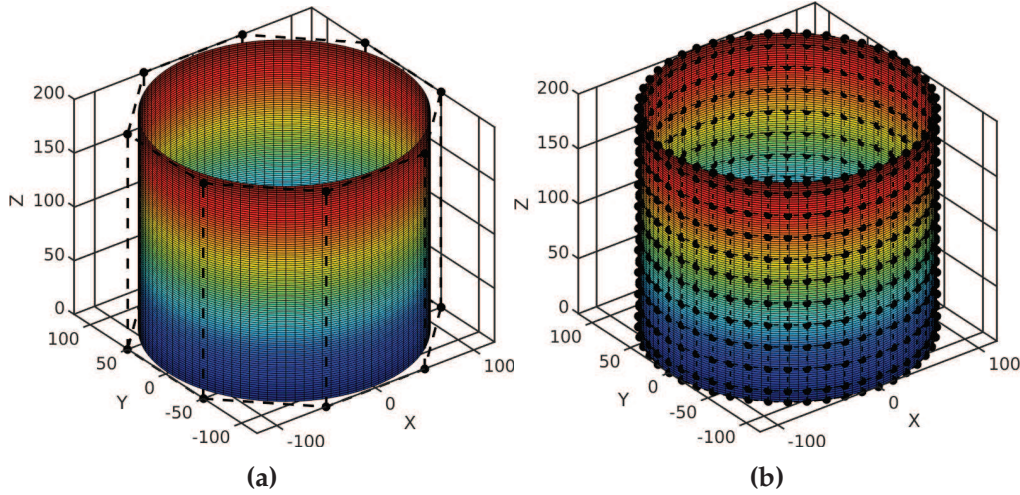


**Figure 3.9** (a) Control polygon of a not-refined cylindric surface. (b) Control polygon of the same cylindric surface, but  $k$ -refined. In particular the order of the spline has been raised from  $p = 1$  to  $q = 2$  only along  $v$ , whereas knot insertion has been performed along  $u$  &  $v$ . Moreover, note how the original (a) and the elevated (b) surfaces are parametrically and geometrically equal.

tensor-product structure of the NURBS geometry. We remark that given the adopted 8-node brick shape functions, only  $C^0$  continuity is enforced at the evaluation points location in the FEA model. We modified this strategy in order to be able to create FEM meshes starting from their unclamped counterparts. In particular, given an unclamped IgA mesh, its clamped counterpart is retrieved and then transformed to a FEA mesh. For an example of FEA mesh derived from the IgA clamped surface depicted in Figure 3.4a, see Figure 3.10. The knots vectors along  $u$  and  $v$  for the IgA surface in Figure 3.10a are both equal to  $[0 \ 0 \ 0 \ 0.3333 \ 0.6667 \ 1 \ 1 \ 1]$ , with  $C^1$  continuity in the internal knots, whereas for the FEA surface in Figure 3.10b, the knots vectors along  $u$  and  $v$  are both equal to  $[0 \ 0 \ 0.3333 \ 0.6667 \ 1 \ 1]$  with  $C^0$  continuity in the internal knots. What the reader has to keep in mind is that, in case an analysis has to be solved in FEAP using the IgA and FEA meshes shown in Figure 3.10 (or some examples obtained using the same strategy), for *both* meshes the IgA solver will be used (in the second case is the IgA  $C^0$  solver). If the "real" FEA solver should be employed, we introduced in FEAP two commands that allow the user to create both a linear and a higher-order (quadratic) mesh, given its clamped/unclamped IgA counterpart in input. These commands, respectively "O\_FE <QUADratic,LINEar>", output quadratic order elements (bricks with 27 nodes) and linear order elements (brick with 8 nodes) for a mesh that can be 1,2,3 dimensional. This command has to be input in iterative mode.

In this work, the knot vectors types employed to obtain the patient-specific vascular surface model of TAA we are interested in are: an *unclamped* knot

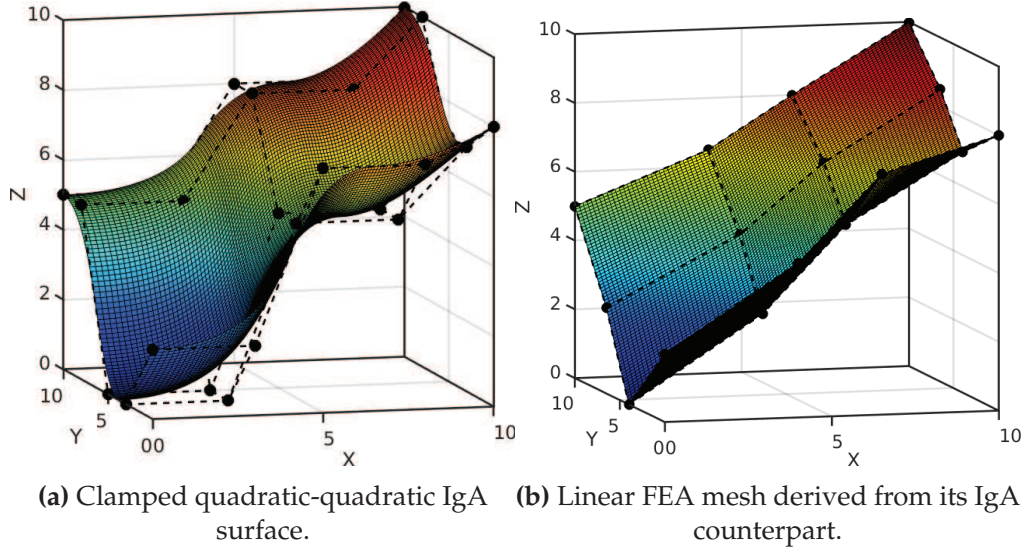


**Figure 3.10** Example of FEA mesh obtained from its IgA counterpart.

vector along the parametric  $u$  direction and a clamped one along the parametric  $v$  direction. The choice of different types of knot vectors along different parametric directions will be explained in Chapter 4.

### 3.2.4 Non-uniform rational B-splines (NURBS)

Given a knot vector  $\Xi = \{\xi_1, \xi_2, \dots, \xi_{n+p+1}\}$ , a set of rational basis functions  $\mathbf{R} = \{R_{A,p}\}_{A=1}^n$ , and a set of control points  $\mathbf{P} = \{\mathbf{P}_A\}_{A=1}^n$ , a NURBS can be defined as:

$$\mathbf{C}(\xi) = \sum_{A=1}^n R_{A,p}(\xi) \mathbf{P}_A \quad (3.11)$$

where NURBS basis functions are defined as:

$$\begin{aligned} R_{a,p}(\xi) &= \frac{N_{A,p}(\xi)w_A}{W(\xi)} \\ &= \frac{N_{A,p}(\xi)w_A}{\sum_{B=1}^n N_{B,p}(\xi)w_B} \end{aligned} \quad (3.12)$$

A rational curve in  $\mathbb{R}^n$  can be obtained by projective transformations of B-spline curves in the projective space  $\mathbb{P}^n$ . This means that if  $\mathbf{P}_A$  is a control point of a NURBS curve, the corresponding control point in the projective space is  $\tilde{\mathbf{P}}_A = \{w_A \mathbf{P}_A, w_A\}^T$ . Therefore, given a NURBS curve defined in  $\mathbb{R}^n$  by Equation 3.2.4, the corresponding B-spline curve defined in  $\mathbb{P}^n$  is:

$$\mathbf{C}(\xi) = \sum_{A=1}^n R_{A,p}(\xi) \tilde{\mathbf{P}}_A \quad (3.13)$$

In this way, the algorithms operating on B-splines can be applied to NURBS. By selecting appropriate values for the  $w_A$  permits the description of many different types of curves, including polynomials and circular arches. For the special case in which  $w_A = \text{constant}$ ,  $A = 1, 2, \dots, n$ , the NURBS basis reduces to the B-spline one. For simple geometries, the weights can be defined analytically (Piegl and Tiller, 1997), whereas for complex geometries they can be obtained from CAD packages such as Rhino (*Rhinoceros: NURBS modeling for Windows*).

### 3.2.5 NURBS surfaces and solids

A mapping  $\tilde{A}$  is now introduced between the tensor product space and the global indexing of the basis functions and control points in order to maintain the following single-index notation for T-splines, that will be introduced later on. Let  $i = 1, 2, \dots, n$ ,  $j = 1, 2, \dots, m$ , and  $k = 1, 2, \dots, l$ . The mapping  $\tilde{A}$  is then defined as follows:

$$\begin{aligned} \tilde{A}(i, j) &= m(i - 1) + 1 \\ \tilde{A}(i, j, k) &= (l m)(i - 1) + l(j - 1) + k \end{aligned} \quad (3.14)$$

Given three knot vectors  $\Xi^1 = \{\xi_1, \xi_2, \dots, \xi_{n+p+1}\}$ ,  $\Xi^2 = \{\eta_1, \eta_2, \dots, \eta_{m+q+1}\}$ ,  $\Xi^3 = \{\zeta_1, \zeta_2, \dots, \zeta_{l+r+1}\}$ , (one for each direction), and their associate univariate B-spline basis functions  $N_{i,p}(\xi)$ ,  $M_{j,q}(\eta)$ , and  $L_{l,r}(\zeta)$ , NURBS basis functions for surfaces and volumes are defined by the tensor product of the univariate B-spline basis functions. In two dimensions, the surface NURBS basis functions are defined as:

$$R_A^{p,q}(\xi, \eta) = \frac{N_{i,p}(\xi) M_{j,q}(\eta) w_A}{\sum_{\hat{i}=1}^n \sum_{\hat{j}=1}^m N_{\hat{i},p}(\xi) M_{\hat{j},q}(\eta) w_{\hat{A}}} \quad (3.15)$$

where  $A = \tilde{A}(i, j)$  and  $\hat{A} = \tilde{A}(\hat{i}, \hat{j})$ . In three dimensions, the volume NURBS basis functions are defined as:

$$R_A^{p,q,r}(\xi, \eta, \zeta) = \frac{N_{i,p}(\xi) M_{j,q}(\eta) L_{k,r}(\zeta) w_A}{\sum_{\hat{i}=1}^n \sum_{\hat{j}=1}^m \sum_{\hat{k}=1}^l N_{\hat{i},p}(\xi) M_{\hat{j},q}(\eta) L_{\hat{k},r}(\zeta) w_{\hat{A}}} \quad (3.16)$$

Given a control mesh  $\{\mathbf{P}_A\}$ , where  $A = 1, 2, \dots, (n x m)$  for surfaces and  $A = 1, 2, \dots, (n x m x l)$  for volumes, a NURBS surface is defined as:

$$\mathbf{S}(\xi, \eta) = \sum_{A=1}^{n \times m} R_A^{p,q}(\xi, \eta) \mathbf{P}_A \quad (3.17)$$

and a NURBS volume is defined as:

$$\mathbf{V}(\xi, \eta, \zeta) = \sum_{A=1}^{n \times m \times l} R_A^{p,q,r}(\xi, \eta, \zeta) \mathbf{P}_A \quad (3.18)$$

For an example of NURBS surface and its corresponding control net, please see Figure 3.11. For a most extensive review on rational splines, the interested reader is referred to (Farin and Farin, 2002; Piegl and Tiller, 1997; Rogers, 2000).

### 3.2.6 Limitations of NURBS-based IgA

As a design tool, a multivariate NURBS discretization, does not provide a natural possibility for *local* mesh refinement, due to the rigid tensor product structure. In the context of refinement, adding new control points to a NURBS surface means adding entire rows or columns of control points to maintain the tensor product surface. This implies that:

- A large percentage of NURBS control points contain no geometric information, but they are only needed to satisfy topological constraints.
- NURBS refinement is global and not local, since knot lines must extend through the entire domain.
- Complex geometry of arbitrary shape can only be represented by multiple NURBS patches which are generally discontinuous across patch boundaries.

NURBS-based deficiencies have a negative impact on analysis:

- A large percentage of DOF are needed to satisfy topological constraints only;
- Resolution of local features is prohibitively expensive, since all refinement propagates globally.
- For multi-patch domains inconsistencies at patch boundaries lead to  $C^0$  continuity at the interface or, sometimes, gaps and overlaps between patches. This lack of watertightness destroys the analysis-suitable nature of the discretization.

### 3.2.7 The unstructured T-mesh

A valid alternative in the literature, especially for local refinement in IgA, is represented by T-splines. They are an enhancement of NURBS surfaces that

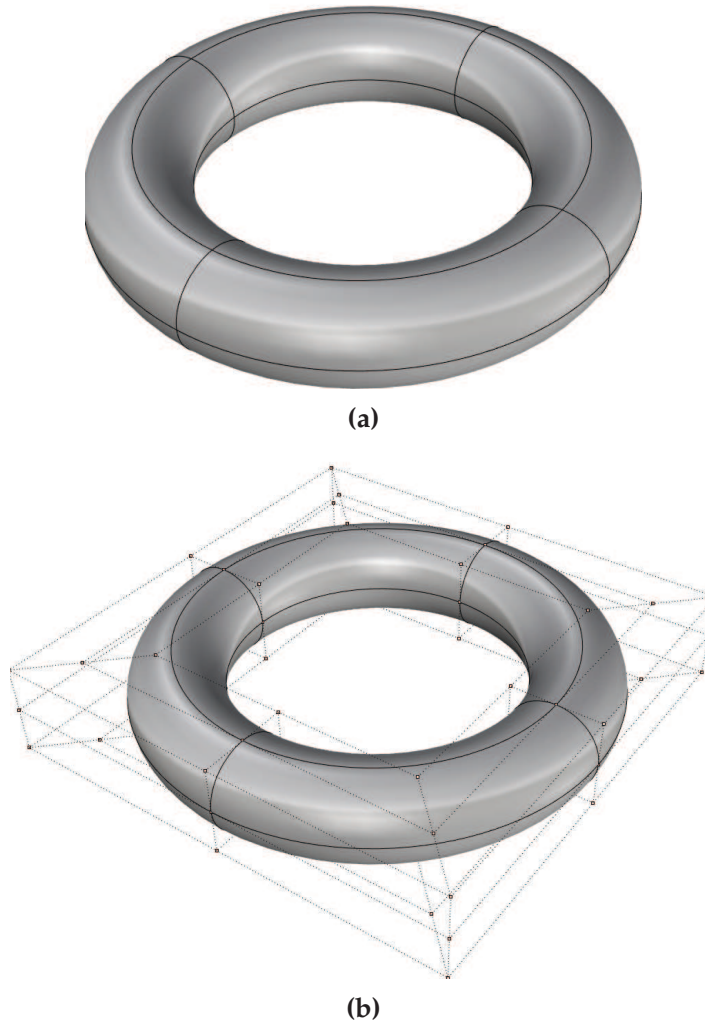


**Figure 3.11** Toroidal geometry: (a) surface, (b) and its control net.

allow the presence of T-junction control points, and the removal of superfluous control points in a mesh. At present, bi-cubic T-spline surface modeling has reached sufficient maturity, for which watertight parameterizations of surfaces can be built for geometrically and topologically complex engineering designs that can be used directly as finite element meshes in structural analyses of many 3D solids eliminating gaps and overlaps of NURBS patches.

The T-spline technology is based on the definition of a control grid named T-mesh. For surfaces, a T-mesh is a polygonal mesh and we will refer to its constituent polygons as elements or faces. Each element is a quadrilateral whose edges are permitted to contain T-junctions - vertices that are analogous to hanging nodes on finite elements. To each vertex in the T-mesh, a control point,  $P_A \in \mathbb{R}^{d_s}$ ,  $d_s = 2, 3$  and a control weight  $w_A \in \mathbb{R}$ , where the index  $i$  denotes a global control point number, can be assigned. The valence of a vertex is the number of edges that touch the vertex. An extraordinary



point is an interior vertex that is not a T-junction and whose valence does not equal four. The spoke edges that come from the extraordinary points are  $G^1$  continuous while the remaining edge interfaces of the one-ring of Bèzier patches surrounding the extraordinary point are  $C^1$  continuous with neighboring patches. When generating real world T-spline models, the presence of extraordinary points in the T-mesh can not be avoided. For T-splines, knot intervals represent the method to assign and retrieve parameter information to and from the T-mesh since no origin is required. To each vertex,  $A$ , of the T-mesh, a set of *local knot interval vectors*,  $\Delta \Xi = \{\Delta \Xi_A^i\}_{i=1}^{d_s}$  is assigned, from which the corresponding set of *local knot vectors*,  $\Xi_A = \{\Xi_A^i\}_{i=1}^{d_s}$  can be derived. After defining the sets of local knot vectors  $\Xi_A$ , a *local basis function domain*,  $\hat{\Omega}_A \subset \mathbb{R}^{d_s}$  can be defined, over which a single T-spline basis function is identified. The local basis function domain for  $d_s = 2$  is defined as follows:

$$\hat{\Omega}_A = \hat{\Omega}_A^1 \otimes \hat{\Omega}_A^2 \quad (3.19)$$

where  $\hat{\Omega}_A^1 \subset \mathbb{R}$ . Each local basis function domain carries a coordinate system  $(\xi_A, \eta_A)$ , named as the basis coordinate system. Using the knot coordinate system, an explicit formula for a *T-spline surface* can be written as follows:

$$\mathbf{P}(\xi, \eta) = (x(\xi, \eta), y(\xi, \eta), z(\xi, \eta), w(\xi, \eta)) = \sum_{A=1}^n \mathbf{P}_A N_A(\xi, \eta) \quad (3.20)$$

where  $P_A = (x_A, y_A, z_A, w_A)$  are control points in  $P^4$  with weights  $w_A$ , and Cartesian coordinates  $\frac{1}{w_A}(x_A, y_A, z_A)$ . The Cartesian coordinates of points on the surfaces are given as:

$$\frac{\sum_{A=1}^n (x_A, y_A, z_A) N_A(\xi, \eta)}{\sum_{A=1}^n w_A N_A(\xi, \eta)} \quad (3.21)$$

The *local basis functions* in equation 3.2.7,  $N_A(\xi, \eta)$ , can be expressed as the tensor product of the univariate basis functions as:

$$N_A(\xi, \eta) = N(\xi)N(\eta) \quad (3.22)$$

where  $N(\xi)$  and  $N(\eta)$  are the cubic B-spline basis functions associated with the knot vectors  $\Xi_A^1$  and  $\Xi_A^2$  respectively. The univariate basis functions in Equation 3.2.7 can be rewritten in a compact way as:

$$N_A(\xi_A|\Xi_A) = \prod_{i=1}^{d_s} N_A^i(\xi_A^i|\Xi_A^i) \quad (3.23)$$

The T-spline equation is very similar to the equation for a tensor-product rational B-spline surface. The difference between them is based on how the knot vectors  $\Xi_A^1$  and  $\Xi_A^2$  are determined for each function  $N_A(\xi, \eta)$ . For T-splines, knot vectors  $\Xi_A^1$  and  $\Xi_A^2$  are inferred from the T-mesh neighborhood of  $\mathbf{P}_A$ , based on the following rule: if  $A$  is not adjacent to an extraordinary point,  $N_A$  is comprised of a  $4 \times 4$  grid of polynomials. Otherwise the polynomials comprising  $N_A$  do not form a  $4 \times 4$  grid but rather an unstructured grid of polynomials. A T-spline element  $\Omega^e \subset \mathbb{R}^{d_s}$  is defined as the region in the physical space which is bounded by knot lines, i.e. lines of reduced continuity in the T-spline basis. The basis functions defined in the T-spline element are  $C^\infty$ . Over each element domain exist a set of non-zero T-spline basis functions which are in one-to-one correspondence with the T-mesh control points and are indexed by the global control point numbers. The local basis function number  $a$ , and the element number  $e$ , are directly mapped through the IEN array to the corresponding global control point number  $A$ . In other words  $A = \text{IEN}(a, e)$ . Differently from NURBS basis functions where all the elements support exactly  $(p+1)^{d_p}$  basis functions, a variable number of T-spline basis functions can be supported by each element of the mesh. For more details regarding T-splines, the reader is referred to (Scott et al., 2013).

In this work, T-splines from finite element point of view are developed utilizing Bèzier extraction (Borden et al., 2011). This provides a finite element representation of T-splines, and facilitates the incorporation into existing finite element programs like FEAP. The idea is to extract a linear transformation which maps the Bernstein polynomial basis on Bèzier elements, to the global T-spline basis as follows:

$$\mathbf{N}^e(\tilde{\xi}) = \mathbf{C}^e \mathbf{B}(\tilde{\xi}) \quad (3.24)$$

where  $\tilde{\xi} \in \tilde{\Omega}$  is a coordinate in a standard Bèzier parent element domain,  $\mathbf{N}^e(\tilde{\xi}) = \{N_a^e(\tilde{\xi})\}_{a=1}^n$  is a vector of T-spline basis functions which are non-zero over the Bèzier element  $e$ ,  $\mathbf{B}(\tilde{\xi}) = \{B_i(\tilde{\xi})\}_{i=1}^m$  is the vector of tensor product Bernstein polynomial basis functions defining Bèzier element  $e$ , and  $\mathbf{C}^e \in \mathbb{R}^{n \times m}$  is the element extraction operator, defined through the coefficients,  $c_{a,i}^e$ , as follows:

$$\mathbf{C}^e = \begin{pmatrix} c_{1,1}^e & c_{1,2}^e & \cdots & c_{1,m}^e \\ c_{2,1}^e & c_{2,2}^e & \cdots & c_{2,m}^e \\ \vdots & \vdots & \ddots & \vdots \\ c_{n,1}^e & c_{n,2}^e & \cdots & c_{n,m}^e \end{pmatrix} \quad (3.25)$$

Moreover, the use of the linear operator allows us to standardize the form of the element basis on the parent domain. The transpose of the extraction operator maps the control points of the global T-spline to the control points of the Bernstein polynomials. This provides a finite element representation of T-splines, and facilitates the incorporation of T-splines into existing finite element programs. Only the shape function subroutine needs to be modified, as it has been done in our case. All the other aspects of the finite element program remain the same. Moreover, Bèzier extraction is automatic and can be applied to any T-spline regardless of the topological complexity or the polynomial degree. In particular, it represents an elegant treatment for T-junctions and extraordinary points. For T-spline, the computation of the element extraction operators has been performed in (Scott et al., 2011). Roughly, the extraction algorithm for T-spline is based on the following main steps:

- Infer the T-spline basis from the T-mesh.
- Refine the T-mesh.
- For a T-spline basis function determine the Bèzier elements which are in its support.
- For a T-spline basis function perform Bèzier extraction.
- The last two steps are repeated for each T-spline basis function.

For more details regarding how Bèzier extraction works with T-spline, please see (Scott et al., 2011). In FEAP, the data input is provided by an output from the refinement program developed at the University of Texas by Mike Scott, and included as an extension of the T-splines plug-in (*T-Splines, Inc.*) for Rhino (*Rhinoceros: NURBS modeling for Windows.*). For more details, the interested reader is referred to Chapter 5.

### 3.2.8 Conclusion

In this Chapter we introduced the basic concepts of B-splines, NURBS and T-splines, which we are going to use as basis for both modeling and analysis in the following chapters. Particular attention has been given to the so-called (and so far not extensively used in the IgA community) "unclamped" concept, for the construction of closed and periodic curves and surfaces. The unclamped concept is the key for the creation of a semi-automatic pipeline for the generation and analysis of reliable patient-specific isogeometric models of Thoracic Aortic Aneurysms, starting from DICOM images, that will be described in details in Chapter 4. In the field of cardio-vascular modeling like ours, a NURBS-based cylindrical parameterization of the arteries will be straightforward due to their inherent tubular structure. Despite this, we decided not to adopt a NURBS-based but a B-spline based cylindrical approximation for our geometries even if we know that B-splines are not capable of representing conic sections. We made this choice because, as will be



explained in Chapter 4, we do not need a perfect circle to create the patient-specific TAA geometries we are interested in and this is linked to the mapping operation we use to obtain them. In Chapter 5 we will first expand the pipeline introduced in Chapter 4 for the creation of multipatch NURBS branched geometries characterized by a tree-like shape, and subsequently we will adopt T-spline basis functions, via Rhino Autodesk T-spline plug-in, in order to create more complex, patient-specific geometries of aortic arteries, characterized by arbitrary topology. Moreover, we are going to use a NURBS-based discretization to investigate in Chapter 6 frictionless contact interactions between stent devices and deformable surfaces.



## Chapter 4

# Patient-specific geometrical modeling of thoracic aortic aneurysms

### 4.1 Introduction

#### 4.1.1 The patient-specific concept in biomechanics

Patient-specific modeling is a relatively new paradigm in medical planning that employs computational tools on anatomical and physiological data to individualize patient-care. It can help optimizing surgical procedures and improving diagnosis and treatment of a number of common illnesses. To fulfill this task, image-based patient-specific modeling techniques have been used to study various organs and tissue dynamics including the heart, the brain, bones, teeth, kidneys, tumors, lungs and cardiovascular systems (Taylor and Figueroa, 2009). Patient-specific cardiovascular modeling (PSCVM) has enjoyed a great deal of attention from researchers since some pioneering works (Taylor, Hughes, and Zarins, 1998; Taylor, Hughes, and Zarins, 1996) and still remains an active field of study (Antiga et al., 2008; Taylor and Steinman, 2010; Kim et al., 2010). PSCVM makes possible the detection of thoracic and abdominal as well as cerebral aneurysms (Doyle et al., 2009). It usually involves three fundamental steps: (1) image processing, (2) analysis suitable model generation, and (3) analysis (see Figure 4.1).

In details, first the scanned images are segmented and classified into meaningful regions to extract the geometry of the object of interest. Next, an analysis suitable solid geometrical model is generated from the segmented images. As can be read in (Neal and Kerckhoffs, 2009), typically, solid models are constructed by (a) extracting a set of points (a contour) approximating the inner and outer arterial wall boundaries of a vessel on an offset stack of segmented two dimensional (2D) image slices, (b) interpolating the contour with a curve, (c) lofting a surface through the interpolated curves, (d) joining the surfaces to create a network and (e) meshing the bounded surfaces to define the object of interest. Finally, a finite element or a finite-element-based IgA scheme is adopted to solve the equations that control the phenomenon under study. As already said, among the existing finite-element patient-specific analysis

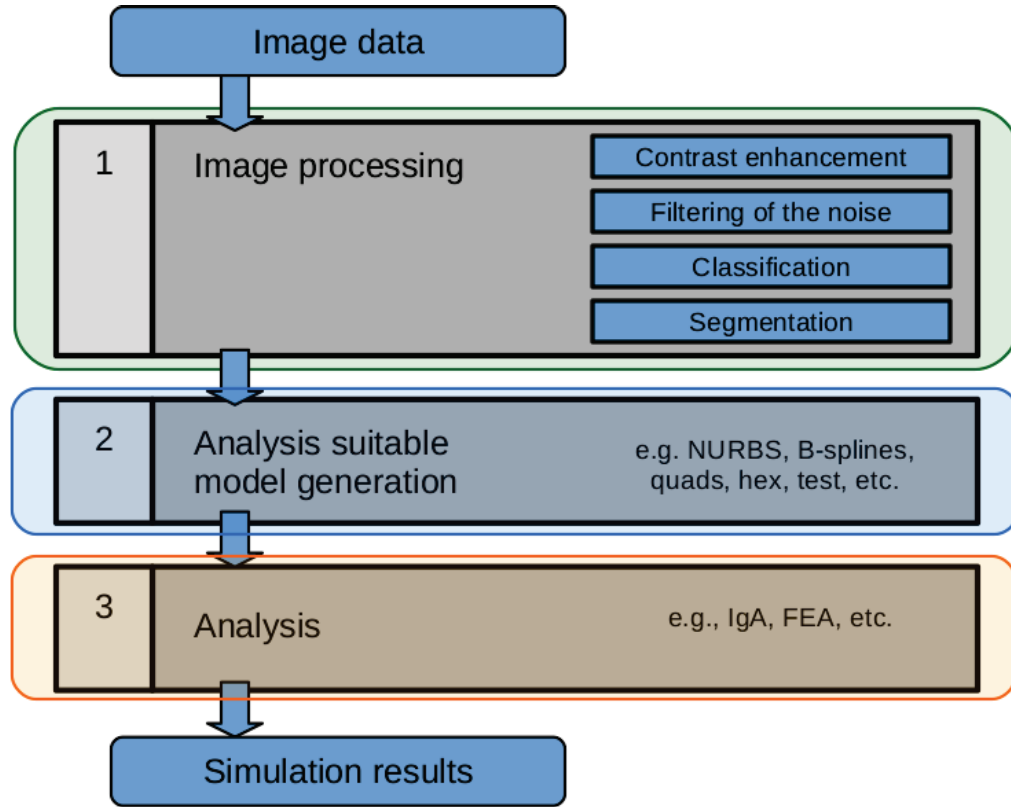


**Figure 4.1** Flowchart depicting the main steps in a typical patient-specific vascular modeling pipeline: 1) Image processing, 2) Analysis suitable model generation and 3) Analysis.

techniques, Isogeometric Analysis (IgA) has gained significant popularity in the recent years. Before IgA was conceived, performing finite element analysis on a computer-aided designed (CAD) object required the creation of an analysis suitable mesh that could only approximate the original object extracted from medical images. This reduce the accuracy of the final solution and, for large objects, creating an analysis suitable mesh can take a design team a few weeks or more to complete, consuming up to 80% of the total analysis time (Hughes, Cottrell, and Bazilevs, 2005). In an attempt to circumvent the generation process and its unnecessary geometry approximations altogether, IgA employs the same basis functions for approximating the solution space as the ones used in representing the geometry in CAD softwares. Within this isoparametric framework ideally, the analysis suitable model becomes equivalent to the CAD model. Therefore, IgA has the unique advantage of performing analysis on exact geometries, even for the coarsest mesh. Moreover, the IgA approach can take advantage of extensive CAD software functionalities in producing geometric models and corresponding geometric information. Once a geometric model is created in CAD, also a traditional FE mesh can be constructed if desired. Given all these reasons, we decided to use IgA for the construction and analysis of our patient-specific models of

TAA and for the approximation of the equations under study. This part of the work has been done in collaboration with Dr. Elena Faggiano.

### 4.1.2 Aim of the chapter

In this Chapter, our new procedure to obtain an analysis-suitable B-spline representation of the thoracic aorta from medical (DICOM) images is illustrated and applied to patient-specific cases of TAA (see Figure 4.21). One consideration has to be done: in this section our interest is focused only on the aneurysm and on explaining the details of our innovative pipeline to create analysis-suitable IgA models. This novel framework is straightforward and capable of recreating a trustworthy geometry, i.e., characterized by a very small distance from the original surface extracted from medical images by means of segmentation operation. We would like to demonstrate how the creation of a patient-specific IgA-suitable model of TAA can be done quasi automatically by performing a limited number of relatively easy steps, once the Computed-Tomography (CT) images have been acquired, preprocessed, and segmented. We will also show how the total time (measured in minutes) that is required to perform all these passages is very short, once the object of interest has been acquired from CT images by means of a segmentation process, which usually takes 20 minutes to complete if performed by an expert user (see Table 4.1). Up to this point, the presence of the supra-aortic vessels is neglected, but it will be introduced in our models in the following chapter. The main steps of our pipeline include post-processing of a triangulated TAA surface mesh obtained from segmented 3D imaging data (Section 4.2), extraction of a set of points (contours) approximating the inner and outer arterial wall boundaries by solving the Laplace problem along it (Section 4.3), construction of the spline surfaces by means of a B-spline mapping operation of a primitive unclamped B-spline geometry onto a target-image based surface, and finally creating solid splines from the spline surfaces (Section 4.3). Please see Figure 4.2 for a summary of the passages we just underlined.

## 4.2 Triangulated Surface Mesh Post-Processing

Computed-Tomography (CT) is the investigation choice for the urgent evaluation of patients with acute aortic syndromes (Hartnell, 2001). It represents an efficient tool for thoracic aortic aneurysms reconstruction; as a matter of fact, the aortic lumen can be highlighted by means of a contrast agent (Erbel et al., 2015). The first step in our framework consists of the reconstruction of the three-dimensional (3D) inner lumen surface of the TAA from patient-specific CT data by means of a gradient-based 3D level sets segmentation method (Fedkiw and Osher, 2002) implemented in VMTK (Vascular Modeling Toolkit) software suite (Antiga and Steinman, 2006) and employing the Fast Marching Method (Piccinelli et al., 2009; Antiga et al., 2008) as initialization type. In short, this method enables you to select a vascular segment

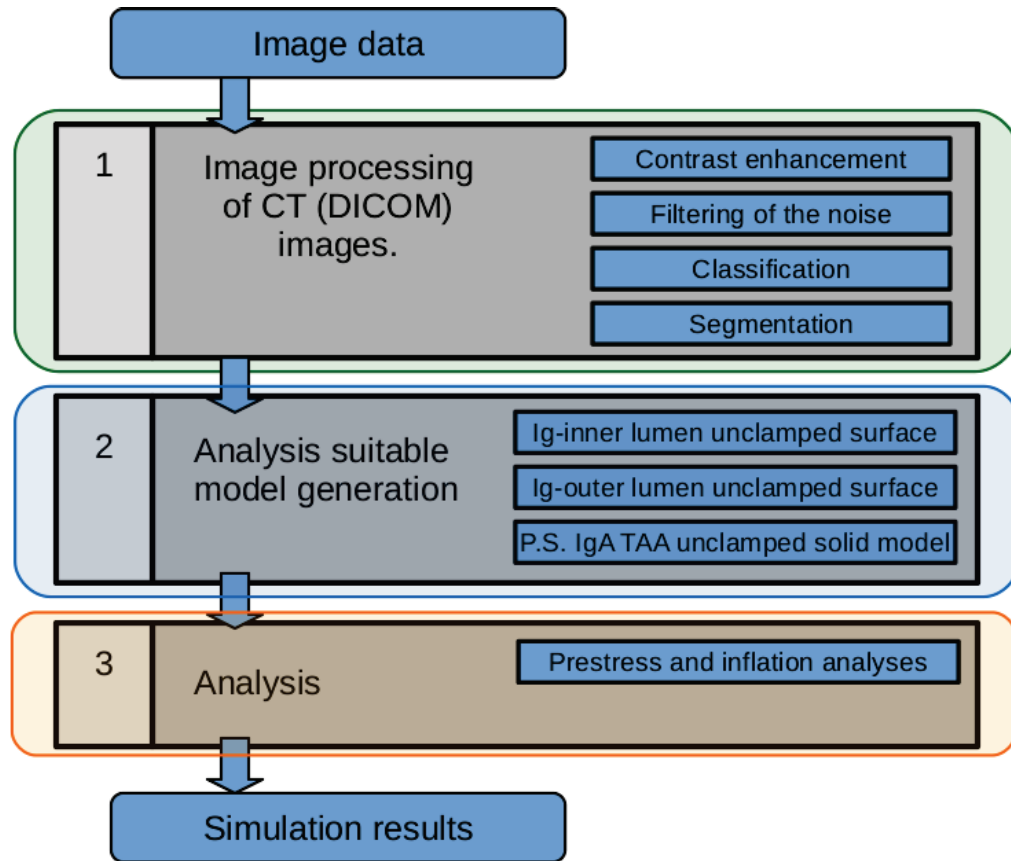


**Figure 4.2** Flowchart depicting the main steps in our patient-specific (cardio)vascular modeling pipeline: 1) Image processing, 2) Analysis suitable model generation and 3) Analysis.

comprised between two points automatically ignoring side branches, no parameters involved. Segmenting a complex vascular tract becomes equal to select the endpoints of a branch, letting level set by attracted to gradient peaks. This operation has to be repeated for all the branches, which, in the end, have to be merged in a single model. The result is a triangulated surface mesh of the segmented TAA. Please see Figure 4.3 for an example of application of level sets segmentation method on a vascular tract (Antiga et al., 2008).

Since the obtained triangulated surface may contain geometric features and degeneracies that may prohibit downstream processes, it is first smoothed using VMTK to avoid artifactual bumps that can affect wall stress local distribution, and cropped in Paraview (Ahrens, Geveci, and Law, 2005) in order to focus only on the aneurysm site and to remove the presence of the supra-aortic branches. Subsequently, the holes created by removing the supra-aortic branches are carefully capped by means of an in-house VTK-based Python code (that is part of the work of Dr. Elena Faggiano) that permits to manually delineate a region on the triangulated surface, eliminate and cap it. For an example of how this code works, please see Figure 4.5.

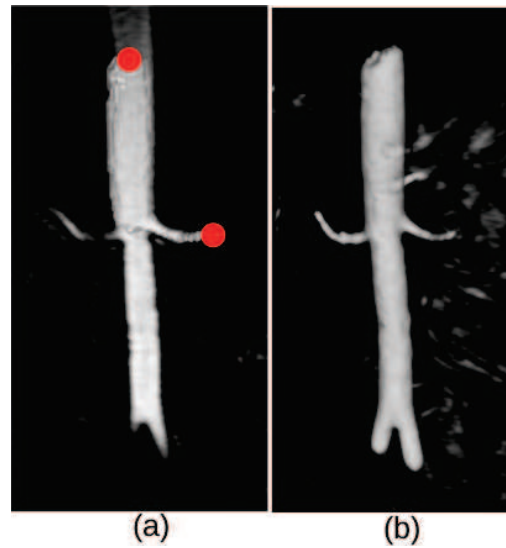


**Figure 4.3** Example of segmentation of an abdominal aorta from CT images. (a) Interactive initialization of a branch through the specification of two seed points (depicted in red color), one within the suprarenal aorta and the other within the right renal artery; (b) result of segmentation after level set evolution.

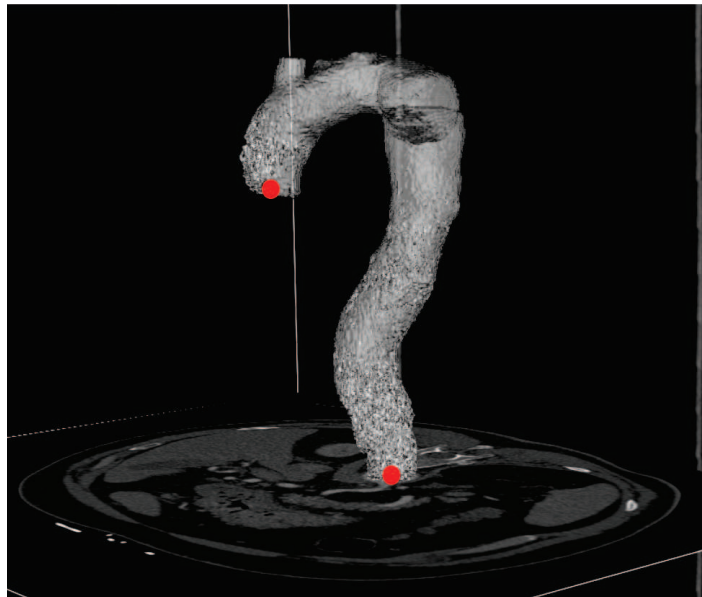


**Figure 4.4** Example of segmentation of a thoracic aorta from CT images. Interactive initialization of the main vascular tract through the specification of two seed points (depicted in red color).

Finally, a remeshing step is carried out semi-automatically using VMTK. In performing all the previous operations, care must be taken not to distort, smooth or remove important characteristics and attributes found in the raw

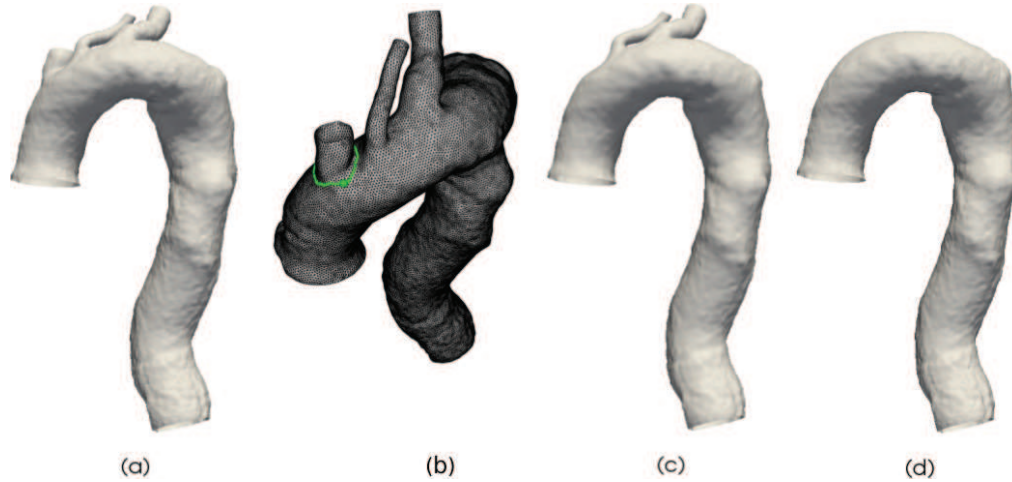


**Figure 4.5** Example of removing and capping the supra-aortic branches of a patient-specific TA. (a) Original TA. (b) Manual selection of the branch that has to be removed. (c) Removal of only one branch. (d) Complete removal and subsequent capping of the branches.

data. This is mainly carried out visually at the discretion of the user, although VMTK do offer valuable metrics as feedback when applying various operations. The smoothed and cropped version of the 3D inner lumen serves as an input object for all the subsequent steps.

### 4.3 Conduction-based method to get cross-sections of points

Next, we describe a new procedure we developed to build a B-spline unclamped representation of the TAA inner lumen surface from the “clean” triangulated surface mesh we obtained in the previous step. In particular, what we need to perform this task are cross-sections of points defined on the triangulated mesh. These cross-sections of points have to satisfy two important criteria:

1. two cross-sections of points cannot intersect;
2. each cross-section of points has to be orthogonal to the vessel wall.

The robust solution we conceived and implemented to produce cross-sections of points with these characteristics is solving the Laplace’s equation in the TAA vessel with Dirichlet boundary conditions at the tube ends (i.e. the two open boundaries). This strategy corresponds to a steady thermal conduction problem with temperature  $t = 0$  at the vessel inlet and  $t = 1$  at the vessel outlet. Laplace’s equation is a very well conditioned equation; therefore, virtually any *reasonable* mesh/discretization may be good for the task, also because in this step we are more focused on satisfying the non-intersection and orthogonality criteria than accuracy. Hence, we employ finite-element



for the conduction problem. Specifically, first we identify the boundaries of our tube-like triangulated base mesh and assign them temperature values ( $t = 0$  at the vessel inlet and  $t = 1$  at the vessel outlet). Then, we construct an harmonic function over the base mesh using the temperature we just set as boundary condition. Next, we spline-interpolate the boundary at  $t = 1$  with a number of points defined by the user and we perform steepest gradient descent from boundary with  $t = 1$  downward to temperature  $t = 0$ , along diffused temperature values. Once  $t$  is known, we extract and spline-interpolate with a user-defined number of points all the isolines for a monotonically increasing sequence of temperatures  $0 < t_1 < t_2 < \dots < t_m = 1$ . These operations will produce a set of cross-sections of points that satisfy the desired non-intersecting and orthogonality conditions. Each cross-section of points has to be closed and the starting points of each section have to be aligned (see Figure 4.6, last image). If sections of points are not closed and their first points not aligned, the final IgA model can be distorted after mapping operation. The  $t_i$  can be chosen such that each cross-section of points has the desired separation in the Euclidean space. Please see Figure 4.6 and Figure 4.7 for a clarification of the aforementioned operations.

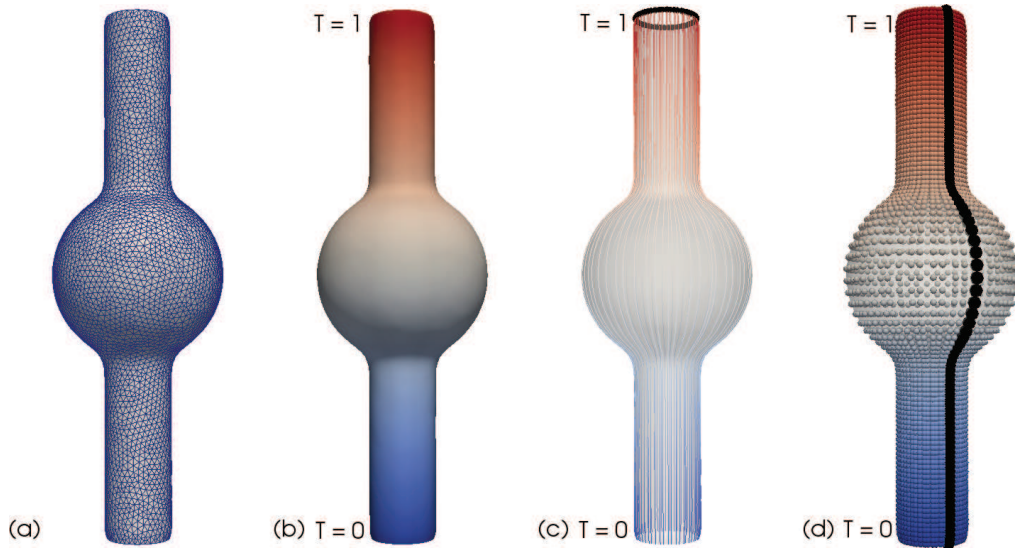


**Figure 4.6** Example on a test case of the "conduction-based" method we use to get cross-sections of points. (a) Triangulated base mesh. (b) Perform harmonic mapping using the temperature as boundary conditions (i.e., diffuse the temperature). (c) Spline interpolation of the boundary at  $t = 1$  with a number of points specified by the user (black points).

Perform steepest gradient descent from boundary with temperature  $t=1$  downward to temperature  $t=0$ , along diffused temperature values. (d) Spline-interpolation of isolines for monotonically increasing temperature values. Starting points for each cross-section have to be aligned to avoid unpleasant effects in the final IgA model.

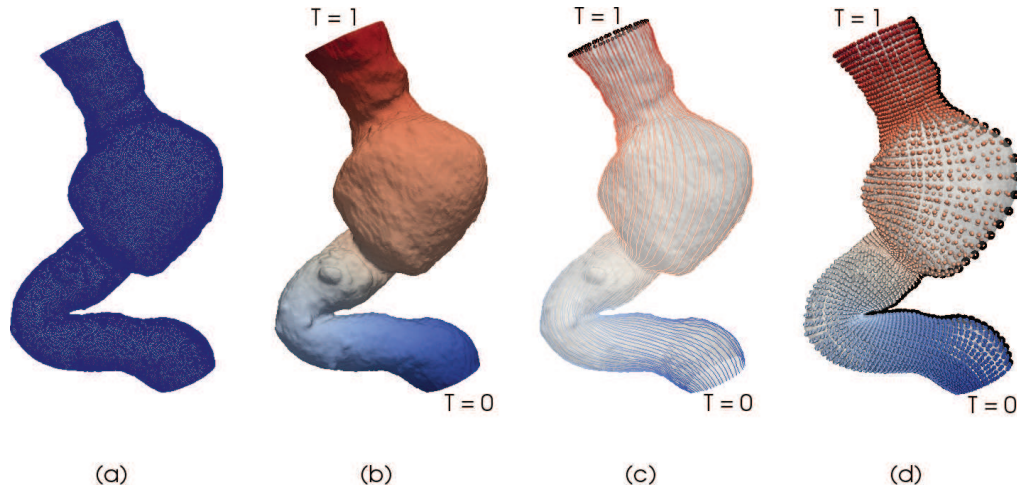


**Figure 4.7** Example on a patient-specific case of the "conduction-based" method we use to get cross-sections of points. (a) Triangulated patient-specific base mesh. (b)

Perform harmonic mapping using the temperature as boundary conditions (i.e., diffuse the temperature). (c) Spline interpolation of the boundary at  $t = 1$  with a number of points specified by the user (black points). Perform steepest gradient descent from boundary with temperature  $t=1$  downward to temperature  $t=0$ , along diffused temperature values. (d) Spline-interpolation of isolines for monotonically increasing temperature values. Starting points for each cross-section have to be aligned to avoid unpleasant effects in the final patient-specific IgA model.

The proposed algorithm was further extended in order to perform a sort of "local refinement" of the sections of points in the zones of the geometry that show a higher value of surface curvature. For an example of application of this concept on a test case, please see Figure 4.8.

By using this "conduction-based" algorithm, we completely removed any operational dependency on the centerline. As a matter of fact, according to the experience we gained prior to the adoption of this method for the creation of ordered sections of points, the creation of sections along the centerline do not always satisfy the non-intersection and orthogonality criteria described above. In particular, this occurs where the geometry is really angulated. Dependency on the centerline is a very well known issue in templates-based method too (Urlick et al., 2017). This concept will be better described once introduced the mapping operation in the following section.

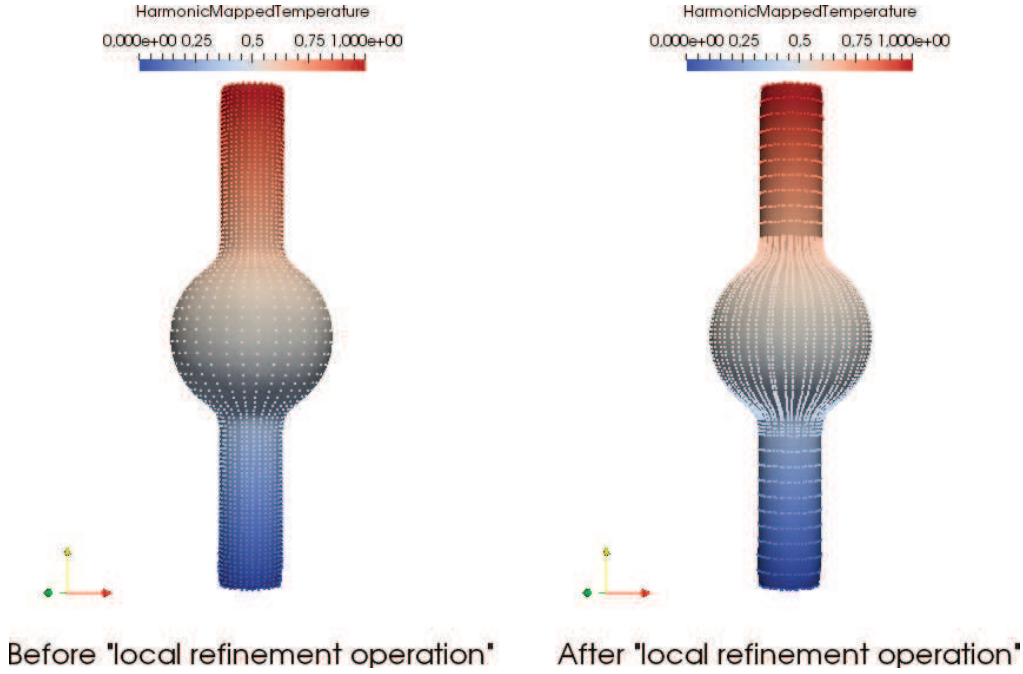


**Figure 4.8** Example of the application on a test case of the conduction based method including "local refinement" of the sections of points in the regions on the surface that show higher curvature. In particular, the harmonic mapping result obtained using the temperature as boundary condition is shown.

## 4.4 From cross-sections of points to an IgA-suitable unclamped surface model

In order to obtain the IgA patient-specific solid model of the TAA starting from a set of ordered sections of points, the mapping procedure performed in (Morganti et al., 2015) has been adopted and modified to make possible the use of unclamped knot vectors along the parametric  $u$  direction of the model. Hence, in this work, the knot vector types employed to obtain patient-specific TAA surface models of both the inner lumen and outer aortic wall surfaces are: unclamped knot vector along the parametric  $u$  direction and clamped one along the parametric  $v$  direction. Please see Figure 4.9 for a clarification on the parametric directions we employed.

As in (Morganti et al., 2015), the main idea behind the mapping procedure is to map a basic primitive B-spline geometry (e.g., a cylinder) onto a target image-based surface. In particular, the best position of the  $N_{cp}$  control points of the primitive surface is determined by means of a least square algorithm in order to represent the target surface evaluated at a *sufficient* number of  $N_s$  sampling points. In other words, this means that  $N_s > N_{cp} = m \times n$ .

In details, a generic NURBS in  $\mathbb{R}^3$  can be described with the following relation:

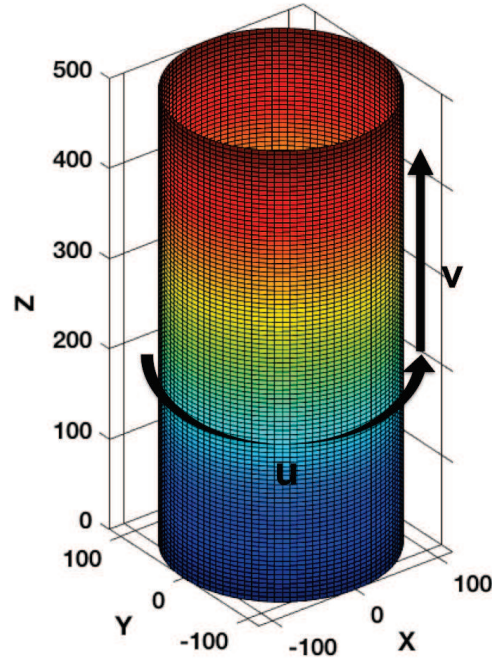


**Figure 4.9** Parametric directions adopted in the construction of each patient-specific IgA geometry.

$$S(u, v) = \frac{\sum_i \sum_j N_{i,p}(u) M_{j,q}(v) \mathbf{B}_{i,j} w_{i,j}}{\sum_i \sum_j N_{i,p}(u) M_{j,q}(v) w_{i,j}} \quad (4.1)$$

where  $\mathbf{B}_{i,j}$  and  $w_{i,j}$  represent the  $i,j$ -th control points coordinates and weights, respectively, and  $N_{j,q}$  and  $M_{i,p}$  are the  $i$ -th,  $j$ -th shape functions of order  $p$  and  $q$  respectively, related to each parametric direction,  $u, v$ . For more details regarding NURBS, the reader is referred to Chapter 3, Section 3.2.4. By assuming constant weights and by performing some simple algebraic manipulations, Equation (4.4) can be rearranged in order to get the matricial form that reads:

$$S_T^r = C * B_{vec}^r \quad (4.2)$$

where  $S_T^r$  represents the  $r$ -th cartesian nodal component of the sampling points belonging to the target surface,  $B_{vec}^r$  is the  $r$ -th Cartesian component of the control points of the reference surface ordered in vectorial form, whereas  $C$  roughly contains the products between shape functions values in both parametric directions. It can be observed that Equation 4.4 represents a linear system that can be solved in a least-square sense to obtain the  $r$ -th component of the mapped control points, i.e., the control points of the IgA-suitable patient-specific TAA surface model. Since we are using an unclamped knot vector along  $u$ , we are solving the linear system just taking into account all

the control points except for those that are overlapping. This means that we are condensing some unknown DOF and recasting the original Eq. 4.4 set in terms of fewer unknowns. Once the system is solved and thus the control points coordinates of the IgA patient-specific TAA surface model have been found, coordinates are also assigned to the overlapping  $p$  control points along  $u$ , according to which control point they are wrapped around with in the original reference geometry. All the previous operations are performed in an in-house Matlab (MATLAB, 2018) code based on the NURBS toolbox (Falco, Reali, and Vázquez, 2011; Spink, 2014) and a set of routines implementing the algorithms included in (Piegl and Tiller, 1997).

The idea is illustrated in Figure 4.10 by mapping an unclamped along  $u$  B-spline cylinder onto a TAA surface mesh. We decide to use a B-spline cylinder due to the inherent tubular structure of the arteries. Even if we know that B-splines are not capable of representing conic sections, we decided not to use a NURBS-based cylindrical parameterization of the arteries to create the patient-specific TAA geometries. First because in equation (4.4) all the weights are constant and thus the NURBS basis "naturally" reduces to the B-spline one. Second, because we do not need a perfect circle over which to construct a cylinder if then the position of the control points has to be moved due to the mapping operation to match the reference surface. The cylinder surface is obtained by sweeping the unclamped ring (Figure 4.10a) introduced in Chapter 3 over a vertical distance  $h$  (Figure 4.10b). The mesh is refined by knot insertion along both parametric directions (Figure 4.10c) as described in Chapter 3, to obtain a reproduction of the thoracic aortic aneurysm as close as possible to the one extracted from medical images (Figures 4.10d & 4.10e). For a summary of all the passages we perform starting from the TAA inner lumen triangulated surface mesh extracted from medical images to get its IgA representation, please see Figure 4.11.

This procedure was originally tested with clamped knot vectors along the  $u$  direction of each model and then modified to be able to work with unclamped ones. The reason why we decided to change the knot vector type along  $u$  can be seen in Figure 4.12: the main drawback of using a clamped knot vector along the circumferential direction is the presence of the *unphysical*  $C^0$  line(s) that crosses the model vertically and causes discontinuity of the stress field (as we are going to point out in one of the following sections). In this Figure, both IgA models have the same number of DOF and spline degree along the two parametric directions. This  $C^0$  line is exactly the evolution of the blue dot that can be seen in Figure 4.12 in the clamped closed ring control polygon case, if such a ring is extruded vertically. Accordingly to the clamped knot vector used to define the clamped closed ring, the number of  $C^0$  lines in the final IgA model may be different. As an example, if the clamped closed ring is defined on the clamped knot vector  $[0 \ 0 \ 0 \ 0.25 \ 0.25 \ 0.5 \ 0.75 \ 0.75 \ 1 \ 1 \ 1]$ , with  $p = 2$  and number of control points equal to nine (9), the final number of  $C^0$  lines in the geometrical model will be four (4). On the other hand, if the clamped knot vector is  $[0 \ 0 \ 0 \ 0.34 \ 0.34 \ 0.67 \ 0.67 \ 1 \ 1 \ 1]$ , with  $p = 2$  and number of control points equal to seven (7), the final number of  $C^0$



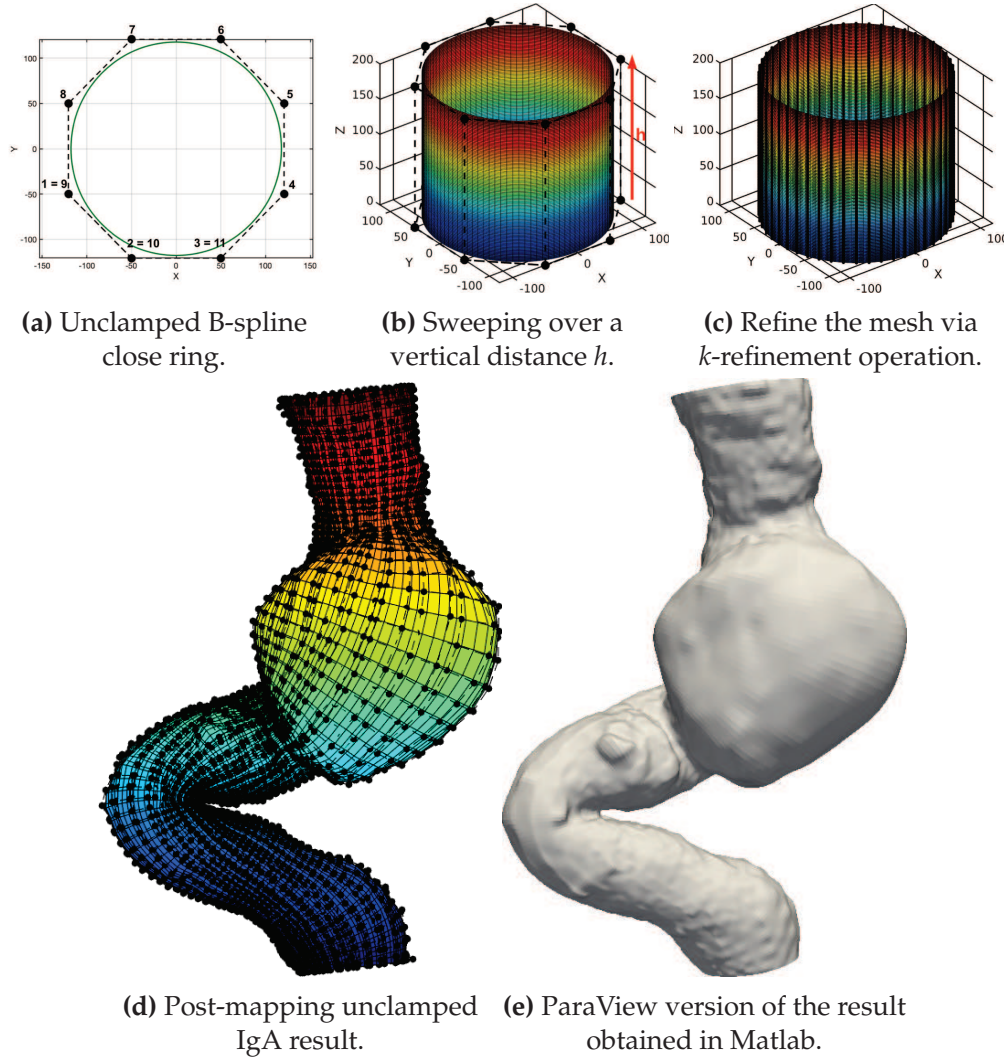


**Figure 4.10** Mapping procedure example on a patient-specific case. In Figure 4.10b, 4.10c and 4.10d, models are shown with their associated control polygon.

lines will be three (3).

Some clarifications have to be done: the first one is that, in order to obtain a *reliable* (i.e., close to the one extracted from medical images) IgA representation of the patient-specific TAA, the B-spline primitive cylinder used as reference geometry in the mapping operation just described, has to be *properly* refined along both parametric directions using the  $k$ -refinement algorithm described in Chapter 3. As already said, the  $k$ -refinement approach allows one to elevate the polynomial order and, at the same time, to increase the smoothness of the basis functions, which also means that it is based on two operations, i.e., degree elevation followed by knot insertion, that cannot commute. If the B-spline primitive cylinder is not properly refined, the mapping error, computed in terms of point-wise distance (measured in [mm]) between the original surface extracted from medical images by means of segmentation

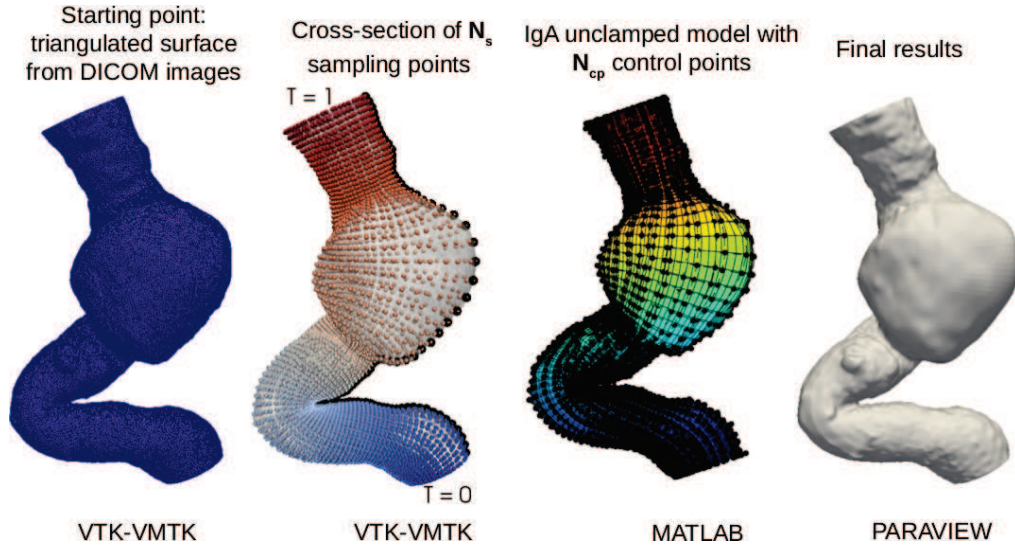


**Figure 4.11** Summary of the main steps we perform to get the patient-specific unclamped surface model of TAA starting from the triangulated mesh extracted from medical images.

method and the one obtained via mapping algorithm, just increases. Therefore, since we are interested in getting the most accurate IgA model possible, after testing our code, we can say that by "properly refined" we mean: starting from the B-spline reference cylinder shown in Figure 4.10b, with knot vector along parametric  $u$  direction equal to  $[0 \ 1 \ 2 \ 3 \ 4 \ 5 \ 6 \ 7 \ 8 \ 9 \ 10 \ 11 \ 12 \ 13 \ 14]$ , knot vector along parametric  $v$  direction equal to  $[0 \ 0 \ 1 \ 1]$ , polynomial degree  $p = 3$  along parametric  $u$  direction and polynomial degree  $q = 1$  along parametric  $v$  direction, we first perform degree elevation along parametric  $v$  direction, so that  $q = 2$  and then knot insertion along  $u$  and  $v$  parametric directions, with the following indices for the refinement:  $nx = 6$  and  $ny = (\text{number of ordered sections of points along parametric } v \text{ direction}) - 5$ . These two indices mean that the new knot values that are actually inserted in both knot vectors, always within their interval of definition and for each knot spans (for references, see Chapter 3 and (Piegl and Tiller, 1997)) are 6 along  $u$  and  $(\text{number of ordered sections of points along parametric } v \text{ direction}) - 5$ , along  $v$ . The result is the refined cylinder depicted in Figure 4.10c. These are the refinement indices used for *all* the patient-specific geometries we mapped in this thesis work.

As a second clarification, as already specified in Section 4.3, each cross-section of points has to be closed and the starting points of each section have to be aligned (see Figure 4.6, last image). If sections of points are not closed and their first points not aligned, the final IgA model can be distorted after mapping operation (see Figure 4.13).

In Figure 4.15, using a function (`vmtksurfacedistance`) available inside VMTK



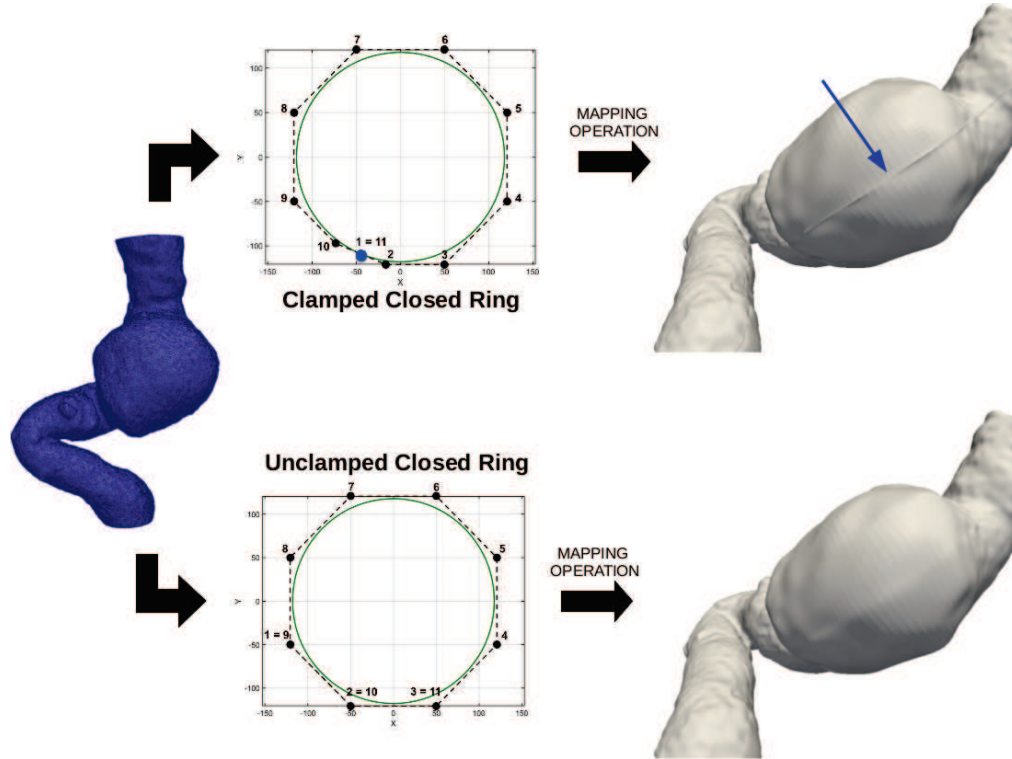


**Figure 4.12** Difference in results in the mapping operation if a clamped (top view) or an unclamped (bottom view) knot vector is used along the circumferential direction of each patient-specific model. The blue arrow helps to focus the attention of the unphysical  $C^0$  line(s) that crosses the model vertically if a clamped knot vector is used along  $u$ .

software suite, we calculated the point-wise minimum distance [mm] between the (clipped and capped) original surface extracted from medical images and three other input surfaces: the first one obtained using the old version of the mapping algorithm, i.e., the one that uses clamped knot vectors along  $u$ ,  $v$  and  $w$  (in this case, for the circumferential direction, we use the clamped knot vector  $[0 \ 0 \ 0 \ 0.34 \ 0.34 \ 0.67 \ 0.67 \ 1 \ 1 \ 1]$ , which means that the final IgA patient-specific model shows 3  $C^0$  lines along  $u$ ); the second one obtained using the new version of the mapping algorithm, i.e., the one that employs an unclamped knot vector along  $u$ , and clamped ones along  $v$  and  $w$ ; a third one using always unclamped knot vectors along  $u$  but with the "local refinement" of the sections of points addition where the curvature of the surface is higher. The original branched patient-specific surface from which these models have been obtained is depicted in Figure 4.14.

In this image we can see how the method we described so far is really able to create a trustworthy geometry in terms of point-wise distance computed

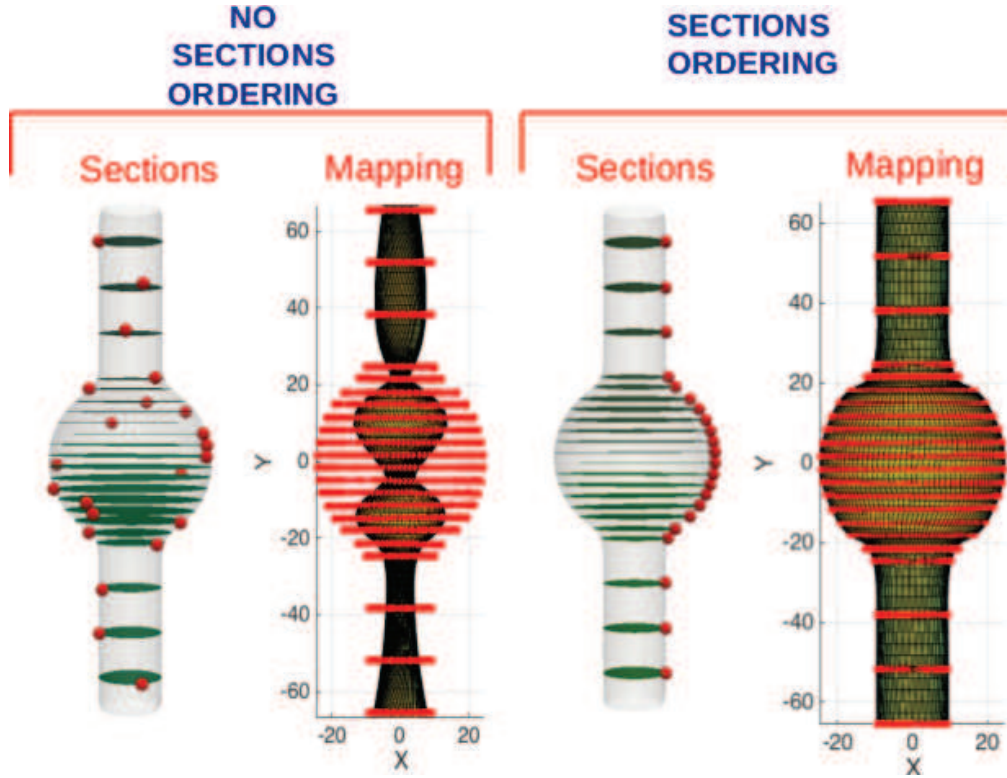


**Figure 4.13** Example on a test case of what can happen after mapping operation if starting points of the sections are not aligned.

between the IgA mapped and the original surface extracted from medical images. For example, in the last image, we are committing a maximum point-wise error of  $0.9972 \cdot 10^{-1}$  mm. This means that if the real geometry is approximately 35 cm long, we are committing an error of approximately 0.3% over the entire surface.

Before adopting the "conduction-based" method described in the previous Section 4.3, the ordered sections of points to be used as input for the IgA mapping operation (originally performed with clamped knot vectors along each parametric direction) were computed along the centerline of the model under study by means of a function (`vmtkcenterline`) included in VMTK software suite. As already pointed out, the creation of sections along the centerline *do not always* satisfy the non-intersection and orthogonality criteria we, instead, *strictly* require. Not satisfying these criteria can result in really distorted IgA geometries after mapping operation, especially in those cases where the target geometry is very angulated (e.g., the one shown in Figure 4.14). In order to convince the reader about the importance and effectiveness of our "conduction-based" method, we will show some initial results we got while working with sections of points computed on the centerline (Figure 4.16) of the patient-specific model shown in Figure 4.14. As an early



**Figure 4.14** Original branched patient-specific surface used to test the "local refinement" capability addition to the "conduction-based" method, after clipping and capping operations performed using the VTK-based Python code described in Section 4.2.

attempt, we also tried to work on a strategy to "adjust and fix" these intersecting sections. Nonetheless, we, on purpose, are not providing specific details of this "adjust and fix" strategy, because this attempt resulted in mapped IgA geometries with a much higher point-wise distance from the original surface extracted from DICOM images than the one shown in Figure 4.15, which absolutely justified the adoption of the "conduction-based" method to obtain more reliable and trustworthy IgA geometries. For a comparison of mapping operation (with clamped knot vector along  $u$  and  $v$  parametric directions) primitive results obtained using cross-sections of points got with the "conduction-based" method and with intersecting cross-sections of points computed along the centerline, please see Figure 4.17.

## 4.5 From an IgA unclamped surface model to an IgA solid model.

Once the IgA representation of the inner lumen surface has been obtained, we normally extrude of a radius-dependent thickness the 3D inner lumen surface extracted from DICOM images (see 4.2), in order to obtain the 3D representation of the outer arterial wall surface. The code we use for the normal extrusion is `vmtkboundarylayer.py`, included in VMTK software suite

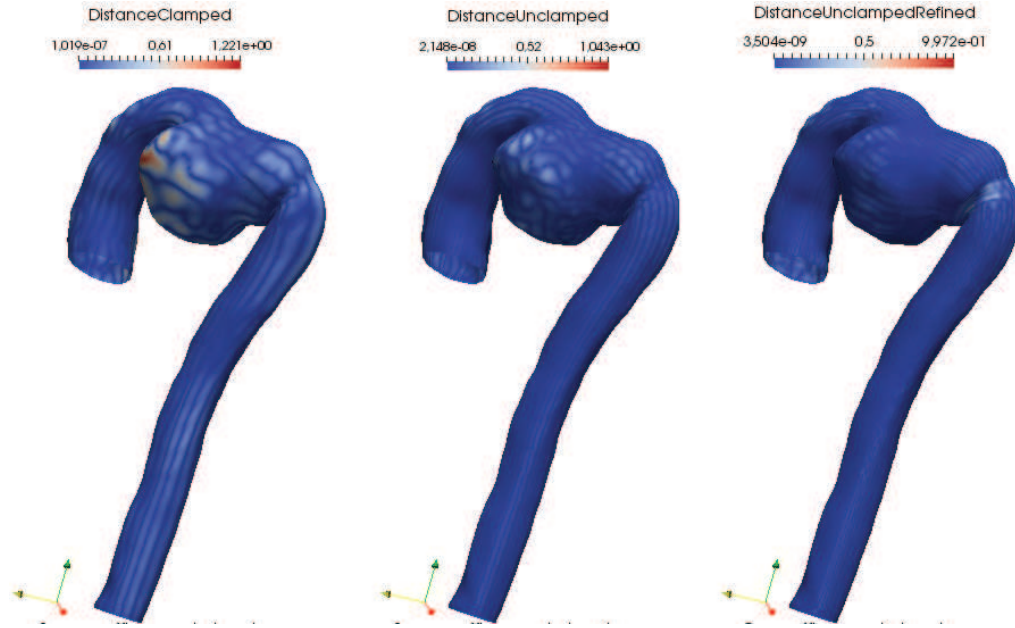


**Figure 4.15** Example of application on the patient-specific case depicted in Figure 4.14 of the "conduction-based" method with the "local refinement" addition in the regions on the surface that show higher curvature. Distance [mm] with respect to the (clipped and capped) original surface extracted from medical images is shown in three cases: IgA model constructed using clamped knot vectors along all the parametric directions (left), IgA model constructed using unclamped knot vectors along the circumferential direction of the model (middle), IgA model obtained using unclamped knot vectors along the circumferential direction of the model and "local refinement" in the zones with higher curvature of the surface, while performing the conduction-based method to get the ordered section of points (right).

(Faggiano, Formaggia, and Antiga, 2013). It allows for the generation of prismatic (or tetrahedral) boundary layers along surface normals. In details, it first computes outward normals and then creates prisms or tetrahedra by warping surface triangles of a constant amount. It gives you the normally extruded outer surface too and this is what we are interested in for the downstream operations. There is also the possibility of computing a scalar quantity on the surface (e.g., proportional to the local radius, a scalar quantity computed in VMTK on the centerline of the model) and use it as local thickness. This is what we decided to perform and code in a in-house VTK-based Python code, with specific attention to the aneurysm site, where the thickness should be higher since the local radius is higher. We do not want the arterial wall to be thicker at the aneurysm location since it has been proved in literature to be thinner than the rest of the arterial wall (Raut et al., 2013). As a matter of fact, differently from (Raghavan et al., 2000; Fillinger et al., 2002; Fillinger et al., 2003), we did not make the assumption of a uniform

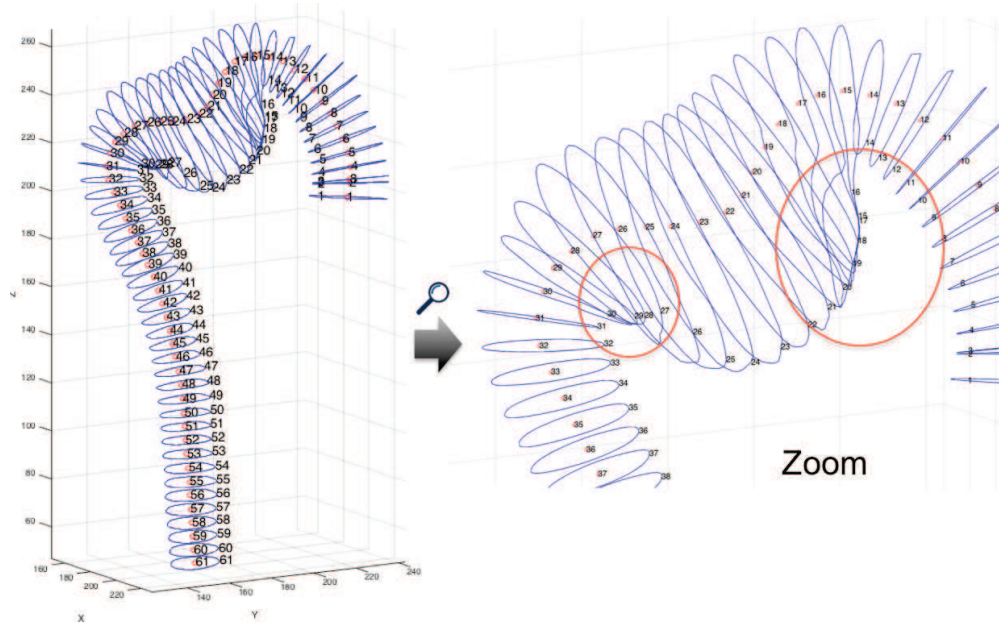


**Figure 4.16** Some of the sections computed along the centerline of the capped and cropped version of the model shown in Figure 4.14 are intersecting because of how the algorithm we adopted to compute sections of points along the centerline (`vmtkcenterline.sections`) actually works.

wall thickness, since it may not be adequate when attempting to characterize the response of the aneurysm (Morris et al., 2004).

Once we obtain the 3D outer arterial wall surface by means of normal extrusion operation, we have to get its IgA representation too. Therefore, the "conduction-based" algorithm described in section 4.3, needs to be applied to the normally-extruded 3D outer arterial wall surface. Before doing this, the "conduction-based" algorithm needs to be slightly modified, because we require the cross-sections of points not only to satisfy the desired non-intersecting and orthogonality conditions (see section 4.3) but also to be correspondent along the thickness with the cross-sections of points that belong to the 3D inner lumen surface. In case they do not correspond, distortions may occur in the final solid IgA model. In order to create cross-sections of points on the 3D outer arterial wall surface correspondent to the ones lying on the 3D inner lumen surface, we identify on the 3D outer wall surface mesh the points that are closest (in a nearest neighbor sense) to the ones on the 3D inner lumen surface mesh from which we start performing steepest gradient descent operation (black dots in Figure 4.11c). Once identified these points, we perform steepest gradient descent and all the subsequent steps on the 3D outer arterial wall surface as previously described to get cross-sections of points (see section 4.3). Mapping operation is then performed using the newly obtained cross-sections of points to get the correspondent 3D IgA representation of the outer wall surface.



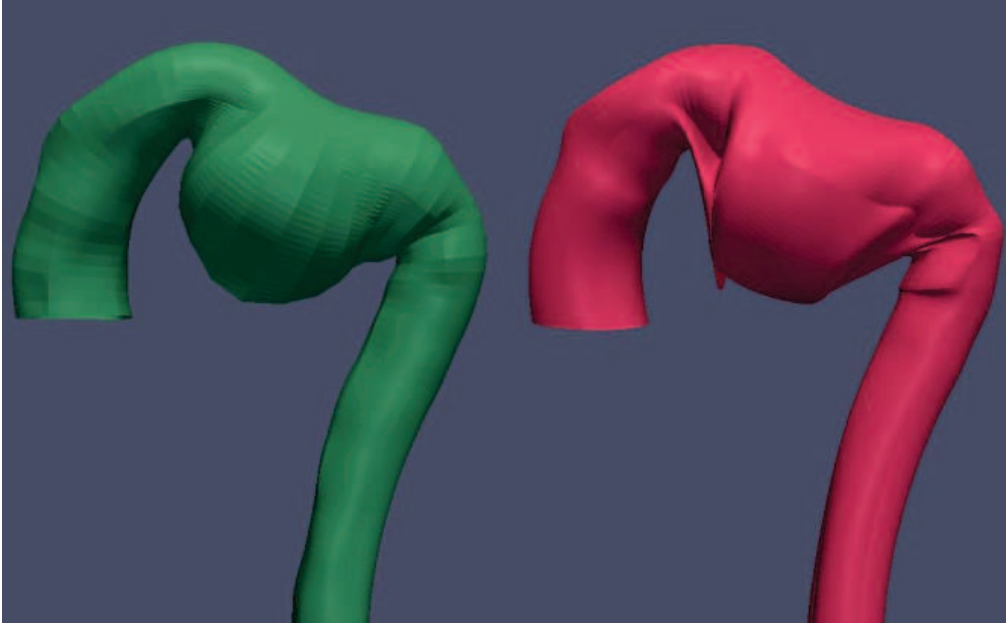


**Figure 4.17** Comparison between the original mapping operation (i.e., the one employing clamped knot vectors along  $u$  and  $v$  parametric directions) result using cross-sections of points obtained with the "conduction-based" method (left figure) and cross-sections of points computed along the centerline of the model (right figure). This picture wants to demonstrate how the unsuitability of the approach that computes cross-sections of points along the centerline was evident since the very beginning of the work, besides the use of clamped knot vector along  $u$  and  $v$  parametric directions.

Hence, in order to create a 3D solid model for the TAA from the IgA B-spline inner lumen and outer arterial wall surfaces generated above, a linear clamped B-spline is then introduced in Matlab between them. This operation corresponds to specify a control net in the three coordinate directions along with a trivariate knot vector set to generate the B-spline solid model. In particular, this is possible because we impose the control points of the inner and outer arterial walls to correspond along  $w$ , i.e., the thickness. Each cross-section of control points (holding  $v$  constant) contains the same number of circumferential control points, where the first and last  $p$  control points coincide. Along  $w$ , it is possible to perform IgA k-refinement operation, i.e., degree elevation followed by knot insertion. Any choice of degree and knot complexity can be introduced in the three coordinate directions in order to capture desired geometric details and to provide higher order of continuity for more accurate solutions. As a matter of fact, the 3D IgA models we use for the simulation are of degree 3 (three) along the circumferential direction  $u$  and of degree two (2) along the longitudinal direction  $v$  and the thickness  $w$  (see Figure 4.20).

## 4.6 Thoracic Aortic Geometry

The proposed computational framework is benchmarked with 10 CT scans of patients affected by thoracoabdominal aneurysms available at IRCCS Policlinico San Donato, San Donato M.se, Milan, Italy (see Figure 4.21). Other types of aneurysms, e.g., those secondary to connective tissue disorders, infectious diseases, as well as aneurysms with concomitant aortic dissections are excluded. Patients enrolled in the study do not represent an homogeneous population from the point of view of age, sex, diameter and location of the aneurysm.

## 4.7 Analysis Setup

In this sections, all the ingredients employed to run isogeometric structural simulations on patient-specific TAAs models are illustrated. The ultimate goal of these simulations is to check the von Mises stress quantity at the vessel wall in order to identify patients potentially at risk of aneurysm rupture. Inflation simulations are performed for each one of the patients in Figure 4.21 using a finite element program, FEAP (Taylor, 2017), and its IgA embedded module. We would like to remark that our work aims at evaluating the performance of IgA applied to patient-specific modeling and analysis of TAAs. Therefore, the quantitative comparison of numerical and experimental results is beyond the scope of this study. In particular, a quantitative comparison requires further investigation in terms of material parameters calibration from experimental data and analysis of experimental boundary conditions.

Given the refinement techniques for IgA presented in Chapter 3, the basic primitive unclamped along  $u$  cylinder (see Figure 4.10b) used as reference geometry in the mapping operation described in Section 4.4 has been refined using IgA  $k$ -refinement algorithm, with the same combination of subdivision indexes and the same polynomial degrees along the two main parametric directions (see Figure 4.10c) for all the studied geometries.  $k$ -refinement technique has been also applied to each one of the patient-specific TAA solid models (see Section 4.5) along the thickness (see Figure 4.20), with the same subdivision indexes and polynomial degree for all the geometries.

### 4.7.1 Material Properties

The arterial wall is modeled using the hyperelastic, isotropic, nearly incompressible material model described in (Raghavan and Vorp, 2000). The strain energy function  $W$  for this model may be expressed as follows:

$$W = C_1 (I_B - 3 - 2 \log(J)) + C_2 (I_B - 3)^2 + U(J) \quad (4.3)$$

$$U(J) = \lambda * \left[ \frac{1}{4} (J^2 - 1) - \frac{1}{2} \log(J) \right] \quad (4.4)$$



where the constants  $C_1$  and  $C_2$  represent material parameters for the arterial wall and  $I_B$  is the first invariant of the left Cauchy-Green tensor  $\mathbf{B}$  ( $I_B = \text{tr}(\mathbf{B})$ ).  $U(J)$  is a volumetric term with  $J$  equal to the determinant of the deformation gradient and  $\lambda$  the first Lamè parameter, empirically set to 1000 MPa, to enforce near incompressibility. Population mean values taken from (Shang et al., 2013a) of  $C_1 = 0.174$  MPa and  $C_2 = 1.881$  MPa are adopted in this work. More information about this constitutive model and its formulation in FEAP are given in Appendix B.

### 4.7.2 Numerical simulations

The blood pressure within the TAA acts on its inner wall surface. Therefore, the average blood pressure in a single cardiac cycle (i.e., MAP = Mean Arterial Pressure), previously computed by means of Computational Fluid Dynamics (CFD) simulations, is numerically applied as *uniformly distributed* internal forces acting outwardly on the TAA wall. In particular, in the CFD simulations, the vessel wall is considered as rigid, and RCR boundary-conditions are applied and calibrated in a patient-specific way as extensively detailed in (Romarowski et al., 2018). This method incorporates the real cuff-pressure of the patient and the real flow distribution among the boundaries of the aorta. Since for three cases the MAP from CFD simulations was not available, the mean value of the MAP for the other seven cases (101.3 mmHg) was applied. Contact with adjacent structures, including the spine and other organs was not considered. The shear stress induced by blood flow was neglected in this study (Raghavan et al., 2000), although the effects of blood flow have been shown to reduce wall stress by 10% in uniformly thick-walled ideal models and by up to 30% in variable wall thickness models of abdominal aortic aneurysms (Scotti et al., 2005). The aorta was translationally fixed at the proximal and distal ends (see yellow dots in Figure 4.22b), whereas generalized Robin Boundary Conditions were used to represent the viscoelastic behavior of the tissues surrounding the thoracic aorta (Moireau et al., 2012). They require the definition of two parameters:  $k_s$  and  $c_s$ , dependent on space and, possibly, on time (see Figure 4.22b). They are used to model an elastic and viscoelastic response of the external tissue (e.g., the spine). In the present work, no time-dependent parameters were employed and just the elasticity term  $k_s$  was taken into account, with  $k_s = 10$  MPa as proposed in (Moireau et al., 2012).

Since we are dealing with three-dimensional geometries reconstructed from medical images, they represent a configuration under “in-vivo” loading, such as blood pressure. The most common approach in simulations is to neglect the pre-deformation of the object of interest under “in-vivo” loads and to assume the obtained configuration as stress-free. This is a over-simplified approach that can lead to unphysically large deformation and strains. Therefore, the evaluation of a stress state correspondent to a given spatial configuration (the three-dimensional geometry extracted from medical images) under known external loads (blood pressure) is necessary (Gee et al., 2009).

Hence, prestress analysis, based on the method proposed in (Bols et al., 2013), is performed to retrieve the zero-pressure geometry. In particular, after getting the patient-specific IgA solid model of TAA, we solve for the zero-pressure geometry by iteratively updating the nodal coordinates towards the unknown unloaded configuration, using a fixed-point algorithm. All that is required in this method is an update of the nodal coordinates: therefore, it allows for a straightforward implementation in combination with the structural solver FEAP adopted in this work. Once the Zero-Pressure ("Z-P" in Figures 4.23b and 4.23d) geometry is obtained, then, the arterial pressure present in diastole at the moment of imaging (i.e., 80 mmHg) is applied, to fully recover the "in-vivo" measured geometry, restoring at the same time its stress state. The zero-pressure geometry found for each patient is used as the initial configuration. For an example of application of this method on both a test and a patient-specific case, please see Figure 4.23. This code was originally written for clamped geometries and subsequently adapted for unclamped ones. For the boundary conditions used in the simulations, the control points at the ending cross sections are only allowed to move in a radial direction, as specified in (Bols et al., 2013). Hence:

$$\begin{cases} U_\theta &= 0 \\ U_z &= 0 \end{cases} \quad (4.5)$$

The artery wall behavior is modeled using the Vorp material model, with the same parameters specified in Section 4.7.1.

Subsequently, the von Mises stress at the vessel wall can be computed to identify patients potentially at risk of aneurysm enlargement and rupture. A summary of the simulation details is provided:

- **Type of Analysis:** IgA Inflation simulations. Radial expansion under a normally applied internal load. Such a load is defined with respect to the outward normal to the internal surface of the vessel, in the deformed configuration.
- **Aneurysm Type:** Thoraco-Abdominal Aneurysms. Ten different aneurysms have been studied.
- **Boundary Conditions:** Robin Type. Used to simulate the presence of the surrounding organs. Only the elasticity term is considered. Spring stiffness:  $k_s = 10\text{MPa}$ .
- **Pressure:** Patient-specific values derived from CFD analyses have been used for all the cases except that for three of them (lack of data).
- **Thickness:** Proportional to the local radius. Particular attention in the presence of the aneurysm.
- **Constitutive model for the arterial wall:** Non-linear, hyperelastic formulation derived from (Raghavan and Vorp, 2000). Arterial wall is

assumed to be hyperelastic, omogeneous and isotropic. Constitutive parameters:  $C_1 = 0.174MPa$ ,  $C_2 = 1.88MPa$ .

### 4.7.3 Surface extraction operator in FEAP

Before showing the results of the inflation simulations we run using the ingredients described above, in this subsection we are going to briefly explain how we are extracting in IgA-FEAP, starting from NURBS patches, the surfaces or segments of surfaces on which to apply the pressure field or the Robin boundary conditions. This may be achieved by using a new solution command, "**N\_EXtract**", we introduced in IgA-FEAP. It employs extraction operators to get the IgA surfaces on which to apply loads or boundary conditions. This command should be issued in an *interactive mode of solutions*. This means that, to initiate the extraction in IgA-FEAP, it is necessary to first display a plot of the problem in graphics mode. For two dimensional problem, this can be achieved by giving the command:

```
PLOT MESH
```

then followed by:

```
N_EXtract
```

The program will then display each one of the boundary segments for each NURBS patch and the user may choose to output a file or reject it. For three dimensional problems, the graphics commands are the following:

```
PLOT PERSpective
PLOT HIDE
PLOT MESH
```

then followed by:

```
N_EXtract
```

After completing the selection, a set of text files containing all the information regarding the surface segment extractions will be created. In order to be used, another text file "**Bxxx\_m**", with xxx being the characters (3:5) of the IgA-FEAP input file name, should be added to the mesh part of the input file by means of the **INCLude** command. The "Bxxx\_m" file contains the list of files for each surface segment extractions. For more information regarding this command, the interested reader is referred to Taylor, 2017.

By using this command, it is possible to extract the outer arterial surface on which to apply Robin boundary conditions used to simulate the organs surrounding the thoracic aorta. We are going to provide an example of IgA-FEAP input data for the Robin boundary conditions as well. We remind the reader that, at present, no time-dependent parameters are employed and just the elasticity term  $k_s$  is taken into account. The input data for the Robin boundary conditions in IgA-FEAP are:

```

MATERial ma
Robin 5
    elastic ks value
NURBs <option> q1 q2
plot <option> on/off
! Blank record

```

where "ma" is the material number, q1 and q2, the number of quadrature points in the 1 and 2 directions. The plot command can be activated or deactivated. We recommend the reader to switch this command to off when solving an analysis.

## 4.8 Results

We now present the results obtained from implicit nonlinear isogeometric analyses using the model described in the previous sections. In particular, the von Mises stress distribution on the TAA of each studied patient is plotted and observed to easily represent and interpret the computational stress analysis results (Martin, Sun, and Elefteriades, 2015; Gasser, 2016).

In order to better understand the effect that the use of clamped or unclamped knot vectors along the parametric  $u$  (circumferential) direction have on patient-specific TAA stress analysis results (as anticipated in section 4.4), the difference between the von Mises stress distribution in just one clamped and unclamped patient-specific study model is shown in Figure 4.24. In detail, the main drawback of using clamped B-splines along the circumferential direction is the discontinuity of the stress field along the unphysical  $C^0$  line that crosses the model vertically (see Figure 4.24). This  $C^0$  line is exactly the evolution of the blue dot of Figure 3.2a, if such a ring is extruded vertically over a certain height.

The von Mises stress distribution for each unclamped patient-specific case in Figure 4.21 is depicted in Figure 4.25.

It can be observed that the von Mises stress has complex distributions with large regional variations. The sites of von Mises stress peaks coincide in the majority of the cases and they are localized in correspondence of the aneurysm neck, while they reduce across the entire surface of the TAA. Moreover, wall stress peaks are located at inflection points, as previously reported

in idealized models of abdominal aortic aneurysms, both numerically (Vorp, Raghavan, and Webster, 1998b; Callanan, Morris, and McGloughlin, 2004; Scotti et al., 2005) and experimentally (Morris et al., 2004). Note that with an inflection point we mean a point on the TAA surface where the local TAA shape changes from convex to concave (Vorp, Raghavan, and Webster, 1998b).

Despite the small patient population studied, following what Raghavan and colleagues stated for AAAs in (Raghavan et al., 2000), according to clinical thinking, patients with highest TAA diameters would be thought as being at greater risk for rupture. Such patients in this work are:

- Case 001. TAA diameter = 6.817 cm. MAP = 101.64 mmHg (from CFD).
- Case 003. TAA diameter = 6.789 cm. MAP = 101.57 mmHg (from CFD).
- Case 004. TAA diameter = 7.871 cm. MAP = 100.9 mmHg (from CFD).
- Case 009. TAA diameter = 7.345 cm. MAP = 101.3 mmHg (mean of the patient-specific pressure values obtained from CFD).

Case	Definition of computational domain [min]	Computational IgA Geometry Construction [min]	FEAP Analysis CPU time [min]
001	1.61	1.51	30
002	1.9	1.56	36
003	1.45	1.14	26
004	6.23	1.57	65
005	5.02	1.62	35
006	3.51	0.76	32
007	2.11	1.57	36
008	0.96	1.57	30
009	6.57	1.2	29
010	3.36	1.08	35

**Table 4.1** Summary of the time required to perform the operations previously described in Section 4.3, 4.4 and 4.5, to derive the 3D IgA solid geometry for each one of the 10 patient-specific cases under study. In particular, in the column “Definition of computational domain”, the time required to perform steps described in Section 4.3 is indicated, without taking into account the time for the segmentation process and triangulated surface mesh post-processing (see Section 4.2), which usually takes 20 minutes if performed by an expert user. The column “Computational geometry” shows the time required to fulfill steps described in Sections 4.4 and 4.5. Once obtained the stress-free configuration, each derived model is inflated with pressure. The time required to run such structural simulations in IgA-FEAP is listed in column “FEAP CPU time”.

Therefore, Patient 4 and 9 should have greater risk of rupture among all the patients and among the patients with highest diameter in the study. However, our computational stress analysis reveals that the von Mises wall stress peak for the TAA of Patients 004 and 009, is comparable with those of the other patients. Hence, there is a disagreement between conventional thinking and the results of the present study. This can be attributed to the fact that both the shape and a non-uniform and non-constant wall thickness along the TAA are taken into account in our analyses to assess rupture potential, differently from the clinical practice.

Regarding the use of IgA as computational framework instead of FEA, Indrakusuma and colleagues in (Indrakusuma et al., 2016), states that FEA is frequently applied in the field of computational biomechanics of pathological arteries, but the methodology has not been standardized and its technical limitations have been only marginally improved. IgA can help overcoming FEA limitations from many viewpoints, as already stated in the Introduction and demonstrated by other works from our group (Auricchio et al., 2015; Morganti et al., 2015). One of the benefit of its use is the computational time required for each stress analysis. CPU time employed by IgA-FEAP for the analysis is reported in Table 4.1, together with the time required for the creation of the isogeometric solid model of each studied subject, once the corresponding CAD representation has been obtained. Each stress analysis has been run on a 3,7 GHz Quad-Core Desktop Computer using just one CPU and the external Pardiso solver (<https://www.pardiso-project.org/>), its duration varying from approximatively 25 to 36 minutes, with just one model taking more than this time. The number of degrees of freedom employed for each studied patient-specific model to reach these results is around fifty thousand.

This concept can also be reinforced by looking at the comparison between the computational cost that is required to go from the surface extracted from medical images to the results of the stress analysis, with both IgA and linear FEA ("h-FEA"; see Figure 4.26). The h-FEA meshes we used for the comparison have been obtained from their IgA counterparts, employing the refinement technique described in Chapter 3. In particular, the h-FEA mesh is recovered by means of iterative knot insertion operation performed on the correspondent highly regular IgA mesh previously described. The comparison of the performances between IgA and h-FEA is made on a per-degree-of-freedom basis with respect to the strain energy of the model. Focusing on the last block, it can be seen that in order to have h-FEA results comparable to IgA ones, on a strain energy basis, more than 30 hours of computational time are required. In terms of degrees of freedom, the h-FEM mesh requires almost three times the number of DOFs of the IgA one. This concept entails and justifies the results shown in Figure 4.26. It is important to clarify that in all the analyses we presented, both h-FEM and IgA, since the adopted material is nearly incompressible, the three-field mixed formulation described in (Taylor, 2011) is used. Moreover, the analyses are performed as a finite deformation problem.



## 4.9 Conclusions

This study focus on isogeometric structural simulations of patient-specific unclamped TAA models. In particular, we have demonstrated how creating a patient-specific IgA-suitable model of TAA can be done almost automatically by performing a limited number of relatively easy steps, once CT images have been acquired, preprocessed, and segmented. The "conduction-based" method we conceived and use to obtain in an easy way cross-sections of points to be given in input to the mapping algorithm is really straightforward and capable of creating cross-sections of points that are not intersecting and orthogonal to the vessel wall, completely removing any operational dependency on the centerline. Our final goal is the identification of patients potentially at risk of TAA enlargement and rupture. We certainly know that to fulfill this task and, thus, give the physicians a consistent and objective decision-making tool to improve the surgery planning operation-phase in the context of thoracic aneurysms rupture risk, other ingredients (e.g., supra-aortic carotid branches and iliac arteries, a TAA-suitable constitutive model, inclusion of the intraluminal thrombus, use of patient-specific variable pressure distributions derived from CFD analyses) need to be considered in our pipeline. However, we think that our simulation models and analysis settings already represent a good compromise between computational time and accuracy, sufficient to reach the main goal of this study. It is also clear that the proposed framework can represent a promising and adequate starting point for the development of the aforementioned decision-making tool to be used in real-time by physicians (instead of the current use of the largest TAA diameter criterion) to decide whether is worth operating a patient or not.

For the work done in this Chapter, I strongly acknowledge Ph.D. Elena Faggiano: with her great expertise in patient-specific 3D geometrical modeling, she made possible the development of most of the pipeline described in this chapter, always supporting, helping and introducing me to the fantastic world of VTK-based Python programming for geometrical modeling. Without her help, this part of the thesis would have been impossible to be performed alone.



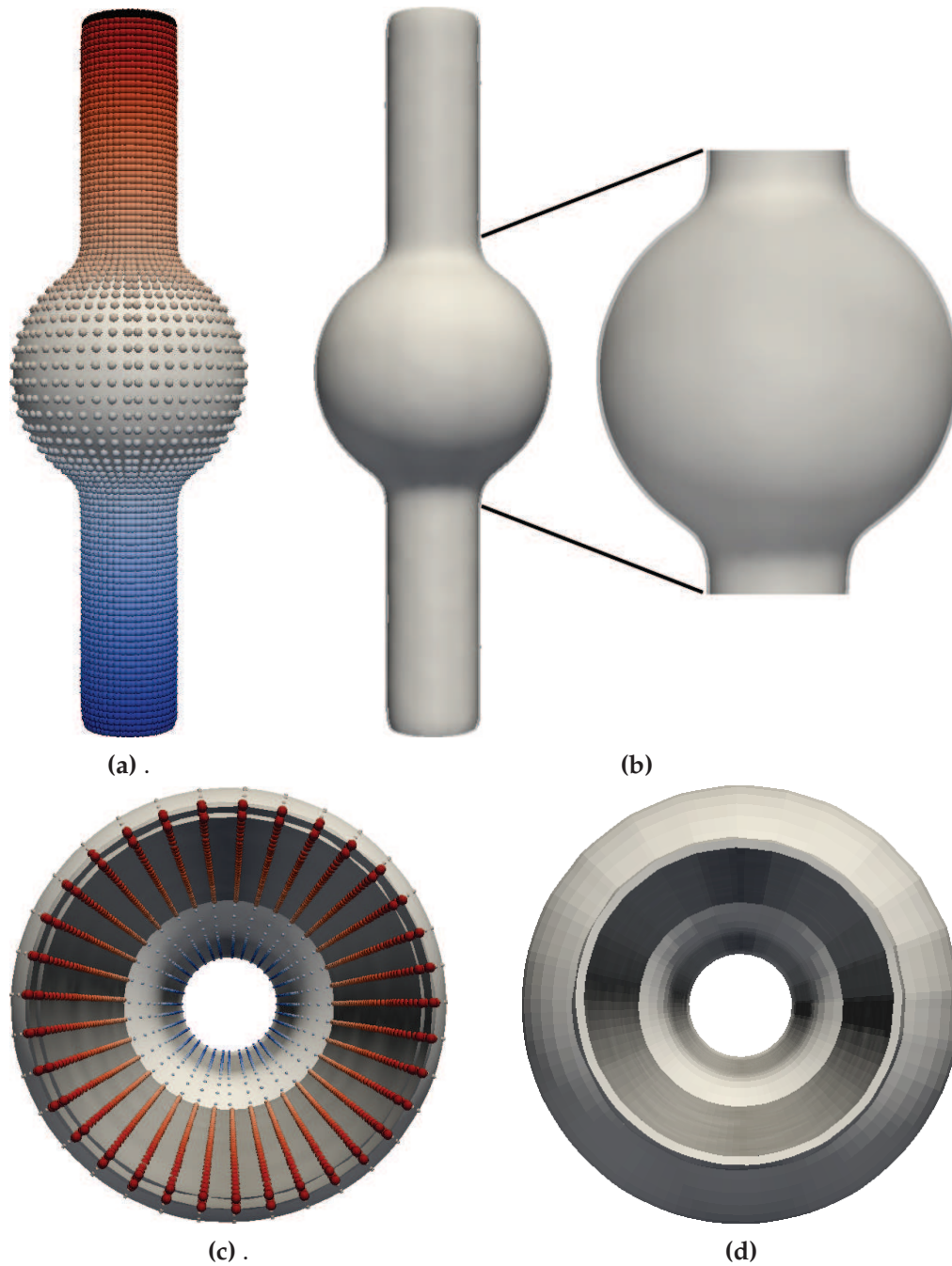


**Figure 4.18** (a) Cross-section of points of the 3D inner lumen surface plus source points for the steepest gradient descent operation (black points). (b) Normal extrude of a radius-dependent thickness the 3D inner lumen surface to get the 3D outer arterial wall surface. (c) Correspondent cross-sections of points between the inner and outer 3D surfaces (top view). (d) Solid model obtained imposing a linear clamped B-splines between the 3D IgA representations of the inner lumen and outer aortic wall.

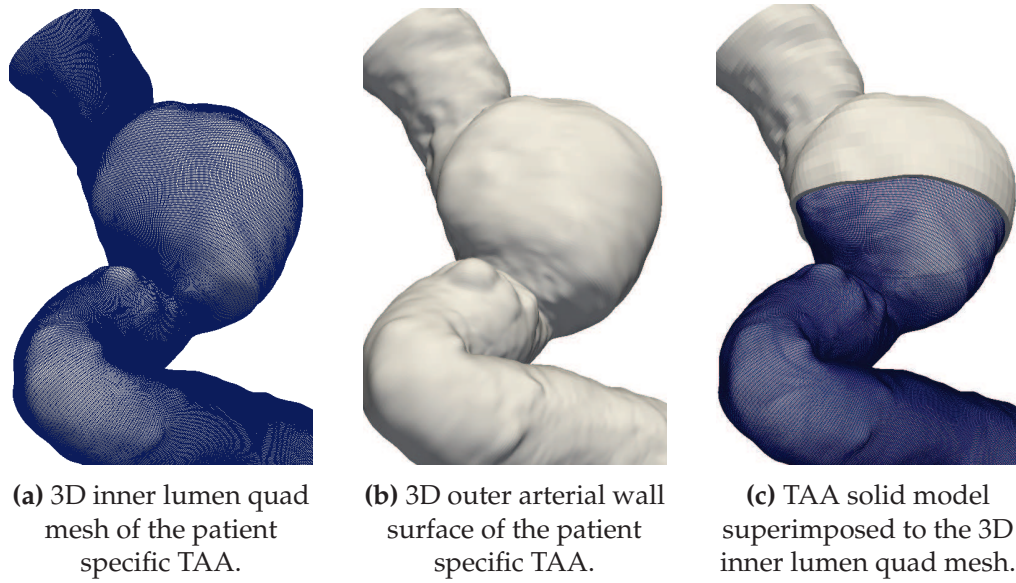


**Figure 4.19** Construction of the solid model (c) starting from the 3D inner lumen (a) and outer arterial wall (b) surfaces for a patient specific case. The 3D inner lumen surface is depicted as a quadrilateral mesh (a - Paraview version) just to highlight the difference with the outer arterial wall surface (b - Paraview version) and the solid final model (c - Paraview version).

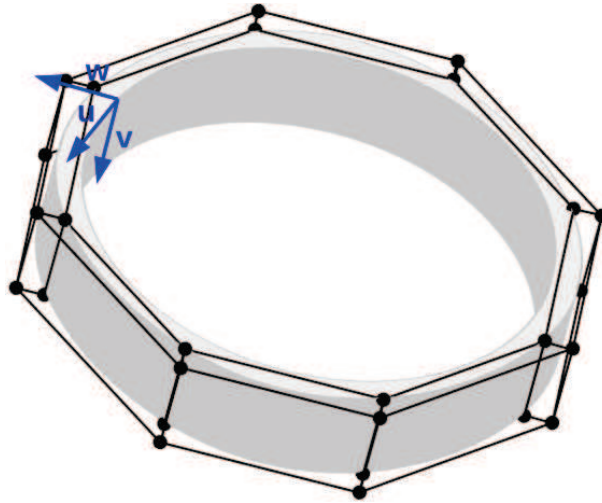


**Figure 4.20** Parametric directions adopted in the construction of each patient-specific IgA solid model.  $P=3$  is adopted along the circumferential parametric direction  $u$ .  $Q=2$  and  $R=2$  are adopted along the longitudinal parametric direction  $v$  and along the thickness, respectively.

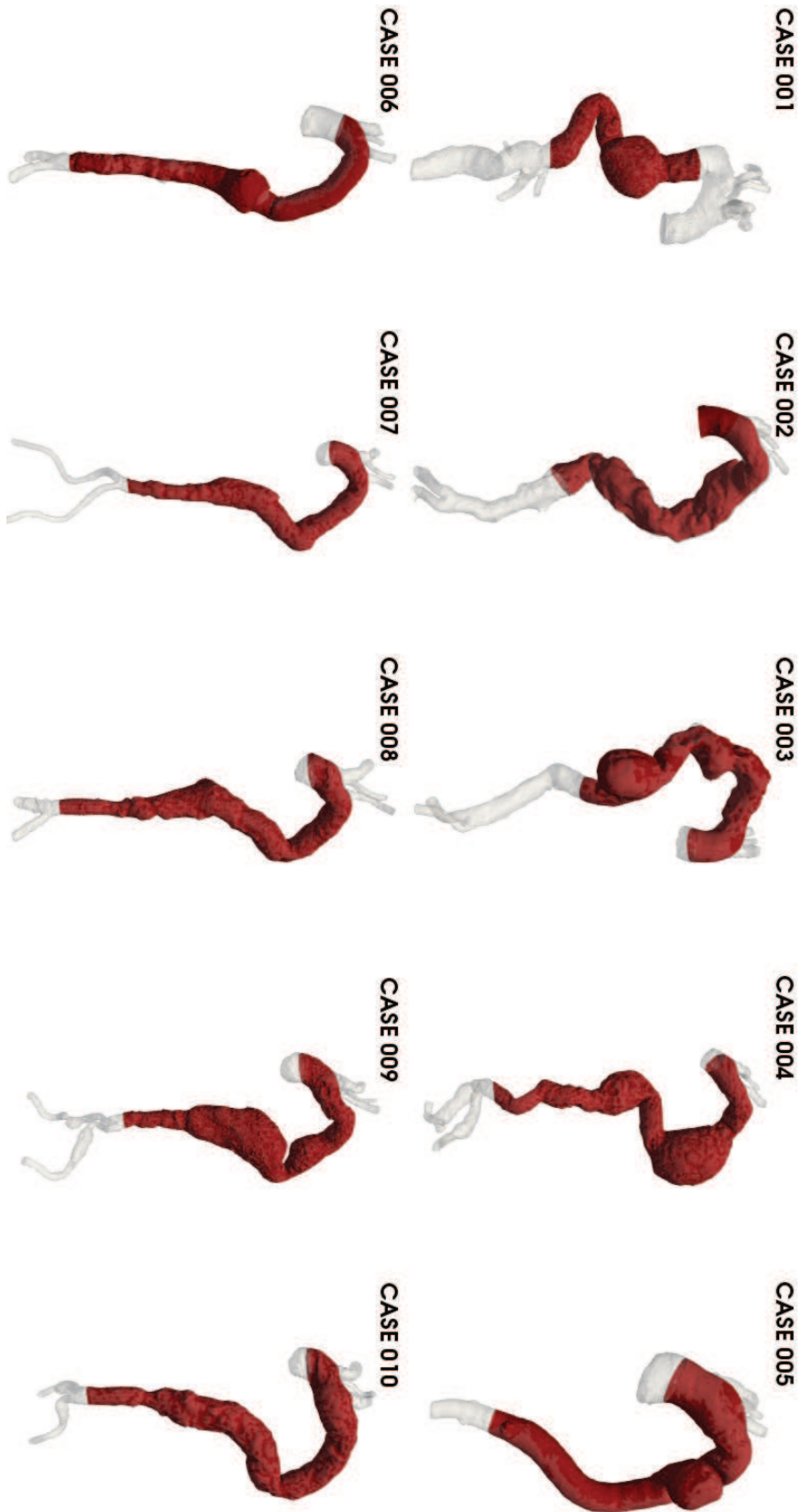
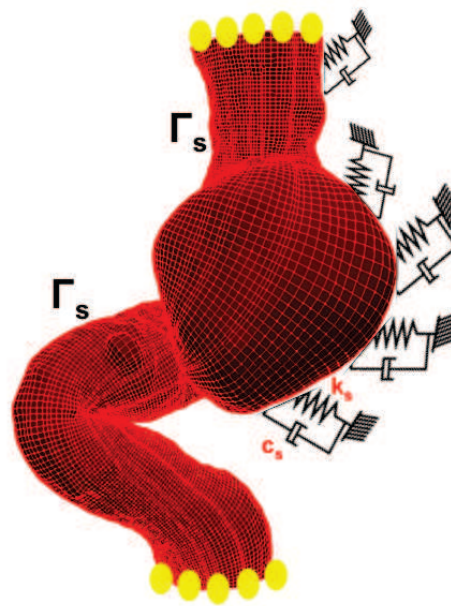
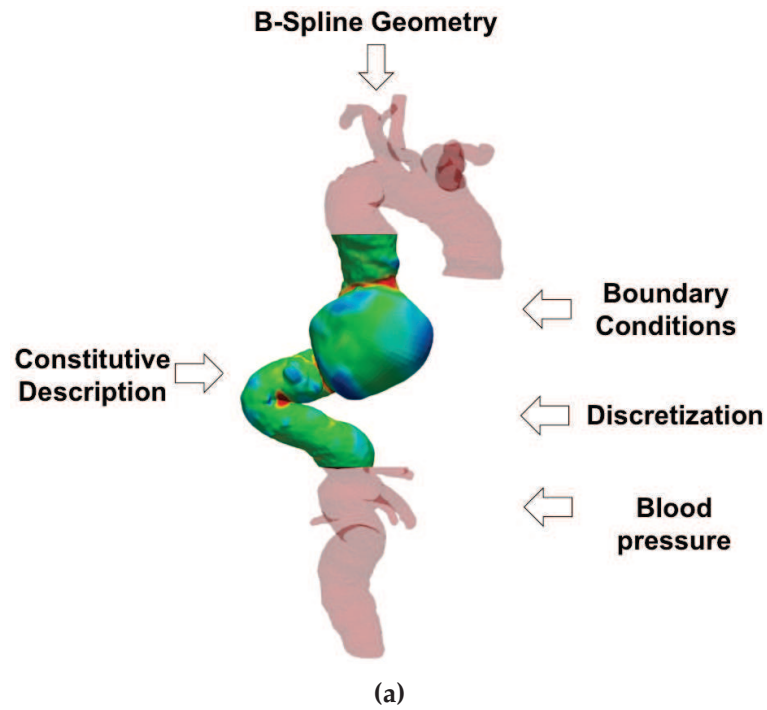
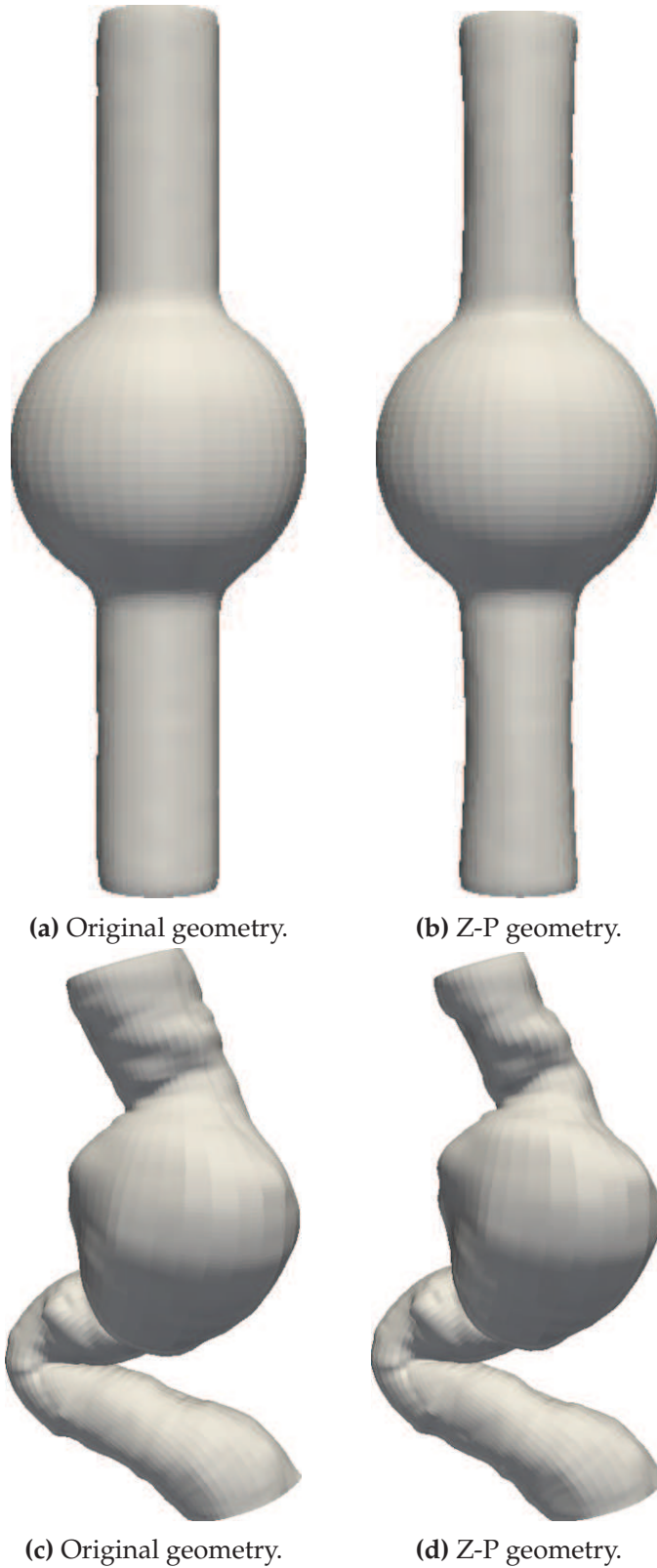


Figure 4.21 Thoracoabdominal aneurysms considered in the study.



**Figure 4.22** a) Key ingredients for IgA TAA Inflation simulations. b) Boundary conditions and model domain.



**Figure 4.23** Zero-pressure geometries obtained using the method proposed in (Bols et al., 2013). Application on a test - images (a) and (b) - and on a patient-specific case images (c) and (d)).



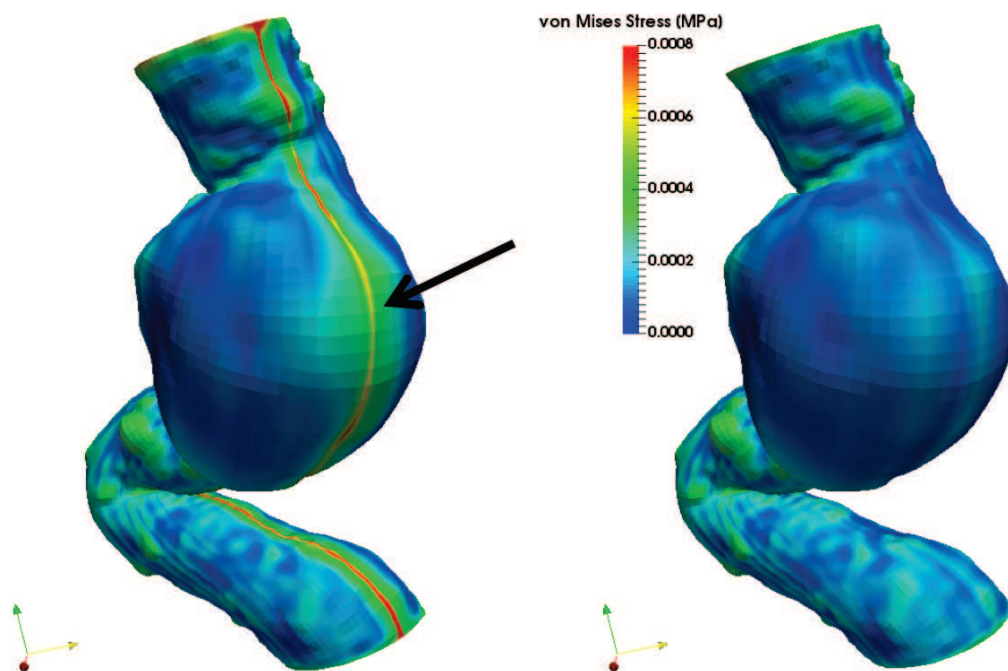
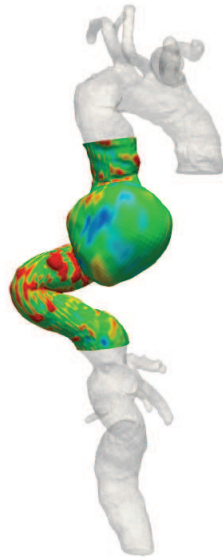


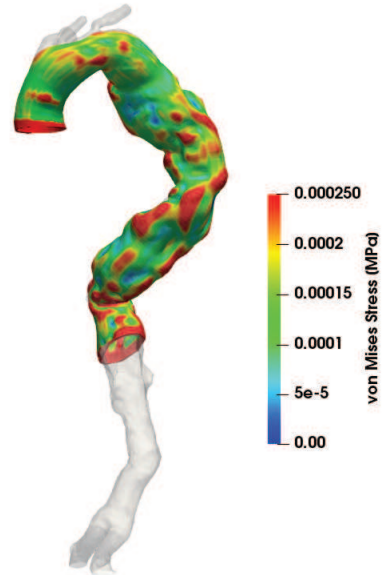
**Figure 4.24** Difference between a clamped (left) and an unclamped (right) patient-specific geometry in terms of von Mises stress distribution. Discontinuity in the stress field can be seen in the figure on the left and it is also highlighted by a black arrow.



CASE 001



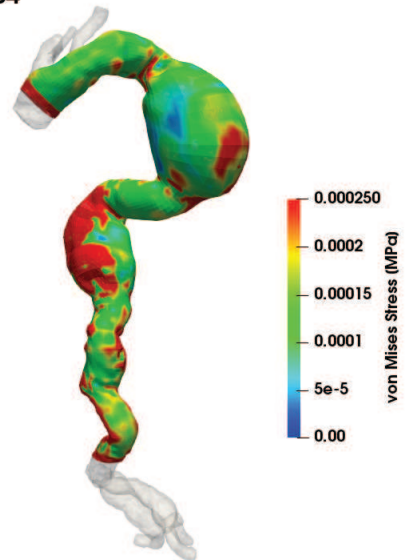
CASE 002



CASE 003



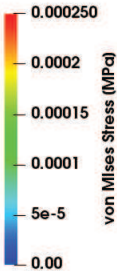
CASE 004



CASE 005



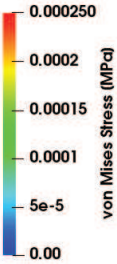
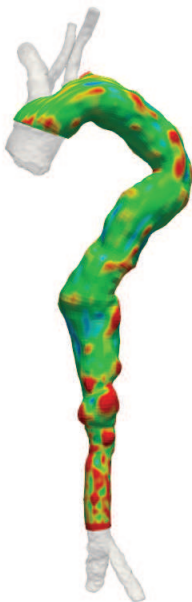
CASE 006



CASE 007



CASE 008



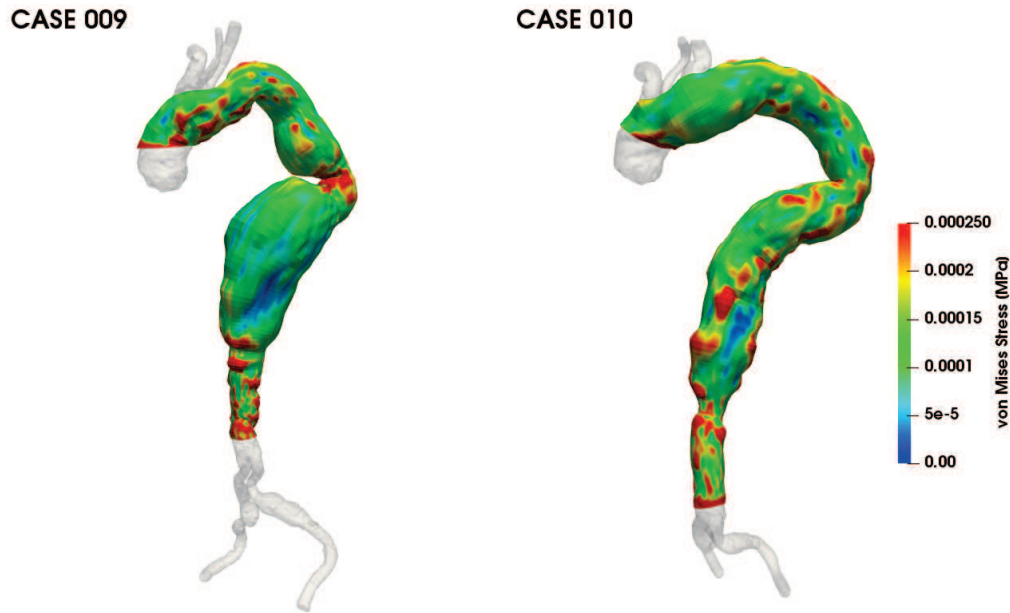


**Figure 4.25** Results in terms of von Mises stress ([MPa]) at the vessel wall obtained from IgA-FEAP inflation simulations. In all cases, blue represents the lowest stress magnitude, and red the highest stress magnitude.

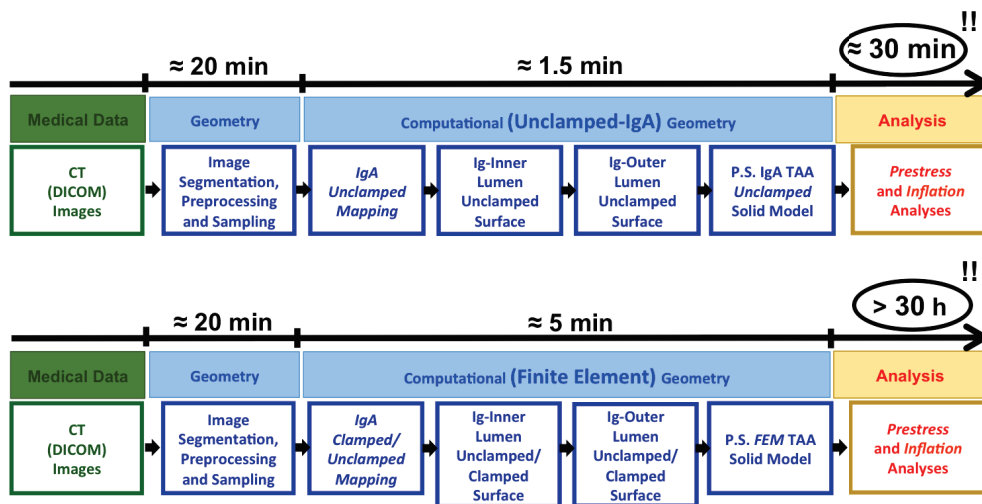


**Figure 4.26** From medical images to analysis: comparison between how much time is required to perform each operation of the pipeline presented in Sections 4.2, 4.3, 4.4 and 4.5 and introduced in Figure 7.3 in case of IgA (top) and FEA (bottom).

The names “Definition of computational domain” and “Computational IgA/FEM geometry”, are linked to the labels of the columns of Table 4.1.

## Chapter 5

# Patient-specific modeling of bifurcated geometries

### 5.1 Introduction

In the previous Chapter, we described the pipeline we created to obtain the most suitable patient-specific IgA representation of the aneurysmatic thoracic aorta, starting from medical images. As we already pointed out, the geometries we presented in Figure 4.21 are not provided with supra-aortic branches, because the mapping algorithm we use to get the IgA TAA model starting from sections of points and a cylindric reference surface, at present, does not work for branched geometries but only for single-patch tube-like ones. Not taking into account the presence of supra-aortic branches in the inflation simulations on TAA we showed in the previous Chapter, presumably means that we are neglecting important constitutive parts of the aorta that may affect the distribution of the von Mises stress at the vessel wall when looking for patients potentially at risk of aneurysm enlargement and rupture. For this reason, in this Chapter we are going to show how the pipeline we created can be extended for the creation of a particular type of branched geometries, characterized by a "Y" shape (e.g., carotid artery). This part of the work has been done in collaboration with Dr. John Eric Dufour.

Since in this thesis work, we are mostly dealing with thoracic aortas (TA) and not with "Y"-shaped arterial networks, a new framework based on the T-spline technology for the creation of any kinds of branched geometries will be introduced.

### 5.2 Preliminary branched geometries

The first, natural attempt we made in order to get IgA branched geometries was obtained expanding the pipeline we presented in Chapter 4. In particular, as a preliminary hypothesis, we made the assumption that the vascular segment of interest has a tree-like topology, i.e., one inlet and several outlets. This is quite a strong assumption, which in general holds true for arterial segments like carotid artery, and not so much for the thoracic aorta. Therefore, in the following, our attention will be focused on a patient-specific carotid

artery geometry, to show our main idea. It relies on the skeleton (i.e., the centerlines of the branches) to create a multi-patch NURBS mesh close enough to the one extracted from medical images. The centerline of the artery is obtained by means of a routine implemented in VMTK. Once the skeleton is obtained, the centerline has to be divided into polylines between nodes (i.e., its main constituent) like in a graph structure, and the vascular segment has to be splitted into its constitutive branches. This is obtained by using two other routines included in VMTK.

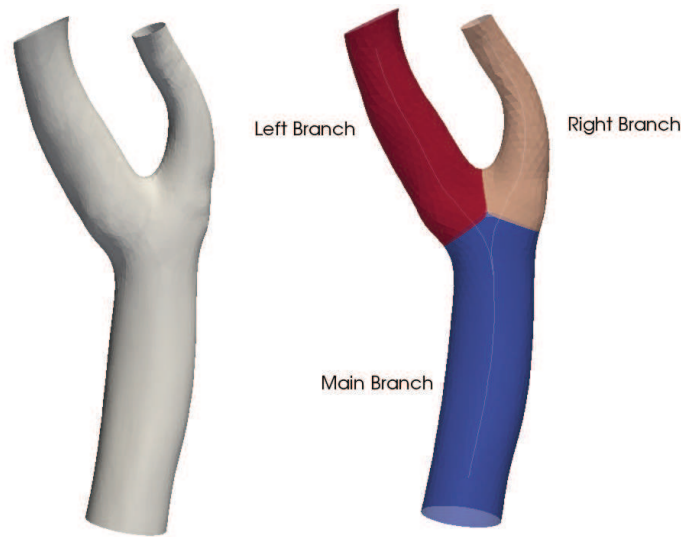


**Figure 5.1** Example of branch splitting on a patient-specific carotid artery geometry. Original carotid artery (left). Carotid artery splitted into its main constitutive branches (right).

Focusing on the centerline of an artery, it may have a really complicated structure; each polyline can be easily classified into three (3) different categories by simply looking at the connectivity of the graph (see Figure 5.2):

- Starting line
- Middle line
- Ending line

Moreover, the graph can always be separated into two (2) and only two (2) subgraphs when looking at a node (this is true for all the nodes except for the starting and ending ones). This means that three-way branching is not possible with this strategy. This also means that each node will always have a starting line (i.e. the branch from which it comes from on the graph) and two branches (left and right). This shape is commonly called a "Y". If exists at least one branch and the graph can be divided into two subgraphs, then it is possible to represent it as a succession of "Y-shaped" structures.

At this stage, each branch of the arterial network (see Figure 5.1, right) is topologically equivalent to a cylinder and, consequently, can be mapped onto a rectangular parametric space. For each branch of the arterial network, the

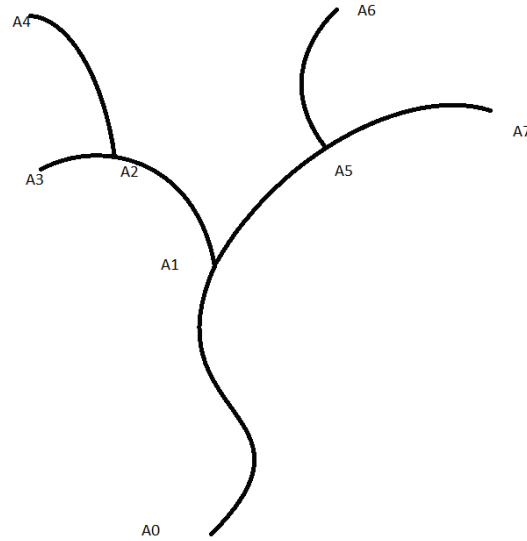


**Figure 5.2** Example of a skeleton of an artery turned into a graph. A's represents the connecting nodes and the polylines are the arteries' centerlines.

"AngularMetric" array has to be computed in the circumferential direction by means of a function contained in VMTK software suite. It represents the periodic circumferential coordinate of mesh points around the centerline. It spans the interval  $(-\pi, +\pi)$ . In the longitudinal direction of each branch, a parameterization is also generated using the harmonic mapping method presented in Chapter 4, section 4.3. In particular, a Laplacian partial differential equation is solved on each branch surface, by using "temperature" variable as boundary condition. See Figure 5.3a for an example of application on a carotid artery patient-specific case. The output of this last operation are sections of points for each branch (see Figure 5.3b).

The sections of points belonging to each branch have to be ordered according to some criteria, in order to facilitate the subsequent mapping operation, necessary to obtain the correspondent IgA representation of the carotid artery. The "AngularMetric" map was used to perform the task: for each branch sections, the points have to be ordered with respect to ascending values of the "AngularMetric" array. The first point of each section is the one with the lowest value of the "AngularMetric" array. In order to obtain a good result in this step, the triangulated branched mesh in input should be carefully refined. Moreover, the higher the number of sections and points per section, the better is the final result in terms of ordering of the points. See Figure 5.4 for the result we obtained on the patient-specific carotid artery geometry under study.

Once obtained the sections of points for each branch, the mapping algorithm introduced in Chapter 4, section 4.4 can be used to create the IgA model of the aortic network. In details, the sections of points belonging to each branch are uploaded in an in-house Matlab code. According to the total number



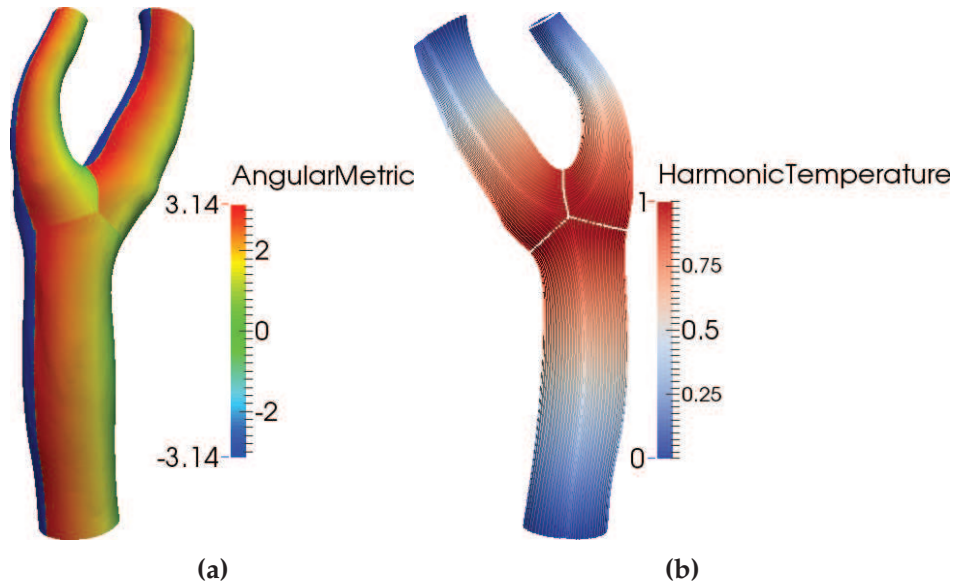


**Figure 5.3** (a) Example on a carotid artery patient-specific case of the circumferential map that takes into account the position of each point on the surface mesh, parameterized with respect to the centerline. It spans the interval  $(-\pi, +\pi)$ . (b) Sections of points for each branch obtained using the harmonic mapping methods we presented in Chapter 4.

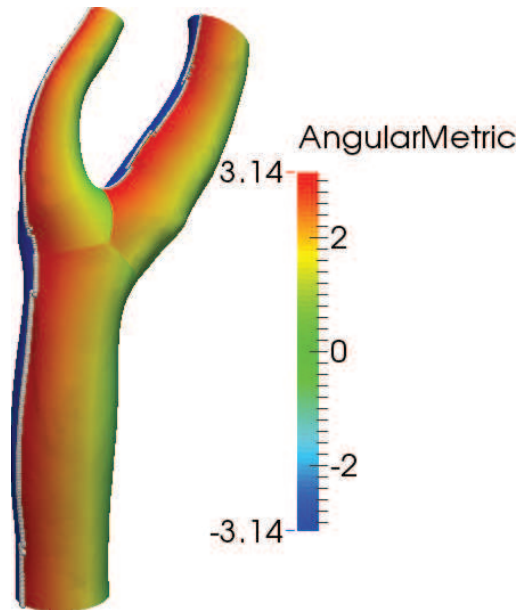


**Figure 5.4** Ordered (according to the "AngularMetric" array) sections of points for each branch.

of branches of the arterial network, a "Y" template made of a succession of conforming cylindrical patches with connected control points is created by means of another in-house Matlab code. To the control points belonging to

each cylindrical patch a global (to the all "Y" shape) and a local (to the single cylindrical patch) numbering scheme has to be given: connecting nodes should have the same global number. An example of two possible multi-patch NURBS "Y" templates, that can be created using our in-house Matlab code, can be found in Figure 5.5. Please note how more complicated "Y" templates, like the one in Figure 5.5b, are made up of multiple "Y"s, according to the topology of the original arterial network. This code for the creation of the multi-patch NURBS "Y" template is automatic and allows the user to create a network of conforming cylindrical NURBS patches just inserting the number of desired cylindrical patches and the radius for each cylinder.

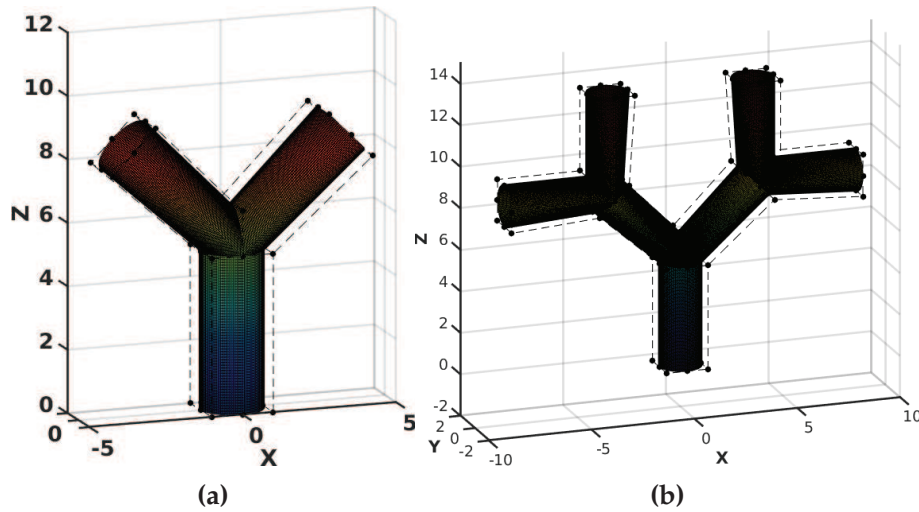


**Figure 5.5** (a) Example of NURBS "Y" basic template (1 "Y") and its control polygon. (b) Example of NURBS "Y" template with 3 "Y"s and its control polygon.

Recalling what we said in Chapter 4, section 4.4, in order to perform the mapping operation to create an IgA object, we need ordered sections of points and a reference surface. Given the sections of points we obtained for each branch of the arterial network, the reference surface is the "Y" template just described. In particular, there should be a one to one correspondence between the sections of points for a branch and its correspondent cylindrical NURBS patch on the "Y" template.

Not only sections of points for each branch have to be ordered circumferentially according to the "AngularMetric" array, but also longitudinally, accordingly to the orientation of the longitudinal direction for each NURBS patch. In details, the first section of points for each branch should be located where the longitudinal parametric coordinate  $v$  of its correspondent cylindrical NURBS patch is equal to zero (0). If not ordered in this way, unpleasant effects may occur later while combining the NURBS patches after mapping operation. For a clarification on this concept, please see Figure 5.6.

Subsequently, for each branch of the arterial network, the local matrix of shape functions has to be constructed, as described in Chapter 4, section 4.4.

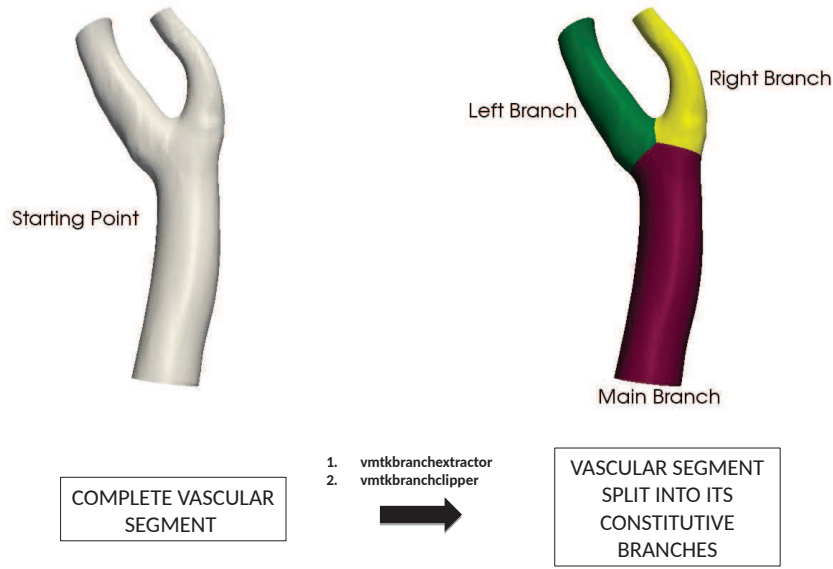


**Figure 5.6** Sections of points for each branch has to be ordered accordingly to the orientation of the longitudinal direction of each patch. The position of the first section of points for each branch in (a) should coincide with  $v = 0$  in the correspondent cylindrical patch in (b).

This matrix is local to the single branch. Hence, given a branch, it takes into account all the sections of points for this branch and its correspondent NURBS cylindrical patch in the "Y" template, but not the presence of coincident control points between cylindrical patches.

Then, using the global indexing scheme obtained before, and thus, taking into account the control points in common with other cylindrical patches,  $\mathbf{N}$ , the global shape functions matrix of the full Y-shape skeleton (i.e., with all the branches) can be assembled, starting from the local ones. This passage is very important because it means that the connectivity between the branches is hidden in the shape function operator  $\mathbf{N}$  and no further linking between control points is required later on. Doing so, a single physical point is only solved once. The construction of this  $\mathbf{N}$  matrix is a little more costly than just evaluating shape functions, since columns should be added/removed or simply manipulated, according to the global indexing scheme. In any case, it can still be handled automatically since the whole connectivity between control points is known as soon as the skeleton is known.

At this point, the global problem  $\mathbf{B}^r = \mathbf{N} * \mathbf{dP}_{vec}^r$  (rearranged in matricial form) represents a linear system that can be solved in a least square fashion, with  $\mathbf{N}$  being the global shape functions matrix of the whole Y-shape skeleton, roughly containing the product between shape functions values in both

parametric directions for the full Y-shape skeleton,  $\mathbf{B}^r$  the  $r^{th}$  Cartesian component of the sampling points, and  $\mathbf{dP}_{vec}^r$  being a set of unknown, i.e. the  $r^{th}$  Cartesian component of the coordinates of the mapped IgA object ordered in vectorial form. Once obtained the "global" control points coordinates, they have to be rearranged using the local indexing scheme previously obtained and assigned to each local mapped surface. For an example of two mapped carotid arteries using the method we just described, please see Figure 5.7.

The use of clamped knot vectors for the creation of the multi-patch NURBS "Y" template is evident in Figure 5.7, because of the presence of the  $C^0$  lines that cross each branch longitudinally. It is also very evident where the three (3) branches join together, creating an extraordinary point at the intersection.

In the previous section, we presented our first attempt in creating patient-specific branched geometries. The described algorithm is valid only for "Y" shaped geometries and thus it is limited to a certain type of arterial networks. It can be for sure improved, requiring a little bit of more coding. For example, the radius of each cylindrical NURBS patch can be image-driven obtained instead of being input by the user; the creation of the "Y" template is now based on how many branches compose the patient-specific arterial network. By inserting the number of desired branches and the radius, the code automatically creates the "Y" template. It may be different: in particular, the centerline can be used to create a succession of cylindrical NURBS patches of arbitrary diameter. Starting from the top of the skeleton and going down, patches can be recursively created and the connection between patches easily determined by looking at the connection at a node. In this way, each path on the skeleton must then be followed. Subsequently, each patch can be then connected to its neighbor leading to a succession of conforming patches centerline-based.

### 5.3 Patient-specific complete model of TAA using T-spline

As a flexible and efficient alternative, we are going to present a new pipeline for the creation of complex patient-specific branched IgA geometries that relies on the T-spline technology. The first attempt we made in order to create IgA branched geometries was limited to arterial network characterized by a tree-like topology, i.e., one inlet and several outlets. This assumption is quite strong because in general holds true for some arterial segments like carotid arteries, but not, for example, for the thoracic aorta. Our work mostly deals with thoracic aortas; hence, a new automatic framework able to reproduce in a straightforward way complex aortic artery geometries starting from DICOM images was required. In the following, the new T-spline based pipeline will be introduced, together with some IgA-FEAP results of inflation simulations performed on these geometries.

As already pointed out in Chapter 3, T-splines were introduced in the CAD community as a generalization and extension of NURBS allowing for local

refinement and coarsening, and representation of geometry of arbitrary topological genus. T-splines have been applied successfully in the context of IgA (Bazilevs et al., 2010b; Dörfler, Jüttler, and Simeon, 2010; Bazilevs, Hsu, and Scott, 2012; Schillinger et al., 2012; Scott et al., 2013; Dimitri et al., 2014) and have been further improved to meet the demands of analysis (Li et al., 2012; Scott et al., 2012; Veiga et al., 2012; Li and Scott, 2014; Evans et al., 2015). Some attempts to construct trivariate solid T-splines can be found in (Wang et al., 2011; Escobar et al., 2011; Wang et al., 2012; Zhang, Wang, and Hughes, 2012; Zhang, Wang, and Hughes, 2013; Wang et al., 2013; Liu et al., 2014; Liu et al., 2015). In general, T-splines are a powerful technology for creating surfaces in CAD softwares. They are compatible with the traditional CAD NURBS technology and offer improvements in flexibility, editability and ease-of-use. T-splines help overcoming the limitations of the rigid tensor product structure of B-splines and NURBS.

In this thesis Rhino CAD software ver. 5 SR14 64-bit (*Rhinoceros: NURBS modeling for Windows.*) is used together with the embedded Autodesk T-spline plug-in (*Autodesk T-Splines Plug-in for Rhino. T-Splines, Inc.*), for the creation of patient-specific analysis suitable T-spline models of aortic arteries. We chose Rhino because it gives designers a variety of functions that are required to build complex, multi-patch NURBS surfaces as well as to create and manipulate T-spline surfaces. This is an important enhancement allowing one to move away from a fairly restrictive NURBS-patch-based geometry design to a completely unstructured, watertight surface definition while respecting all the constraints imposed by analysis. The plug-in is still distributed but not maintained. Figures 5.8a and 5.8b show a snapshot of the Rhino CAD modeling software interface, with the T-spline plug-in integrated. This Figure also shows a first example of a patient-specific model of thoracic aorta represented using T-spline technology.

T-spline surfaces may be created from scratch inside the T-spline plug-in for Rhino. For an example, see Figure 5.9. This T-spline surface has been created starting from a primitive surface (a torus) then modified. T-spline primitives can be created with axial or radial symmetry (radial, in this specific case). When a T-spline has symmetry enabled, the isocurves on the symmetry borders are highlighted to show the symmetry boundaries. In Figure 5.9, they are highlighted in green.

Another way to create T-spline smooth surfaces is to convert T-spline from a mesh. Not all the meshes are good candidates for conversion. There is only one type of mesh that is well suited for conversion to T-spline and it is the quadrilateral-based ("quad-based") ".obj" mesh, mainly composed of four-sided polygons and usually created by means of digital content applications like Blender (Blender - a 3D modeling and rendering package, <http://www.blender.org>), Autodesk Maya (<https://www.autodesk.eu/products/maya/overview>), etc. It is still good to have some triangles and  $n$ -sided faces (with  $n$  equal to 5,6), but the mesh should be under 10,000 to 100,000 faces, depending on the power of the computer and how many triangles are in the mesh. Stereolithography file (".stl") meshes *cannot* be directly converted to



T-spline because they are too finely refined; the risk in performing a direct conversion from a ".stl" meshes to a T-spline object is running out of memory. Given a quad-based mesh, the correspondent T-spline mesh can be created by pushing the "T-spline converter" button available in the T-spline plug-in for Rhino. After the conversion is done, the mesh still looks faceted as before, even though it is a different object (if its properties are checked). In particular, all the T-spline surfaces that will be illustrated in this thesis are bicubic.

In our case, the starting point of the pipeline is the triangulated surface mesh of the aortic artery extracted from DICOM images, with the same modalities described in Chapter 4, Section 4.2 but without the need of cutting and capping the supra-aortic branches this time. This mesh is in ".stl" format. Therefore, it has to be converted into a quad-based ".obj" mesh and this can be done using Autodesk ReCap Photo software (<https://www.autodesk.com/products/recap/overview>), that allows the user to import the ".stl" file, manipulate the model and export it out at quad-based ".obj", deciding at the same time how many faces the model should be composed of (between 10,000 and 100,000). Performing a transformation between a ".stl" into a ".obj" file essentially means performing a nodes reduction operation while changing, at the same time, the shape of the element (from triangulated to quadrilateral elements). For an example of transformation between ".stl" and ".obj" file of a patient-specific TA case, please see Figure 5.10.

Other more complicated examples of patient-specific T-meshes created by converting an ".stl" file into a ".obj" file and then the ".obj" file into a T-mesh are shown in Figure 5.11. Figure 5.11a shows an example of TA (with just the supra-aortic branches) provided us by doctors from IRCCS Policlinico San Donato, San Donato M.se, Milan, Italy, whereas Figure 5.11b shows an example of the complete aorta, from the ascending aorta to the iliac artery, given us by prof. A. Kamensky, from University of Nebraska Medical Center.

Once converted, it is possible to manage the number of faces of the T-spline mesh. This is achieved by the "tsSubdivide" command, that splits a single T-spline face into multiple faces. This command provides the simplest way to add more details to a T-spline model. There are two modes: simple and exact. "tsSubdivide-Simple", allows you to selected the face(s) to be splitted and provides more control points in that region, without adding or changing any other control points to the model. "tsSubdivide-Exact" allows the user to add more details without changing the surface shape. To achieve this, in some areas of the surface, such as near extraordinary points, the tool needs to shift existing control points in order to maintain the surface shape. The T-spline mesh that can be seen in Figure 5.11a, is obtained with the "tsSubdivide-Exact" command. When generating real world T-spline models, the presence of extraordinary points in the T-mesh can not be avoided, as we already said in Chapter 3. For an example of extraordinary points on the patient-specific T-mesh shown in Figure 5.11a, see Figure 5.12.

Once the design of a T-spline is complete, the model can be saved as an



analysis-suitable model automatically, without the need for mesh generation or geometry clean-up steps. It is possible to export T-splines for use in standard IgA simulations as well as collocation and boundary elements simulations. The ".iga" file format is the file extension in Rhino that permits the export of T-spline analysis model file. This file format is the one accepted by IgA-FEAP for loading the T-spline object. For more information regarding all the fields that compose this file, please see (Scott et al., 2014). Once the T-mesh has been imported in IgA-FEAP, note the fine mesh locations around extraordinary points (not avoidable - Figure 5.13).

We made IgA-FEAP able to perform the calculation of isogeometric objects represented by T-spline utilizing Bèzier extraction (Scott et al., 2011). This provides a finite element representation of T-splines, and facilitates the incorporation into existing finite element programs. In short, the solution is obtained using an *extraction operator* form in which the element shape functions are expressed in terms of the shape functions given as:

$$\mathbf{N}^e = \mathbf{C}^e \mathbf{R}^e \quad (5.1)$$

where  $\mathbf{R}^e$  are Bèzier representation of NURBS,  $\mathbf{C}^e$  is the element extraction operator and  $\mathbf{N}^e$  are the T-spline shape function. For more details regarding Bèzier extraction with T-splines, the reader is referred to Chapter 3 and (Scott et al., 2011). Only surface data is provided and thus analyses are restricted to bodies that are represented by surfaces (e.g., 2-d solid bodies, membranes and shells). In this thesis work, we are using shells for the analyses. At present, in IgA-FEAP, only the Kirchhoff-Love thin-shell element is available. For more details regarding the isogeometric formulation of the Kirchhoff-Love thin shell element, please see (Kiendl et al., 2009).

Following the analysis details described in Chapter 4, Section 4.7.2, using the T-meshes created by means of the Autodesk T-spline plug-in exported in ".iga" format to IgA-FEAP, we run preliminary inflation simulations on patient-specific arteries of different types. Up to now, the linear elastic theory is adopted (i.e., small strains and small displacement); in particular, the constitutive model adopted for the simulations is the linear elastic one with parameters derived from literature (Nathan et al., 2011), with  $E = 3$  MPa and  $\nu = 0.46$ . Generalized Robin Boundary Conditions were used to represent the viscoelastic behavior of the tissues surrounding the aorta (Moireau et al., 2012). Just the elasticity term  $k_s$  was taken into account, with  $k_s = 10$  MPa as proposed in (Moireau et al., 2012). An internal pressure of  $120\text{mmHg}$  was imposed. Constant thickness value equal to  $0.1$  mm is used for the thin-shell elements.

The von Mises stress distribution at the vessel wall is checked. Simulations were performed using 1 CPU and the external Pardiso solver (<https://www.pardiso-project.org/>) on a Intel(R) Core(TM) i7-3537U laptop computer. Some simulations results can be seen in Figures 5.14, 5.15, 5.16.

Mesh label	DOF number	CPU time [mins]
CA-1	6,102	5.074
CA-2	31,434	14.53
TA-1	32,604	15.89
A-1	32,622	16.01

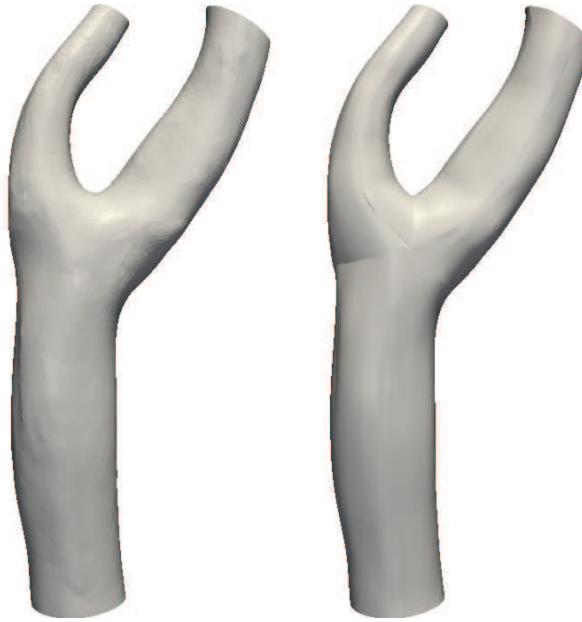
**Table 5.1** CPU time for the inflation simulations whose results are shown in Figures 5.14, 5.15, 5.16.

The presented results are just preliminary: we were mainly interested in finding a straightforward way to create complete and complex patient-specific geometries starting from a mesh derived from DICOM images, without the need of cutting and capping arterial branches that may have an important impact on the von Mises stress distribution at the vessel wall, as demonstrated by (Nathan et al., 2011). This pipeline takes from 20 to 30 minutes to complete, depending on the computer (without taking into account the segmentation time that, if performed by an expert user, usually takes around 20 minutes). Moreover, we were interested in making IgA-FEAP able to work smoothly with T-meshes. In its previous versions (v. 8.4), IgA-FEAP was already able to work with simple T-spline meshes but some features within the Autodesk T-spline plug-in were modified, together with the format of the export file. Therefore a big work has been done in order to permit IgA-FEAP to properly work with T-splines objects, starting from memory allocation problems to the capability to plot them properly. CPU time for the inflation simulations we run on the geometries in Figures 5.14, 5.15, 5.16, are shown in Table 5.1. Having now the opportunity to run analyses in a really short time with T-splines-based patient-specific models like the one shown in Figure 5.11b, is a big achievement in terms of IgA-FEAP capabilities.

### 5.3.1 Conclusion

In this Chapter, we described two methodologies to obtain patient-specific IgA geometries with branches. The first one is multi-patch-NURBS based and is suitable for arterial networks with a tree-like topology whereas the second one is T-spline based (via the Autodesk T-splines plug-in embedded in Rhino) and is suitable for any type of arterial network. Both frameworks can be for sure extended and improved. In particular, focusing on the second one, at present, just linear-elastic T-splines-based inflation simulations can be performed in IgA-FEAP and prestress analyses on T-splines geometries are not executed. Moreover, the adoption of a variable thickness throughout the aorta for the thin-shells elements should be taken into account together with the development and use of a volumetric T-spline model for the aorta. Nevertheless, this framework shows promising results in terms of CPU time and accuracy. Therefore, with the proper extensions, e.g, prestressed geometry, inclusion of a patient-specific constitutive model for the aorta, variable shell thickness according to the different portion of the aorta, inclusion of the intraluminal thrombus, etc., it may represent a more suitable tool than

the one presented in Chapter 4 to be used real-time by physicians during the preoperative planning operations phase.

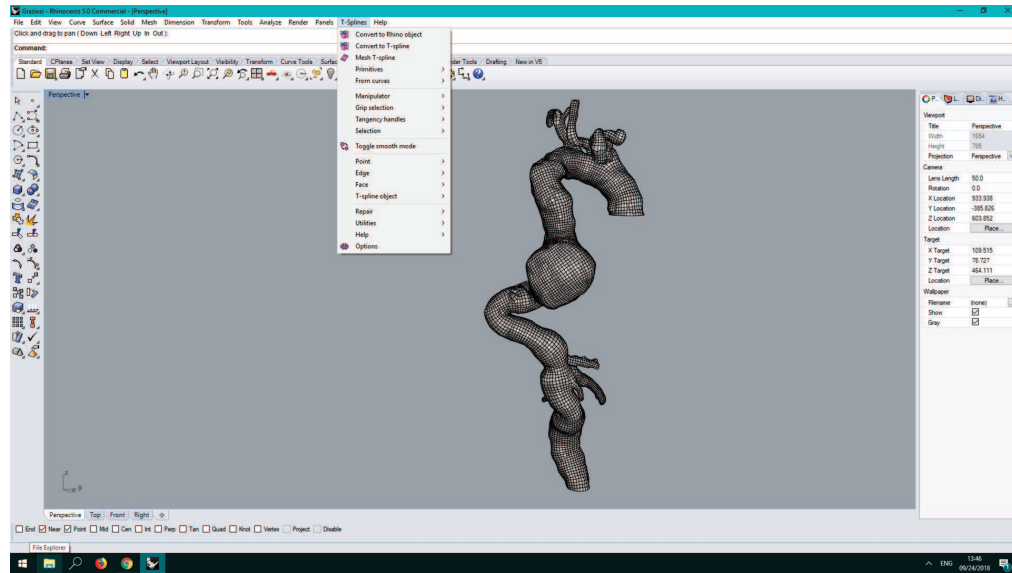


(a) First example of carotid artery mapping. Left: original geometry. Right: mapped IgA geometry.

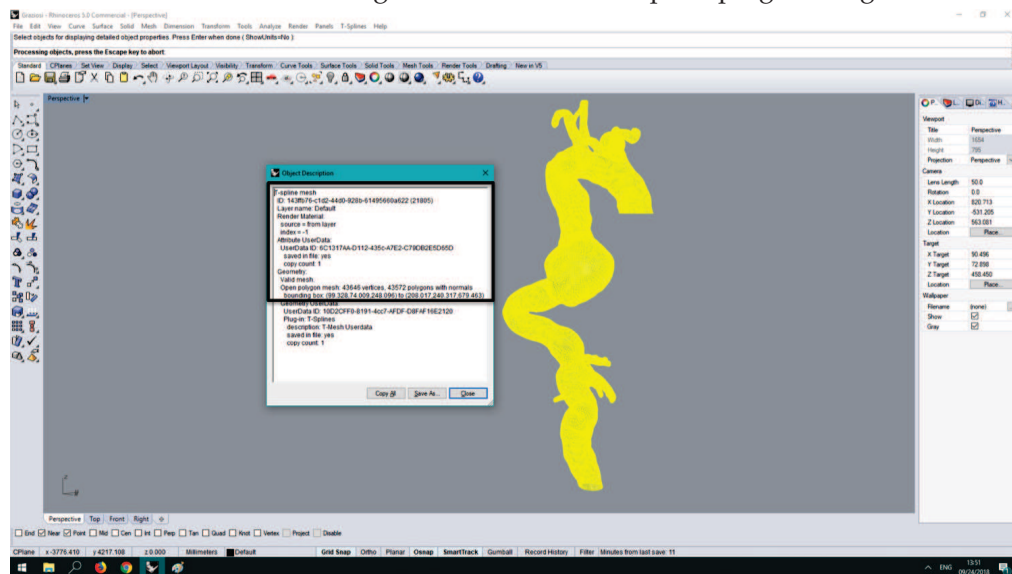


(b) Second example of carotid artery mapping. Left: original geometry. Right: mapped IgA geometry.

**Figure 5.7** Examples of IgA mapping of two patient-specific carotid arteries.



(a) Rhino CAD modeling software with the T-spline plug-in integrated.



(b) First example of T-mesh in Rhino CAD modeling software. Detailed object properties may be displayed using "what" command.

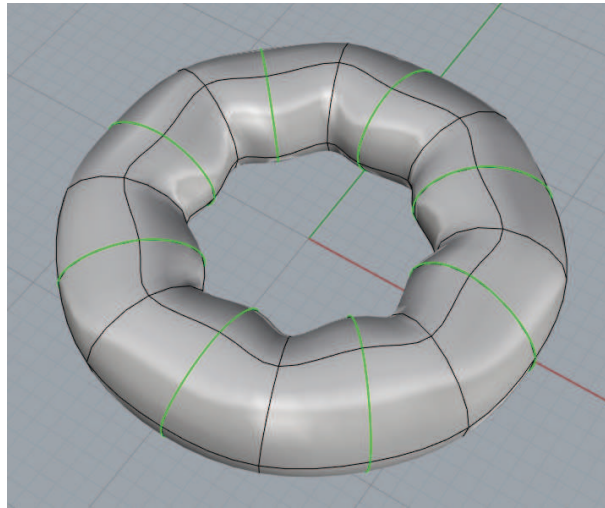


**Figure 5.9** Example of T-spline surface created from scratch inside the T-spline plug-in for Rhino.

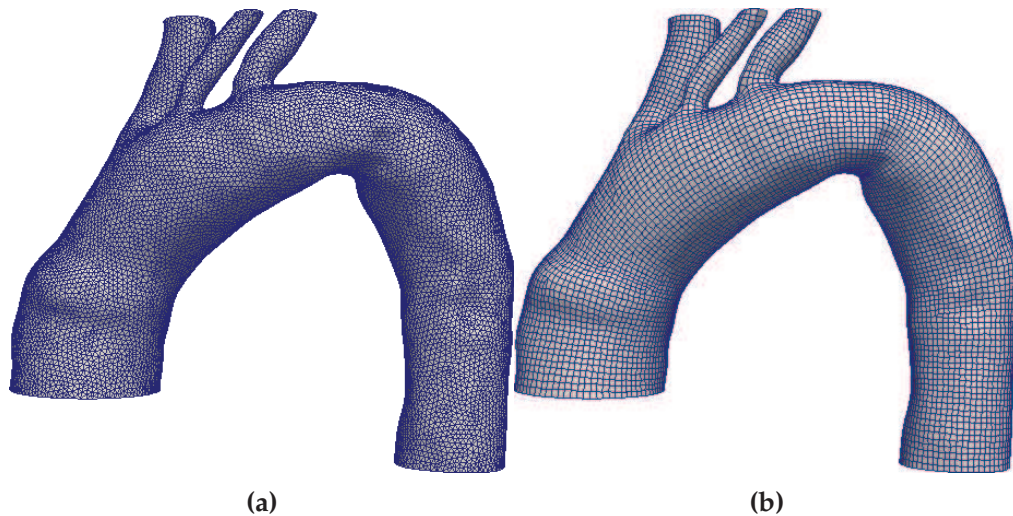


**Figure 5.10** Examples of transformation of a ".stl" file (a) into a quad-based ".obj" file (b) using the Autodesk ReCap Photo software.



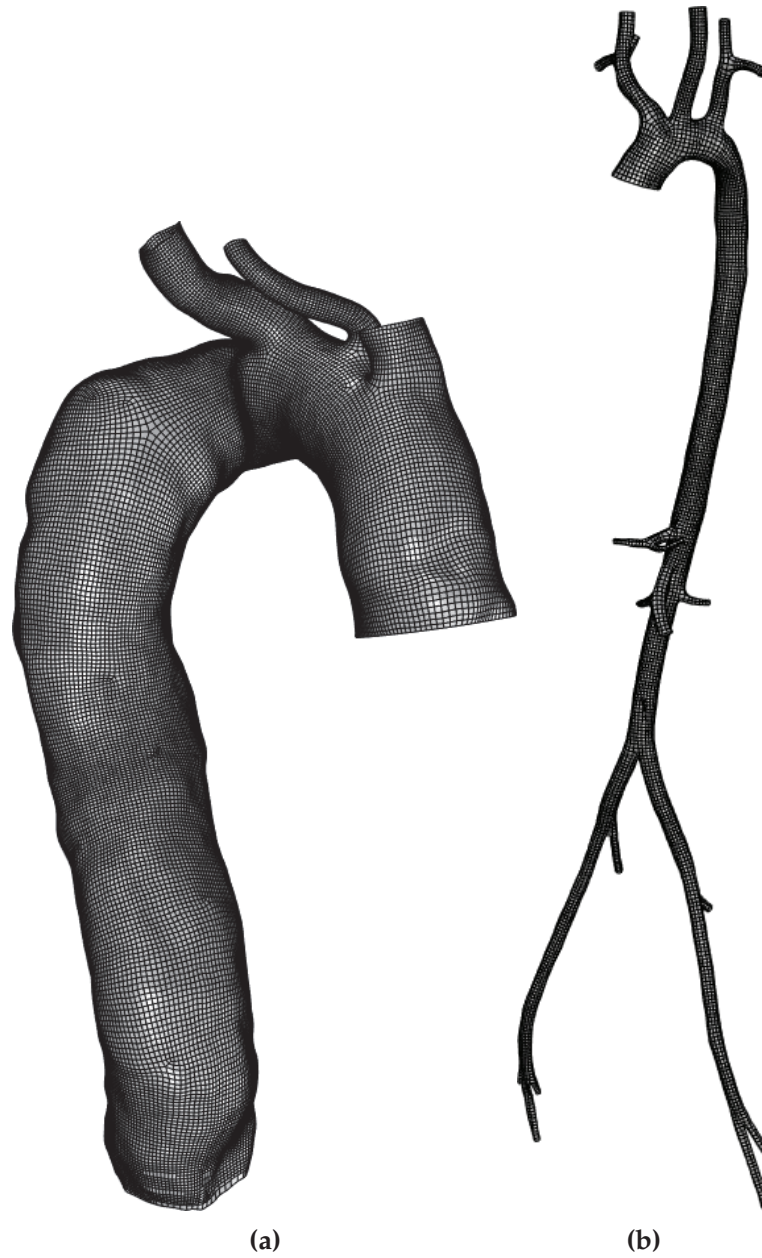


**Figure 5.11** Examples of patient-specific T-meshes created by converting an ".stl" file into a ".obj" file and then the ".obj" file into a T-mesh.

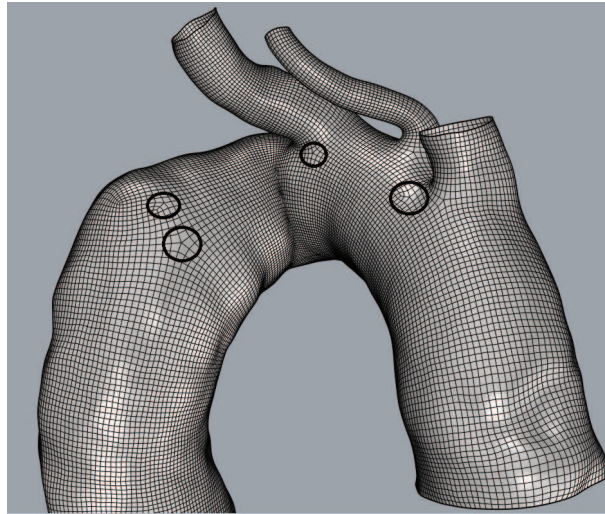


**Figure 5.12** Example of extraordinary points on the T-mesh shown in Figure 5.11a (Rhino view).



**Figure 5.13** Fine mesh location around extraordinary points in IgA-FEAP for the patient-specific model depicted in Figure 5.11a.

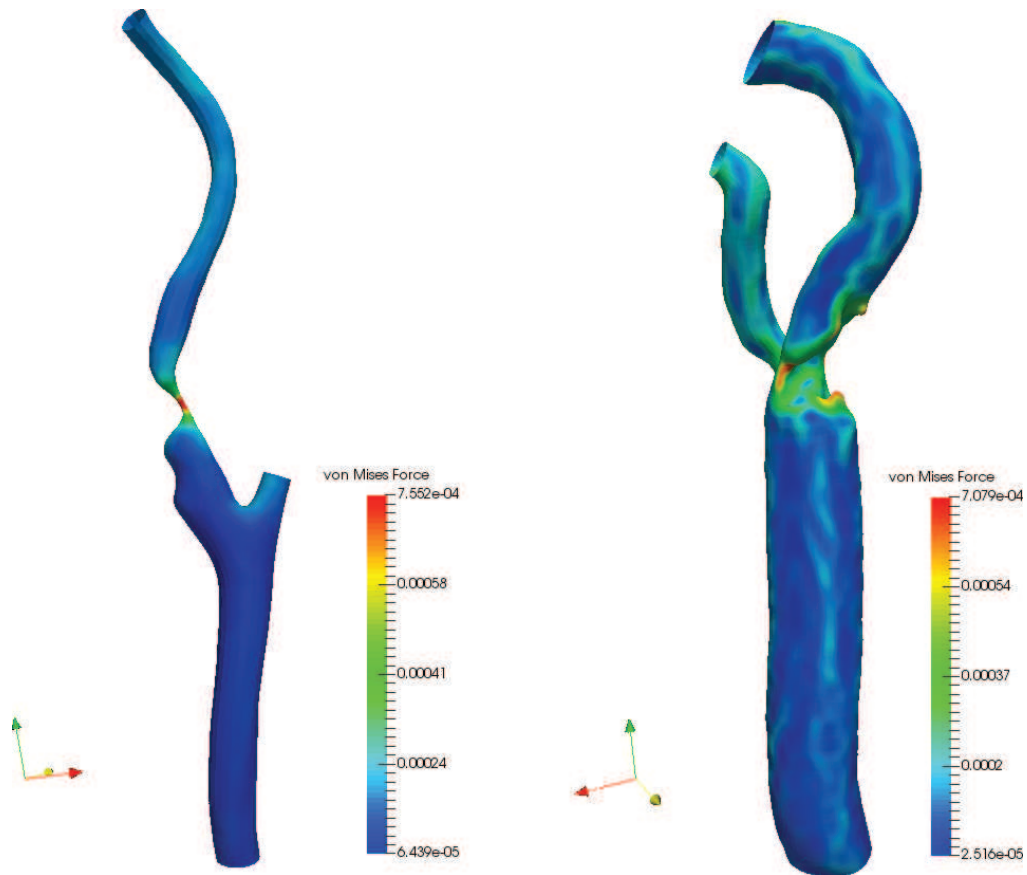


**Figure 5.14** von Mises stress results on two examples of pathological carotid arteries (CA-1 & CA-2) T-spline meshes.

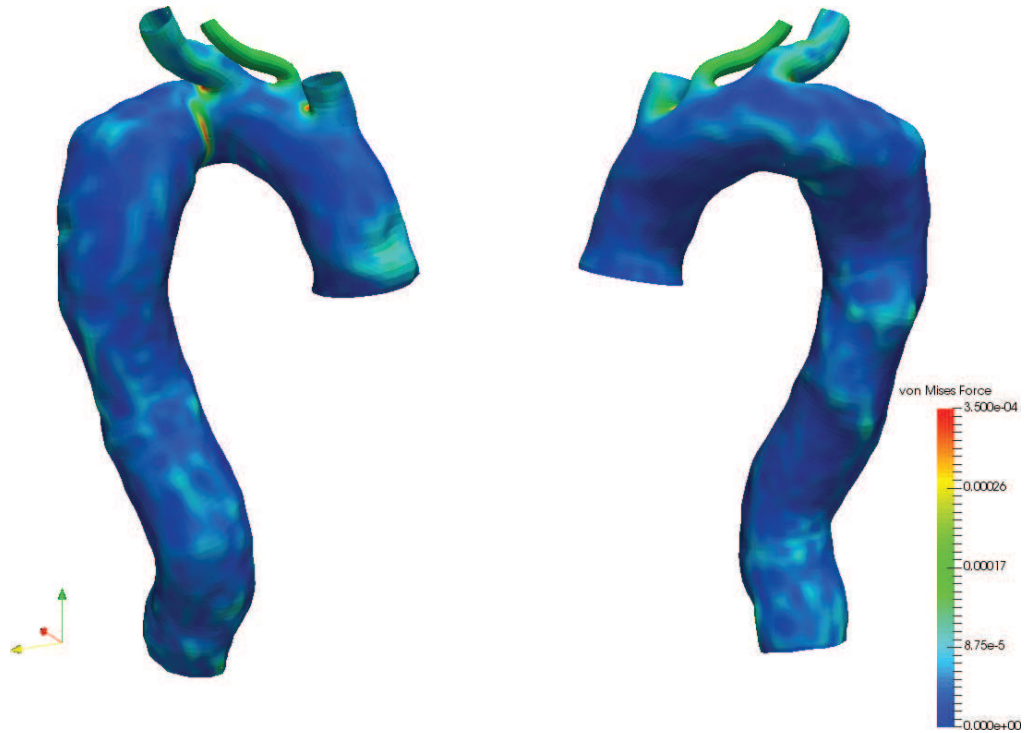


**Figure 5.15** von Mises stress result on a patient-specific TA T-spline mesh (TA-1).

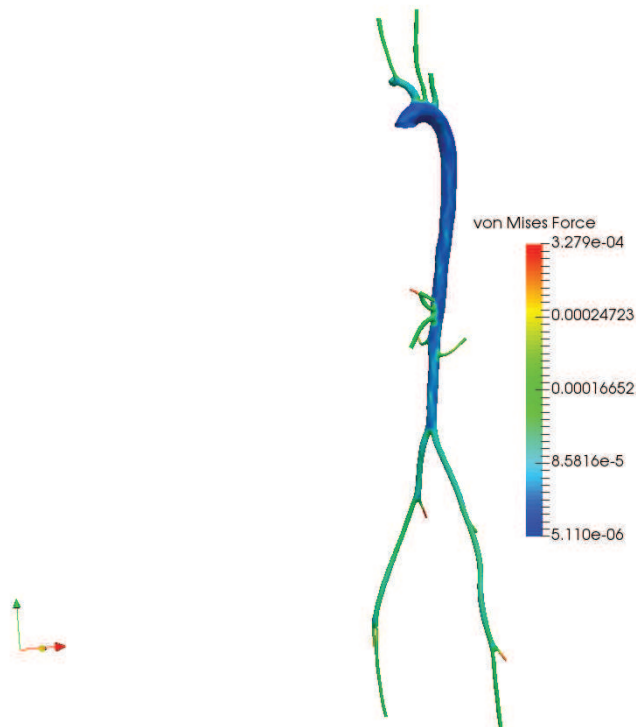


**Figure 5.16** von Mises stress result on a complete patient-specific aorta T-spline mesh (A-1).



## Chapter 6

# Towards an accurate simulation of complex contact interactions in biomechanics problems using IgA

Contact problems are an hot topic in computational biomechanics, where an accurate and robust contact representation is essential to evaluate many important biomedical device features to accurately simulate a wide variety of surgical procedures for pre-operative planning. In this context, IgA can provide a reliable tool to exactly represent the contact surfaces, also taking advantage of its higher regularity with respect to traditional FEA. This Chapter aims at showing some applications of frictionless contact interactions between stent devices and deformable surfaces, in the context of Carotid Artery Stenting (CAS). In particular, following the PhD thesis work by Dr. Mauro Ferraro, we are going to apply the robust IgA contact framework he set up to the evaluation in IgA-FEAP of contact forces between a complex geometry, i.e., a stent, and a deformable surface like a catheter or an artery, resorting to a reduced number of DOFs with respect to classical FEA.

Since this thesis is mainly focused on thoracic aortic aneurysms, we would like to remind that CAS is a minimally-invasive procedure widely employed for the treatment of arteriosclerosis of carotid arteries. In particular, the CAS procedure restores the physiological blood flow by means of expansion of a metallic endoprosthesis, i.e., the stent, which is driven to the target lesion by means of an endoluminal path. Nowadays, CAS is considered a cost-effective alternative to the traditional open surgery approach, leading to minimal hospitalization and reduced social and economic costs (Roffi and Mathias, 2013; Brott et al., 2010). Nevertheless, it is important to remark that stent delivery is in general a complex procedure, since the stent needs to accommodate the tortuous path from the incision to the lesion location, avoiding straightening the carotid artery in order to limit vessel injuries. Stent design plays a crucial role in determining the mechanical properties of the device. Therefore, since experimental tests are often not applicable due to the high costs of prototype manufacturing, and because experimentally reproducing the realistic working conditions can be difficult, modern computational methods, mainly



based on FEA (Conti et al., 2011; Grogan, Leen, and McHugh, 2012; Auricchio et al., 2011; Kleinstreuer et al., 2008; Mortier et al., 2010), are used also in this case as a tool to simulate clinical procedures for pre-operative planning.

## 6.1 Contact problems in vascular biomechanics

Computational contact mechanics principles are widely employed in vascular biomechanics to numerically reproduce important experimental benchmarks (e.g. stent radial strength evaluation) and, more in general, to simulate the interaction between a cardiovascular device and a biological structure, which represents one of the most important sources of nonlinearity in structural biomechanics and the most important in terms of extrapolation of clinical relevant information for surgical preoperative planning. By "coupling" the pipeline we described in Chapter 4 and the contact framework by Dr. M. Ferraro, another step toward real-life applications in cardiovascular biomechanics using IgA can be made.

The goal of this section is to provide the reader with some basic concepts of computational contact mechanics, justifying at the same time the need of IgA to better represent and solve contact problems, and to show in action a multi-patch double-side contact driver (i.e., both cylinder-stent and stent-vessel) applied to crimping and deployment on a patient-specific vessel.

The following specification should be made: in this Chapter, the type of knot vectors employed along all the parametric directions of the solid NURBS-based models under investigations are *clamped* knot vectors. The use of unclamped knot vectors in this type of applications has not been investigated yet and will be the object of future studies.

### 6.1.1 Basic concepts in computational contact mechanics

The typical contact boundary value problem involves two deformable bodies undergoing finite deformations. The most common approach identifies two basic entities, i.e., a *slave* body  $\mathbf{B}^s$  and a *master* body  $\mathbf{B}^m$  (see Figure 6.1).

If contact occurs during deformation, it is possible to identify the contact surface  $\Gamma_c$ . This boundary value problem is inherently non-linear, since the contact condition introduces additional kinematics constraints to prevent the compenetration of the two bodies. The discrete counterpart of contact boundary value problems employed FEA for many years (Wriggers and Nackenhorst, 2006). Along the boundary  $\Gamma_c$  of the two bodies, different contact models can be introduced. In the simulations we are going to present, we focused on the simplest model, i.e., *frictionless* contact, in which the only non-zero component of the contact traction is normal to the contact surfaces.

Contact pairs are the basic entities in computational contact mechanics. These are couples of points (one for the slave body and one for the master body) where the contact constraint is locally enforced. For FEA contact problems,

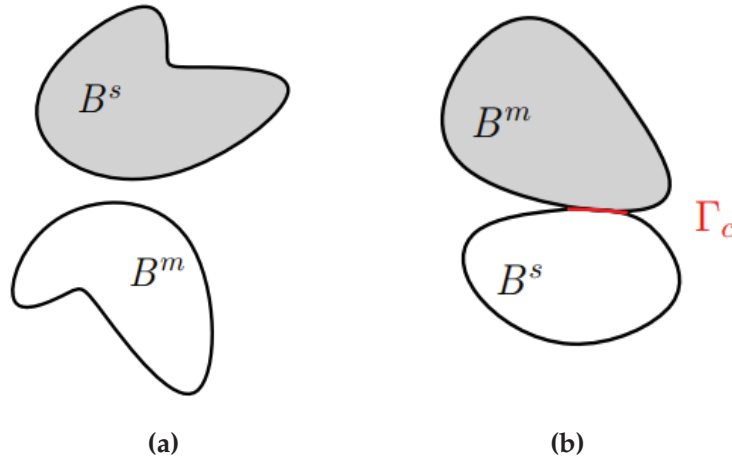


**Figure 6.1** 2D contact problem. (a) no contact; (b) contact state.

the most implemented approach to define the contact pairs is the node-to-segment (NTS) algorithm, where each contact pair is defined by a node coming from the *slave* surface and its projection on the *master* surface (Figure 6.2). In general, the projection not necessarily coincides with a node.

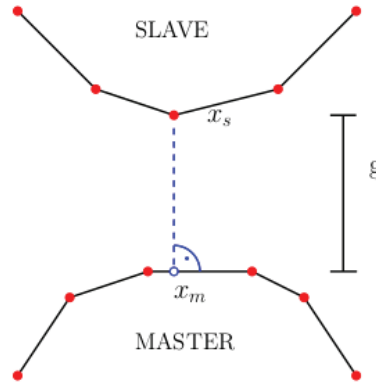


**Figure 6.2** Node To Surface (NTS) contact.

Given the intrinsic  $C^0$  continuity along the inter element FEA nodes and the lack of smoothness in the geometric description of the contact surfaces, it may occur that the computation of the projection of the slave node to the master segment is not unique (Figure 6.3 - Left). Moreover, it is also possible that the projection is not unique and, at the same time, it is not located in the interior of the master segments (Figure 6.3 - Right). For this reason, IgA, a discretization technique able to guarantee higher order continuity along the elements, could provide an ideal framework to overcome these issues in terms of surface smoothness.

The NTS approach cannot be naturally extended to IgA because of the non-interpolatory nature of the control points: to overcome this limitation, the NTS approach has been first replaced by the Knot-to-Segment (KTS) one

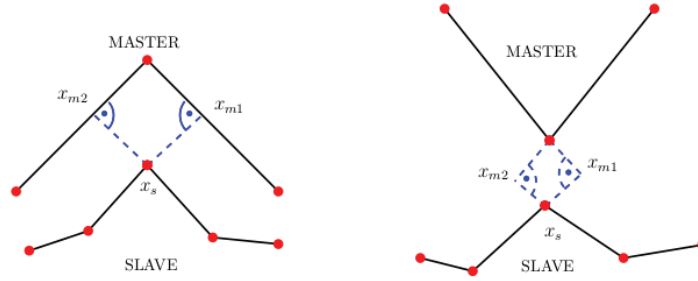


**Figure 6.3** Not uniqueness of the master projection. Left: two projection on the master side. Right: no projection on the master side.

proposed by (Temizer, Wriggers, and Hughes, 2011), where the contact constraint is not imposed on the slave nodes but at the Gauss points belonging to each slave contact surface (see Figure 6.4).

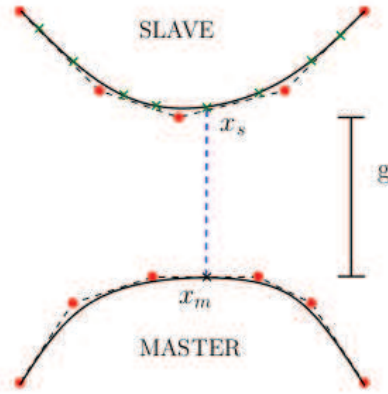


**Figure 6.4** Knot-to-segment contact: the Gauss points on the slave surface are highlighted as x.

This first formulation of the KTS approach has been modified because it led to an over-constrained problem induced by the discrepancy between the total number of degrees of freedom of the contact surfaces and the number of contact pairs, i.e., the number of Gauss points. The new mortar-based KTS formulation proposed by (Temizer, Wriggers, and Hughes, 2011) and (De Lorenzis et al., 2011) relaxed the over-constrained KTS one, exhibiting at the same time superior results over the classic KTS and NTS approaches.

A contact driver reproducing the mortar-KTS algorithm proposed by (De Lorenzis et al., 2011) for NURBS discretization and by (Dimitri et al., 2014) for T-spline discretization is implemented in the embedded IgA package for FEAP. For a more extensive description of each block of the IgA-FEAP contact driver, the reader is referred to the thesis work by Dr. M. Ferraro.

Once the pairs are established, the gap  $g$  determines which nodes are in contact. The entity  $g$  is defined as:

$$g = [x_s - x_m] \cdot \mathbf{n}_c \quad (6.1)$$

where  $x_s$  and  $x_m$  are the slave node and its master projection location in the deformed configuration,  $\mathbf{n}_c$  the outward normal evaluated in the projection point. If  $g > 0$  there is no contact, while if  $g < 0$  compenetrations may occur. Given the total energy of the system  $\Pi$ , a proper contact contribution  $\Pi_c$  should be taken into account when contact occurs. Several techniques have been developed and three big families can be roughly identified: Lagrangian Multiplier functional form, Augmented Lagrangian functional form and Penalty functional form (Wriggers and Nackenhorst, 2006). In the simulations we are going to present, the contact constraint is regularized with a penalty method for which holds:

$$\Pi_c = \Pi(u) = \int_{\gamma_c} \epsilon g^2 d\gamma, \quad (6.2)$$

where  $\epsilon$  is an user-defined penalty coefficient. By expressing  $\Pi_c$  in this way, the final gap is not zero and so, some compenetrations can occur, depending on the value of the parameter  $\epsilon$  (high values of  $\epsilon$  reduce the final gap). The main advantage of this method is that it does not require any other additional degrees of freedom. The principal drawback is that there is no general rule to identify a proper value of  $\epsilon$ ; it should not be extremely high, because this may lead to ill-conditioned problems. The contact constraint in IgA-FEAP can also be regularized with the augmented Uszawa algorithm (Wriggers and Nackenhorst, 2006), instead with the penalty one. In this way, a sensitive increase of gap accuracy can be achieved (see Dr. M. Ferraro's work).

## 6.1.2 Stent crimping simulations

In the following, the IgA contact driver we just cited is tested with some real-life application examples, including stent geometries, real artery models and inelastic constitutive models. In particular, as a first study, we are interested in evaluating the performance of different discretization strategies, i.e., IgA, linear FEA (h-FEA) and higher order FEA (p-FEA), applied to the study of stent crimping on one ring of a real-life stent.

Linear discretization represents a *de facto* standard for the numerical evaluation of the stent mechanical features (Carnelli et al., 2011; Petrini et al., 2004; Petrini et al., 2005), while the employment of higher order elements allows an accurate representation of the stent geometry combined with better approximation properties with respect to linear FEA. Stent crimping represents the step before stent deployment and activation of the contact between stent and vessel. The quantitative comparison between numerical and experimental results is beyond the scope of this study: a quantitative comparison requires further investigations in terms of material parameters calibration from experimental data and analysis of experimental boundary conditions.

The stent model used in these simulations resembles one ring of the commercially available Bard ViVEXX Carotid Stent (C. R. Bard Angiomed GmbH & Co., Germany) used in clinical practice. This stent is a straight, self-expanding open-cell design laser-cut from a low-profile nitinol tube (Rebelo, Fu, and Lawrenchuk, 2009; Thériault et al., 2006). Since no data were available from the manufacturer, the main geometrical features of this device are derived from high-resolution micro-CT scans of the stent in the delivery system (Conti et al., 2011). In brief, the steps required to generate the stent model are the following (Ferraro et al., 2015):

- A planar CAD geometry that corresponds to the stent unfolded configuration is generated in Rhino v. 4.0 SR8 (*Rhinoceros: NURBS modeling for Windows*). Subsequently, a 2D CAD surface is generated for each NURBS patch.
- The NURBS data (i.e., control points, knots and weights) are exported as text (.txt) files by mean of an in-house code developed in Visual Basic Scripting.
- The NURBS surface structure is extruded and rolled by means of an in-house Matlab code, leading to the final stent in open configuration.
- Each patch composing the trivariate NURBS structure is finally exported in a suitable format for the solver FEAP. The control points at the conforming interface between the two adjacent patches are tied in order to obtain the IgA stent.

The stent structure is regular and it is always composed of two patch families, i.e., the linker and the ring patches. The total number of NURBS patches for the stent is 18. The material model originally proposed by Souza (Souza, Mamiya, and Zouain, 1998) and implemented in FEAP in the version proposed by (Auricchio and Petrini, 2004) has been considered for the stent. The hypothesis of large displacements and rotations, but small strains (as typically induced in many biomedical applications (Petrini et al., 2005)) is assumed. In Table 6.1 all the parameters used for the simulations are summarized. For further details regarding this constitutive law, the reader should refer to (Souza, Mamiya, and Zouain, 1998; Auricchio and Petrini, 2004) and Dr. Ferraro's work.

The crimper is the catheter and it is composed by one cylindrical NURBS patch and it is modeled as a rigid body with NeoHookean material ( $E = 250000 \text{ MPa}$ ,  $\nu = 0.3$ ). The stent and its cylindrical crimper are depicted in Figure 6.5.

The boundary conditions employed in the simulations include displacement conditions on the crimper to impose the radius reduction, and the minimal stent constraints to avoid rigid body motions. In particular, the crimper radius is reduced from 4.8 mm to 1.8 mm. The contact constraint is regularized using the penalty method and the penalty coefficient  $\epsilon$  has been set to  $10^4$ .

Souza material parameters		
E	Elastic modulus	53000 MPa
$\nu$	Poisson's ratio	0.33
h	Linear hardening parameter	1000 MPa
$\beta$	Stress-temperature relation parameter	6.1 MPa/K
T_0	Reference temperature	243 K
R	Physiological pressure	100 MPa
$\epsilon_L$	Maximum transformation strain norm	5.6%

**Table 6.1** Parameters values used for the stent in the contact simulations.



**Figure 6.5** Stent model in undeformed configuration with its cylindrical crimper.

For the IgA case we used cubic-quadratic-quadratic elements (for circumferential, longitudinal and thickness directions, respectively) for the stent and quadratic-quadratic-quadratic elements for the crimper. Moreover, we considered 4 meshes: in all 4, **the number of DOFs for the stent has been kept fixed** and equal to 35,829 DOFs, whereas we performed knot-insertion on the crimper so to have a "Coarse" (refinement indices along  $u$ ,  $v$  and  $w = [5, 5, 0]$ ), "Medium" (refinement indices along  $u$ ,  $v$  and  $w = [10, 10, 0]$ ), "Refined" (refinement indices along  $u$ ,  $v$  and  $w = [15, 15, 0]$ ) and "Most Refined" (refinement indices along  $u$ ,  $v$  and  $w = [20, 20, 0]$ ) mesh, with increasing number of DOFs. Both the h-FEM and p-FEM meshes are recovered by iterative knot insertion performed on the highly regular 4 NURBS meshes just described, resorting to 12 meshes in total. Consequently, the number of DOFs of the stent have been kept fixed also in the p-FEA (57,105 DOFs) and h-FEA (54,975 DOFs) meshes. For the p-FEA, we employ cubic-quadratic-quadratic



elements. In particular, the p-FEA polynomial orders are obtained by construction of the 2D NURBS surface for circumferential and longitudinal directions, while the thickness polynomial orders, linear by construction, has been raised to quadratic in order to have the fully high-order p-FEA mesh.

The contour plot for the displacement solution obtained with the most-refined crimper mesh is depicted in Figure 6.8.

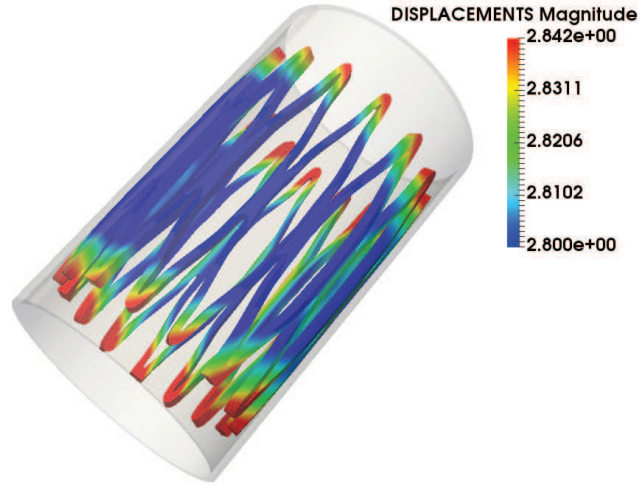


**Figure 6.6** Stent crimping test: radial displacement contour plot.

We are interested in comparing the performances, on a per-degree-of-freedom basis, with respect to the stent resultant radial reaction force quantity ( $[N]$ ), between IgA, p-FEA and h-FEA, in reproducing the stent crimping non-linear phenomenon, when a particular stent design is used. The resultant of the radial reaction force is obtained as the sum of the reaction force contributions in the radial direction of the stent. Moreover, we would like to check if different refinements of the crimper (i.e., the catheter) may have an impact on the stent radial reaction force quantity. For this reason, the radial reaction force at different values (10) of the stent Z coordinate [mm] has been computed and depicted in Figure 6.6, for each one of the 4 meshes belonging to the different considered discretization methods.

The data concerning resultant reaction force values and number of DOFs for each discretization method, are reported in Table 6.2.

Focusing on the IgA results, we can say that there is no need to use the most refined mesh (labeled as "IgA-4") for the crimper in order to catch the behavior of the stent radial reaction force during stent crimping test. With almost 10 thousands degrees of freedom for the crimper, we are able to describe how the stent radial reaction force is changing along the stent Z coordinate. Focusing on the comparison between IgA and p-FEA and h-FEA, we can see that p-FEA presents a better performance with respect to h-FEA on a degree

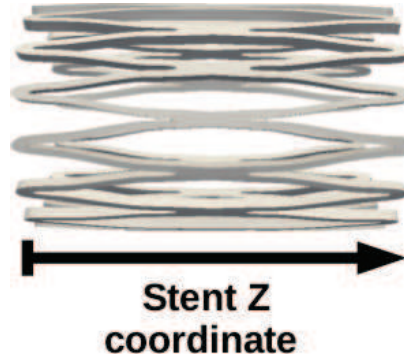
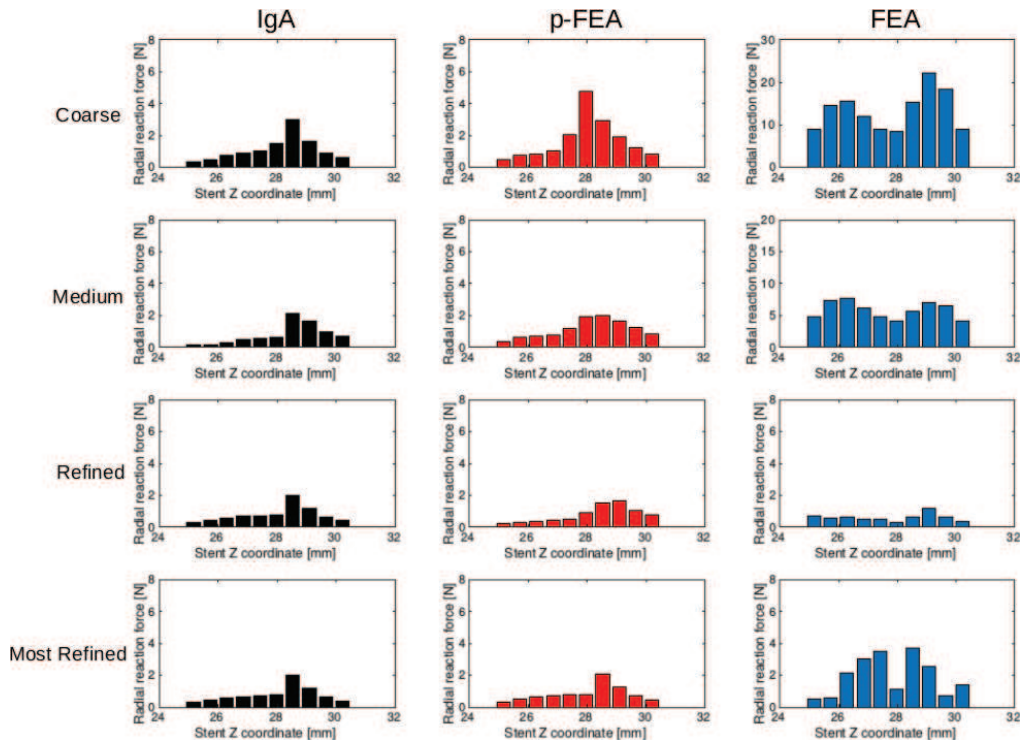
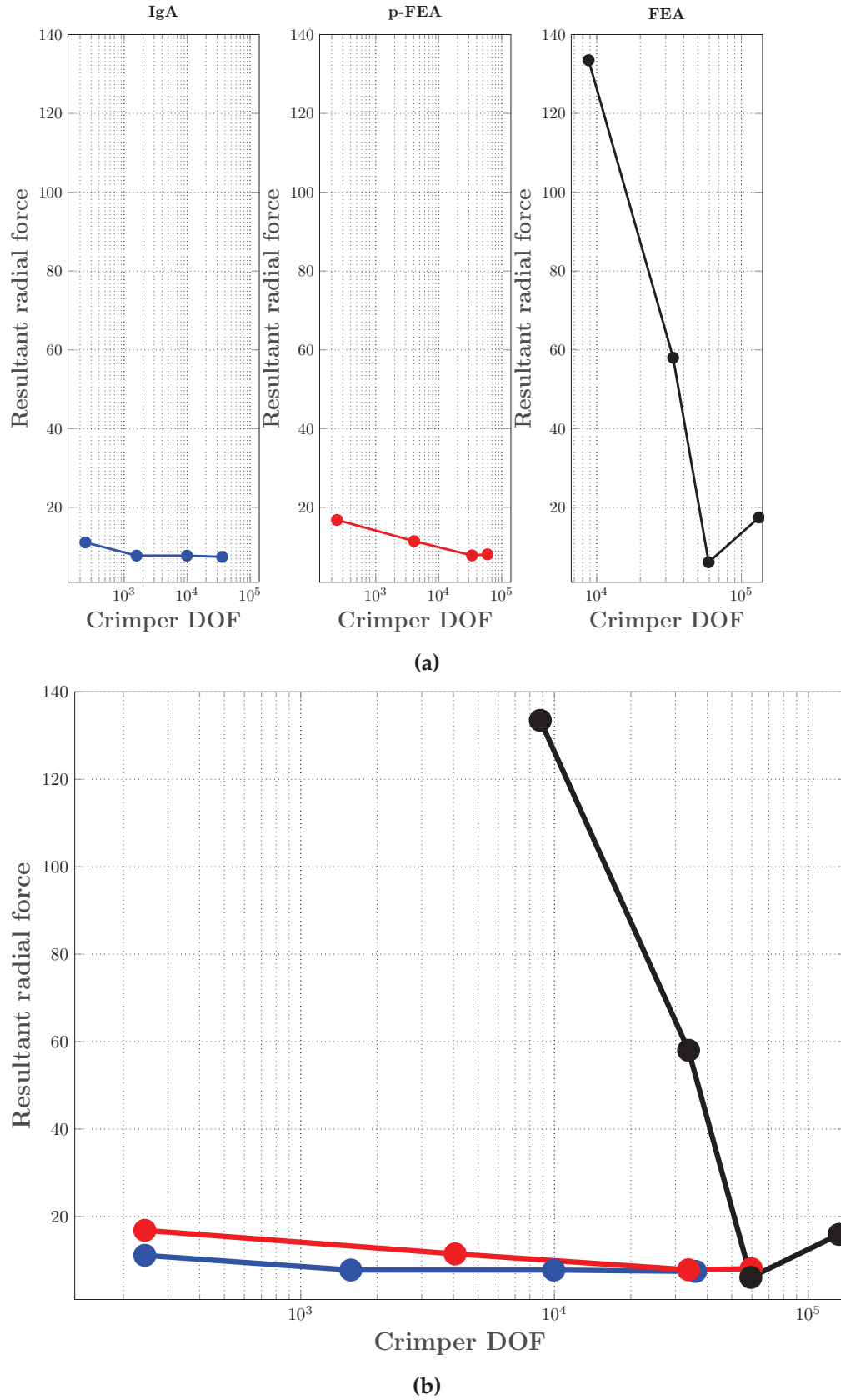


Figure 6.7 Stent Z coordinate.



**Figure 6.8** Stent crimping test results. Radial reaction force ([N]) taken at different values of the stent Z coordinate for different discretization techniques and for different refinement of the crimper mesh.

of freedom basis, as shown also in (Ferraro et al., 2015). For p-FEA, in order to obtain a result similar to the one obtained with the "IgA-3" mesh in terms of radial reaction force, more than three (3) times the number of DOFs is required (see pFEM-3 mesh), with a gain of over one order of magnitude in DOF number for IgA. h-FEA shows different behaviors with different refinements, which may be related to some spurious stress concentrations that may lead to an erroneous reproduction of the crimping deformation path. Not only the results are very different from the IgA and p-FEA ones, but they also seem to diverge while increasing the number of DOFs for the crimper.



**Figure 6.9** Comparison of the performances on a per-degree-of-freedom basis, between IgA, p-FEA and h-FEA with respect to the resultant reaction force quantity ([N]) in reproducing the stent crimping non-linear effect, using a particular stent design.

Mesh Label	DOFs Crimper	Resultant reaction force value ([N])
<b>IgA-coarse</b>	243	11.0987
<b>IgA-medium</b>	1,575	7.7456
<b>IgA-refined</b>	9,945	7.7361
<b>IgA-most refined</b>	36,000	7.7430
<b>FEM-coarse</b>	8,796	133.4788
<b>FEM-medium</b>	33,771	58.0043
<b>FEM-refined</b>	59,409	6.0630
<b>FEM-most refined</b>	132,309	16.2720
<b>pFEM-coarse</b>	243	16.8113
<b>pFEM-medium</b>	4,059	11.4319
<b>pFEM-refined</b>	33,759	7.7997
<b>pFEM-most refined</b>	59,649	8.0754

**Table 6.2** Table summarizing for each mesh for each discretization method the value of the radial resultant reaction force obtained in the non linear stent crimping simulations, as well as the number of DOFs of the crimper.

One clarification should be done: as can be seen from the results reported in Table 6.2, both IgA and p-FEA meshes seem to level off when a certain number of DOFs is reached. Further investigations are needed to understand the reason of this behavior.

Therefore, for this study, we demonstrated the capability of IgA to reproduce nonlinear local effects with a reduced number of DOFs with respect to classical FEA and p-FEA. It is remarkable to observe how low-regularity and low-interpolation order in FEA basis functions can lead to a reduced capability of catching the physics of the problem under investigation.

### 6.1.3 Stent implant simulation

As a second study, the interaction between a stent and a patient-specific vessel model is investigated, always by means of the contact-driver available in IgA-FEAP. In particular, we performed a two-step simulation procedure (Conti et al., 2011; Auricchio et al., 2011; Conti et al., 2009).

In the first step, starting from a straight configuration, the catheter is gradually crimped leading to the stent deformation; the contact between the stent and the vessel is deactivated in this step. As before, the crimper radius is reduced from 4.8 mm to 1.8 mm. The minimal constraints to avoid rigid body motions are applied to the stent. Subsequently, from the crimped configuration, the catheter is re-enlarged and consequently the stent expands against the vessel wall (see Figure 6.11 for analysis setup specification).



**Figure 6.10** Stent implant results from (Conti et al., 2011; Auricchio et al., 2011; Conti et al., 2009)

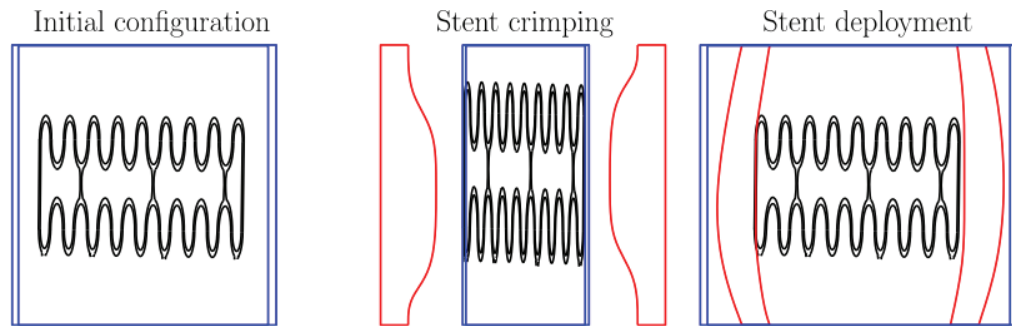


**Figure 6.11** Analysis setup specification for stent implant simulation.

The contact between the stent and the vessel is activated in this step. Also in this second study, the stent represents a portion of the commercially available Bard ViVEXX Carotid Stent and it is composed of two patch families, i.e., the linker and the ring patches. The total number of NURBS patches for the stent is 18 as in the previous case. We employed cubic-quadratic-quadratic elements (for circumferential, longitudinal and thickness directions, respectively) for the stent, quadratic-quadratic-quadratic elements for the catheter and cubic-quadratic-quadratic elements for the patient-specific artery. The stent is modeled as a Souza model (Souza, Mamiya, and Zouain, 1998), with the same parameters values employed for the crimping simulation previously described (see Table 6.1). The artery and the catheter are modeled with a Neo-Hookean model using experimental parameters. In particular, for the catheter,  $E = 70000000$  MPa,  $\nu = 0.3$  and for the aorta  $E = 5$  MPa,  $\nu = 0.3$ . The patient-specific model for the artery is obtained by means of the clamped version of the mapping algorithm described in Chapter 4, starting from DICOM images (see Figure 6.12). The 3D geometry of the patient-specific artery and of the stent in its unloaded configuration is depicted in Figure 6.13a and

6.13b, respectively. In Figures 6.13c and 6.13d the stent deformed configuration after crimping and the stent deformed configuration after deployment are shown.

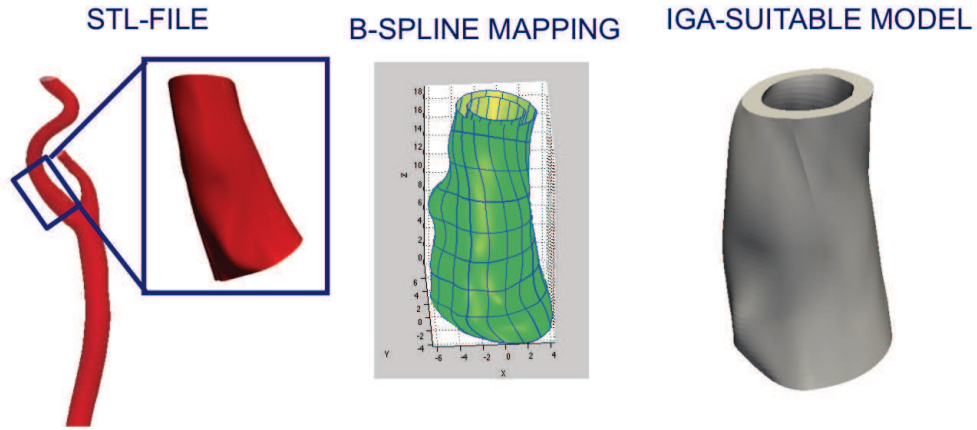


**Figure 6.12** Patient-specific vessel modeling for the stent implant simulation.

We analyzed the results we obtained focusing on the following points: the vessel injury induced by the stent deployment (by evaluating the von Mises stress distribution in the tissue (Auricchio et al., 2011)) and convergence rate of IgA with respect to the deformation energy of the artery. In Figure 6.14 the von Mises stress distribution in post-stenting vessel can be seen and it is higher where the stent is perfectly in contact with the vessel. Figure 6.15 shows the von Mises stress distribution along the stent structure: it is not symmetric due to the vessel shape and it is higher where the stent structure is in contact with the vessel inner wall.

We are also interested in the performances of IgA to reproduce the stent-deployment non-linear phenomenon. For this reason, we considered five (5) IgA meshes; for each mesh, the number of DOFs of the stent and of the crimper has been kept fixed, whereas the number of DOFs of the patient-specific artery has been progressively increased. Artery deformation energy [Nmm] for each one of the 5 meshes, together with the one of the "IgA-overkill" mesh, i.e. the one that shows the finest artery mesh, is depicted in Figure 6.16a, with respect to the analyses simulation times [s]. Artery deformation energy convergence plot with respect to DOFs is reported in Figure 6.16b. Finally the data concerning deformation energy values at the last time step of the analysis and numerical errors evaluated with respect to the deformation energy of the "IgA-overkill" mesh at the last time step of the analysis, are reported for each one of the considered five (5) IgA meshes in Table 6.3.

We were also interested in comparing the performances, on a per-degree-of-freedom basis between IgA and linear FEA with respect to the artery deformation energy [Nmm]. The linear FEA (h-FEA) meshes were obtained by iterative knot insertion performed on the highly regular five NURBS meshes



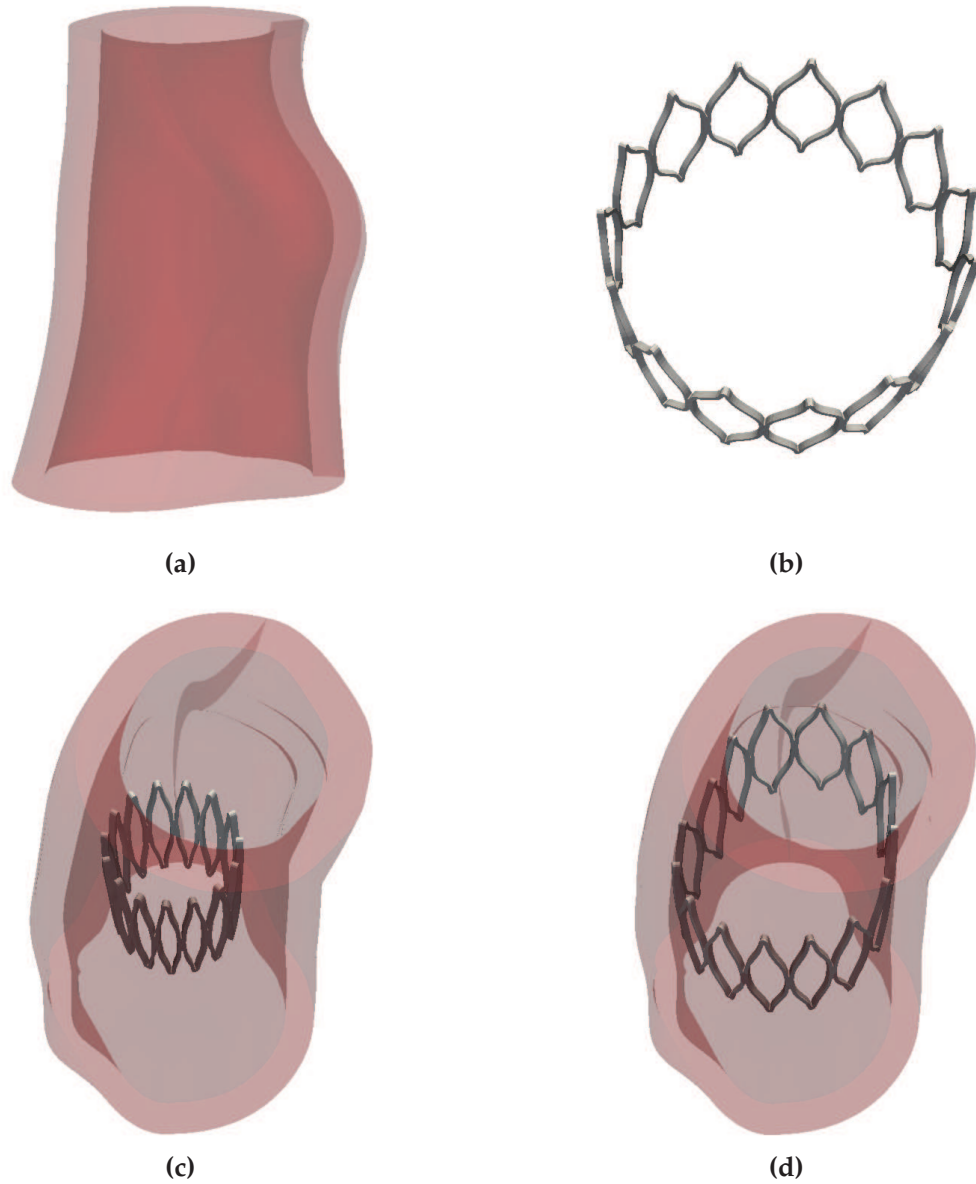


**Figure 6.13** Stent deployment test: (a) vessel model; (b) stent model; (c) Deformed configuration after crimping; (d) Deformed configuration after deployment.

previously described, so to have five low-order NURBS meshes characterized by  $C^0$  continuity everywhere. Therefore, the same contact simulations we performed in IgA-FEAP on the high-order, highly regular NURBS meshes were also run in IgA-FEAP on the low-order NURBS meshes with  $C^0$  continuity everywhere. The results we obtained on the low-order NURBS meshes in terms of artery deformation energy versus simulation times (Figure 6.18) demonstrate how these low-order meshes are far from converging to the same artery deformation energy value of the high-order corresponding ones.

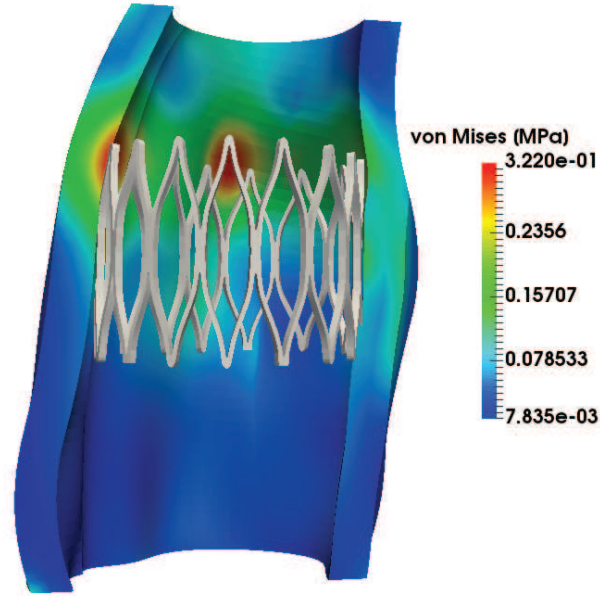


**Figure 6.14** Von Mises stress distribution [MPa] in the post-stenting vessel.

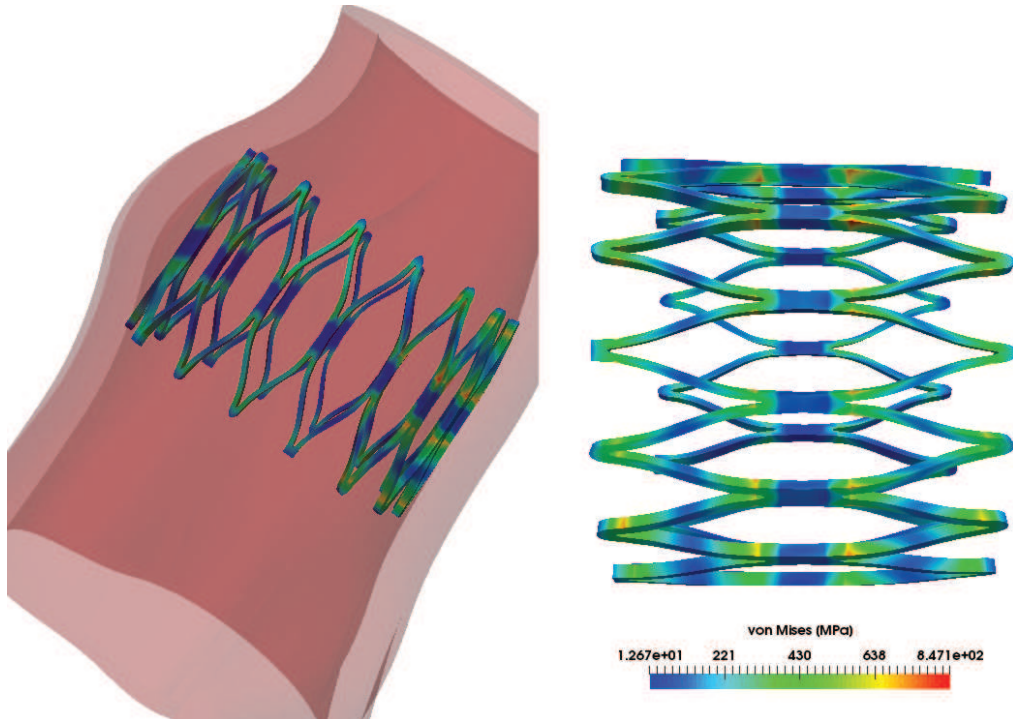


**Figure 6.15** Von Mises stress distribution [MPa] in the stent structure.

In order to investigate this behavior and to see if the artery deformation energy value of the low-order meshes tends to the IgA converged one, the number of DOFs of the artery should be further increased. This operation cannot

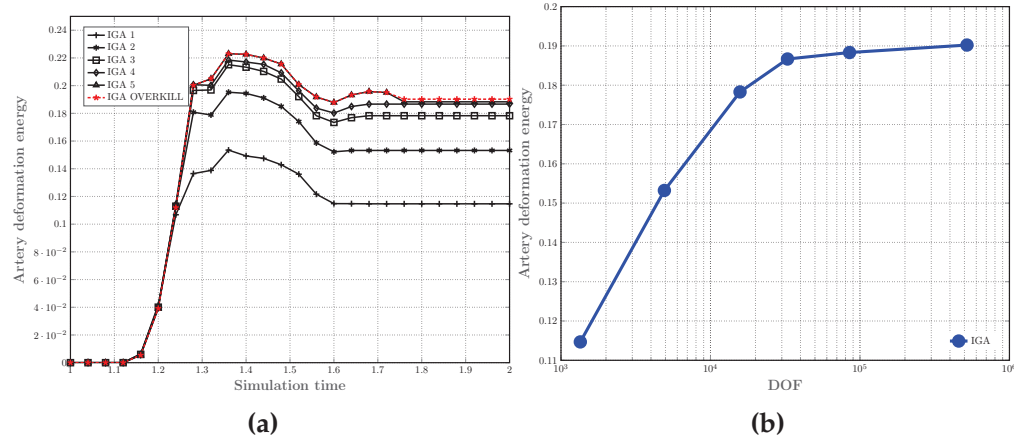


**Figure 6.16** (a) Artery deformation energy [Nmm] plot for each one of the considered five (5) meshes with respect to simulation time [s]. In each mesh, the number of degrees of freedom of the artery has been progressively increased. "IgA-overkill" is the mesh that shows the finest artery model. (b) Artery deformation energy [Nmm] with respect to the artery DOFs.

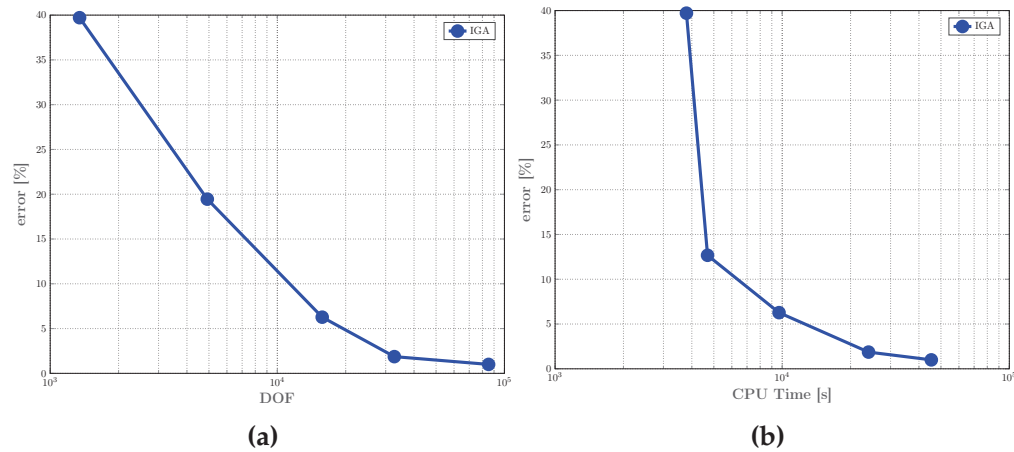


**Figure 6.17** Numerical errors evaluated with respect to the deformation energy of the "IgA-overkill" mesh at the last time-step of the analysis are plot against DOFs (a) and CPU time (b).

Mesh Label	DOFs	Error	CPU-time [h]
<b>IgA-1</b>	1347	39.7119%	1.05
<b>IgA-2</b>	4917	19.4512%	1.30
<b>IgA-3</b>	15765	6.2717%	2.69
<b>IgA-4</b>	32757	1.8663%	5.67
<b>IgA-5</b>	85173	0.9988%	12.56
<b>IgA-overkill</b>	323733	-	27.74

**Table 6.3** Analysis of stent deployment: relative errors are evaluated with respect to the finest IgA simulation, i.e. "IgA-overkill" mesh.

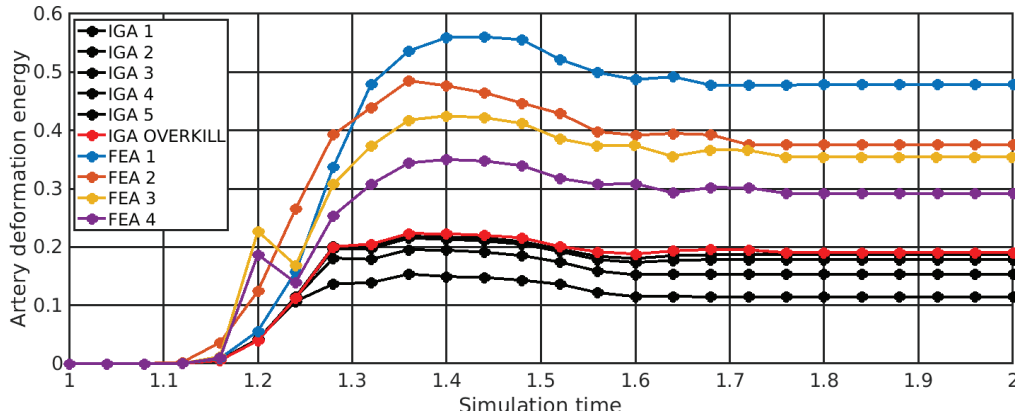


**Figure 6.18** Deformation energy [Nmm] versus simulation time [s] for IgA and the corresponding h-FEA meshes. The results demonstrate how h-FEA low order meshes are far from converging to the same artery deformation energy of the high-order corresponding ones. For this reason, to investigate the issue, we suggest increasing the number of DOFs of the artery as well as running the same contact analyses in another finite element solver like Abaqus.

be done in (IgA-)FEAP over a certain limit due to memory bound problems. For this reason, we thought appropriate to run the same contact simulations in the finite element solver Abaqus/Explicit (v. 6.11 Dassault Systemes, Providence, RI, USA), without resorting to memory bound problem. In the first attempt we made, the analyses were not converging. We think that they were not converging because the number of degrees of freedom of the stent is way larger than the one of the artery, probably causing problems in the slave-master local contact search. However, this statement has not been confirmed yet.

## 6.2 Conclusion

In this Chapter we applied a robust IgA contact framework to the evaluation in IgA-FEAP of contact forces between a complex geometry, i.e., a stent, and

a deformable surface like a catheter or an artery, resorting to a reduced number of DOFs with respect to classical FEA. Our numerical results suggest that the employment of IgA allows one to accurately represent the computational domain and to obtain a better approximation of the solution with a reduced number of degrees of freedom with respect to h-FEA and p-FEA. p-FEA follows the same IgA solution trends but, in order to obtain comparable results in terms of resultant of the radial force measure, the number of degrees of freedom has to be increased. It is evident that IgA, with its high-order and high-regularity basis functions, presents a superior capability to reproduce non-linear effects with respect to linear and high-order FEA.

## Chapter 7

# Patient-specific application of the developed methodologies

## 7.1 Collaboration with IRCCS Policlinico San Donato

This thesis work was born in strong collaboration with the medical research hospital IRCCS Policlinico San Donato, San Donato M.se, Milan, Italy in the context of the iCardioCloud project, which aimed at creating a cloud platform in which doctors can interact with engineers in order to develop new tools for improving endovascular surgery. To achieve this, biomedical technologies associated with imaging and numerical simulations, have to be placed inside the medical decision process. The final goal of the project was to build a Computational Fluid Dynamics (CFD) database of simulations in patients with thoracic aortic diseases. In particular, the project was focused on two main pathologies, TAA and TAD, explained in Chapter 2. When a patient is diagnosed with thoracic aortic disease, informed consent is first asked for enrollment in the study. Subsequently, the following studies are performed: Contrast Enhanced CT of the thorax, Phase Contrast - Magnetic Resonance Imaging, Clinical History. The project moved as a strong collaboration between the University of Pavia and IRCCS Policlinico San Donato, together with the participation of the Department of Mathematics and Computer Science of Emory University, USA. One of the pillars of the iCardioCloud philosophy was to facilitate the exchange of medical data. In general, technical details are difficult to understand for physicians and so protocols should be as simple as possible. Therefore, the iCardioCloud platform relies on a cloud-based repository in which only significant and straightforward information is available. Up to now, 21 patients have been enrolled in the study. For more information regarding the iCardioCloud project, the reader is referred to the thesis work by Dr. R. M. Romarowski, available at: [http://www-2.unipv.it/compmech/phd\\_diss.html](http://www-2.unipv.it/compmech/phd_diss.html).

In the following sections, three studies mainly based on the pipeline we introduced in Chapter 4 and conducted in collaboration with physicians from Policlinico San Donato, will be illustrated in details. Other studies, e.g., the



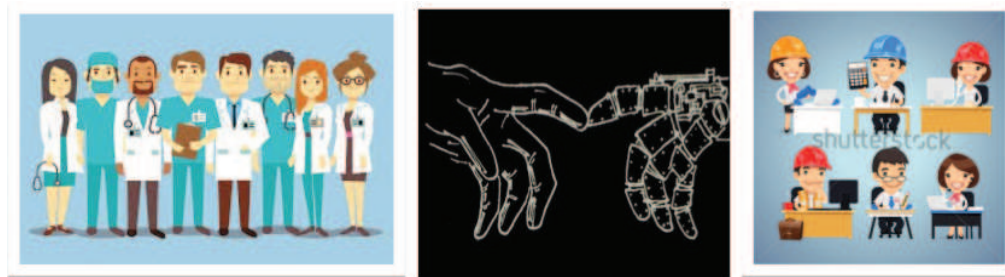


**Figure 7.1** Joint collaboration between doctors from IRCCS Policlinico San Donato (MI) and biomedical engineers from University of Pavia (CompMech Group - DICAR).

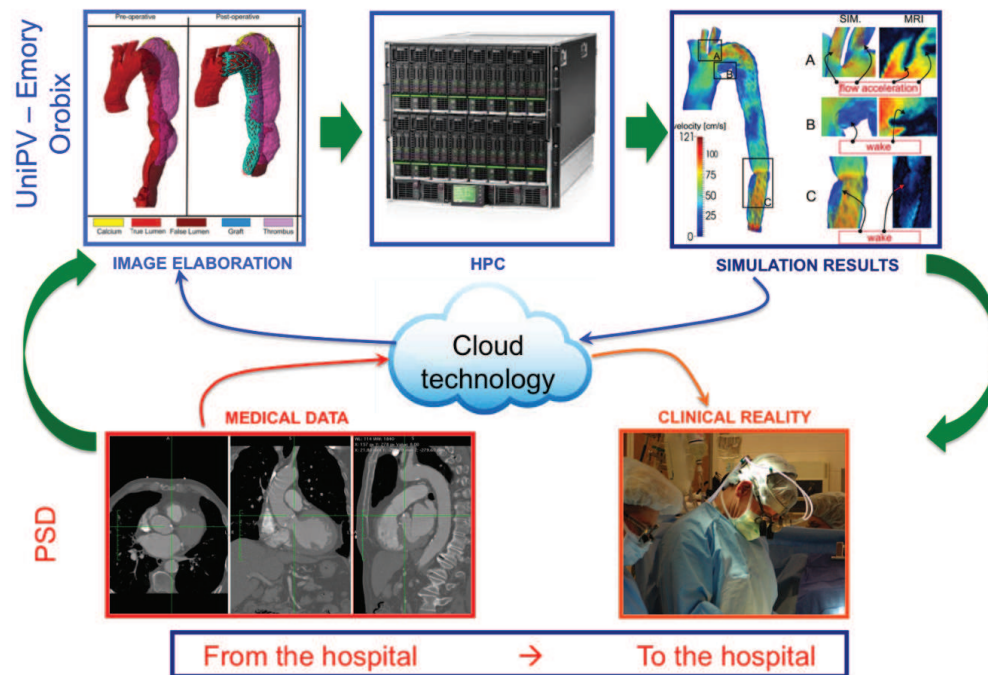


**Figure 7.2** iCardioCloud philosophy. Interaction between doctors and engineers is based on a shared cloud technology for exchanging data.

one based on the framework exploiting the T-spline technology, are still a work in progress and therefore they will not be described.

## 7.2 Patient-specific isogeometric structural analyses on TAAs

The first study we are going to speak about started with the acquisition of ten (10) of the twenty-one (21) Contrast Enhanced CT of the thorax available in the iCardioCloud database, in order to develop and benchmark the pipeline we described in Chapter 4. See Figure 7.4 and Figure 7.3 for a summary

of the main idea and concepts contained in this pipeline. We would like to remark that the patients we selected are affected only by thoraco-abdominal aneurysms (no TAD) and do not represent an homogeneous population from the point of view of age, sex, diameter and location of the aneurysm. The ultimate aim was trying to provide them of a trustworthy decision-making tool to be used real-time to decide whether a patient with TAA is worth operating or not, instead of the current use of the largest TAA diameter criterion.

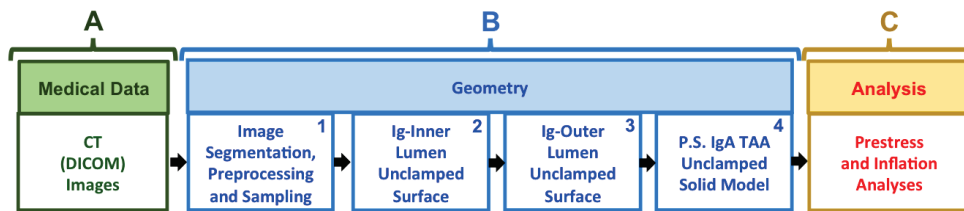


**Figure 7.3** From medical images to analysis: flowchart summarizing the steps required to obtain a complete patient-specific unclamped TAA solid model.

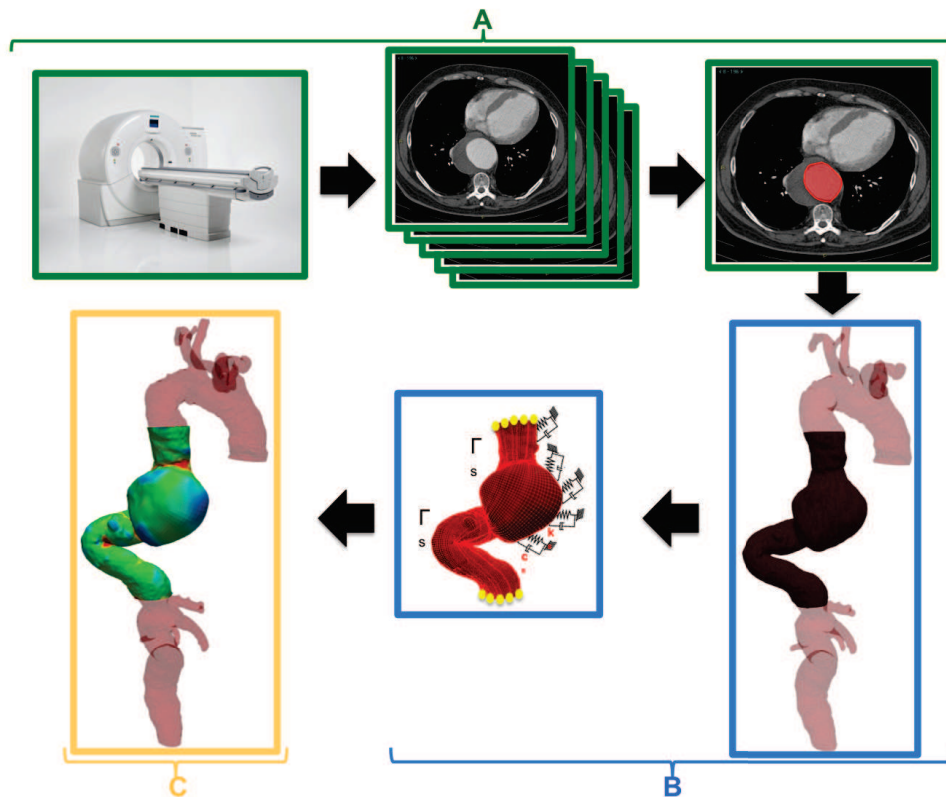


**Figure 7.4** From medical images to analysis: example of application on a patient-specific case of the previously introduced flowchart. Colors around each box are related to their corresponding block in Figure 7.3.

Starting from the fact that physicians from IRCCS Policlinico San Donato were already familiar with the concept of FE-based CFD analyses due to the shared iCardioCloud project, the main goal of this study, was first to introduce them to a new computational framework, the Isogeometric Analysis, based on a different and smoother representation of the surfaces under investigation with respect to traditional FEA and able to run simulations in a quicker way than FEA. Therefore, since they were used to the CFD computational times, once the results presented in Chapter 4, Table ??, were shown to them, the possibility of running (in future) real-time simulations *in* the hospital during the pre-operative planning phase started to grow as an idea.

Moreover, not only we introduce them to the use of IgA in biomechanics, but also to the von Mises stress distribution at the vessel wall as a quantity that can be used to easily represent and interpret the computational stress analysis results (Martin, Sun, and Elefteriades, 2015; Gasser, 2016) we got on TAAs and also as a quantity they could not get with CFD analyses. In particular, the maximum value of stress found anywhere on a particular aortic wall, i.e., the Peak Wall Stress - PWS (Shang et al., 2013b) was also presented them as an alternative to the "maximum diameter criterion" to decide whether a patient with an aneurysm is worth operating or not (Fillinger et al., 2002; Fillinger et al., 2003; Venkatasubramanian et al., 2004; Heng et al., 2008; Li et al., 2010). In Chapter 4, for each one of the 10 patients affected by thoraco-abdominal aneurysm, we considered the maximum value of the von Mises stress at the aortic wall as PWS.

Once the aforementioned pipeline was ready to be tested on patient-specific geometries, by means of all the results shown in Chapter 4 (see Section 4.8, Figure 4.25 and Table ??), we demonstrated the physicians how creating a patient-specific IgA-suitable model of TAA can be done almost automatically by performing a limited number of relatively easy steps in a short time, once the CT images have been acquired, preprocessed, and segmented. Furthermore, given that our final goal is the identification of patients potentially at risk of TAA enlargement and rupture, we showed them how the proposed framework may represent a promising and adequate starting point for the development of the aforementioned decision-making tool to improve the surgery planning operation-phase, even if other ingredients (e.g., supra-aortic carotid branches and iliac arteries, a TAA-suitable constitutive model, inclusion of the intraluminal thrombus, use of a variable pressure distribution) still need to be considered.

### 7.3 Case study on Retrograde Type A dissection

This second study developed as another application of the pipeline described in Chapter 4 and relies in part on the new Modified Arch Landing Areas Nomenclature (MALAN) (Marrocco-Trischitta et al., 2017) and the concept of Displacement Forces (DFs - for details see Chapter 2) that act on the surface of the endograft with every heartbeat. For extended references see (Bakel

et al., 2017), (Marrocco-Trischitta et al., 2018) and Chapter 5 of Dr. R.M. Romarowski's thesis. In particular, after specifically studying the effect of landing zone angulation on DFs magnitude, the group of Dr. M. M. Marrocco-Trischitta at IRCCS Policlinico San Donato, found that larger DFs magnitude occur at systolic peak of the cardiac cycle (Figuerola et al., 2009; Fung et al., 2008; Wang and Li, 2011) and in landing zones with increased angulation. For the direction, the same group analyzed the orientation of the DF vector in various aortic arch configurations and landing zones, founding that the direction of the DF vector is mostly cranial and related to the angulation and position of the landing zones. Please see Figure 7.5 for a clarification on these concept. These data on DFs are yet to be published.

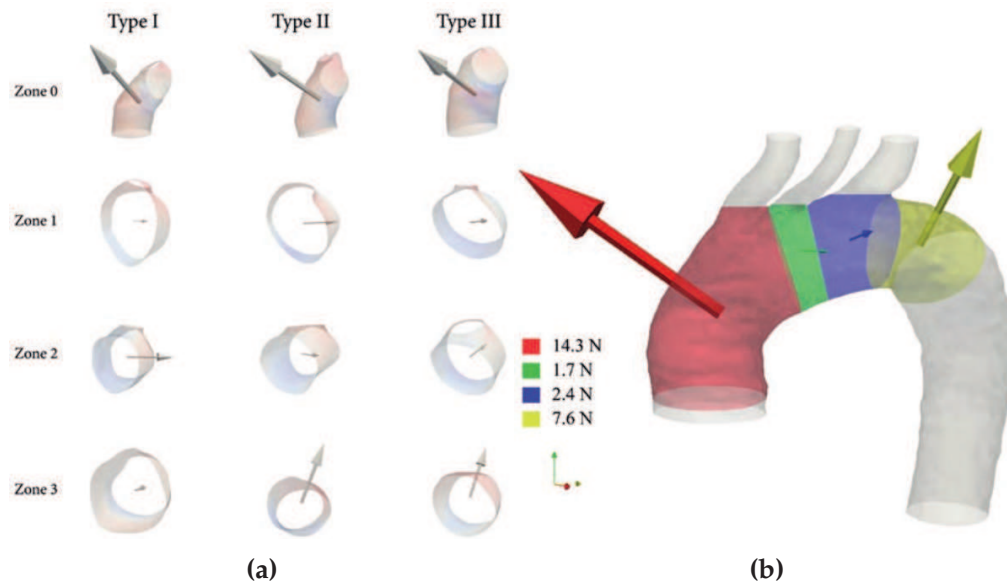


**Figure 7.5** (a) Displacement forces projected in the different proximal landing zones for TEVAR in a Type 2 aortic arch according to the new MALAN classification (Marrocco-Trischitta et al., 2017). Both magnitude and direction of the displacement forces change significantly between adjacent landing zones. (b) Displacement forces mapped in the proximal landing zones for TEVAR per Type of Arch. Displacement forces in zone 3 of Type I arches have smaller magnitude compared to those in zone 3 of Type II and III arches. Both pictures are taken from (Bakel et al., 2017)

For this case study, the subject under investigation is a 61-years-old male with previous EVAR who presented at IRCCS Policlinico San Donato for further endovascular treatment. Pre-operative CT showed a 59 mm aneurysmal dilation starting after the origin of the Left Subclavian Artery (LSA). TEVAR was performed by deploying two Medtronic Valiant stent-grafts (Medtronic, Santa Rosa, CA, USA) after the revascularization of the LSA. Under general anesthesia, the devices (46-46-150 mm and 42-42-150 mm) were successfully deployed showing total exclusion of the aneurysm by intraoperative angiography. No postoperative complications were reported and the control CT

showed no signs of endoleak. The patient came back after surgery complaining of chest pain. The CT angiographic control showed evidence of bleeding from the proximal section of the endoprosthesis near the left common carotid artery. Thus, an immediate arch replacement with the reimplantation of the supraortic vessels was performed because the patient developed a retrograde type A dissection.

CTA processing, based on 3D multiplanar reconstruction, was performed with 3Mensio Vascular software 8.1<sup>®</sup> (3MensioMedicalImagingB.V., Bilthoven, theNetherlands), which provides specific functions for automatic measurements. The angulation of the proximal landing zones was measured as described in detail in (Marrocco-Trischitta et al., 2017). Briefly, the angle between the flow axis of each proximal landing zone and the body of the lesion in Zone 2 (or the hypothetical lesion in Zones 0 and 1) to treat, analogous to the  $\beta$  angle as defined in the Society for Vascular Surgery reporting standards for EVAR (Chaikof et al., 2002), was determined. For this purpose, the center lumen line "tangent angle" function was employed, which calculates the angle between tangent lines drawn for any two points along the center lumen line. The pre-operative CT mesh was segmented with VMTK software suite and thus, the surface of the aorta was extracted. Furthermore, from the image stack showing bleeding in the arch, both the vessel lumen and the stent-graft wires were segmented. Figure 7.6 shows the 3D reconstructions in both cases.



**Figure 7.6** 3D reconstruction of the vessel lumen (a) and the stent-graft wires for the patient under study.



The hypothesis behind this study was that the combined effect of hemodynamic Displacement Forces (DFs) and wall stress concentration promotes retrograde type A dissection after TEVAR.

CFD as well as IgA structural analyses have been performed on both the pre- and post-TEVAR geometry. With CFD, DFs were calculated whereas with IgA structural analysis, von Mises stress at the vessel wall was computed.

CFD simulations require both the definition of the computational domain (i.e. mesh) following the aortic geometry and a set of boundary conditions. A volume mesh composed by tetrahedral elements was created from the pre-operative surface. No patient-specific haemodynamic data were available to tune the boundary conditions (for more details regarding the method to tune boundary conditions for CFD analysis using patient-specific data, see the thesis work by Dr. Romarowski). Hence, inflow and outflow parameters were extracted as follows: a flow waveform representing a cardiac output of 4.88 L/min was used as input, and on the outflow sections, three element Windkessel circuits were attached to mimic the compliance and resistance of the distal vasculature in a reliable way (Romarowski et al., 2018). Finally, a null velocity on the luminal surface was prescribed under the hypothesis of a rigid arterial wall. CFD simulations were performed by using the LifeV software suite (Bertagna et al., 2017) for solving the incompressible Navier-Stokes equations, assuming a constant fluid viscosity. Six cardiac cycles were simulated for each case to ensure the convergence of velocity and pressure fields. DFs were calculated by integrating the wall pressure and the wall shear stress (WSS) at systolic peak along the aortic wall in each MALAN area (Marrocco-Trischitta et al., 2017) using the Paraview software v5.3.0 (Kitware Inc., France). Consistently with previous reports, the contribution of the WSS was found to be negligible (Romarowski et al., 2018).

One clarification has to be done: this part of the work has been performed by engineering experts at IRCCS Policlinico San Donato and carefully explained to us, in charge of computing the von Mises stress at the vessel wall on the pre and post-TEVAR geometries in IgA-FEAP.

### 7.3.1 Results obtained on the pre- and post-TEVAR geometry

The CFD analysis performed on the pre-TEVAR geometry to calculate the DFs shows how the direction of the DF in correspondence of where the lesion developed is completely perpendicular to the arch curvature due to the angulation of the aortic arch whereas the DF magnitude does not have any interesting value. The von Mises stress at the vessel wall does not show any particular concentration area on the surface. These results are illustrated in Figure 7.7.

In the post-TEVAR geometry, a retrograde Type A dissection developed (see Figure 7.8, yellow circle).

Despite all these data, the causes that led to rupture after TEVAR have still to be determined. Nonetheless, in the following section, we are going to



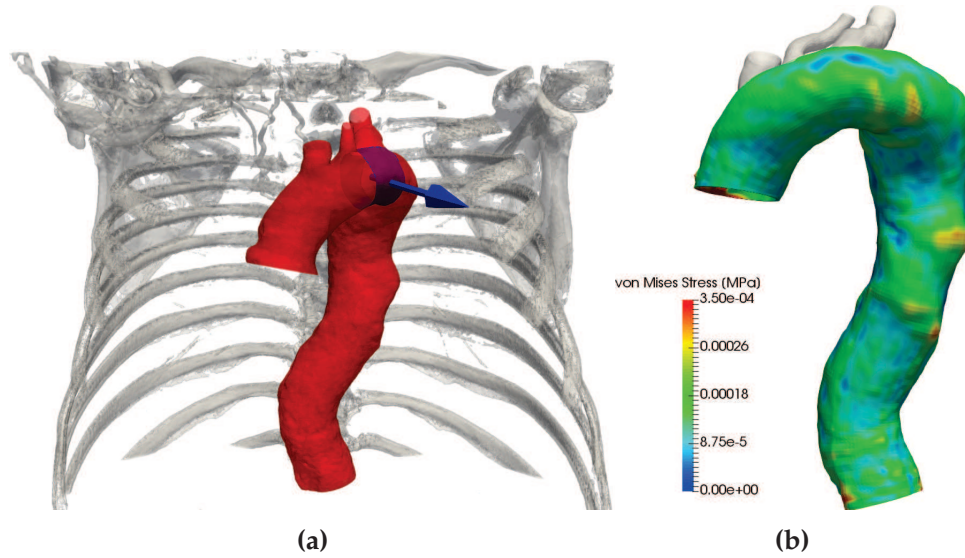


**Figure 7.7** (a) DF on the pre-TEVAR geometry computed by means of CFD analysis. (b) von Mises stress result computed on the pre-TEVAR geometry by means of the pipeline described in Chapter 4.

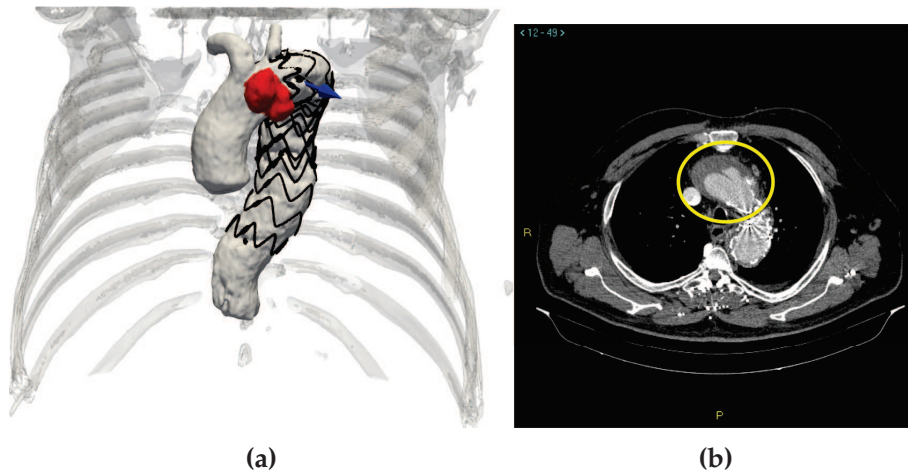


**Figure 7.8** (a) DF on the post-TEVAR geometry computed by means of CFD analysis. (b) CT-scan showing the retrograde Type A dissection.

explain the procedure we adopted in order to run the isogeometric structural simulations on this thoracic aorta case with a stent-graft in place.

The IgA model of the TA under study was created using the framework described in Chapter 4. No supra-aortic branches were considered in the reconstructed model. The IgA mesh is quadratic along each direction. Clamped knot vectors are used along the longitudinal direction and the thickness, whereas an unclamped one is used along the circumferential direction of the IgA model. For the stent, instead of constructing its IgA counterpart with the procedure shown in Chapter 6, we mapped it as a cylinder. In details, we knew where the stent landed thanks to the representation shown in Figure 7.9 provided to us by researchers from IRCCS Policlinico San Donato and obtained by means of an in-house VTK-based Python code starting from the post-TEVAR CT scan. In particular, the zone depicted in grey is the zone where the stent landed. The other two zones (blue and red respectively) represent the native aorta.



**Figure 7.9** Zone subdivision performed on the patient-specific model shown in Figure 7.6. The zone depicted in grey represents the zone where the stent landed. The other two zones represent the native aorta.

Starting from this information, we isolated in Paraview the grey part of the model representing the stent using the threshold filter. Subsequently, we performed *two* mapping operations using the algorithm described in Chapter 4, Section 4.4: one to obtain the patient-specific solid IgA model of the *entire* TA shown in Figure 7.6, and another one to obtain just the portion of the aorta mimicking where the stent landed (i.e., the grey part). This is a surface. These two B-spline representations (i.e., solid IgA model for the entire aorta and surface IgA model for just the portion of the aorta mimicking the stent) were then exported in a suitable format for the solver FEAP and tied together, in order to merge coincident control points, and thus forcing them

to have the same node number. Once in FEAP, using the extraction operator we described in Chapter 4, Section 4.7.3, we extract the following surfaces and segments of surfaces:

- **Complete** inner vessel surface of the solid model on which to apply an internal pressure of 120 mmHg (from literature);
- **Complete** outer vessel surface of the solid model on which to apply generalized Robin Boundary Conditions to simulate the presence of the surrounding organs (see Chapter 4, 4.7.2);
- The *inner portion* of the surface representing the stent.

For the solid model, we employed the nearly-incompressible Vorp constitutive model with parameters derived from literature (Shang et al., 2013a) (see Chapter 4 and Appendix B). The portion of the model mimicking the stent-graft is modelled using *membrane* elements with non-linear formulation, with properties obtained by means of a Representative Volume Element (RVE). The thickness of the membrane elements has been experimentally set to 0.1 mm.

An RVE is the smallest volume over which a measurement can be made that will yield a value that is representative of the whole. We used an RVE because the stent is a "periodic" object made of equal and repeated cells, and because we were looking for a material that represents the effect of the stent-graft on the aorta once in place and *not* just the properties of the stent-graft (like the ones simulated in Chapter 6). In Abaqus/Standard solver ver. 6.11 (Dassault Systèmes, Johnson, RI, USA) we constructed the geometry of the first Medtronic Valiant stent-graft (46-46-150 mm) deployed in the patient under study. To be precise, a planar CAD geometry corresponding to the stent in unfolded configuration was generated in Abaqus, together with its mesh. Then, through appropriate geometrical transformations performed by an in-house Matlab code, the planar mesh was rolled leading to the stent final configuration. Subsequently, using a new command we introduced in FEAP, named "*aba2feap*" which permits to automatically convert an Abaqus ".inp" input file (containing all the geometrical, assembly and mesh details for the construction of the object under study) into a FEAP one, just one quarter of a cell stent has been imported to FEAP and this constitutes our RVE. See Figure 7.10a for an example of application of the aforementioned command "*aba2feap*" and Figure 7.10b for the quarter of cell stent we imported in FEAP.

Once imported the elementary cell in FEAP (in the main finite element program and not in the IgA embedded module), the average properties to be assigned to all the surface representing the stent are computed from the RVE. The basic process in FEAP is carried out by a Hill-Mandel average (Geers, Kouznetsova, and Brekelmans, 2001; Kouznetsova, Brekelmans, and Baaijens, 2001; Zienkiewicz and Taylor, 2005). For this case, the RVE has been



**Figure 7.10** (a) Example of application of the "aba2feap" command. The Medtronic Valiant stent (46-46-150 mm) was first created in Abaqus and then imported in FEAP for testing the conversion code. (b) Quarter of cell of the same stent-graft mesh used for obtaining the properties of the RVE to employ in the simulations.

subjected to periodic boundary conditions, whereas the boundaries are subjected to a deformation gradient. The analysis is performed as a finite deformation problem. In this way, from the homogenized stress and the associated tangent array,  $E = 7.5e04$  MPa can be computed and assigned to all the surface representing the stent modeled as a Saint-Venant Kirchhoff material, with Poisson modulus experimentally set to  $\nu = 0$ .

The results of the IgA inflation simulations we obtained by means of this set-up can be seen in Figure 7.11b.

The von Mises stress scales for both results (Figure 7.11a) have been set to the values obtained in the pre-TEVAR case, just for comparison between the two. From an engineering point of view, this result seems quite obvious: given two coupled tubes with distributed constant pressure inside and different stiffness values (the portion resembling the stent has a higher stiffness value than the native aorta one), at the interface of the two tubes the deformation is different and the "local" solution depends on the properties of the two tubes. To understand that everything was correct, we run another test analysis on a bent pipe with the same specifications and material properties than the patient-specific case just described (*without* setting the von Mises scale equal to the pre-TEVAR one) and the results, on a von Mises stress base, agree with the ones obtained in the patient-specific geometry case (see Figure 7.12).

We certainly know that these results are just preliminary and they cannot provide an answer regarding which is the real cause of the rupture after TEVAR.

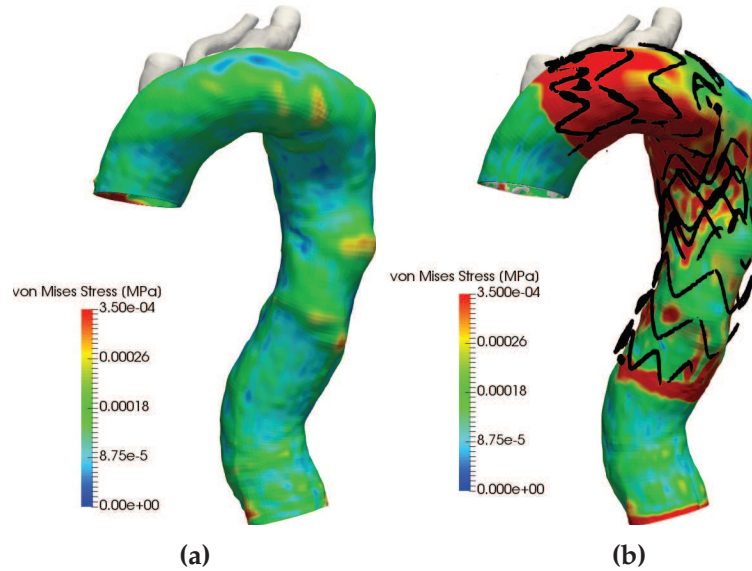


**Figure 7.11** (a) von Mises stress distribution pre-TEVAR and (b) von Mises stress distribution post-TEVAR using homogenized properties for the surface representing the stent.

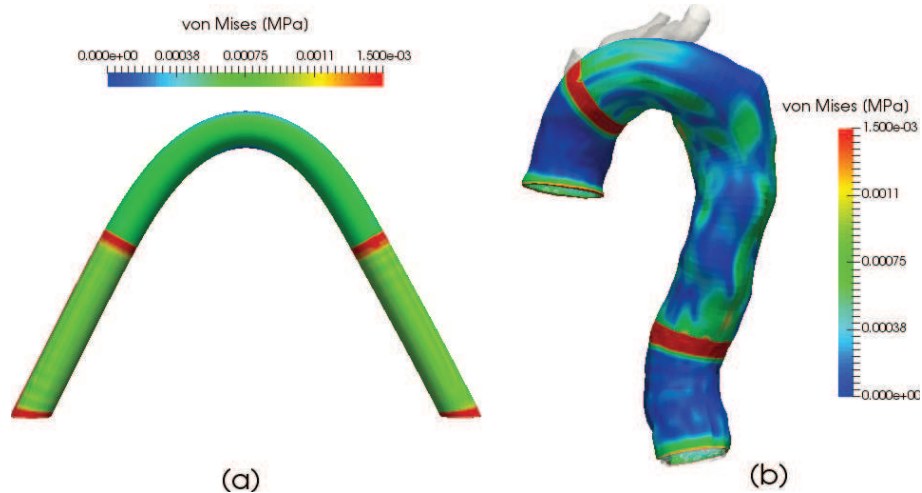


**Figure 7.12** Comparison, on a von Mises stress base, between a test case geometry (a) and the patient-specific case under study, in order to understand if the results we showed in Figure 7.11 were correct. Results between the test and the patient-specific case agree. Results agree also between Figure 7.11b and (b) because they present the same von Mises stress pattern at the vessel wall. Von Mises stress values are different because the ones in Figure 7.11b have been rescaled to the von Mises stress values obtained in the pre-TEVAR case.

Further analyses have to be run in accordance with physicians and engineering experts from IRCCS Policlinico San Donato in order to understand the



real reason of the rupture. In any case, they represented an interesting case-study to test the pipeline we introduced in Chapter 4 as well as to test and introduce some new routines in FEAP and IgA-FEAP. As a matter of fact, as late development, we introduce another command in IgA-FEAP in order to avoid mapping the inner portion of the TA surface representing the stent or, more in general, to avoid performing mapping operation every time the stent landing position is changed. In particular, within the same Matlab code we usually use to perform mapping operation and starting from the representation shown in Figure 7.9, we simply obtain the knot values indices along the longitudinal (i.e., "v") parametric direction of the complete TA IgA inner surface model between which the stent is lying. These indices are used by the new IgA-FEAP command:

```
K_SP
KNOT k k_min k_max
```

with  $k$  indicating the knot vector number in the longitudinal direction of the TA complete *inner* surface model, in order to activate the stent material properties (obtained in this case by means of a RVE) in the knot vector interval comprised between **k\_min** and **k\_max**. By simply changing the values of **k\_min** and **k\_max**, different landing zones scenarios can be taken into account for the analysis.

## 7.4 Application of the patient-specific pressure distribution obtained from CFD analyses

Another algorithm that was born from the collaboration with the physicians, is the one that permits to apply a variable pressure derived from FE-based CFD analyses to the control points of an IgA mesh. This algorithm was born because, from CFD analyses, we certainly know that the pressure distribution inside a TA is not constant (see Dr. R.M. Romarowski thesis and Figure 7.13 for the pressure distribution inside the patient considered in the precedent study and depicted in Figure 7.6). As we said in Chapter 4, Section 4.7.2, in our simulations we are employing the *average blood pressure* in a single cardiac cycle (i.e., MAP = Mean Arterial Pressure) previously computed by means of CFD analysis. Hence, we are employing a constant distributed pressure throughout the aorta. Therefore, in order to check if applying the real patient-specific pressure distribution obtained from CFD analyses on a TA, the distribution of the von Mises stress at the vessel wall changes, a in-house Matlab algorithm was created in order to perform this task. This algorithm has just been tested on a cylinder with a random pressure distribution, simulating the one hypothetically derived from CFD analyses. Hence, the results we have are just preliminary and they still have to be applied on patient-specific TA geometries, in order to check if and how the von Mises



stress distribution changes by applying the patient-specific pressure distribution on the control points of the IgA patient-specific model.

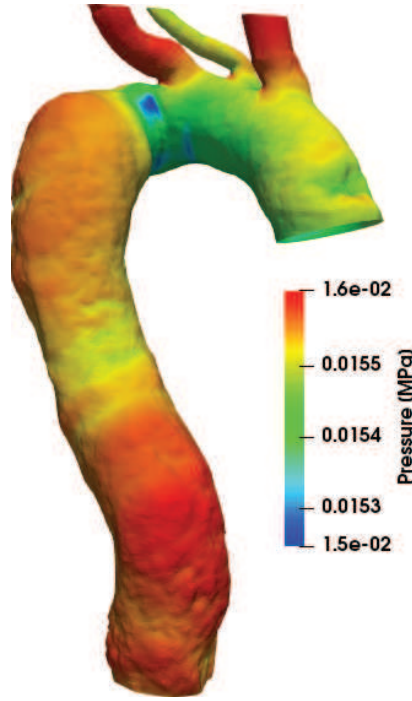


**Figure 7.13** Patient-specific pressure distribution taken at systole and computed by means of CFD analyses on the patient shown in Figure 7.6).

#### 7.4.1 Algorithm details

The algorithm we are going to show is very similar to the one used for obtaining the patient-specific IgA geometry starting from sections of points and a reference geometry (see Chapter 4, Section 4.4). One of the output of the CFD analyses that are run at IRCCS Policlinico San Donato on patient-specific TA geometries is a file containing the pressure values for each FE nodes in the CFD mesh. The pressure values for each FE nodes has to be imported (in vectorial form) in Matlab together with the ".stl" (i.e., triangulated) file of the patient-specific geometry representing the aortic vessel, extracted from DICOM images and its B-splines based unclamped representation. The ".stl" mesh in Matlab will be represented as a structure containing two fields: a matrix containing for each vertex its coordinate in the 3D space and another matrix containing the faces, i.e., each row represents a triangle and contains the indexes numbers for each vertex.

The total number of nodes in the FE mesh, is  $N_{FEM} = (nfem\_x * nfem\_y)$ , whereas the total number of control points in the IgA one is  $N_{CP} = (ncp\_x * ncp\_y)$ . As for the mapping algorithm presented before, the number of nodes in the FE mesh should be *sufficiently* higher than the number of nodes in the IgA one. In particular,  $N_{FEM} > N_{CP}$ . The algorithm is as follows:

- Consider the FE ".stl" mesh and, for each triangle, look for unique nodes (i.e., look for **N\_PT** unique nodes).
- Assign a **global** index number to each one of the **N\_PT** unique nodes just obtained.
- Allocate **C**, sparse matrix of basis functions, with dimensions of **C** being  $C = [N\_PT * N\_CP]$ ;
- For the  $i^{th}$  node belonging to the **N\_PT** unique nodes:
  - Perform nearest-neighbour algorithm to look for its closest IgA control points.
  - Once obtained the closest IgA control point, compute its B-spline basis functions along the parametric directions  $u$  and  $v$  and the product between them. The result containing the product is a vector.
  - Set  $C(i,:)$  equal to the vector containing the product between basis functions.
  - Consider the pressure value of the  $i^{th}$  FEM node.
- Solve  $\mathbf{S} = \mathbf{C} \setminus \mathbf{B}$  by means of a least square approximation (via the QR algorithm), where **S** is the  $[N\_CP \times 1]$  vector containing the pressure values to be applied to each control point in the IgA mesh, **C** the  $[N\_PT \times N\_CP]$  matrix that contains the products between shape functions in both parametric directions and **B** the  $[N\_PT \times 1]$  pressure vector containing the pressure values for each unique FEM nodes.

The  $[N\_CP \times 1]$  vector containing the pressure values for each IgA control point has to be exported (as a .txt file) in a format suitable for the IgA-FEAP solver. In particular, the .txt file should start with the header "temp=Pressure", followed by

N\_node G\_in P\_v

where **N\_node** is the control point index number, **G\_in** the increment to the next node, and **V\_node** the pressure value for each control point. We would like to remark that for overlapped control points the pressure values should not be repeated. An example of this input file is provided below:

```
feap * *
32 24 3 3 3 16 0

MATERial      1
SOLID elmt    0 0 0 0
ELASTic Isotropic 3 3.000000e-01
```

NURBs, ,3 2 2

MATeRial 2  
 press elmt 0 0 0 0  
 nodel  
 nurb quad 3 2  
 plot off

MATeRial 3  
 Robin 5 0 0 0 0  
 elastic ks 10  
 nurb quad 3 2  
 plot off

\*AUTO numbering

NURBs ALL 32

1	0	-1.207000E+02	-5.000000E+01	0.000000E+00	1.000000E+00
2	0	-1.307000E+02	-6.000000E+01	0.000000E+00	1.000000E+00
3	0	-5.000000E+01	-1.207000E+02	0.000000E+00	1.000000E+00
4	0	-6.000000E+01	-1.307000E+02	0.000000E+00	1.000000E+00
5	0	5.000000E+01	-1.207000E+02	0.000000E+00	1.000000E+00
6	0	6.000000E+01	-1.307000E+02	0.000000E+00	1.000000E+00
7	0	1.207000E+02	-5.000000E+01	0.000000E+00	1.000000E+00
8	0	1.307000E+02	-6.000000E+01	0.000000E+00	1.000000E+00
9	0	1.207000E+02	5.000000E+01	0.000000E+00	1.000000E+00
10	0	1.307000E+02	6.000000E+01	0.000000E+00	1.000000E+00
11	0	5.000000E+01	1.207000E+02	0.000000E+00	1.000000E+00
12	0	6.000000E+01	1.307000E+02	0.000000E+00	1.000000E+00
13	0	-5.000000E+01	1.207000E+02	0.000000E+00	1.000000E+00
14	0	-6.000000E+01	1.307000E+02	0.000000E+00	1.000000E+00
15	0	-1.207000E+02	5.000000E+01	0.000000E+00	1.000000E+00
16	0	-1.307000E+02	6.000000E+01	0.000000E+00	1.000000E+00
17	0	-1.207000E+02	-5.000000E+01	5.000000E+02	1.000000E+00
18	0	-1.307000E+02	-6.000000E+01	5.000000E+02	1.000000E+00
19	0	-5.000000E+01	-1.207000E+02	5.000000E+02	1.000000E+00
20	0	-6.000000E+01	-1.307000E+02	5.000000E+02	1.000000E+00
21	0	5.000000E+01	-1.207000E+02	5.000000E+02	1.000000E+00
22	0	6.000000E+01	-1.307000E+02	5.000000E+02	1.000000E+00
23	0	1.207000E+02	-5.000000E+01	5.000000E+02	1.000000E+00
24	0	1.307000E+02	-6.000000E+01	5.000000E+02	1.000000E+00
25	0	1.207000E+02	5.000000E+01	5.000000E+02	1.000000E+00
26	0	1.307000E+02	6.000000E+01	5.000000E+02	1.000000E+00
27	0	5.000000E+01	1.207000E+02	5.000000E+02	1.000000E+00
28	0	6.000000E+01	1.307000E+02	5.000000E+02	1.000000E+00
29	0	-5.000000E+01	1.207000E+02	5.000000E+02	1.000000E+00
30	0	-6.000000E+01	1.307000E+02	5.000000E+02	1.000000E+00

31 0 -1.207000E+02 5.000000E+01 5.000000E+02 1.000000E+00  
32 0 -1.307000E+02 6.000000E+01 5.000000E+02 1.000000E+00

ELEMents NODES= 16 MATE= 1

1	0	1	1	2	3	4	5	6	7	8	17	18	19
20	21												
22	23	24											
2	0	1	3	4	5	6	7	8	9	10	19	20	21
22	23												
24	25	26											
3	0	1	5	6	7	8	9	10	11	12	21	22	23
24	25												
26	27	28											
4	0	1	7	8	9	10	11	12	13	14	23	24	25
26	27												
28	29	30											
5	0	1	9	10	11	12	13	14	15	16	25	26	27
28	29												
30	31	32											
6	0	1	11	12	13	14	15	16	1	2	27	28	29
30	31												
32	17	18											
7	0	1	13	14	15	16	1	2	3	4	29	30	31
32	17												
18	19	20											
8	0	1	15	16	1	2	3	4	5	6	31	32	17
18	19												
20	21	22											

ENURBs

1	1	2	3
2	501	2	3
3	1001	2	3
4	1501	2	3
5	2001	2	3
6	2501	2	3
7	3001	2	3
8	3501	2	3

ELEMents NODES= 8 MATE= 2

1	0	2	1	3	5	7	17	19	21	23
2	0	2	3	5	7	9	19	21	23	25
3	0	2	5	7	9	11	21	23	25	27
4	0	2	7	9	11	13	23	25	27	29
5	0	2	9	11	13	15	25	27	29	31
6	0	2	11	13	15	1	27	29	31	17
7	0	2	13	15	1	3	29	31	17	19

8    0        2   15        1    3        5   31    17    19    21

ENURBs

1	4	5	0
2	504	5	0
3	1004	5	0
4	1504	5	0
5	2004	5	0
6	2504	5	0
7	3004	5	0
8	3504	5	0

ELEMents NODES=8 MATE=3

1	0	3	2	4	6	8	18	20	22	24
2	0	3	4	6	8	10	20	22	24	26
3	0	3	6	8	10	12	22	24	26	28
4	0	3	8	10	12	14	24	26	28	30
5	0	3	10	12	14	16	26	28	30	32
6	0	3	12	14	16	2	28	30	32	18
7	0	3	14	16	2	4	30	32	18	20
8	0	3	16	2	4	6	32	18	20	22

ENURBs

1	6	7	0
2	506	7	0
3	1006	7	0
4	1506	7	0
5	2006	7	0
6	2506	7	0
7	3006	7	0
8	3506	7	0

KNOTs\_outm

Unclamp	1	15	3	0.00000000E+00	1.00000000E+00
2.00000000E+00		3.00000000E+00	4.00000000E+00	5.00000000E+00	
6.00000000E+00		7.00000000E+00	8.00000000E+00	9.00000000E+00	
1.00000000E+01		1.10000000E+01			
1.20000000E+01		1.30000000E+01	1.40000000E+01		
Clamped	2	4	0.00000000E+00	0.00000000E+00	1.00000000E+00
1.00000000E+00					
Clamped	3	4	0.00000000E+00	0.00000000E+00	1.00000000E+00
1.00000000E+00					
Unclamp	4	15	3	0.00000000E+00	1.00000000E+00
2.00000000E+00		3.00000000E+00	4.00000000E+00	5.00000000E+00	
6.00000000E+00		7.00000000E+00	8.00000000E+00	9.00000000E+00	
1.00000000E+01		1.10000000E+01			
1.20000000E+01		1.30000000E+01	1.40000000E+01		

```

Clamped      5      4  0.00000000E+00  0.00000000E+00  1.00000000E+00
1.00000000E+00
Unclamp      6      15      3  0.00000000E+00  1.00000000E+00
2.00000000E+00  3.00000000E+00  4.00000000E+00  5.00000000E+00
6.00000000E+00  7.00000000E+00  8.00000000E+00  9.00000000E+00
1.00000000E+01  1.10000000E+01
1.20000000E+01  1.30000000E+01  1.40000000E+01
Clamped      7      4  0.00000000E+00  0.00000000E+00  1.00000000E+00
1.00000000E+00

```

Include Npress

END mesh

TIE

INTERactive

STOP

with the "Npress" input pressure file being:

```

temp = Pressures
1 0      0.0157310
3 0      0.0159600
5 0      0.0157310
7 0      0.0159600
9 0      0.0157310
11 0     0.0159600
13 0     0.0157310
15 0     0.0159600
17 0     0.0157310
19 0     0.0159600
21 0     0.0157310
23 0     0.0159600
25 0     0.0157310
27 0     0.0159600
29 0     0.0157310
31 0     0.0159600

```

the pressure is expressed in MPa. To test the code, we consider a simple solid cylinder, modeled with a linear elastic model, with generalized Robin Boundary Conditions applied to its external surface, and a constant pressure equal to 125 mmHg applied to its inner surface. In order to obtain a variable distribution for the pressure for each unique FE nodes, in Matlab we create a [N\_PT\*1] vector with all the pressure values equal to 125 mmHg. Then we



applied to each one of them a **random** rumor so that the final pressure distribution is experimentally limited between 118 and 125 mmHg. Subsequently, we run the algorithm we just described in order to find the pressure to be assigned to each control point. The results are shown in Figure 7.14.

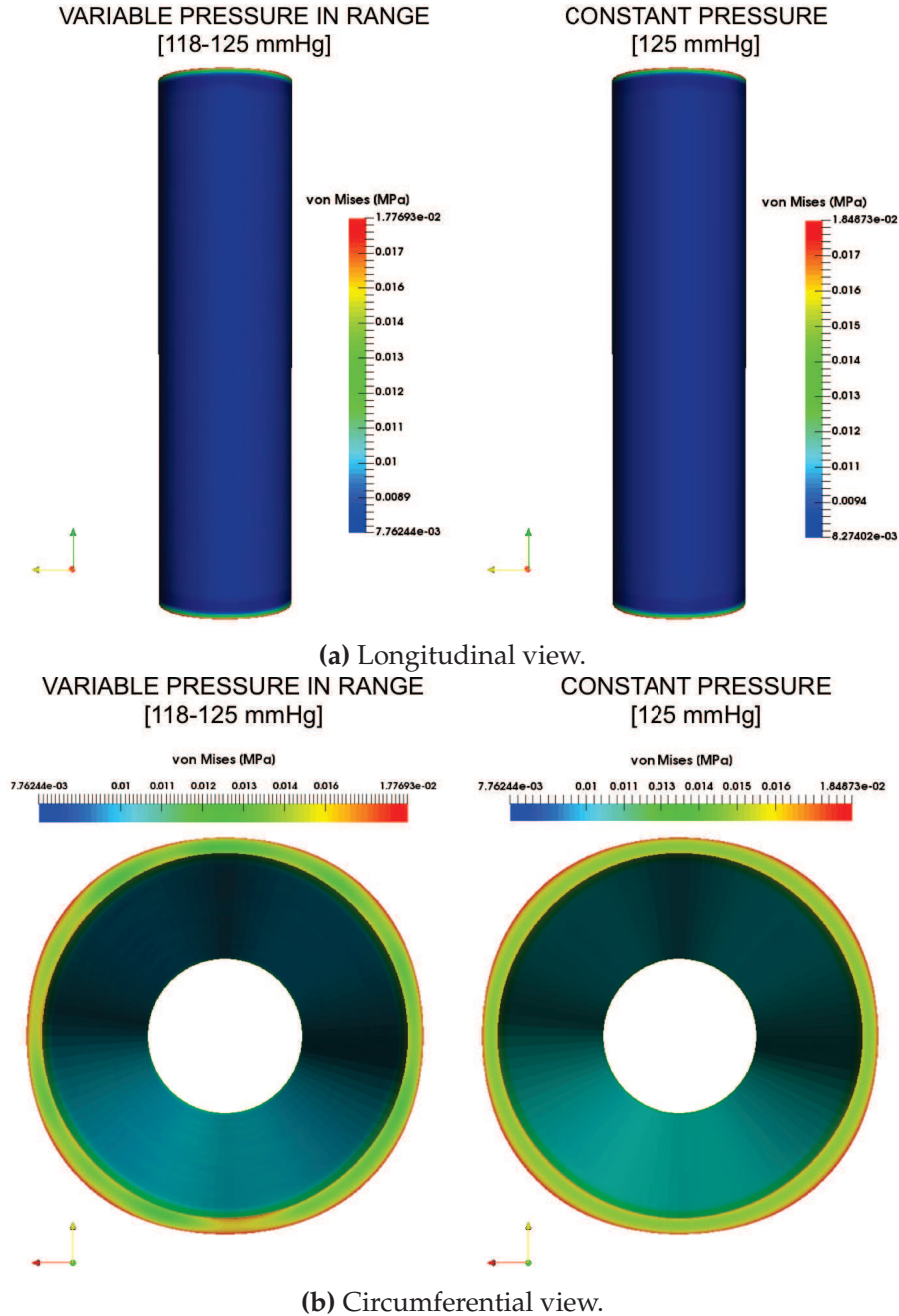


**Figure 7.14** Longitudinal and circumferential view of the results obtained using a variable pressure applied to the control points of the IgA mesh (Left) and a constant one (Right).

As already said, these are just preliminary results obtained on a simple solid

model: therefore, the application of the algorithm on a more complicated case like a patient-specific TA geometry would provide more insights on the effectiveness of the algorithm and on its possible use to understand if variable pressure distributions taken from CFD analyses may be useful to better describe how von Mises stress is distributed in patient-specific thoracic aortas.



## Chapter 8

### Final remarks

In the recent years, the employment of *in silico* (i.e., computational) methods in the medical routine and in the medical device sector has become an important tool for both manufacturers and clinical researchers. From an experimental point of view, computational tools allow to simulate and investigate, prior to the intervention and to device manufacturing, different scenarios. In particular, numerical tools employed in the field of "predictive medicine" help simulating different "what-if" clinical scenarios, trying to tailor the best combination of procedure strategies and medical devices for a specific patient morphology. From the industrial point of view, computational tools help investigating different experimental scenarios including design modifications, new materials, and working conditions that otherwise are difficult (or even impossible) to be reproduced.

From a practical point of view, in order to be reliable in the clinical and industrial practice, these methodologies need to fulfill some requirements such as: i) accurate geometric representation of the computational model with respect to the real one and its components; ii) reliable description of the material behavior of the model and its involved components; iii) appropriate reproduction of the real working conditions within the computational model.

In this context, Finite Element Analysis is widely employed as a reliable and accurate tool to reproduce the goals described above. FEA is, at present, a widely employed and well assessed simulation tool, but it presents some limitations that can affect both the geometrical accuracy of the domain under investigation and the regularity of the approximated solution. In particular, FEA low-order and low-regularity basis functions used to discretize the continuum domain do not permit, in general, to accurately represent complex geometries unless extremely fine meshes are adopted. At the same time, FEA basis functions do not allow, in general, to properly approximate the solution without resorting to a high number of degrees of freedom.

Given this, Isogeometric Analysis has been recently proposed as an exact-geometry, cost-effective alternative to classical FEA. The idea of IgA is that NURBS basis functions used for geometry representation in CAD can be used for both geometry description and analysis in an isoparametric fashion. Moreover, the high-regularity provided by the IgA shape functions extends

the benefits provided by this innovative method to all the boundary value problems where high-continuity is required and plays a prominent role.

The doctoral research described in this dissertation can be collocated within this framework because we aimed at employing innovative computational mechanics techniques to provide support to vascular surgeons during the pre-operative decision making process. In particular, the present doctoral research can be subdivided as follows: i) study and implementation of routines based on a particular type of knot vectors (i.e., unclamped knot vectors), key ingredient of Isogeometric Analysis; ii) set-up of an innovative IgA-based computational framework for the evaluation of the aneurysm risk of rupture in thoracic aortas; iii) extension of the proposed IgA computational framework for the creation of complex arterial networks characterized by arbitrary topology; iv) frictionless contact modeling and simulations for stent implant procedures including performance comparison between IgA and FEA with respect to solution accuracy and computational efficiency; v) application of the introduced frameworks to problems proposed to us by physicians from IRCCS Policlinico San Donato, San Donato M.se, Milan, Italy, whom this doctoral work has been done in collaboration with.

Accordingly, we first investigated the peculiar aspects of unclamped (i.e., closed, periodic) knot vectors for the construction of analysis-suitable closed curves and surfaces characterized by higher than  $C^0$  continuity. Unclamped knot vectors are not widely used in the IgA community, whereas clamped (i.e., open, non periodic) ones are the most commonly employed in all IgA applications. Therefore, the use of unclamped knot vectors required the modification of some pre-existing routines based on clamped knot vectors as well as the implementation of some new ones within the research Finite Element Analysis Program (FEAP) (Taylor, 2017) and Matlab NURBS toolbox (MATLAB, 2018; Falco, Reali, and Vázquez, 2011; Spink, 2014). Unclamped B-splines have been successfully used as a basis for modeling and analysis in a first study in the context of predictive medicine aimed at i) developing a semi-automatic pipeline for the creation of patient-specific IgA-suitable geometries of Thoracic Aortic Aneurysms derived from DICOM images, completely removing any operational dependency on the centerline of the model; ii) implementing additional routines in IgA-FEAP in order to make the structural inflation simulations on TAAs more complete (in particular, the Vorp material model to be used for modeling the arterial wall (Raghavan and Vorp, 2000), and generalized Robin boundary conditions (Moireau et al., 2012) to take into account the presence of the surrounding organs); iii) testing the proposed complete framework (from IgA modeling to analysis) on multiple patient-specific TAA models in order to confirm its effectiveness for the description of the aneurysm enlargement and rupture risk phenomena. The results demonstrated how creating a patient-specific IgA-suitable model of TAA can be done almost automatically by performing a limited number of relatively easy steps, once the DICOM images have been acquired, preprocessed, and segmented. Not only this pipeline contains most of the ingredients that allow numerical simulations in aortic aneurysms to be accurate

and effective (e.g, precise reconstruction of the aneurysm geometry, realistic material properties for the arterial wall, high continuity description of the stress field) but also the overall (from IgA modeling to analysis) computational costs proved to be able to keep the pace with the clinical routine timeline. The final goal of the pipeline is the identification of patients potentially at risk of TAA enlargement and rupture. We certainly know that to fulfill this task and, thus, give the physicians a consistent and objective decision-making tool to improve the surgery planning operation-phase, other ingredients (e.g., supra-aortic carotid branches and iliac arteries, a TAA-suitable constitutive model, inclusion of the intraluminal thrombus, use of a variable pressure distribution) need to be considered. However, we think that our simulation models and analysis settings already represent a good compromise between computational time and accuracy and is sufficient to reach the main goal of this study.

Starting from this pipeline, we moved towards the creation of another one based on the T-spline technology for the creation of patient-specific aortic geometries characterized by complex and arbitrary topology. The need to create this "new" pipeline was born because with the "old" one, the presence of the supra-aortic branches in the TAAs models was neglected. The algorithm we adopted to get the patient-specific unclamped IgA models of the TAA does not work for branched geometries but only for single-patch tube-like ones without bifurcations. Since neglecting the supra-aortic branches presumably means neglecting important constitutive parts of the aorta that may affect the study of the risk of enlargement and rupture of an aneurysm, we introduced another semi-automatic framework able to create patient-specific geometries in a very short time and in a limited number of passages that can be performed also by a non expert user. They involve the use of the Autodesk T-splines plug-in for Rhino for the creation of the T-spline object starting from the triangulated (".stl") mesh extracted from medical images. A big effort in this part of the work has been done in order to make IgA-FEAP able to work properly with T-meshes characterized by a high number of DOFs. In its previous versions (v. 8.4), IgA-FEAP was already able to work with simple T-spline meshes but some features of the Autodesk T-spline plug-in were modified, together with the format of the T-meshes export file. Therefore work has been done in order to permit IgA-FEAP to properly work with T-splines objects characterized by a high-number of DOFs, starting from memory allocation problems to the capability of plotting and exporting them properly. All the additional routines we added, while working with the previous pipeline to make simulations on TAAs more complete, have been adapted to T-splines objects as well. Moreover, a step towards the use of an advanced mesh generation method that avoids the tensor product limitations of B-splines and NURBS has been made. We got preliminary and promising results from inflation simulations aimed at investigating the distribution of the von Mises stress quantity at the vessel wall. At present, simulations on aortic models are run using a linear constitutive model for the aortic artery, and only surface data can be provided, meaning that analyses are restricted to bodies that are represented by surfaces (e.g., 2-d solid bodies, membranes and shells). In



this thesis work, we employed shells for the analyses. At present, in IgA-FEAP, only the Kirchhoff-Love thin-shell element is available. We adopted it with constant shell thickness along the aortic artery.

Subsequently, we investigated the IgA benefits over linear (h-FEA) and higher order FEA (p-FEA) studying two examples of frictionless contact interactions in order to numerically reproduce stent crimping and stent deployment in the context of Carotid Artery Stenting (CAS) pre-operative planning. In particular, we focused on the application of NURBS-based isogeometric analysis to 3D frictionless contact problems between deformable bodies undergoing large deformations. Starting from the framework and the contact driver implemented in the IgA package for FEAP by Dr. Mauro Ferraro, based on the work of (De Lorenzis et al., 2011), we first reviewed the basics of computational contact mechanics and then we performed some numerical tests including stent geometry and non linear constitutive models to simulate the double-sided contact typical of stent implant simulations. The results confirm the capability of the proposed framework to reproduce complex real life problems with reduced DOF number with respect to linear and high-order FEA.

Finally, all the aforementioned pipelines have been applied to problems presented to us by physicians from IRCCS Policlinico San Donato. In particular, besides the application of the first framework we mentioned to 10 patient-specific cases belonging to the iCardioCloud project, whose goal was creating a cloud platform in which doctors can interact with engineers in order to develop new tools for improving endovascular surgery, this pipeline was also applied to a case study on Retrograde Type A dissection, aimed at understanding why the patient developed a Retrograde Type A dissection after TEVAR operation. This study was very beneficial because it permitted us to enrich FEAP of other capabilities, like a non-linear isogeometric model for the membrane element, the use of a Representative Volume Element (RVE) to infer the properties to be given the stent present in the simulations, the creation of a new command for the automatic conversion of Abaqus input files into FEAP ones, allowing the user to create a complex geometry in Abaqus and perform the analysis in FEAP. Finally we had the opportunity to create a command for the automatic conversion of any clamped/unclamped IgA mesh into its FE counterpart, both linear and quadratic. Moreover, since the cause of the rupture is still not clear, both from the CFD and the structural viewpoint, another algorithm for the application of the variable pressure field obtained from CFD analyses on the control points of an IgA mesh has been introduced. In particular, the rationale behind this algorithm was applying the real patient-specific pressure distribution obtained from CFD analyses on the control points of the isogeometric model representing the TA to check if the distribution of the von Mises stress at the vessel wall changes with respect to the application of a constant distributed pressure value. At present, the algorithm has only been tested on a cylinder case. In all the three aforementioned collaborations, results are still preliminary but seem very promising in helping physicians to move the diagnosis to the treatment

by means of computational tools.

## 8.1 Future developments

In this doctoral research we created a set of tools to run accurate and effective numerical simulations on healthy and aneurysmatic aortic arteries, with reduced computational costs to keep the pace with the clinical routine timeline. From the computational viewpoint, we confirm the huge impact that IgA can provide with this topic, both in terms of geometrical representations and cost-effective accuracy. Our results can be the first step for several developments, both in terms of technological improvement and other further applications.

In the following, the main future developments for the present work are summarized.

- The use of patient-specific parameters derived from experimental tests for the constitutive models of the aortic wall, the inclusion of intraluminal thrombus, the use of a patient-specific pressure distribution obtained from CFD analyses together with the use of the T-splines technology for geometric modeling of the aortic aneurysm, may represent a big step forward for the study of TAA risk of enlargement and rupture.
- At present, IgA-FEAP analyses with T-splines are restricted to bodies that are represented only by surfaces (e.g., 2-d solid bodies, membranes and shells). Modeling and analysis based on volumetric T-splines should be introduced and applied to patient-specific aortic geometries.
- Even if the IgA results are a good compromise between computational time and accuracy and they showed improved efficiency and accuracy with respect to linear and higher order FEA in the case of the frictionless contact simulations, it is important to remark the following aspects: i) the current IgA-FEAP package does not include parallel implementation; ii) the performed IgA analysis employed the classical FEA  $p+1$  Gauss quadrature which is not exactly the most efficient choice, given the large support of NURBS shape function. Advancements have been already done in this sense (Hughes, Reali, and Sangalli, 2010; Auricchio et al., 2012; Calabro, Sangalli, and Tani, 2017), but they have not been implemented in FEAP yet.
- The results of this doctoral research coupled with the technological improvements in the CAD-world could provide a promising framework for different applications. Thus, one future development may be the creation of an integrated CAD-IgA software for patient-specific modeling to be used in the clinical reality.



## Appendix A

### FEAP NURBS patch input

The following Appendix is presented to give some examples of FEAP input files that show different KNOT vector specifications. In particular, the input files to obtain some of the examples presented in Chapter 2 are provided. For more details, the reader is referred to FEAP isogeometric manual (Taylor, 2017). For a complete understanding of the input data that will be presented, please take into account the following commands:

- NPATch: should include the list of control points index to define the patch. It is possible to specify the patch for a line, a surface or a solid.
- NURBs: should include the control point data for the patch.
- KNOTs: should include the knot vectors specifications for the patch.

A NURBS patch has to be specified using the minimum number of control points, order of the knot vectors and connectivity between the control points. The description may be subsequently refined within the isogeometric FEAP module, employing the refinement algorithms described in Chapter 2.

Currently, four types of knot vectors may be used in FEAP to construct NURBS patches: CLAMPed (open) knot vectors; UNCLAMPed knot vectors; LCLAMPed knot vectors which is clamped at the start values and unclamped at the end values and RCLAMPed which is unclamped at the start values and clamped at the end values. As already described in Chapter 2, clamped (open) knot vectors are interpolatory at the end control point whereas unclamped knot vectors are not interpolatory at the end control point unless the knot vector is repeated to give a  $C^0$  point. In general, one would like to adopt unclamped knot vectors to create closed surfaces and/or to maintain greater than  $C^0$  continuity between patches.

#### CLAMPed (open) knot vectors

Open knot vectors are specified using the following records:

KNOTs

```
CLAMP n1 lknot1 (vk1(i), i=1, lknot1)
CLAMP n2 lknot2 (vk2(i), i=1, lknot2)
```

```
...
! Terminate with blank record
```

where  $n1$  is the knot number,  $lknot1$  is the length of the knot vector and  $vk1(i)$  is the list of open knot values. Clamped (open) knot vectors must begin and end with repeated values and the number of repeated values should be equal to the order of the knot vector + 1. The IgA-FEAP data for the knot and control points of the clamped ring shown in Figure 3.2a is given by:

```
NURBS
1 0 -45.1167 -108.9167 1.0000
2 0 -16.6667 -120.7000 1.0000
3 0 50.0000 -120.7000 1.0000
4 0 120.7000 -50.0000 1.0000
5 0 120.7000 50.0000 1.0000
6 0 50.0000 120.7000 1.0000
7 0 -50.0000 120.7000 1.0000
8 0 -120.7000 50.0000 1.0000
9 0 -120.7000 -50.0000 1.0000
10 0 -73.5667 -97.1333 1.0000
11 0 -45.1167 -108.9167 1.0000

knots
clamped 1 15 3 3 3 3 4 5 6 7 8 9 10 11 11
11 11 !limit of 16 items/records

npatch
line 1 11 1
1 2 3 4 5 6 7 8 9 10 11
```

### UNCLamped (periodic) knot vectors

An unclamped knot vector is specified in FEAP using the following input form:

```
KNOTs
UNCLamp n1 lknot1 order1 (vk1(i),i=1,lknot1)
UNCLamp n2 lknot2 order2 (vk2(i),i=1,lknot2)
...
! Terminate with blank record
```

The mixed types may be specified as:

## KNOTs

```
LCLamp n1 lknot1 order1 (vk1(i), i=1, lknot1)
RCLamp n2 lknot2 order2 (vk2(i), i=1, lknot2)
```

For an LCLamp type knot vector, the initial values of the  $vk(i)$  must be repeated for  $i = 1, \dots, order1 + 1$  times and vice-versa for the RCLamp type, where the last  $order2 + 1$  values of the  $vk2(i)$  must be the same. In the case of unclamped, lclamped or rclamped knot vectors, the order field record **has to be specified** since the knot vector values are not repeated at the beginning and at the end of the  $vk1(i)$  sequence, as in the case of clamped knot vectors.

The FEAP input data for the unclamped closed ring shown in Figure 3.2b is given by:

## NURBS

```
1 0 -120.7 -50.0 1.0
2 0 -50.0 -120.7 1.0
3 0 50.0 -120.7 1.0
4 0 120.7 -50.0 1.0
5 0 120.7 50.0 1.0
6 0 50.0 120.7 1.0
7 0 -50.0 120.7 1.0
8 0 -120.7 50.0 1.0
9 0 -120.7 -50.0 1.0
10 0 -50.0 -120.7 1.0
11 0 50.0 -120.7 1.0
```

## knots

```
unclamped 1 15 3 0 1 2 3 4 5 6 7 8 9 10 11
12 13 14 !limit of 16 items/records
```

## npatch

```
line 1 11 1
1 2 3 4 5 6 7 8 9 10 11
```

## Mix knot vectors types

It is also possible to mix knot vectors types within the same KNOTs groups, i.e., some may be open while others may be unclamped. An example of input data for a closed cylindric surface which shows an unclamped knot vector along the circumferential direction and a clamped one along the longitudinal direction is given by:



## NURBS

```

1 0 -0.0027 -0.9985 0.0 1.0
2 0 0.9484 -0.3105 0.0 1.0
3 0 0.5881 0.8058 0.0 1.0
4 0 -0.5848 0.8085 0.0 1.0
5 0 -0.9508 -0.3068 0.0 1.0
6 0 -0.0027 -0.9985 0.0 1.0
7 0 0.9484 -0.3105 0.0 1.0
8 0 0.5881 0.8058 0.0 1.0
9 0 -0.0027 -0.9985 1.0 1.0
10 0 0.9484 -0.3105 1.0 1.0
11 0 0.5881 0.8058 1.0 1.0
12 0 -0.5848 0.8085 1.0 1.0
13 0 -0.9508 -0.3068 1.0 1.0
14 0 -0.0027 -0.9985 1.0 1.0
15 0 0.9484 -0.3105 1.0 1.0
16 0 0.5881 0.8058 1.0 1.0

```

## knots

```

unclamped 1 12 3 0 1 2 3 4 5 6 7 8 9 10 11
clamped   2 4 0 0 1 1

```

## npatch

```

surf 1 2 8 2 1
1 9
2 10
3 11
4 12
5 13
6 14
7 15
8 16

```

If the reader is interested in unclamping a  $n$ -piece circle with  $(2n+1)$  CPs (i.e. a circle composed of  $n$  circular arches), where the last point  $P_{2n}$  coincides with  $P_0$ , we suggest the use of the strategy presented in (Lu, 2009), in alternative to the one described in (Piegl and Tiller, 1997) and adopted by us in this thesis. As a matter of fact, if we consider the quadratic full circles shown in Figure A.1, the one on top (left) being composed of 4  $C^0$  lines (i.e., four piece circle) and the one on bottom (left) of 3  $C^0$  lines (i.e., three piece circle), by unclamping them using the algorithm in (Piegl and Tiller, 1997), their control polygons *do not* wrap around. This is because the circles are only  $C^0$  continuous in the homogeneous space. The result of the unclamping operation is that the number of  $C^0$  lines is just decreased by one (1) in the final unclamped circle.

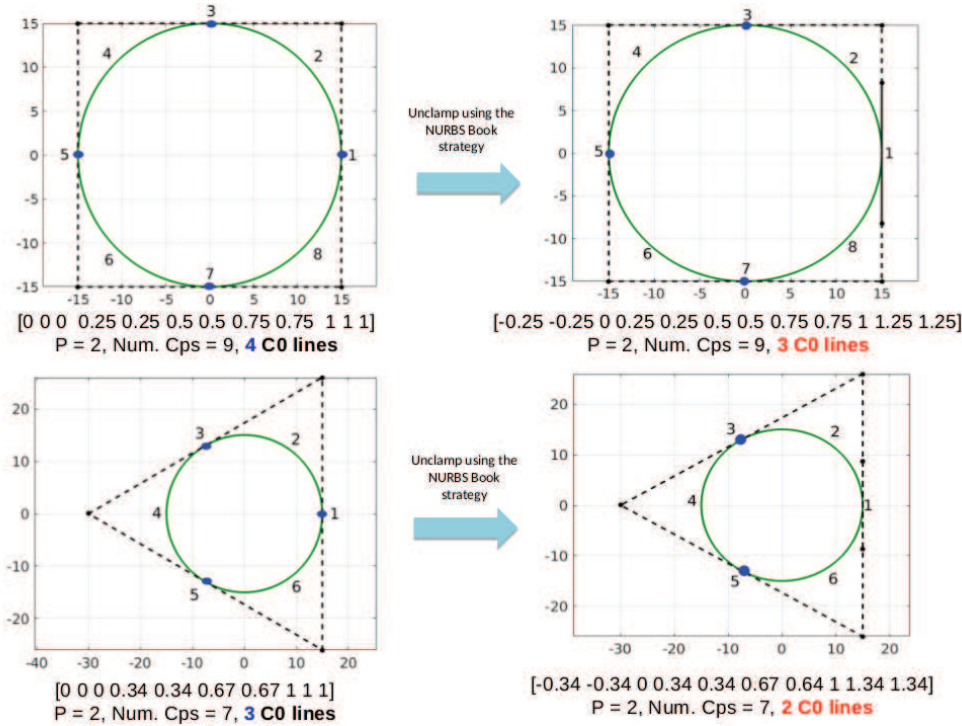
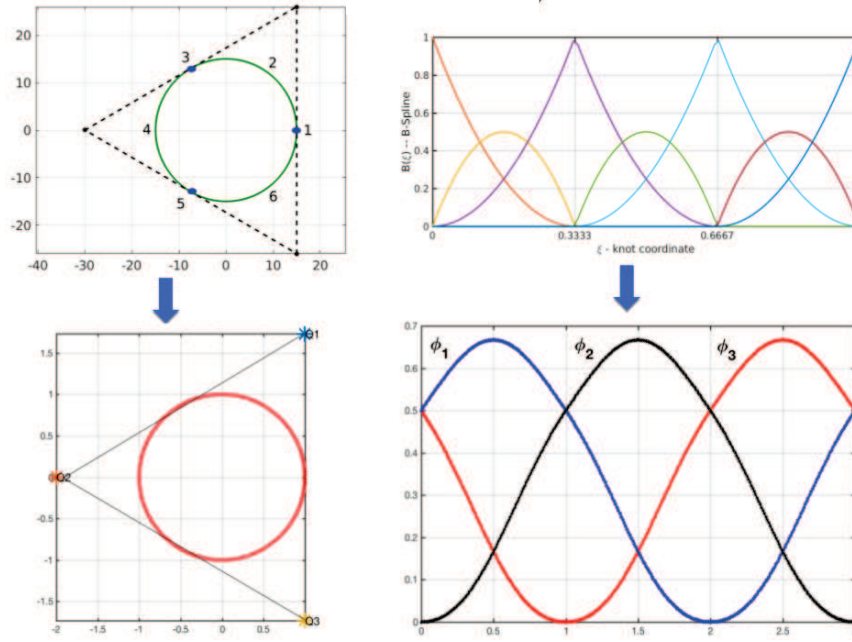
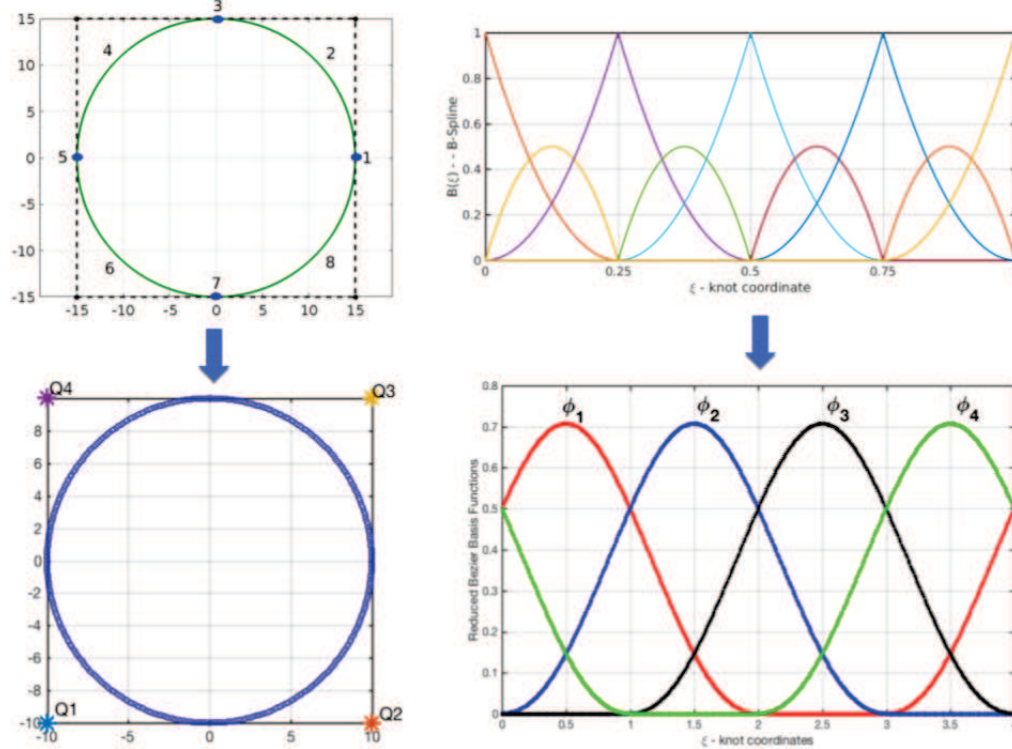


**Figure A.1** Examples of unclamping of a  $n$ -piece circle with  $(2n+1)$  CPs using the strategy described in Chapter 2. The resulting control polygons do not wrap around (see Figures TOP and BOTTOM, RIGHT) because the circles are only  $C^0$  continuous in the homogeneous space. The result of the unclamping is that the number of  $C^0$  lines is just decreased by one (1) in the final unclamped circle.

The use of the strategy proposed in (Lu, 2009), only valid for  $n$ -piece circle with  $(2n+1)$  CPs, permits to perfectly unclamp these circles eliminating all junctions points by setting  $Q_i = P_{2i-1}$  with  $i = 1, 2, \dots, n$  and by re-defining the basis functions in a specific way. The final results show how, by using this algorithm, the total number of control points in the final circle is decreased, together with the number of B-splines basis functions. For an example of application, please see Figures A.2a and A.2b. All that has been said for unclamped B-splines basis functions in Chapter 2, still holds for this algorithm too. In particular, unclamped, uniform B-splines basis functions are all translates of one another, without enjoying at the extremes of a patch the Kronecker delta property, even if still maintaining the partition of unity one. One of the main differences between the strategy in (Piegl and Tiller, 1997) and the one in (Lu, 2009) is that in the second case the B-splines basis functions are redefined in a specific way and their number is decreased with respect to the clamped case. The same, of course, holds for the control point number. This does not happen in the algorithm of (Piegl and Tiller, 1997) because the B-splines basis functions and control points number is kept fixed between the clamped and unclamped model.



(a) Unclamping a circle composed of 3 circular arches.



(b) Unclamping a circle composed of 4 circular arches.

**Figure A.2** Example of unclamping two  $n$ -piece circles by eliminating all junction points (RIGHT, BOTTOM). The difference between the original (RIGHT, TOP) and final (RIGHT, BOTTOM) B-splines basis functions is also showed.

## Appendix B

# Implementation of the Vorp constitutive model in FEAP

The stored energy function for the Raghavan-Vorp model (Raghavan and Vorp, 2000) we implemented in FEAP for the inflation simulations of TAAs may be expressed as:

$$W = C_1 (I_B - 3 - 2 \log(J)) + C_2 (I_B - 3)^2 + U(J) \quad (B.1)$$

$$U(J) = \lambda * \left[ \frac{1}{4} (J^2 - 1) - \frac{1}{2} \log(J) \right] \quad (B.2)$$

with  $U(J)$  being the volumetric term that exists in four models in the current version of FEAP. By replacing  $I_B$  with  $\bar{I}_B = J^{-\frac{2}{3}} I_B$  a similar model for the carbon-black filled rubber developed by O.H. Yeoh (Yeoh, 1990) can be derived. Also this constitutive model is available in FEAP.

The second Piola-Kirchhoff stress can be obtained from the stored energy function  $W$  using:

$$S_{IJ} = 2 \frac{\partial W}{\partial C_{IJ}} = 2\alpha [\delta_{IJ} - C_{IJ}^{-1}] + 4\beta (I_B - 3) \delta_{IJ} \quad (B.3)$$

and the associated tangent moduli:

$$C_{IJKL} = 4 \frac{\partial^2 W}{\partial C_{IJ} \partial C_{KL}} = 2 \frac{\partial S_{IJ}}{\partial C_{KL}} \quad (B.4)$$

$$= -4\alpha \frac{\partial C_{IJ}^{-1}}{\partial C_{KL}} + 8\beta \delta_{IJ} \delta_{KL} \quad (B.5)$$

The derivative of the inverse of  $C_{IJ}$  can be expressed in a symmetric form as:

$$\frac{\partial C_{IJ}^{-1}}{\partial C_{KL}} = -\frac{1}{2}(C_{IK}^{-1}C_{JL}^{-1} + C_{IL}^{-1}C_{JK}^{-1}) \quad (\text{B.6})$$

which gives:

$$C_{IJKL} = 2\alpha(C_{IK}^{-1}C_{JL}^{-1} + C_{IL}^{-1}C_{JK}^{-1}) + 8\beta\delta_{IJ}\delta_{KL} \quad (\text{B.7})$$

These results may be pushed to the current configuration to define the Kirchhoff stress using:

$$\tau_{ij} = F_{iI}S_{IJ}F_{jJ} \quad (\text{B.8})$$

$$c_{ijkl} = F_{iI}F_{jJ}C_{IJKL}F_{kK}F_{lL} \quad (\text{B.9})$$

By applying this to **B** and **B** yields:

$$\tau_{ij} = 2\alpha(b_{ij} - \delta_{ij}) + 4\beta(I_B - 3)b_{ij} \quad (\text{B.10})$$

$$c_{ijkl} = 2\alpha(\delta_{ik}\delta_{jl} + \delta_{il}\delta_{jk}) + 8\beta b_{ij}b_{kl} \quad (\text{B.11})$$

$b_{ij}$  is the left Cauchy-Green tensor. The Cauchy stress and its tangent are then deduced from:

$$\sigma_{ij} = \frac{1}{J}\tau_{ij} \quad (\text{B.12})$$

$$c_{ijkl} = \frac{1}{J}c_{ijkl} \quad (\text{B.13})$$

In order to program it into a finite element framework, which is given in matrix form, the tangent:

$$d\tau_{ij} = c_{ijkl}d\epsilon_{kl} \quad (\text{B.14})$$

is then introduced in matrix form as:

$$d\sigma = Dd\epsilon \quad (\text{B.15})$$

where the stress and its incremental form are given as vectors with 6 components:

$$\sigma = [\sigma_{11} \ \sigma_{22} \ \sigma_{33} \ \sigma_{12} \ \sigma_{23} \ \sigma_{31}]^T \quad (\text{B.16})$$

$$d\epsilon = [d\epsilon_{11} \ d\epsilon_{22} \ d\epsilon_{33} \ d\epsilon_{12} \ d\epsilon_{23} \ d\epsilon_{31}]^T \quad (\text{B.17})$$

with  $d\gamma_{ij} = 2d\epsilon_{ij}$ . Details on the transformation from 9 to 6 components can be found in (Zienkiewicz and Taylor, 2005). The final result for the tangent for the Cauchy stress is given by:

$$D = \frac{2\alpha}{J} \begin{bmatrix} 2 & & & & & \\ & 2 & & & & \\ & & 2 & & & \\ & & & 1 & & \\ & & & & 1 & \\ & & & & & 1 \end{bmatrix} + \frac{8\beta}{J} \mathbf{b}\mathbf{b}^T \quad (\text{B.18})$$

where:

$$\mathbf{b} = [b_{11} \ b_{22} \ b_{33} \ \sqrt{2}b_{12} \ \sqrt{2}b_{23} \ \sqrt{2}b_{31}] \quad (\text{B.19})$$

Two options are now available for the input data in FEAP:

```
ucon vorp
      lambda , , value

      alpha , , value

      beta , , value
```

where "lambda" stands for the first Lamè parameter and "alpha" and "beta" stand for the constants  $C_1$  and  $C_2$  described in Chapter 3. Alternatively, the Young modulus  $E$ , the Poisson modulus  $\nu$  and the "beta" constant (i.e.,  $C_2$ ) can be input:



```

ucon vorp
      E, nu, beta

```

From the values of  $E$  and  $\nu$ , the routine computes "lambda" and "alpha" from:

$$\begin{aligned}\lambda &= \nu * E / (1 + \nu) / (1 - 2 * \nu) \\ \alpha &= E / (1 + \nu) * 4\end{aligned}$$

An example of data for the element type and material property for the Vorp model in FEAP isogeometric module can be given as:

```

PARAMeters
  la = 1000

MATERial 1
  SOLID elmt      0 0 0 0 0
  NURBS, ,3 3 3
  MIXEd
  FINIte VOLUme 1
  UCON VORP
  ELAStic LAMBda la
  ELAStic ALPHa 0.174
  ELAStic BETA 1.881

```

These are the data we used in this work for the inflation simulations of patient-specific TAAs. The material representing the aortic wall is nearly incompressible; consequently the *mixed* formulation described in (Taylor, 2011) is used. All the analyses are performed as a finite deformation problem. Values for the constants  $C_1$  and  $C_2$  are taken from literature (see Chapter 3).

## Appendix C

# T-splines input files for FEAP

In this appendix we are going to provide an example of FEAP input file to run inflation simulations on a T-splines-based object created by means of the Autodesk T-spline plug-in (*Autodesk T-Splines Plug-in for Rhino. T-Splines, Inc.*) embedded in Rhino (*Rhinoceros: NURBS modeling for Windows.*). The T-spline object has to be saved and exported from Rhino in the ".iga" file format. Only surface data can be provided and thus analyses are restricted to bodies that are represented by surfaces (e.g., 2-d solid bodies, membranes and shells). In this thesis work, we are using shells for the analyses. Up to now, in IgA-FEAP, only the Kirchhoff-Love thin-shell element is available. For more details regarding the isogeometric formulation of this shell element, please see (Kiendl et al., 2009).

An example of FEAP input file structure for T-spline is the following:

```
feap * * test on IGA patient-specific T-Spline file
0 0 0 3 3 0
```

MATeRIal 1

```
user 24
elastic isotropic 3 0.46
tspline,,-1,-1 ! Force auto-pick or order
thickness shell 0.1
```

MATeRIal 2

```
press,,1
load,, 0.01596
tspline,,-1,-1 ! Force auto-pick or order
plot off
```

MATeRIal 3

```
robin,,1
elastic ks 10
tspline,,-1,-1 ! Force auto-pick or order
plot off
```

```

! Load the T-spline object
t-spline part=t_spline_file
  plot ints = 1 <1-7> ! Number of subdivision
  material model 1
  file = test.iga

end ! End of data input

inte ! Interactive solution commands

stop ! End of data file

```

In this input file we are loading the "**test.iga**" input file created by means of Autodesk T-spline plug-in for Rhino. Inside "test.iga" all the information required to build the bicubic T-spline mesh shown in Figure C.1 are provided. For a clarification regarding all the fields contained in the ".iga" input file, the reader is referred to (Scott et al., 2014).



**Figure C.1** Example of bicubic T-mesh created in Rhino and imported in FEAP.

We are using the thin-shell element ("**User 24**") to represent the T-spline surface object, with constant thickness equal to 0.1 mm. The constitutive model ("**MATeRial 1**") adopted for this simulation is the linear elastic one, with

parameters from literature ( $E = 3\text{MPa}$ ,  $\nu = 0.46$ ). A constant distributed pressure ("**MATeRial 2**") equal to 120 mmHg (i.e. 0.01596 MPa) is internally applied. With T-spline we also introduced the possibility to use a "variable nodal" pressure, as described in Chapter 7. In this case the input for the pressure should be as follows:

```
MATeRial 2
  pressure,,1
  nodel ! Use "variable nodal" pressure
  tspline,,-1,-1
  plot off

temp=Pressures ! Pressure values
  1 1 1.0
  25 0 1.0
```

In particular, "nodel" is the command that tells FEAP to use "variable nodal" pressure, instead of a constant distributed one. A file containing the pressure values for each T-spline control point should be included and should be provided with the header "temp=Pressure". This file can be directly written in the FEAP input file (as in the example) or simply included using FEAP INCLUDE command. Generalized Robin Boundary Conditions ("**MATeRial 3**") are set to simulate the presence of the organs surrounding the thoracic aorta. Just the elasticity term  $k_s$  is taken into account, with  $k_s = 10$  MPa, as proposed in (Moireau et al., 2012). This structure has been used for all the simulations whose results have been shown in Chapter 4. Once solved the problem, we would like to check the von Mises stress distribution at the vessel wall. This can be achieved in plot mode, by issuing the command "**stre,,16**" for the von Mises force or "**stre,,17**" for the von Mises moment. The von Mises force for the T-spline mesh depicted in Figure C.1, is shown in Figure C.2.

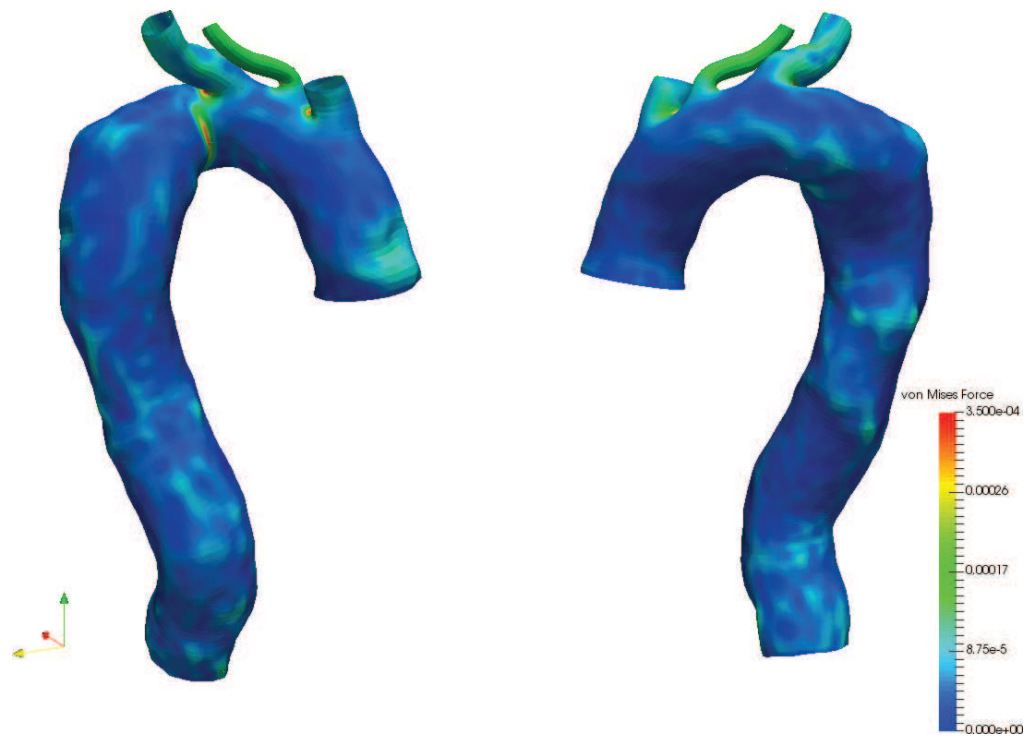


**Figure C.2** von Mises stress result on the patient-specific TA T-spline mesh shown in Figure C.1.

# Bibliography

- Achneck, Hardean E, John A Rizzo, Maryann Tranquilli, and John A Elefteriades (2007). "Safety of thoracic aortic surgery in the present era". In: *The Annals of thoracic surgery* 84.4, pp. 1180–1185 (cit. on p. 10).
- Ahrens, James, Berk Geveci, and Charles Law (2005). "Paraview: An end-user tool for large data visualization". In: *The visualization handbook* 717 (cit. on p. 44).
- Akai, Takafumi, Katsuyuki Hoshina, Sota Yamamoto, Hiroaki Takeuchi, Youkou Nemoto, Marie Ohshima, Kunihiro Shigematsu, Tetsuro Miyata, Haruo Yamauchi, Minoru Ono, et al. (2015). "Biomechanical analysis of an aortic aneurysm model and its clinical application to thoracic aortic aneurysms for defining "saccular" aneurysms". In: *Journal of the American Heart Association* 4.1, e001547 (cit. on p. 15).
- Akkerman, I, Y Bazilevs, VM Calo, TJR Hughes, and S Hulshoff (2008). "The role of continuity in residual-based variational multiscale modeling of turbulence". In: *Computational Mechanics* 41.3, pp. 371–378 (cit. on p. 20).
- Altnji, H-E, B Bou-Said, and H Walter-Le Berre (2015). "Morphological and Stent Design Risks Factors to Prevent Migration Phenomena and Type 1a Endoleak for Thoracic Aneurysm: A Numerical Analysis". In: *European Journal of Vascular and Endovascular Surgery* 49.6, pp. 746–747 (cit. on p. 13).
- Antiga, Luca and David A Steinman (2006). "VMTK: vascular modeling toolkit". In: *VMTK, San Francisco, CA, accessed Apr 27, p. 2015* (cit. on p. 43).
- Antiga, Luca, Marina Piccinelli, Lorenzo Botti, Bogdan Ene-Iordache, Andrea Remuzzi, and David A Steinman (2008). "An image-based modeling framework for patient-specific computational hemodynamics". In: *Medical & biological engineering & computing* 46.11, p. 1097 (cit. on pp. 41, 43, 44).
- Auricchio, F, Francesco Calabro, Thomas JR Hughes, A Reali, and G Sangalli (2012). "A simple algorithm for obtaining nearly optimal quadrature rules for NURBS-based isogeometric analysis". In: *Computer Methods in Applied Mechanics and Engineering* 249, pp. 15–27 (cit. on pp. 20, 141).
- Auricchio, F, M Conti, M Ferraro, S Morganti, A Reali, and RL Taylor (2015). "Innovative and efficient stent flexibility simulations based on isogeometric analysis". In: *Computer Methods in Applied Mechanics and Engineering* 295, pp. 347–361 (cit. on pp. 18, 66).
- Auricchio, Ferdinando and Lorenza Petrini (2004). "A three-dimensional model describing stress-temperature induced solid phase transformations: solution algorithm and boundary value problems". In: *International Journal for Numerical Methods in Engineering* 61.6, pp. 807–836 (cit. on p. 102).
- Auricchio, Ferdinando, Michele Conti, Matthieu De Beule, Gianluca De Santis, and Benedict Verhegghe (2011). "Carotid artery stenting simulation:



- from patient-specific images to finite element analysis". In: *Medical engineering & physics* 33.3, pp. 281–289 (cit. on pp. 98, 107–109).
- Autodesk T-Splines Plug-in for Rhino. <http://www.tsplines.com/products/tsplines-for-rhino.html>. 2015 (cit. on pp. 84, 153).
- Azadani, Ali N, Sam Chitsaz, Alex Mannion, Aart Mookhoek, Andrew Wisneski, Julius M Guccione, Michael D Hope, Liang Ge, and Elaine E Tseng (2013). "Biomechanical properties of human ascending thoracic aortic aneurysms". In: *The Annals of thoracic surgery* 96.1, pp. 50–58 (cit. on p. 16).
- Bakel, TM van, HW De Beaufort, RM Romarowski, M Conti, JA van HERWAARDEN, FL Moll, F Auricchio, Trimarchi S, and MM Marrosso-Trischitta (2017). "Computational analysis of hemodynamic displacement forces in the aorta". In: *ESVB - European Symposium of Vascular Biomaterials* (cit. on pp. 13, 118, 119).
- Bazilevs, Y and I Akkerman (2010). "Large eddy simulation of turbulent Taylor–Couette flow using isogeometric analysis and the residual-based variational multiscale method". In: *Journal of Computational Physics* 229.9, pp. 3402–3414 (cit. on p. 19).
- Bazilevs, Y, VM Calo, JA Cottrell, TJR Hughes, A Reali, and G Scovazzi (2007). "Variational multiscale residual-based turbulence modeling for large eddy simulation of incompressible flows". In: *Computer Methods in Applied Mechanics and Engineering* 197.1-4, pp. 173–201 (cit. on p. 19).
- Bazilevs, Y, JR Gohean, TJR Hughes, RD Moser, and Y Zhang (2009). "Patient-specific isogeometric fluid–structure interaction analysis of thoracic aortic blood flow due to implantation of the Jarvik 2000 left ventricular assist device". In: *Computer Methods in Applied Mechanics and Engineering* 198.45-46, pp. 3534–3550 (cit. on p. 19).
- Bazilevs, Y, Christian Michler, VM Calo, and TJR Hughes (2010a). "Isogeometric variational multiscale modeling of wall-bounded turbulent flows with weakly enforced boundary conditions on unstretched meshes". In: *Computer Methods in Applied Mechanics and Engineering* 199.13-16, pp. 780–790 (cit. on p. 19).
- Bazilevs, Yuri, M-C Hsu, and MA Scott (2012). "Isogeometric fluid–structure interaction analysis with emphasis on non-matching discretizations, and with application to wind turbines". In: *Computer Methods in Applied Mechanics and Engineering* 249, pp. 28–41 (cit. on p. 84).
- Bazilevs, Yuri, Victor M Calo, Yongjie Zhang, and Thomas JR Hughes (2006). "Isogeometric fluid–structure interaction analysis with applications to arterial blood flow". In: *Computational Mechanics* 38.4-5, pp. 310–322 (cit. on p. 19).
- Bazilevs, Yuri, Victor M Calo, Thomas JR Hughes, and Yongjie Zhang (2008). "Isogeometric fluid-structure interaction: theory, algorithms, and computations". In: *Computational mechanics* 43.1, pp. 3–37 (cit. on p. 19).
- Bazilevs, Yuri, Victor M Calo, John A Cottrell, John A Evans, Thomas Jr R Hughes, S Lipton, Michael A Scott, and Thomas W Sederberg (2010b). "Isogeometric analysis using T-splines". In: *Computer Methods in Applied Mechanics and Engineering* 199.5-8, pp. 229–263 (cit. on p. 84).

- Ben-Shlomo, Yoav, Melissa Spears, Chris Boustred, Margaret May, Simon G Anderson, Emelia J Benjamin, Pierre Boutouyrie, James Cameron, Chen-Huan Chen, J Kennedy Cruickshank, et al. (2014). "Aortic pulse wave velocity improves cardiovascular event prediction: an individual participant meta-analysis of prospective observational data from 17,635 subjects". In: *Journal of the American College of Cardiology* 63.7, pp. 636–646 (cit. on p. 14).
- Bertagna, Luca, Simone Deparis, Luca Formaggia, Davide Forti, and Alessandro Veneziani (2017). "The LifeV library: engineering mathematics beyond the proof of concept". In: *arXiv preprint arXiv:1710.06596* (cit. on p. 121).
- Bols, Joris, Joris Degroote, Bram Trachet, Benedict Verhegghe, Patrick Segers, and Jan Vierendeels (2013). "Inverse modelling of image-based patient-specific blood vessels: zero-pressure geometry and in vivo stress incorporation". In: *ESAIM: Mathematical Modelling and Numerical Analysis* 47.4, pp. 1059–1075 (cit. on pp. 62, 72).
- Borden, Michael J, Michael A Scott, John A Evans, and Thomas JR Hughes (2011). "Isogeometric finite element data structures based on Bézier extraction of NURBS". In: *International Journal for Numerical Methods in Engineering* 87.1-5, pp. 15–47 (cit. on pp. 20, 26, 37).
- Borden, Michael J, Clemens V Verhoosel, Michael A Scott, Thomas JR Hughes, and Chad M Landis (2012). "A phase-field description of dynamic brittle fracture". In: *Computer Methods in Applied Mechanics and Engineering* 217, pp. 77–95 (cit. on p. 19).
- Braverman, Alan C, Robert W Thompson, and Luis A Sanchez (2012). "Diseases of the aorta". In: *Braunwald's Heart Disease: A Textbook of Cardiovascular Medicine*, 2, pp. 1309–1337 (cit. on p. 7).
- Brott, Thomas G, Robert W Hobson, George Howard, Gary S Roubin, Wayne M Clark, William Brooks, Ariane Mackey, Michael D Hill, Pierre P Leimgruber, Alice J Sheffet, et al. (2010). "Stenting versus endarterectomy for treatment of carotid-artery stenosis". In: *New England Journal of Medicine* 363.1, pp. 11–23 (cit. on p. 97).
- Brown, Louise C, Janet T Powell, et al. (1999). "Risk factors for aneurysm rupture in patients kept under ultrasound surveillance". In: *Annals of surgery* 230.3, p. 289 (cit. on p. 7).
- Bueno, Jesus, Carles Bona-Casas, Yuri Bazilevs, and Hector Gomez (2015). "Interaction of complex fluids and solids: theory, algorithms and application to phase-change-driven implosion". In: *Computational Mechanics* 55.6, pp. 1105–1118 (cit. on p. 19).
- Buffa, Annalisa, Giancarlo Sangalli, and Rafael Vázquez (2010). "Isogeometric analysis in electromagnetics: B-splines approximation". In: *Computer Methods in Applied Mechanics and Engineering* 199.17-20, pp. 1143–1152 (cit. on p. 19).
- Calabro, Francesco, Giancarlo Sangalli, and Mattia Tani (2017). "Fast formation of isogeometric Galerkin matrices by weighted quadrature". In: *Computer Methods in Applied Mechanics and Engineering* 316, pp. 606–622 (cit. on pp. 20, 141).

- Callanan, A, LG Morris, and TM McGloughlin (2004). "Numerical and experimental analysis of an idealised abdominal aortic aneurysm". In: *European Society of Biomechanics, S-Hertogenbosch, Netherlands* (cit. on p. 65).
- Carnelli, Davide, Giancarlo Pennati, Tomaso Villa, Luigi Baglioni, Bernhard Reimers, and Francesco Migliavacca (2011). "Mechanical Properties of Open-Cell, Self-Expandable Shape Memory Alloy Carotid Stents". In: *Artificial organs* 35.1, pp. 74–80 (cit. on p. 101).
- Casquero, Hugo, Carles Bona-Casas, and Hector Gomez (2015). "A NURBS-based immersed methodology for fluid–structure interaction". In: *Computer Methods in Applied Mechanics and Engineering* 284, pp. 943–970 (cit. on p. 19).
- Casquero, Hugo, Lei Liu, Carles Bona-Casas, Yongjie Zhang, and Hector Gomez (2016). "A hybrid variational-collocation immersed method for fluid-structure interaction using unstructured T-splines". In: *International Journal for Numerical Methods in Engineering* 105.11, pp. 855–880 (cit. on p. 19).
- Casquero, Hugo, Lei Liu, Yongjie Zhang, Alessandro Reali, Josef Kiendl, and Hector Gomez (2017). "Arbitrary-degree t-splines for isogeometric analysis of fully nonlinear kirchhoff–love shells". In: *Computer-Aided Design* 82, pp. 140–153 (cit. on p. 19).
- Chaikof, Elliot L, Mark F Fillinger, Jon S Matsumura, Robert B Rutherford, Geoffrey H White, Jan D Blankensteijn, Victor M Bernhard, Peter L Harris, K Craig Kent, James May, et al. (2002). "Identifying and grading factors that modify the outcome of endovascular aortic aneurysm repair". In: *Journal of vascular surgery* 35.5, pp. 1061–1066 (cit. on p. 120).
- Chau, Katherine H. and John A. Elefteriades (2013). "Natural History of Thoracic Aortic Aneurysms: Size Matters, Plus Moving Beyond Size". In: *Progress in Cardiovascular Diseases* 56.1, pp. 74–80 (cit. on p. 7).
- Choke, E, G Cockerill, WRW Wilson, S Sayed, J Dawson, I Loftus, and MM Thompson (2005). "A review of biological factors implicated in abdominal aortic aneurysm rupture". In: *European Journal of Vascular and Endovascular Surgery* 30.3, pp. 227–244 (cit. on p. 16).
- Coady, Michael A, John A Rizzo, Graeme L Hammond, Divakar Mandapati, Umer Darr, Gary S Kopf, and John A Elefteriades (1997). "What is the appropriate size criterion for resection of thoracic aortic aneurysms?" In: *The Journal of thoracic and cardiovascular surgery* 113.3, pp. 476–491 (cit. on p. 16).
- Conti, Michele, Ferdinando Auricchio, Matthieu De Beule, and Benedict Verhegghe (2009). "Numerical simulation of Nitinol peripheral stents: from laser-cutting to deployment in a patient specific anatomy". In: *8th European Symposium on Martensitic Transformations (ESOMAT 2009)*. EDP Sciences (cit. on pp. 107, 108).
- Conti, Michele, Denis Van Loo, Ferdinando Auricchio, Matthieu De Beule, Gianluca De Santis, Benedict Verhegghe, Stefano Pirrelli, and Attilio Odero (2011). "Impact of carotid stent cell design on vessel scaffolding: a case study comparing experimental investigation and numerical simulations". In: *Journal of Endovascular Therapy* 18.3, pp. 397–406 (cit. on pp. 98, 102, 107, 108).

- Cottrell, J Austin, Thomas JR Hughes, and Yuri Bazilevs (2009). *Isogeometric analysis: toward integration of CAD and FEA*. John Wiley & Sons (cit. on pp. 19, 20).
- Cottrell, J Austin, Alessandro Reali, Yuri Bazilevs, and Thomas JR Hughes (2006). "Isogeometric analysis of structural vibrations". In: *Computer methods in applied mechanics and engineering* 195.41-43, pp. 5257–5296 (cit. on p. 19).
- Criado, Frank J (2011). "Aortic dissection: a 250-year perspective". In: *Texas Heart Institute Journal* 38.6, p. 694 (cit. on p. 8).
- Dalcin, Lisandro, Nathan Collier, Philippe Vignal, AMA Côrtes, and Victor M Calo (2016). "PetIGA: A framework for high-performance isogeometric analysis". In: *Computer Methods in Applied Mechanics and Engineering* 308, pp. 151–181 (cit. on p. 19).
- D'Angella, Davide, Stefan Kollmannsberger, Ernst Rank, and Alessandro Reali (2018). "Multi-level Bézier extraction for hierarchical local refinement of Isogeometric Analysis". In: *Computer Methods in Applied Mechanics and Engineering* 328, pp. 147–174 (cit. on p. 20).
- Davies, Ryan R, Lee J Goldstein, Michael A Coady, Shawn L Tittle, John A Rizzo, Gary S Kopf, and John A Elefteriades (2002). "Yearly rupture or dissection rates for thoracic aortic aneurysms: simple prediction based on size". In: *The Annals of thoracic surgery* 73.1, pp. 17–28 (cit. on p. 16).
- De Lorenzis, L, I Temizer, P Wriggers, and G Zavarise (2011). "A large deformation frictional contact formulation using NURBS-based isogeometric analysis". In: *International Journal for Numerical Methods in Engineering* 87.13, pp. 1278–1300 (cit. on pp. 19, 100, 140).
- Dimitri, R, L De Lorenzis, MA Scott, P Wriggers, RL Taylor, and G Zavarise (2014). "Isogeometric large deformation frictionless contact using T-splines". In: *Computer methods in applied mechanics and engineering* 269, pp. 394–414 (cit. on pp. 84, 100).
- Dörfel, Michael R, Bert Jüttler, and Bernd Simeon (2010). "Adaptive isogeometric analysis by local h-refinement with T-splines". In: *Computer methods in applied mechanics and engineering* 199.5-8, pp. 264–275 (cit. on p. 84).
- Doyle, Barry J, Anthony Callanan, Paul E Burke, Pierce A Grace, Michael T Walsh, David A Vorp, and Timothy M McGloughlin (2009). "Vessel asymmetry as an additional diagnostic tool in the assessment of abdominal aortic aneurysms". In: *Journal of vascular surgery* 49.2, pp. 443–454 (cit. on p. 41).
- Eggebrecht, Holger, Matt Thompson, Herve Rousseau, Martin Czerny, Lars Lönn, et al. (2008). *Retrograde Ascending Aortic Dissection During or After Thoracic Aortic Stent-Graft Placement-Insights from the European Registry on EVAR Complications (EUREC)* (cit. on p. 14).
- Elefteriades, John A (2002). "Natural history of thoracic aortic aneurysms: indications for surgery, and surgical versus nonsurgical risks". In: *The Annals of thoracic surgery* 74.5, S1877–S1880 (cit. on pp. 7, 14, 16).
- Elefteriades, John A and Emily A Farkas (2010). "Thoracic aortic aneurysm". In: *Journal of the American College of Cardiology* 55.9, pp. 841–857 (cit. on p. 16).



- Erbel, Raimund, Victor Aboyans, Catherine Boileau, Eduardo Bossone, Roberto Di Bartolomeo, Holger Eggebrecht, Arturo Evangelista, Volkmar Falk, Herbert Frank, Oliver Gaemperli, et al. (2015). "2014 ESC Guidelines on the Diagnosis and Treatment of Aortic Diseases". In: *Revista Espanola de Cardiologia (English Edition)* 3.68, p. 242 (cit. on pp. 5–7, 11, 13, 15, 43).
- Escobar, JM, JM Cascón, E Rodríguez, and R Montenegro (2011). "A new approach to solid modeling with trivariate T-splines based on mesh optimization". In: *Computer Methods in Applied Mechanics and Engineering* 200.45–46, pp. 3210–3222 (cit. on p. 84).
- Evans, EJ, MA Scott, X Li, and DC Thomas (2015). "Hierarchical T-splines: Analysis-suitability, Bézier extraction, and application as an adaptive basis for isogeometric analysis". In: *Computer Methods in Applied Mechanics and Engineering* 284, pp. 1–20 (cit. on p. 84).
- Faggiano, Elena, Luca Formaggia, Luca Antiga, et al. (2013). "An open-source tool for patient-specific fluid-structure vessel mesh generation". In: (cit. on p. 57).
- Falco, Carlo de, Alessandro Reali, and Rafael Vázquez (2011). "GeoPDEs: a research tool for Isogeometric Analysis of PDEs". In: *Advances in Engineering Software* 42.12, pp. 1020–1034 (cit. on pp. 19, 29, 51, 138).
- Farin, Gerald E and Gerald Farin (2002). *Curves and surfaces for CAD: a practical guide*. Morgan Kaufmann (cit. on pp. 19, 22, 23, 34).
- Fedkiw, Stanley Osher Ronald and Stanley Osher (2002). "Level set methods and dynamic implicit surfaces". In: *Surfaces* 44, p. 77 (cit. on p. 43).
- Ferraro, Mauro, Ferdinando Auricchio, Elisa Boatti, Giulia Scalet, Michele Conti, Simone Morganti, and Alessandro Reali (2015). "An efficient finite element framework to assess flexibility performances of SMA self-expandable carotid artery stents". In: *Journal of functional biomaterials* 6.3, pp. 585–597 (cit. on pp. 102, 105).
- Figuerola, C Alberto, Charles A Taylor, Allen J Chiou, Victoria Yeh, and Christopher K Zarins (2009). "Magnitude and direction of pulsatile displacement forces acting on thoracic aortic endografts". In: *Journal of Endovascular Therapy* 16.3, pp. 350–358 (cit. on p. 119).
- Fillinger, Mark (2007). "Who Should We Operate On and How Do We Decide: Predicting Rupture and Survival in Patients with Aortic Aneurysm". In: *Seminars in Vascular Surgery* 20.2, pp. 121–127 (cit. on p. 16).
- Fillinger, Mark F, Madhavan L Raghavan, Steven P Marra, Jack L Cronenwett, and Francis E Kennedy (2002). "In vivo analysis of mechanical wall stress and abdominal aortic aneurysm rupture risk". In: *Journal of vascular surgery* 36.3, pp. 589–597 (cit. on pp. 17, 57, 118).
- Fillinger, Mark F, Steven P Marra, Madhavan L Raghavan, and Francis E Kennedy (2003). "Prediction of rupture risk in abdominal aortic aneurysm during observation: wall stress versus diameter". In: *Journal of vascular surgery* 37.4, pp. 724–732 (cit. on pp. 16, 17, 57, 118).
- Fillinger, Mark F, Roy K Greenberg, James F McKinsey, and Elliot L Chaikof (2010). "Reporting standards for thoracic endovascular aortic repair (TEVAR)". In: *Journal of vascular surgery* 52.4, pp. 1022–1033 (cit. on p. 14).

- Fung, George SK, SK Lam, Stephen WK Cheng, and KW Chow (2008). "On stent-graft models in thoracic aortic endovascular repair: a computational investigation of the hemodynamic factors". In: *Computers in biology and medicine* 38.4, pp. 484–489 (cit. on p. 119).
- Gasser, T Christian (2016). "Biomechanical rupture risk assessment: A consistent and objective decision-making tool for abdominal aortic aneurysm patients". In: *AORTA Journal* 4.2, p. 2 (cit. on pp. 64, 118).
- Gee, MW, Ch Reeps, HH Eckstein, and WA Wall (2009). "Prestressing in finite deformation abdominal aortic aneurysm simulation". In: *Journal of biomechanics* 42.11, pp. 1732–1739 (cit. on p. 61).
- Geers, MGD, V Kouznetsova, and WAM Brekelmans (2001). "Gradient-enhanced computational homogenization for the micro-macro scale transition". In: *Le Journal de Physique IV* 11.PR5, Pr5–145 (cit. on p. 124).
- Goldfinger, Judith Z, Jonathan L Halperin, Michael L Marin, Allan S Stewart, Kim A Eagle, and Valentin Fuster (2014). "Thoracic aortic aneurysm and dissection". In: *Journal of the American College of Cardiology* 64.16, pp. 1725–1739 (cit. on pp. 7, 14).
- Gomez, Hector and Laura De Lorenzis (2016). "The variational collocation method". In: *Computer Methods in Applied Mechanics and Engineering* 309, pp. 152–181 (cit. on p. 20).
- Gómez, Héctor, Victor M Calo, Yuri Bazilevs, and Thomas JR Hughes (2008). "Isogeometric analysis of the Cahn–Hilliard phase-field model". In: *Computer methods in applied mechanics and engineering* 197.49-50, pp. 4333–4352 (cit. on p. 19).
- Gomez, Hector, Thomas JR Hughes, Xesús Nogueira, and Victor M Calo (2010). "Isogeometric analysis of the isothermal Navier–Stokes–Korteweg equations". In: *Computer Methods in Applied Mechanics and Engineering* 199.25-28, pp. 1828–1840 (cit. on p. 19).
- Goodney, Philip P, Lori Travis, F Lee Lucas, Mark F Fillinger, David C Goodman, Jack L Cronenwett, and David H Stone (2011). "Survival after open versus endovascular thoracic aortic aneurysm repair in an observational study of the Medicare population". In: *Circulation*, CIRCULATIONAHA-111 (cit. on p. 11).
- Gopaladas, Raja R, Joseph Huh, Tam K Dao, Scott A LeMaire, Danny Chu, Faisal G Bakaeen, and Joseph S Coselli (2010). "Superior nationwide outcomes of endovascular versus open repair for isolated descending thoracic aortic aneurysm in 11,669 patients". In: *The Journal of thoracic and cardiovascular surgery* 140.5, pp. 1001–1010 (cit. on p. 11).
- Grabenwöger, Martin, Fernando Alfonso, Jean Bachet, Robert Bonser, Martin Czerny, Holger Eggebrecht, Arturo Evangelista, Rossella Fattori, Heinz Jakob, Lars Lönn, et al. (2012). "Thoracic Endovascular Aortic Repair (TEVAR) for the treatment of aortic diseases: a position statement from the European Association for Cardio-Thoracic Surgery (EACTS) and the European Society of Cardiology (ESC), in collaboration with the European Association of Percutaneous Cardiovascular Interventions (EAPCI)". In: *European heart journal* 33.13, pp. 1558–1563 (cit. on p. 14).



- Grogan, James A, Sean B Leen, and Peter E McHugh (2012). "Comparing coronary stent material performance on a common geometric platform through simulated bench testing". In: *Journal of the mechanical behavior of biomedical materials* 12, pp. 129–138 (cit. on p. 98).
- Hartnell, George G (2001). "Imaging of aortic aneurysms and dissection: CT and MRI". In: *Journal of thoracic imaging* 16.1, pp. 35–46 (cit. on p. 43).
- Heng, Michael S., Michael J. Fagan, Jason W. Collier, Grishma Desai, Peter T. McCollum, and Ian C. Chetter (2008). "Peak wall stress measurement in elective and acute abdominal aortic aneurysms". In: *Journal of Vascular Surgery* 47.1, pp. 17–22 (cit. on pp. 17, 118).
- Hsu, Ming-Chen, David Kamensky, Fei Xu, Josef Kiendl, Chenglong Wang, Michael CH Wu, Joshua Mineroff, Alessandro Reali, Yuri Bazilevs, and Michael S Sacks (2015). "Dynamic and fluid–structure interaction simulations of bioprosthetic heart valves using parametric design with T-splines and Fung-type material models". In: *Computational mechanics* 55.6, pp. 1211–1225 (cit. on pp. 18, 19).
- Hughes, Thomas JR, John A Cottrell, and Yuri Bazilevs (2005). "Isogeometric analysis: CAD, finite elements, NURBS, exact geometry and mesh refinement". In: *Computer methods in applied mechanics and engineering* 194.39-41, pp. 4135–4195 (cit. on pp. 17, 19, 42).
- Hughes, Thomas JR, Alessandro Reali, and Giancarlo Sangalli (2010). "Efficient quadrature for NURBS-based isogeometric analysis". In: *Computer methods in applied mechanics and engineering* 199.5-8, pp. 301–313 (cit. on pp. 20, 141).
- Indrakusuma, R, H Jalalzadeh, RN Planken, HA Marquering, DA Legemate, MJW Koelemay, and R Balm (2016). "Biomechanical Imaging Markers as Predictors of Abdominal Aortic Aneurysm Growth or Rupture: A Systematic Review". In: *European Journal of Vascular and Endovascular Surgery* 52.4, pp. 475–486 (cit. on p. 66).
- Johnston, K Wayne, Robert B Rutherford, M David Tilson, Dhiraj M Shah, Larry Hollier, James C Stanley, et al. (1991). "Suggested standards for reporting on arterial aneurysms". In: *Journal of vascular surgery* 13.3, pp. 452–458 (cit. on p. 7).
- Kallenbach, Klaus, Dubravka Kojic, Merve Oezsoez, Thomas Bruckner, Stany Sandrio, Rawa Arif, Carsten J Beller, Alexander Weymann, and Matthias Karck (2013). *Treatment of ascending aortic aneurysms using different surgical techniques: a single-centre experience with 548 patients* (cit. on p. 10).
- Kälsch, Hagen, Nils Lehmann, Stefan Möhlenkamp, Anna Becker, Susanne Moebus, Axel Schmermund, Andreas Stang, Amir A Mahabadi, Klaus Mann, Karl-Heinz Jöckel, et al. (2013). "Body-surface adjusted aortic reference diameters for improved identification of patients with thoracic aortic aneurysms: results from the population-based Heinz Nixdorf Recall study". In: *International journal of cardiology* 163.1, pp. 72–78 (cit. on p. 7).
- Kicska, Gregory and Harold Litt (2009). "Preprocedural planning for endovascular stent-graft placement". In: *Seminars in interventional radiology*. Vol. 26. 1. Thieme Medical Publishers, p. 44 (cit. on p. 11).

- Kiendl, Josef, K-U Bletzinger, J Linhard, and Roland Wüchner (2009). "Isogeometric shell analysis with Kirchhoff–Love elements". In: *Computer Methods in Applied Mechanics and Engineering* 198.49-52, pp. 3902–3914 (cit. on pp. 19, 86, 153).
- Kiendl, Josef, Ming-Chen Hsu, Michael CH Wu, and Alessandro Reali (2015). "Isogeometric Kirchhoff–Love shell formulations for general hyperelastic materials". In: *Computer Methods in Applied Mechanics and Engineering* 291 (cit. on p. 18).
- Kim, HJ, IE Vignon-Clementel, JS Coogan, CA Figueroa, KE Jansen, and CA Taylor (2010). "Patient-specific modeling of blood flow and pressure in human coronary arteries". In: *Annals of biomedical engineering* 38.10, pp. 3195–3209 (cit. on p. 41).
- Kleinstreuer, C, Z Li, CA Basciano, S Seelecke, and MA Farber (2008). "Computational mechanics of Nitinol stent grafts". In: *Journal of biomechanics* 41.11, pp. 2370–2378 (cit. on p. 98).
- Kouznetsova, V, WAM Brekelmans, and FPT Baaijens (2001). "An approach to micro-macro modeling of heterogeneous materials". In: *Computational mechanics* 27.1, pp. 37–48 (cit. on p. 124).
- Krishnan, Kapil, Liang Ge, Henrik Haraldsson, Michael D Hope, David A Saloner, Julius M Guccione, and Elaine E Tseng (2015). "Ascending thoracic aortic aneurysm wall stress analysis using patient-specific finite element modeling of in vivo magnetic resonance imaging". In: *Interactive cardiovascular and thoracic surgery* 21.4, pp. 471–480 (cit. on p. 17).
- Ku, David N, Don P Giddens, Christopher K Zarins, and Seymour Glagov (1985). "Pulsatile flow and atherosclerosis in the human carotid bifurcation. Positive correlation between plaque location and low oscillating shear stress." In: *Arteriosclerosis, thrombosis, and vascular biology* 5.3, pp. 293–302 (cit. on p. 8).
- Kuratani, Toru (2014). "Best surgical option for arch extension of type B dissection: the endovascular approach". In: *Annals of cardiothoracic surgery* 3.3, p. 292 (cit. on p. 12).
- Kuzmik, Gregory A, Adam X Sang, and John A Elefteriades (2012). "Natural history of thoracic aortic aneurysms". In: *Journal of vascular surgery* 56.2, pp. 565–571 (cit. on pp. 7, 14).
- Lam, Carolyn SP, Vanessa Xanthakis, Lisa M Sullivan, Wolfgang Lieb, Jayashri Aragam, Margaret M Redfield, Gary F Mitchell, Emelia J Benjamin, and Ramachandran S Vasan (2010). "Aortic root remodeling over the adult life course: longitudinal data from the Framingham Heart Study". In: *Circulation* 122.9, pp. 884–890 (cit. on p. 6).
- Li, Xin and Michael A Scott (2014). "Analysis-suitable T-splines: Characterization, refineability, and approximation". In: *Mathematical Models and Methods in Applied Sciences* 24.06, pp. 1141–1164 (cit. on p. 84).
- Li, Xin, Jianmin Zheng, Thomas W Sederberg, Thomas JR Hughes, and Michael A Scott (2012). "On linear independence of T-spline blending functions". In: *Computer Aided Geometric Design* 29.1, pp. 63–76 (cit. on p. 84).
- Li, Zhi-Yong, Umar Sadat, U Jean, Tjun Y Tang, David J Bowden, Paul D Hayes, Jonathan H Gillard, et al. (2010). "Association Between Aneurysm

- Shoulder Stress and Abdominal Aortic Aneurysm Expansion". In: *Circulation* 122.18, pp. 1815–1822 (cit. on pp. 17, 118).
- Liu, Lei, Yongjie Zhang, Thomas JR Hughes, Michael A Scott, and Thomas W Sederberg (2014). "Volumetric T-spline construction using Boolean operations". In: *Engineering with Computers* 30.4, pp. 425–439 (cit. on p. 84).
- Liu, Lei, Yongjie Zhang, Yang Liu, and Wenping Wang (2015). "Feature-preserving T-mesh construction using skeleton-based polycubes". In: *Computer-Aided Design* 58, pp. 162–172 (cit. on p. 84).
- Lorentz, George G (2012). *Bernstein polynomials*. American Mathematical Soc. (cit. on p. 21).
- Lu, Jia (2009). "Circular element: Isogeometric elements of smooth boundary". In: *Computer methods in applied mechanics and engineering* 198.30-32, pp. 2391–2402 (cit. on pp. 146, 147).
- Malek, Adel M, Seth L Alper, and Seigo Izumo (1999). "Hemodynamic shear stress and its role in atherosclerosis". In: *Jama* 282.21, pp. 2035–2042 (cit. on p. 8).
- Marrocco-Trischitta, Massimiliano M, Hector W de Beaufort, Francesco Secchi, Theodorus M van Bakel, Marco Ranucci, Joost A Van Herwaarden, Frans L Moll, and Santi Trimarchi (2017). "A geometric reappraisal of proximal landing zones for thoracic endovascular aortic repair according to aortic arch types". In: *Journal of vascular surgery* 65.6, pp. 1584–1590 (cit. on pp. 118–121).
- Marrocco-Trischitta, Massimiliano M, Theodorus M van Bakel, Rodrigo M Romarowski, Hector W de Beaufort, Michele Conti, Joost A van Herwaarden, Frans L Moll, Ferdinando Auricchio, and Santi Trimarchi (2018). "The Modified Arch Landing Areas Nomenclature (MALAN) Improves Prediction of Stent Graft Displacement Forces: Proof of Concept by Computational Fluid Dynamics Modelling". In: *European Journal of Vascular and Endovascular Surgery* 55.4, pp. 584–592 (cit. on p. 119).
- Martin, Caitlin, Wei Sun, and John Elefteriades (2015). "Patient-specific finite element analysis of ascending aorta aneurysms". In: *American Journal of Physiology-Heart and Circulatory Physiology* 308.10, H1306–H1316 (cit. on pp. 17, 64, 118).
- Martufi, Giampaolo, Arianna Forneris, Jehangir J Appoo, and Elena S Di Martino (2016). "Is there a role for biomechanical engineering in helping to elucidate the risk profile of the thoracic aorta?" In: *The Annals of thoracic surgery* 101.1, pp. 390–398 (cit. on p. 17).
- MATLAB (2018). *version 9.4.0 (R2018a)*. Natick, Massachusetts: The MathWorks Inc. (cit. on pp. 51, 138).
- Moireau, Philippe, Nan Xiao, Matteo Astorino, C Alberto Figueroa, Dominique Chapelle, CA Taylor, and J-F Gerbeau (2012). "External tissue support and fluid–structure simulation in blood flows". In: *Biomechanics and modeling in mechanobiology* 11.1-2, pp. 1–18 (cit. on pp. 61, 86, 138, 155).
- Morganti, S, F Auricchio, DJ Benson, FI Gambarin, S Hartmann, TJR Hughes, and A Reali (2015). "Patient-specific isogeometric structural analysis of aortic valve closure". In: *Computer Methods in Applied Mechanics and Engineering* 284, pp. 508–520 (cit. on pp. 18, 49, 66).

- Moro, Hisanaga, Jun-ichi Hayashi, and Masakazu Sogawa (1999). "Surgical management of the ruptured aortic arch." In: *The Annals of thoracic surgery* 67.2, pp. 593–594 (cit. on p. 9).
- Morris, L, P O'Donnell, P Delassus, and T McGloughlin (2004). "Experimental assessment of stress patterns in abdominal aortic aneurysms using the photoelastic method". In: *Strain* 40.4, pp. 165–172 (cit. on pp. 58, 65).
- Mortier, Peter, Gerhard A Holzapfel, Matthieu De Beule, Denis Van Loo, Yves Taeymans, Patrick Segers, Pascal Verdonck, and Benedict Verhegghe (2010). "A novel simulation strategy for stent insertion and deployment in curved coronary bifurcations: comparison of three drug-eluting stents". In: *Annals of biomedical engineering* 38.1, pp. 88–99 (cit. on p. 98).
- Nathan, Derek P, Chun Xu, Joseph H Gorman III, Ron M Fairman, Joseph E Bavaria, Robert C Gorman, Krishnan B Chandran, and Benjamin M Jackson (2011). "Pathogenesis of acute aortic dissection: a finite element stress analysis". In: *The Annals of thoracic surgery* 91.2, pp. 458–463 (cit. on pp. 86, 87).
- Neal, Maxwell Lewis and Roy Kerckhoffs (2009). "Current progress in patient-specific modeling". In: *Briefings in bioinformatics* 11.1, pp. 111–126 (cit. on p. 41).
- Pasta, Salvatore, Antonino Rinaudo, Angelo Luca, Michele Pilato, Cesare Scardulla, Thomas G Gleason, and David A Vorp (2013). "Difference in hemodynamic and wall stress of ascending thoracic aortic aneurysms with bicuspid and tricuspid aortic valve". In: *Journal of biomechanics* 46.10, pp. 1729–1738 (cit. on p. 15).
- Pauletti, M Sebastian, Massimiliano Martinelli, Nicola Cavallini, and Pablo Antolin (2015). "Igatools: An isogeometric analysis library". In: *SIAM Journal on Scientific Computing* 37.4, pp. C465–C496 (cit. on p. 19).
- Perreas, Konstantinos, George Samanidis, Stergios Dimitriou, Panagiotis Kalogris, Marina Balanika, Christina Antzaka, Mazen Khoury, and Alkiviadis Michalis (2012). "Outcomes after ascending aorta and proximal aortic arch repair using deep hypothermic circulatory arrest with retrograde cerebral perfusion: analysis of 207 patients". In: *Interactive cardiovascular and thoracic surgery* 15.3, pp. 456–461 (cit. on p. 10).
- Petrini, Lorenza, Francesco Migliavacca, Ferdinando Auricchio, and Gabriele Dubini (2004). "Numerical investigation of the intravascular coronary stent flexibility". In: *Journal of biomechanics* 37.4, pp. 495–501 (cit. on p. 101).
- Petrini, Lorenza, Francesco Migliavacca, Paolo Massarotti, Silvia Schievano, Gabriele Dubini, and Ferdinando Auricchio (2005). "Computational studies of shape memory alloy behavior in biomedical applications". In: *Journal of biomechanical engineering* 127.4, pp. 716–725 (cit. on pp. 101, 102).
- Piccinelli, Marina, Alessandro Veneziani, David A Steinman, Andrea Remuzzi, and Luca Antiga (2009). "A framework for geometric analysis of vascular structures: application to cerebral aneurysms". In: *IEEE transactions on medical imaging* 28.8, pp. 1141–1155 (cit. on p. 43).
- Piegl, LA and Wayne Tiller (1997). *The Nurbs Book (Monograph in Visual Communications)* (cit. on pp. 19, 22, 23, 25, 29, 33, 34, 51, 53, 146, 147).



- Polzer, Stanislav and T Christian Gasser (2015). "Biomechanical rupture risk assessment of abdominal aortic aneurysms based on a novel probabilistic rupture risk index". In: *Journal of The Royal Society Interface* 12.113, p. 20150852 (cit. on p. 16).
- Raghavan, Madhavan L, David A Vorp, Michael P Federle, Michel S Makaroun, and Marshall W Webster (2000). "Wall stress distribution on three-dimensionally reconstructed models of human abdominal aortic aneurysm". In: *Journal of vascular surgery* 31.4, pp. 760–769 (cit. on pp. 57, 61, 65).
- Raghavan, ML and David A Vorp (2000). "Toward a biomechanical tool to evaluate rupture potential of abdominal aortic aneurysm: identification of a finite strain constitutive model and evaluation of its applicability". In: *Journal of biomechanics* 33.4, pp. 475–482 (cit. on pp. 60, 62, 138, 149).
- Raut, Samarth S, Anirban Jana, Victor De Oliveira, Satish C Muluk, and Ender A Finol (2013). "The importance of patient-specific regionally varying wall thickness in abdominal aortic aneurysm biomechanics". In: *Journal of biomechanical engineering* 135.8, p. 081010 (cit. on p. 57).
- Rebelo, Nuno, Rachel Fu, and Michael Lawrenchuk (2009). "Study of a nitinol stent deployed into anatomically accurate artery geometry and subjected to realistic service loading". In: *Journal of materials engineering and performance* 18.5-6, pp. 655–663 (cit. on p. 102).
- Rhinoceros: NURBS modeling for Windows. <http://www.rhino3d.com> (cit. on pp. 33, 38, 84, 102, 153).
- Roffi, M and K Mathias (2013). "History of carotid artery stenting." In: *The Journal of cardiovascular surgery* 54.1, pp. 1–10 (cit. on p. 97).
- Rogers, David F (2000). *An introduction to NURBS: with historical perspective*. Elsevier (cit. on pp. 19, 22, 23, 34).
- Romarowski, Rodrigo M, Adrien Lefieux, A Veneziani, S Morganti, and Ferdinando Auricchio (2018). "Patient-Specific CFD modeling in the Thoracic Aorta with PC-MRI Based Boundary Conditions: a Least-Square 3-Element Windkessel approach". In: *International journal for numerical methods in biomedical engineering* (cit. on pp. 61, 121).
- Sachs, Teviah, Frank Pomposelli, Robert Hagberg, Allen Hamdan, Mark Wyers, Kristina Giles, and Marc Schermerhorn (2010). "Open and endovascular repair of type B aortic dissection in the Nationwide Inpatient Sample". In: *Journal of vascular surgery* 52.4, pp. 860–866 (cit. on p. 11).
- Schillinger, Dominik, Luca Dede, Michael A Scott, John A Evans, Michael J Borden, Ernst Rank, and Thomas JR Hughes (2012). "An isogeometric design-through-analysis methodology based on adaptive hierarchical refinement of NURBS, immersed boundary methods, and T-spline CAD surfaces". In: *Computer Methods in Applied Mechanics and Engineering* 249, pp. 116–150 (cit. on p. 84).
- Scott, MA, TJR Hughes, TW Sederberg, and MT Sederberg (2014). "An integrated approach to engineering design and analysis using the Autodesk T-spline plugin for Rhino3d. ICES REPORT 14-33". In: *The Institute for Computational Engineering and Sciences, The University of Texas at Austin* (cit. on pp. 86, 154).

- Scott, Michael A, Michael J Borden, Clemens V Verhoosel, Thomas W Sederberg, and Thomas JR Hughes (2011). "Isogeometric finite element data structures based on Bézier extraction of T-splines". In: *International Journal for Numerical Methods in Engineering* 88.2, pp. 126–156 (cit. on pp. 20, 38, 86).
- Scott, Michael A, Xin Li, Thomas W Sederberg, and Thomas JR Hughes (2012). "Local refinement of analysis-suitable T-splines". In: *Computer Methods in Applied Mechanics and Engineering* 213, pp. 206–222 (cit. on p. 84).
- Scott, Michael A, Robert N Simpson, John A Evans, Scott Lipton, Stephane PA Bordas, Thomas JR Hughes, and Thomas W Sederberg (2013). "Isogeometric boundary element analysis using unstructured T-splines". In: *Computer Methods in Applied Mechanics and Engineering* 254, pp. 197–221 (cit. on pp. 37, 84).
- Scotti, Christine M, Alexander D Shkolnik, Satish C Muluk, and Ender A Finol (2005). "Fluid-structure interaction in abdominal aortic aneurysms: effects of asymmetry and wall thickness". In: *Biomedical engineering online* 4.1, p. 64 (cit. on pp. 61, 65).
- Shang, Eric K, Derek P Nathan, Shanna R Sprinkle, Ronald M Fairman, Joseph E Bavaria, Robert C Gorman, Joseph H Gorman, and Benjamin M Jackson (2013a). "Impact of wall thickness and saccular geometry on the computational wall stress of descending thoracic aortic aneurysms". In: *Circulation* 128.11 suppl 1, S157–S162 (cit. on pp. 61, 124).
- Shang, Eric K., Derek P. Nathan, Shanna R. Sprinkle, Sarah C. Vigmostad, Ronald M. Fairman, Joseph E. Bavaria, Robert C. Gorman, Joseph H. Gorman, Krishnan B. Chandran, and Benjamin M. Jackson (2013b). "Peak Wall Stress Predicts Expansion Rate in Descending Thoracic Aortic Aneurysms", in: *The Annals of Thoracic Surgery* 95.2, pp. 593–598 (cit. on pp. 15, 17, 118).
- Souza, Angela C, Edgar N Mamiya, and Nestor Zouain (1998). "Three-dimensional model for solids undergoing stress-induced phase transformations". In: *European Journal of Mechanics-A/Solids* 17.5, pp. 789–806 (cit. on pp. 102, 108).
- Spink, M (2014). "NURBS toolbox". In: *Matlab Central [online]* 15 (cit. on pp. 29, 51, 138).
- T-Splines, Inc. <http://www.tsplines.com/products/tsplines-for-rhino.html> (cit. on pp. 38, 84, 153).
- Taylor, Charles A and CA Figueroa (2009). "Patient-specific modeling of cardiovascular mechanics". In: *Annual review of biomedical engineering* 11, pp. 109–134 (cit. on p. 41).
- Taylor, Charles A, Thomas JR Hughes, and Christopher K Zarins (1996). "Computational investigations in vascular disease". In: *Computers in Physics* 10.3, pp. 224–232 (cit. on p. 41).
- (1998). "Finite element modeling of three-dimensional pulsatile flow in the abdominal aorta: relevance to atherosclerosis". In: *Annals of biomedical engineering* 26.6, pp. 975–987 (cit. on p. 41).
- Taylor, Charles A and David A Steinman (2010). "Image-based modeling of blood flow and vessel wall dynamics: applications, methods and future



- directions". In: *Annals of biomedical engineering* 38.3, pp. 1188–1203 (cit. on p. 41).
- Taylor, RL (2011). "Isogeometric analysis of nearly incompressible solids". In: *International Journal for Numerical Methods in Engineering* 87.1-5, pp. 273–288 (cit. on pp. 66, 152).
- Taylor, R.L. (2017). *FEAP - A Finite Element Analysis Program, User Manual*. [projects.ce.berkeley.edu/feap](http://projects.ce.berkeley.edu/feap). University of California, Berkeley. (cit. on pp. 2, 24, 60, 63, 138, 143).
- Temizer, I, P Wriggers, and TJR Hughes (2011). "Contact treatment in isogeometric analysis with NURBS". In: *Computer Methods in Applied Mechanics and Engineering* 200.9-12, pp. 1100–1112 (cit. on p. 100).
- Thériault, Philippe, Patrick Terriault, Vladimir Brailovski, and Richard Gallo (2006). "Finite element modeling of a progressively expanding shape memory stent". In: *Journal of biomechanics* 39.15, pp. 2837–2844 (cit. on p. 102).
- Urick, B, TM Sanders, SS Hossain, Y Zhang, and TJR Hughes (2017). "Patient-Specific Vascular Modeling: Template-based Isogeometric Framework and the Case for CAD. ICES REPORT 14-33". In: *The Institute for Computational Engineering and Sciences, The University of Texas at Austin* (cit. on p. 48).
- Veiga, L Beirao da, Annalisa Buffa, D Cho, and G Sangalli (2012). "Analysis-suitable T-splines are dual-compatible". In: *Computer methods in applied mechanics and engineering* 249, pp. 42–51 (cit. on p. 84).
- Venkatasubramaniam, A.K, M.J Fagan, T Mehta, K.J Mylankal, B Ray, G Kuhan, I.C Chetter, and P.T McCollum (2004). "A Comparative Study of Aortic Wall Stress Using Finite Element Analysis for Ruptured and Non-ruptured Abdominal Aortic Aneurysms". In: *European Journal of Vascular and Endovascular Surgery* 28.2, pp. 168–176 (cit. on pp. 17, 118).
- Verhoosel, Clemens V, Michael A Scott, Thomas JR Hughes, and Rene De Borst (2011a). "An isogeometric analysis approach to gradient damage models". In: *International Journal for Numerical Methods in Engineering* 86.1, pp. 115–134 (cit. on p. 19).
- Verhoosel, Clemens V, Michael A Scott, Rene De Borst, and Thomas JR Hughes (2011b). "An isogeometric approach to cohesive zone modeling". In: *International Journal for Numerical Methods in Engineering* 87.1-5, pp. 336–360 (cit. on p. 19).
- Vilanova, Guillermo, Ignasi Colominas, and Hector Gomez (2013). "Capillary networks in tumor angiogenesis: From discrete endothelial cells to phase-field averaged descriptions via isogeometric analysis". In: *International journal for numerical methods in biomedical engineering* 29.10, pp. 1015–1037 (cit. on p. 19).
- (2014). "Coupling of discrete random walks and continuous modeling for three-dimensional tumor-induced angiogenesis". In: *Computational Mechanics* 53.3, pp. 449–464 (cit. on p. 19).
- Vorp, David A (2007). "Biomechanics of abdominal aortic aneurysm". In: *Journal of biomechanics* 40.9, pp. 1887–1902 (cit. on p. 16).
- Vorp, David A., M.L. Raghavan, and Marshall W. Webster (1998a). "Mechanical wall stress in abdominal aortic aneurysm: Influence of diameter and asymmetry". In: *Journal of Vascular Surgery* 27.4, pp. 632–639 (cit. on p. 16).

- Vorp, David A, ML Raghavan, and Marshall W Webster (1998b). "Mechanical wall stress in abdominal aortic aneurysm: influence of diameter and asymmetry". In: *Journal of Vascular Surgery* 27.4, pp. 632–639 (cit. on p. 65).
- Vriz, Olga, Caterina Driussi, Manola Bettio, Francesco Ferrara, Antonello D'Andrea, and Eduardo Bossone (2013). "Aortic root dimensions and stiffness in healthy subjects". In: *The American journal of cardiology* 112.8, pp. 1224–1229 (cit. on p. 6).
- Wall, Wolfgang A, Moritz A Frenzel, and Christian Cyron (2008). "Isogeometric structural shape optimization". In: *Computer methods in applied mechanics and engineering* 197.33-40, pp. 2976–2988 (cit. on p. 19).
- Wang, Wenyan, Yongjie Zhang, Michael A Scott, and Thomas JR Hughes (2011). "Converting an unstructured quadrilateral mesh to a standard T-spline surface". In: *Computational Mechanics* 48.4, pp. 477–498 (cit. on p. 84).
- Wang, Wenyan, Yongjie Zhang, Guoliang Xu, and Thomas JR Hughes (2012). "Converting an unstructured quadrilateral/hexahedral mesh to a rational T-spline". In: *Computational Mechanics* 50.1, pp. 65–84 (cit. on p. 84).
- Wang, Wenyan, Yongjie Zhang, Lei Liu, and Thomas JR Hughes (2013). "Trivariate solid T-spline construction from boundary triangulations with arbitrary genus topology". In: *Computer-Aided Design* 45.2, pp. 351–360 (cit. on p. 84).
- Wang, Xiaohong and Xiaoyang Li (2011). "Fluid-structure interaction based study on the physiological factors affecting the behaviors of stented and non-stented thoracic aortic aneurysms". In: *Journal of Biomechanics* 44.12, pp. 2177–2184 (cit. on p. 119).
- Wisneski, Andrew D, Aart Mookhoek, Sam Chitsaz, Michael D Hope, Julius M Guccione, Liang Ge, and Elaine E Tseng (2014). "Patient-specific finite element analysis of ascending thoracic aortic aneurysm". In: *The Journal of heart valve disease* 23.6, p. 765 (cit. on p. 17).
- Wriggers, Peter and Udo Nackenhorst (2006). *Analysis and simulation of contact problems*. Vol. 1. Springer (cit. on pp. 98, 101).
- Xu, Fei, Simone Morganti, Rana Zakerzadeh, David Kamensky, Ferdinando Auricchio, Alessandro Reali, Thomas JR Hughes, Michael S Sacks, and Ming-Chen Hsu (2018). "A framework for designing patient-specific bioprosthetic heart valves using immersogeometric fluid–structure interaction analysis". In: *International journal for numerical methods in biomedical engineering* 34.4, e2938 (cit. on p. 18).
- Xu, Jiangping, Guillermo Vilanova, and Hector Gomez (2016). "A mathematical model coupling tumor growth and angiogenesis". In: *PloS one* 11.2, e0149422 (cit. on p. 19).
- Yeoh, OH (1990). "Characterization of elastic properties of carbon-black-filled rubber vulcanizates". In: *Rubber chemistry and technology* 63.5, pp. 792–805 (cit. on p. 149).
- Zhang, Yongjie, Wenyan Wang, and Thomas JR Hughes (2012). "Solid T-spline construction from boundary representations for genus-zero geometry". In: *Computer Methods in Applied Mechanics and Engineering* 249, pp. 185–197 (cit. on p. 84).
- (2013). "Conformal solid T-spline construction from boundary T-spline representations". In: *Computational Mechanics* 51.6, pp. 1051–1059 (cit. on p. 84).

- Zhang, Yongjie, Yuri Bazilevs, Samrat Goswami, Chandrajit L Bajaj, and Thomas JR Hughes (2007). "Patient-specific vascular NURBS modeling for isogeometric analysis of blood flow". In: *Computer methods in applied mechanics and engineering* 196.29-30, pp. 2943–2959 (cit. on p. 18).
- Zienkiewicz, Olek C and Robert L Taylor (2005). *The finite element method for solid and structural mechanics*. Elsevier (cit. on pp. 124, 151).